Secular evolution of stellar clusters

Kerwann Tep

To cite this version:

Kerwann Tep. Secular evolution of stellar clusters. Astrophysics [astro-ph]. Sorbonne Université, 2023. English. NNT : 2023SORUS700 . tel-04557629

HAL Id: tel-04557629
https://theses.hal.science/tel-04557629v1

Submitted on 24 Apr 2024

Sorbonne Université

Ecole doctorale 127 Astronomie et Astrophysique d'Ile-de-France
Institut d'Astrophysique de Paris

Secular evolution of stellar clusters

Par Kerwann Tep

Thèse de doctorat d'Astronomie & Astrophysique

Dirigée par M. Christophe Pichon
M. Jean-Baptiste Fouvry

Présentée et soutenue publiquement le 18 septembre 2023

Devant un jury composé de :

M.	Michael Joyce	Président du jury
M.	Christophe Pichon	Directeur de thèse
M.	Jean-Baptiste Fouvry	Co-directeur de thèse
M.	Douglas C. Heggie	Rapporteur
M.	Eugene Vasiliev	Rapporteur
Mme	Anna Lisa Varri	Examinatrice
M.	John Magorrian	Examinateur
M.	Sven de Rijcke	Examinateur

Abstract

Stellar systems in the Universe are mainly driven by gravity, a long-range force affecting every massive object. Recent surveys have produced a formidable quantity of data capturing the kinetic properties of the Galaxy and its components (such as globular clusters and its nucleus). Decades of research have allowed the astrophysical community to reach a good understanding of the formation of gravitationally bound structures: the Λ-CDM model. Still, the long-term evolution of these systems remains an ongoing subject of research.

My thesis is focused on the evolution of gravitational systems on such secular timescales. My triple objective is: (i) to understand the particular mechanisms which operate on these long timescales; (ii) to identify the origin of the observed differences depending on the nature of these objects (geometry, kinematics, composition, ...); (iii) to deduce diagnostics for dark matter experiments (e.g., the identification of populations of intermediate mass black holes).

In practice, this thesis aims at describing the secular fate of isolated stellar clusters by relying on kinetic theory. The master equation describing self-gravitating clusters over many orbital times is the Balescu–Lenard diffusion equation. It captures perturbatively the effect of resonant interactions between noise-driven fluctuations within the system. In this thesis, I specifically study two approximations of the Balescu–Lenard equation: (i) the inhomogeneous Landau limit, in which collective amplification is neglected; (ii) the (orbit-averaged) Chandrasekhar limit, in which local, incoherent deflections dominate over long-range resonances.

I apply these formalisms to a variety of systems. First, I study the Galactic nucleus, where I present a fiducial likelihood analysis to probe the presence of intermediate mass black holes around Sgr A*. Second, I consider globular clusters with kinematic anisotropy and ultimately rotation. I first apply the extended non-resonant approach, which I validate by using large sets of direct N-body simulations. This allows me to investigate the rate of core collapse and the diffusion of orbital inclinations. I also study the impact of resonant relaxation on the effective Coulomb logarithm from the non-resonant formulation. Finally, I probe the space of physical parameters of galactic discs which are prone to bi-symmetric instabilities. Using linear response theory, I study the onset of bars. This allows me to understand the lack of bars in galactic discs observed in current hydrodynamical simulations.

Résumé

Les systèmes stellaires de l'Univers sont principalement régis par la gravité, une force à longue portée qui affecte tous les objets massifs. Des études récentes ont permis de recueillir une quantité considérable de données sur la cinétique de la Galaxie et de ses composants (tels que ses amas globulaires et son noyau). Des décennies de recherche ont permis à la communauté astrophysique de parvenir à une bonne compréhension de la formation des structures gravitationnellement liées : le modèle Λ-CDM. Cependant, l'évolution à long terme de ces systèmes reste un sujet de recherche intense.

Ma thèse se concentre sur l'évolution des systèmes gravitationnels sur ces échelles de temps séculaires. Mes objectifs sont triples: (i) comprendre les mécanismes particuliers qui opèrent sur ces échelles de temps longs ; (ii) identifier l'origine des différences observées en fonction de la nature de ces objets (géométrie, cinématique, composition, ...) ; (iii) déduire des diagnostics pour des expériences de matière noire (par exemple, l'identification de populations de trous noirs de masse intermédiaire).

Cette thèse vise donc à décrire le destin séculaire des amas stellaires isolés en s'appuyant sur la théorie cinétique. L'équation maîtresse décrivant les amas autogravitants sur de nombreux temps orbitaux est l'équation de diffusion de Balescu–Lenard. Elle capture de manière perturbative l'effet des interactions résonantes entre les fluctuations issues du bruit au sein du système. Dans cette thèse, j'étudie deux approximations de l'équation de Balescu–Lenard : (i) la limite de Landau inhomogène, dans laquelle l'amplification collective est négligée ; (ii) la limite de Chandrasekhar (moyennée sur les orbites), dans laquelle les déviations locales incohérentes dominent sur les résonances à longue portée.

J'applique ces formalismes à des systèmes variés. Tout d'abord, j'étudie le noyau Galactique, où je présente une analyse de vraisemblance pour sonder la présence de trous noirs de masse intermédiaire autour de Sgr A*. Deuxièmement, je considère les amas globulaires avec une anisotropie cinématique et éventuellement de la rotation. J'applique d'abord une extension de l'approche non-résonante, que je valide en utilisant un jeu important de simulations directes à N-corps. Cela me permet d'étudier le taux d'effondrement du noyau et la diffusion des inclinaisons orbitales. J'étudie également l'impact de la relaxation résonante sur le logarithme de Coulomb effectif qui intervient dans la formulation non-résonante. Enfin, je sonde l'espace des paramètres physiques des disques galactiques qui sont sujets à des instabilités bi-symétriques. En utilisant la théorie de la réponse linéaire, je quantifie le contexte propice à l'apparition des barres. Cela me permet d'expliquer l'absence de barres dans les disques galactiques observée dans les simulations hydrodynamiques actuelles.

Plagiarism disclaimer

I hereby declare that I am the author of all the following, except when stated explicitly.

Section 2.2 is inspired from Chavanis (2012) and Fouvry (2020).

Section 3.2 relies on Fouvry et al. (2017), while the rest of the chapter relies on results from Tep et al. (2021).

Chapter 4 is based on results from Tep et al. (2022).

The derivation presented in section 6.2 is based on the work of Aoki et al. (1979). The rest of the chapter is based on my contribution to Reddish et al. (2022).

Data distribution

The codes used in this thesis are distributed on `Github` at the following URLs:

- Chapter 3: https://github.com/KerwannTEP/JuDOKA.
- Chapter 4: https://github.com/KerwannTEP/CAT.
- Chapter 5: https://github.com/KerwannTEP/CARP.
- Chapter 6: https://github.com/KerwannTEP/LiRA.

Contents

Chapter 1

Introduction

Studying the long-term evolution of astrophysical objects is a fascinating yet challenging task because it typically involves non-linear processes. Physicists have attempted to address this challenge over many decades by the use of three main techniques: observation, simulation and kinetic theory. For the most massive objects in the Universe, the principal force which drives the evolution is gravity, a long-range interaction. Its action is the cause for many observable phenomena. Gravity indeed drives the evolution of numerous large and complex structures, from entire galaxies to stellar clusters such as galactic nuclei or globular clusters.

Until recently, the precision of observations of globular clusters were found to be in agreement with the convenient model of isotropic stellar systems with no rotation. For this reason, most theoretical and numerical works have focused on this particular restrictive class of objects. However, the last few decades have been especially fruitful in the evolution of the precision of observations (HST, VLT, GAIA, ...), but also in the development of the precision and size of numerical simulations. Indeed, because these objects can also be straightforwardly studied using numerical simulations – either via N-body or Monte-Carlo methods – they have become fantastic laboratories to study spheroidal systems with complex kinematics.

For *spheroidal galaxies*, integral field spectroscopy now allows for a precise reconstruction of their galactic phase space structure (Wisnioski et al., 2019). These galaxies present anisotropy and rotation. Such kinematic features may reflect their past dynamical history. Recent astrometric data on Galactic globular clusters also unveiled the $6D$ phase space of such structures as never probed before, revealing that anisotropy and rotation are usually present at various degrees (Bianchini et al., 2018; Sollima et al., 2019; Vasiliev, 2019b). Finally, integral field spectroscopy also revealed the high degree of rotation of *nuclear star clusters* (NSCs) (Seth et al., 2008b; Feldmeier et al., 2014). These observations can be used to constrain formation scenarii for NSCs, in relation with the build-up of the angular momentum of supermassive black holes (SMBHs) (Seth et al., 2008a).

Hence most stellar clusters, from galactic to nuclear, have some level of a kinetic reservoir of free energy, which allows them to evolve into more likely configurations given enough stimuli (internal or external). The topic of my Ph.D. is to study such an evolution in the regime where it operates sufficiently slowly so that it can be described perturbatively. This evolution then falls into the framework of kinetic theory, which I will describe and apply in the next chapters. I will in particular show how it recovers the mean behaviour of N-body simulations when averaging over the range of possible initial conditions.

1.1 Context

The Λ-CDM model (Springel et al., 2006; Weinberg et al., 2013) is the product of years of accumulated research, and is currently the best model to describe our observations of the Universe. The evolution of the Universe can be roughly described along the following chronology. First, immediately after the Big Bang, quantum field fluctuations in the density of non-baryonic dark matter occurred (Bardeen et al., 1986). Then, as a result of a very short period of inflation (Guth, 1981; Linde, 1982), these fluctuations were stretched by the fast expansion of space-time. This mechanism produced the temperature fluctuations seen in the cosmic microwave background (CMB) (see Fig. 1.1). This map, which probes the temperature map of the early Universe (see, e.g., Schlegel et al., 1998; Hinshaw et al., 2013; Planck Collaboration et al., 2020) can be linked to the present large structures of the observable Universe. Indeed, after the end of the inflation era, gravity accentuates over-densities and under-densities. With enough time, this has led to the formation (Davis et al., 1985; Bond et al., 1996) of hierarchical over-dense regions (see Fig. 1.2), in which galaxies were able to develop (Frenk & White, 2012).

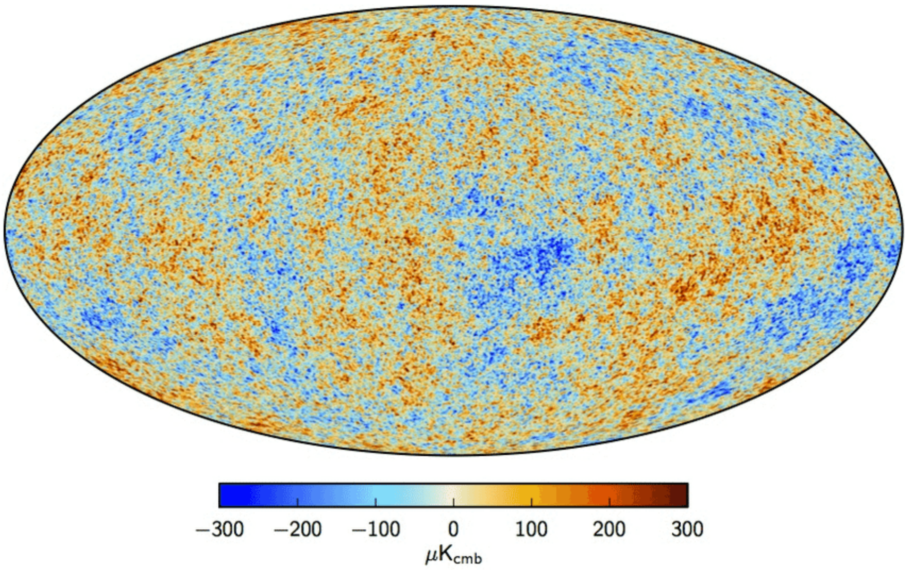

Figure 1.1: The map of CMB temperature fluctuations $\Delta T/T$ over the whole sky, as measured by the Planck satellite (Planck Collaboration et al., 2016). The foreground emission from the Milky Way galaxy and the dipole component due to the motion of the galaxy relative to the CMB have been removed. The colours from blue to red indicate the magnitude of under-density to over-density. The large structures we observe in the Universe come from these density fluctuations.

In this picture, galaxies are naturally embedded in their cosmic environment. As such, their respective evolutions are inevitably coupled with each other. They can be impacted by violent and destructive events such as mergers (Fig. 1.3) with other galaxies (see, e.g., Murali et al., 2002). They can also undergo smoother perturbing events such as constructive inflows of cold gas along a cosmic filament (see, e.g., Katz et al., 2003; Kereš et al., 2005; Pichon et al., 2011). Additionally, perturbations of a more stochastic nature can impact a galaxy's evolution regardless of its cosmic neighbourhood. On the one hand, one can mention violent, punctual but recurrent events such as supernovae explosions (Fig. 1.4; see, e.g., Spitzer, 1978; Madau & Dickinson, 2014) or turbulence-driven noise (see, e.g., Frisch, 1995). On the other hand, one can highlight the finite-N nature of the galaxy (i.e. the finite number of stars or clumps it contains, such as giant molecular clouds). This induces Poisson fluctuations of its internal gravitational potential, hence can drive a slow, long-term evolution. As an example, this seemingly tight in-

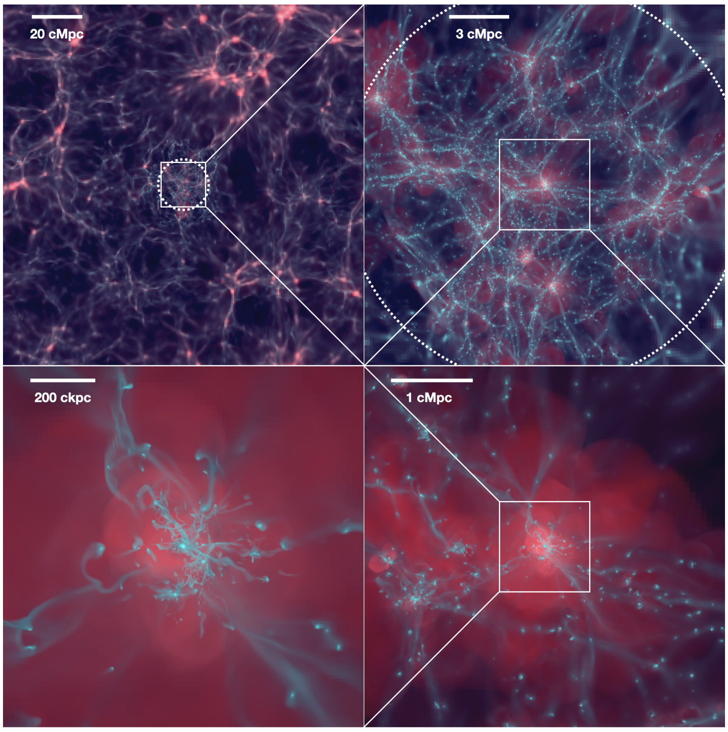

Figure 1.2: From fig. 1 of Dubois et al. (2021). Sequential zoom (clockwise from top left) over the projected density (silver blue colours) and projected temperature (red) of the NewHorizon simulation at redshift $z = 2$. Units are in co-moving Mpc. On large scales (top panels), one can observe the filamentary structure. Through the successive zoom-ins, the hierarchical structure of the large scale structures appears. On the bottom left panel, massive galaxies make up the node where very narrow filaments converge together, feeding them with cold gas to form stars.

Figure 1.3: Imaging of *Stephan's Quintet* by the James Webb Space Telescope (JWST). Four of the five galaxies (excluding the leftmost one) are physically close and are merging with one another. In the process, this interaction disturbs the distribution of gas in the galaxies, which triggers, e.g., star formation events. Such events also perturb the gas flow in its vicinity, hence induce potential fluctuations. Image credit: NASA, ESA, CSA, and STScI.

Figure 1.4: Imaging of the supernova 1994D in the galaxy NGC 4526 (the luminous dot located at the bottom left of the galaxy) by the Hubble Space Telescope (HST). During a brief time period, supernovae emit a considerable amount of light, comparable to that of their host galaxy. Credit: NASA/ESA.

terplay between inner and external perturbations can drive the apparition of bars in the centre of galaxies (Combes & Elmegreen, 1993; Sellwood, 2012; Reddish et al., 2022). This is what I refer to as *secular evolution*, because it operates on long timescales and induces slow changes in the mean field, hence changes the galaxy's orbital structure. This competition is also the rule for other stellar systems: (i) galactic nuclei, which are stellar systems dominated by a supermassive object at their centre – a SMBH; (ii) globular clusters, which are very dense stellar clusters containing 10^5 – 10^6 stars typically within $\sim 1\mathrm{pc}^3$.

An open question in that context is to determine which of inner or external perturbations tend to dominate the secular fate of these objects. To do so, it is necessary to determine the relative impact of each perturbation. In addition, the acceleration of the expansion of the universe as a result of *dark energy* (Planck Collaboration et al., 2020) tends to rarefy violent merging events – and more generally any interaction with the cosmic environment. One may argue that the eventual future of stellar clusters is isolation from their environment, which makes their study interesting on its own.

A combination of factors motivates this study now more than ever before.

First, the emergence of new data, e.g., GAIA (Gaia Collaboration et al., 2016, 2018, 2021) and other grand surveys such as 4MOST (de Jong et al., 2019), JWST (Gardner et al., 2006) and Weave (Dalton et al., 2012, 2016; Jin et al., 2023), make it now possible to have access to samples of many galaxies (together with some knowledge of their internal kinematics) over secular times. This can be achieved either by studying the kinematics of the present-day galaxies (*galactic archaeology*), or by studying the evolution of galaxies as a function of cosmic time (lightcone studies). This opens the prospect of stacking galaxies so as to leverage the expected diversity of their individual long-term non-linear evolution.

Moreover, important advancements have been achieved in gravitational kinetic theory – which aims at describing the long-term behaviour of a whole system – in the past decade. Historically, the description of the long-term evolution of stellar clusters relied on local, two-body deflections (see, e.g., Chandrasekhar, 1943; Hénon, 1961; Cohn & Kulsrud, 1978; Cohn, 1979, 1980; Inagaki & Wiyanto, 1984; Spitzer, 1987; Lee, 1987; Quinlan & Shapiro, 1989; Chernoff & Weinberg, 1990; Murphy et al., 1991; Merritt, 2009, 2013; Vasiliev, 2015, 2017) using simplifying assumptions such as local homogeneity and infinite extent.

These approaches did not attempt to take into account the importance of self-gravity, which can be expected to impact significantly the secular fate of dynamically cold objects (such as discs, see e.g., Sellwood, 2012). Nonetheless, several steps have been achieved in that direction early on. Kalnajs (1976) developed the matrix method to study the linear response theory of self-gravitating galactic discs. Starting from the inhomogeneous Landau equation derived by Polyachenko & Shukhman (1982), Weinberg (1993) carried out a first seminal investigation of the importance of collective effects. In particular, he showed how the properties of the noise present in the systems can impact the orbital diffusion coefficients (see also Weinberg, 2001a,b). Rauch & Tremaine (1996) highlighted an enhanced rate of angular momentum relaxation in galactic nuclei which cannot be explained using Chandrasekhar relaxation theory. However, it is only recently that a full description of the effects of fluctuations was derived, in the form of the Balescu–Lenard equation (Heyvaerts, 2010; Chavanis, 2012; Fouvry & Bar-Or, 2018; Hamilton, 2021). This equation describes the secular (long-term) *collisional* (i.e. under the effect of internal fluctuations) evolution of a self-gravitating system, and takes into account the amplification of fluctuations by self-gravity. In particular, it encompasses the previously mentioned formalisms, such as the Landau equation (Chavanis, 2013b).

The Balescu–Lenard equation captures the diffusion of the orbital structure, a phenomenon sharing deep similarities with the process of diffusion (Fig. 1.5) studied by Einstein (1905) and Langevin (1908) and rooted in the fundamental fluctuation-dissipation theorem. Under the action of the fluctuations of the gravitational forces of the cluster, the orbits of the stars undergo a non-local, resonant diffusion.

Figure 1.5: A picture of the diffusion of ink in water. The process of *long-range resonant orbital diffusion* discussed in this thesis – occurring in *action space* – is similar to the process of *local diffusion* of ink – occurring in *physical space*.

Most interestingly, the Balescu–Lenard equation was applied recently to a variety of systems. Among those, I can mention the following applications:

- The first investigation was the secular evolution of a *tepid galactic disc*. Using first a Wentzel–Kramers–Brillouin (WKB) approximation (Fouvry et al., 2015a) and then the matrix method

(Fouvry et al., 2015c; De Rijcke et al., 2019a), these authors were able to recover the numerical observations made earlier by Sellwood (2012) for razor-thin and thick galactic discs.

- Its application to *galactic nuclei* led to the description of eccentricity relaxation of the quasi-Keplerian orbits (Bar-Or & Fouvry, 2018), and recovered numerical observations made by Merritt et al. (2011).
- The secular evolution of bars was investigated in the context of the so-called *inhomogeneous Hamiltonian mean field model* (Benetti & Marcos, 2017). It showed how collective effects could affect the secular relaxation of a system.
- Using the *periodic cube* as a proxy for multiperiodic stellar systems, Weinberg (1993) and Magorrian (2021) explored the impact of collective effects near the Jeans instability, i.e. near marginal stability.
- Later on, Roule et al. (2022) studied *1D self-gravitating systems* and showed that collective effects could damp the system's response instead of amplifying it.
- Interestingly, the relaxation of *isotropic globular clusters* (Hamilton et al., 2018; Lau & Binney, 2019; Fouvry et al., 2021) was shown to only weakly involve collective effects while resonant interactions seemed to have little impact on the overall relaxation.
- This formalism was transposed to the study of more exotic systems, such as *2D point vortices* (Fouvry et al., 2016; Chavanis, 2023), secular dynamics on a *sphere* (Fouvry et al., 2019a) or *kinetic blockings* (Fouvry, 2022). The latter characterises the impact of shot noise on systems for which symmetry leads to an exactly vanishing Balescu–Lenard flux. These systems were shown to diffuse over timescales scaling like $1/N^2$ at most (Fouvry & Roule, 2023). This implies that correlations beyond three stars are never important in long-range interacting systems.

Overall, these studies test the robustness of the Balescu–Lenard equation, and its limits (see, e.g., Hamilton & Heinemann, 2020, 2023).

In this context, my Ph.D. is focused on the evolution on secular timescales of *isolated* gravitational systems presenting kinematic diversity (anisotropy, rotation). It relies on the Balescu–Lenard formalism and various approximations of it. Building upon them, I will aim at: (i) understanding the mechanisms which are typical of a long-term diffusion (i.e. departures from the mean field driven by potential fluctuations); (ii) determining the impact of the nature of these objects (e.g., their geometry, kinematics or composition) w.r.t. the observed differences ; (iii) setting up methods for dark matter experiments in order to probe the existence of unresolved or faint families of objects (e.g., intermediate mass black holes (IMBHs) in the Galactic nucleus).

My work will focus on three scales: the Galactic nucleus (at the centre of the Milky Way), globular clusters, and finally galaxies as a whole. To that end, I will rely on the recent advances in kinetic theory I discussed, and extend their applicability to wider classes of objects (anisotropic, rotating). I will show in particular how this secular theory recovers quantitatively the mean expectation of various quantities extracted from sets of simulations averaged over their initial conditions.

Before delving into the actual re-derivation of secular theory and my contributions to it, it is useful to review the general dynamics of an N-body system. In section 1.2, I motivate the framework in which kinetic theory is derived. I describe tools and results of Hamiltonian dynamics applied to N-body self-gravitating systems, and highlight a few mechanisms that are crucial in the evolution of stellar systems.

1.2 Hamiltonian dynamics

A dynamical system is described by its Hamiltonian, H, which is a function of the *canonical coordinates* $(\boldsymbol{q}, \boldsymbol{p})$ (see, e.g., Arnold, 1978). The time evolution of these coordinates is given by *Hamilton equations*

$$\frac{\mathrm{d}\boldsymbol{q}}{\mathrm{d}t} = \frac{\partial H}{\partial \boldsymbol{p}} \quad ; \quad \frac{\mathrm{d}\boldsymbol{p}}{\mathrm{d}t} = -\frac{\partial H}{\partial \boldsymbol{q}}. \tag{1.2.1}$$

The N-dimension space in which the coordinates $\boldsymbol{q}$ live is called the *configuration space*, while the coordinates $\boldsymbol{p}$ live in the *associated momentum space*. The *phase space* is defined as the space containing all $(\boldsymbol{q}, \boldsymbol{p}) = \boldsymbol{w}$ coordinates. This space is given an antisymmetric operation called the *Poisson bracket*, defined by

$$[F, G] = \frac{\partial F}{\partial \boldsymbol{q}} \cdot \frac{\partial G}{\partial \boldsymbol{p}} - \frac{\partial G}{\partial \boldsymbol{q}} \cdot \frac{\partial F}{\partial \boldsymbol{p}}, \tag{1.2.2}$$

with F, G being functions of the canonical coordinates $\boldsymbol{w}$. This allows me to rewrite Hamilton eqs. (1.2.1) under the form

$$\frac{\mathrm{d}\boldsymbol{w}}{\mathrm{d}t} = [\boldsymbol{w}, H]. \tag{1.2.3}$$

The phase space coordinates satisfy the canonical commutation relations

$$[w_\alpha, w_\beta] = \mathbf{J}_{\alpha\beta}, \tag{1.2.4}$$

where $\mathbf{J}$ is the $2N$ symplectic matrix

$$\mathbf{J} = \begin{pmatrix} 0 & -I_N \\ I_N & 0 \end{pmatrix}. \tag{1.2.5}$$

Here, N is the number of particles of the system and I_N the N-dimensional identity matrix. Because Hamiltonian dynamics describes the system's dynamics in phase space, it allows for generalised change of coordinates. Some phase space coordinates $\boldsymbol{W}$ are said to be canonical if they satisfy the canonical relations given in eq. (1.2.4). A *canonical transformation*, $\boldsymbol{w} \to \boldsymbol{W}$, conserves the form of Hamilton equations, Poisson brackets, as well as the infinitesimal phase space volume $\mathrm{d}\boldsymbol{w} = \mathrm{d}\boldsymbol{W}$.

Another key aspect of Hamiltonian dynamics is the determination of *integrals of motion*. By this, I mean functions of $\boldsymbol{w}$ which are invariant along the orbits, i.e. the trajectories of the stars. An integral of motion $I(\boldsymbol{w})$ is said to be isolating if for any value in the image of $I(\boldsymbol{w})$, the region of phase space which reaches this value is a smooth manifold of dimension $2N - 1$. For example, a trivial isolating integral of motion is the energy. Finally, a system is said to be integrable if it has at least N independent integrals of motion. For those systems, one can obtain a set of canonical coordinates $(\boldsymbol{\theta}, \boldsymbol{J})$, called *angle-action coordinates*, such that the actions $\boldsymbol{J}$ are independent isolating integrals of motion. These coordinates are constructed in a way that the Hamiltonian can be expressed only in actions, i.e. $H = H(\boldsymbol{J})$. As a key corollary, Hamilton eqs. (1.2.1) become angle-independent, hence read

$$\frac{\mathrm{d}\boldsymbol{\theta}}{\mathrm{d}t} = \frac{\partial H}{\partial \boldsymbol{J}} = \boldsymbol{\Omega}(\boldsymbol{J}) \quad ; \quad \frac{\mathrm{d}\boldsymbol{J}}{\mathrm{d}t} = -\frac{\partial H}{\partial \boldsymbol{\theta}} = 0, \tag{1.2.6}$$

where $\boldsymbol{\Omega}$ are the motion frequencies (Fig. 1.6). In this space, trajectories, which have a complex shape in phase space $(\boldsymbol{q}, \boldsymbol{p})$, are reduced to straight lines in angle-action space, where

$$\boldsymbol{\theta}(t) = \boldsymbol{\theta}_0 + \boldsymbol{\Omega}(\boldsymbol{J})t \quad ; \quad \boldsymbol{J}(t) = \boldsymbol{J}. \tag{1.2.7}$$

To illustrate this property, I exhibit the case of the one-dimensional harmonic oscillator in Fig. 1.6. The orbits in (q, p)-space, which were circles, become straight lines in angle-action space.

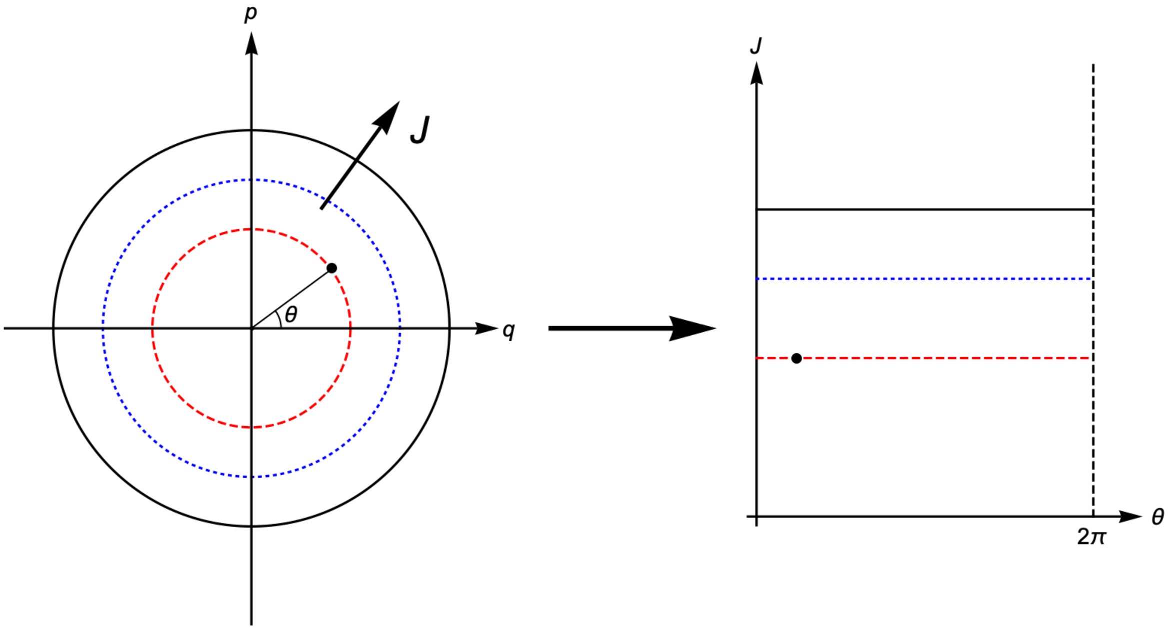

Figure 1.6: Phase space diagram of a 1D harmonic oscillator. On the left, three orbits are represented in the physical phase space (q, p). They take the form of concentric circles along which the particles move. In the right, the same orbits are represented in angle-action space (θ, J). The trajectories have been transformed into straight lines, labelled by a constant action. The particle moves with a constant frequency along the angle θ.

Based on these observations, let me consider that the self-gravitating system can be described by a distribution function (DF), $F(\boldsymbol{w}) = F(\boldsymbol{q}, \boldsymbol{p})$. In particular, $F(\boldsymbol{w})\mathrm{d}\boldsymbol{w}$ is proportional to the probability of finding a particle in a phase space region of volume $\mathrm{d}\boldsymbol{w}$ around $\boldsymbol{w}$. During its evolution, probability in phase space must be conserved, hence F evolves according to the continuity equation

$$\frac{\partial F}{\partial t} + \frac{\partial}{\partial \boldsymbol{w}} \cdot \left(F\dot{\boldsymbol{w}}\right) = 0. \tag{1.2.8}$$

Using Hamilton eqs. (1.2.3), eq. (1.2.8) can be expressed as

$$\frac{\partial F}{\partial t} + [F, H] = 0. \tag{1.2.9}$$

Equation (1.2.8) is usually known as the *Liouville equation* (for an N-body system), or the *collisionless Boltzmann equation* (for the DF of one particle in the mean field limit), or the *Vlasov* *equation* (in the mean field limit). Because gravity is a long-range interaction, the mean field limit works especially well. Therefore, if the number of particles N is large enough, I can define a set of angle-action coordinates $(\boldsymbol{\theta}, \boldsymbol{J})$ for the mean field limit. Then, using the conservation of Poisson brackets through a canonical transformation, eq. (1.2.9) can be expressed under the form

$$\frac{\partial F}{\partial t} + \boldsymbol{\Omega} \cdot \frac{\partial F}{\partial \boldsymbol{\theta}} = 0. \tag{1.2.10}$$

Steady states of the collisionless Boltzmann eq. (1.2.10) appear naturally: they are given by DFs of the form $F = F(\boldsymbol{J})$. This assertion corresponds to Jeans theorem (Jeans, 1915), which is crucial in the case of self-gravitating system due to two mechanisms.

First, self-gravitating systems undergo *phase mixing*, as shown in Fig. 1.7. Hamilton equations in angle-action (eqs. 1.2.6) show that the orbital phase $\boldsymbol{\theta}$ of a particle with action $\boldsymbol{J}$ follows a straight line in angle-action space, with frequency $\boldsymbol{\Omega}(\boldsymbol{J})$. While $\boldsymbol{\Omega}(\boldsymbol{J})$ was independent of the action for a harmonic oscillator (Fig. 1.6), it is not the case in general. Therefore, two particles initially close in angle-action space will stream with different frequencies. This induces a dephasing of these particles, and more generally creates a shearing in angle-action space. As time progresses, finer and finer structures in the DF will be created, ultimately converging to an angle-independent DF $F(\boldsymbol{J})$ when coarse grained (i.e. locally smoothed or analysed with finite resolution).

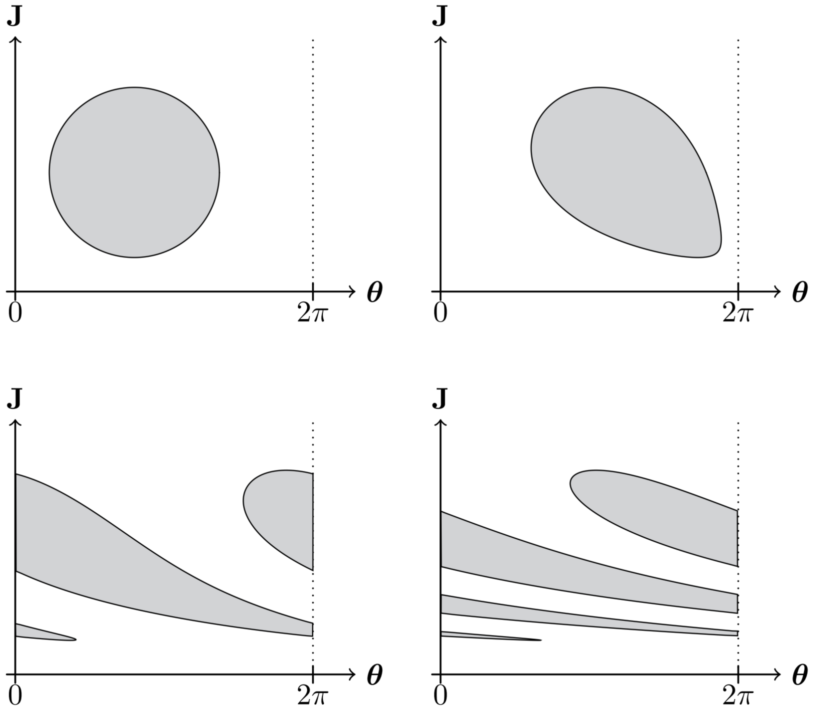

Figure 1.7: From fig. 2.4 of Fouvry (2020). In angle-action space, trajectories are simple straight lines (see Fig. 1.6). Particle move along these lines at a frequency depending on the action $\boldsymbol{J}$. This leads to a dephasing of the particles, which is shown for various times in the panels. This is *phase-mixing mechanism*, one of the main motivations behind orbit-averaging and the $\boldsymbol{J}$-dependence only of the DF.

Second, a system far from equilibrium undergoes *violent relaxation* (Lynden-Bell, 1967). During this period, the system undergoes a series of violent and abrupt variations of its mean potential. This leads to a redistribution of its particles' energy. This process is very efficient in allowing the system to reach a quasi-stationary state (QSS) in a few dynamical times.[a]

After violent relaxation and phase mixing, the system is locked into a stationary state for the mean field limit. If it were only subjected to its mean field, then it would be frozen on its QSS. Yet, it is still subject to fluctuations in its potential (e.g., induced by the shot noise from its finite number of stars). It is this departure from the mean field which allows the system to slowly evolve from one QSS to another (see, e.g., Joyce et al., 2016; Marcos et al., 2017), and drives secular evolution. If the perturbations are sufficiently small (e.g., a large enough number of stars, or a weak external perturbation), this departure from the mean field can be treated perturbatively. It corresponds to a slow diffusion of the actions (which label the orbits). If this process is sufficiently slow, it may build up through the recurrence of interactions occurring at resonances.

1.3 Angle-action coordinates in spherically symmetric systems

In this section, let me introduce two sets of angle-action variables which I will use in the subsequent chapters. Importantly, these actions label the orbits and will slowly drift with cosmic time on secular timescales, should the cluster be subject to coherent potential fluctuations.

1.3.1 Spherically symmetric system

In a spherically symmetric system with a static central potential, it is known that the energy of a given test particle, E, as well as its angular momentum vector, $\boldsymbol{L}$, are conserved quantities. From these conserved quantities, one can derive a set of canonical variables composed of three independent isolating integrals (see, e.g., Torrielli, 2016). One such integral is the *radial action*

$$J_{\mathrm{r}} = \frac{1}{\pi} \int_{r_{\mathrm{p}}}^{r_{\mathrm{a}}} \mathrm{d}r \, v_r, \tag{1.3.1}$$

where r_{p} (resp. r_{a}) is the pericentre (resp. the apocentre) of the radial motion of the particle (Fig. 1.8) and v_r the radial velocity of the particle. The two other actions are the norm of the angular momentum, L, and its projection along the z-direction, L_z. Once again, I can illustrate the crucial role of angle-action coordinates in capturing the mean motion of such dynamical systems. The case of a central Plummer potential is shown in Fig. 1.8, where I represent the orbits of two particles with different orbital parameters, in their orbital planes. The complexity of this orbital motion appears in the fact that orbits are typically not closed. This is typical for most systems beyond the one-dimensional case.[b] One may obtain the orbital frequencies (see, e.g., Tremaine & Weinberg, 1984) Ω_r and Ω_L

$$\frac{2\pi}{\Omega_r} = 2 \int_{r_{\mathrm{p}}}^{r_{\mathrm{a}}} \frac{\mathrm{d}r}{v_r}, \tag{1.3.2a}$$

$$\frac{\Omega_L}{\Omega_r} = \frac{L}{\pi} \int_{r_{\mathrm{p}}}^{r_{\mathrm{a}}} \frac{\mathrm{d}r}{r^2 v_r}, \tag{1.3.2b}$$

---

[a] Together, these mechanisms are two of the motivations behind the orbit-average presented in chapter 2.

[b] For spherically symmetric systems subjected to a central potential $U = U(r)$, only the Keplerian system and the harmonic oscillator have systematically closed orbits (Bertrand, 1873).

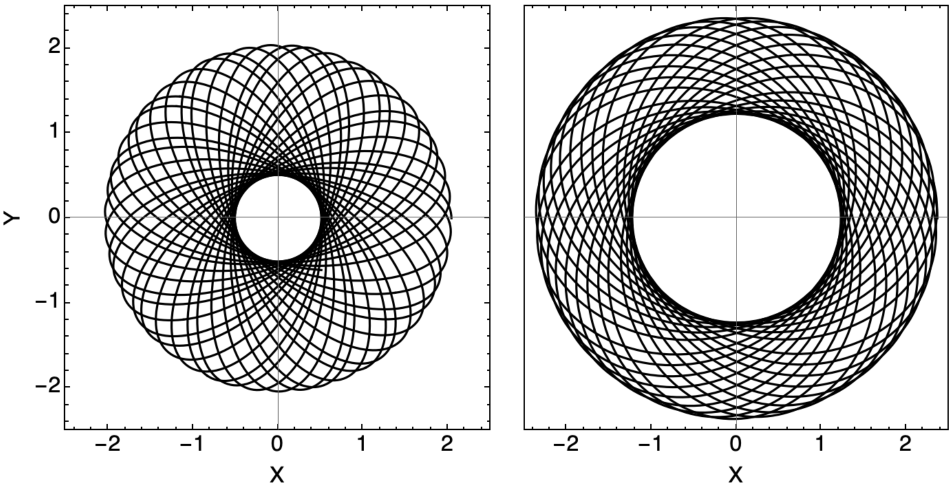

Figure 1.8: Illustration of Plummer orbits (see eq. 4.2.1) projected on their orbital plane. One can observe the *rosette*-like nature of these orbits, which are not closed in physical space. As can be seen, these orbits will (typically) fill the available physical radius given enough time.

while $\Omega_{L_z} = 0$ because of spherical symmetry. Then one may obtain the evolution of the angles (see, e.g., Tremaine & Weinberg, 1984)

$$\theta_r = \int_{r_\mathrm{p}}^{r} \frac{\mathrm{d}r\,\Omega_r}{v_r}, \tag{1.3.3a}$$

$$\theta_L = \theta + \int_{r_\mathrm{p}}^{r} \frac{\mathrm{d}r\,(\Omega_L - L/r^2)}{v_r}, \tag{1.3.3b}$$

where θ is the ascending node and r is the radius of the star (see Fig. 2.9).

1.3.2 Test star in a Keplerian potential

Depending on the system that is studied, other sets of angle-action coordinates might be more adapted (see, e.g., Morbidelli, 2002). For the Newtonian two-body problem, the *Delaunay variables* (Delaunay, 1860) are the most appropriate.

First, let me observe that the Keplerian system is a spherically symmetric system. Therefore it has a set of angle-action (J_r, L, L_z), as detailed in section 1.3.1. Using these actions, I can rewrite the Keplerian Hamiltonian under the form (see, e.g., appendix E of Binney & Tremaine, 2008)

$$H_\mathrm{Kep} = \frac{v^2}{2} - \frac{GM_\bullet}{|\boldsymbol{r}|} = -\frac{(GM_\bullet)^2}{2(J_\mathrm{r}+L)^2}, \tag{1.3.4}$$

where $M_\bullet$ is the mass of the central massive object. In particular, the orbital frequencies are given by

$$\Omega_r = \Omega_L = \frac{(GM_\bullet)^2}{2(J_\mathrm{r}+L)^3} \quad ; \quad \Omega_{L_z} = 0. \tag{1.3.5}$$

Because only the combination of actions $J_\mathrm{r}+L$ occurs in the Hamiltonian (eq. 1.3.4), it is useful to define this combination as a new action. This transformation $(J_\mathrm{r}, L, L_z) \mapsto (L_\mathrm{c}, L, L_z)$ is a canonical transformation in this case (see, e.g., Goldstein, 1980), where

$$L_\mathrm{c} = J_\mathrm{r} + L.$$

These new actions are called the (specific) Delaunay actions. As a Keplerian orbit is usually described by its semi-major axis (sma) a, its eccentricity e and its orbital inclination I (see Fig. 1.9), one may express the specific Delaunay actions as (see, e.g., Duncan et al., 1998)

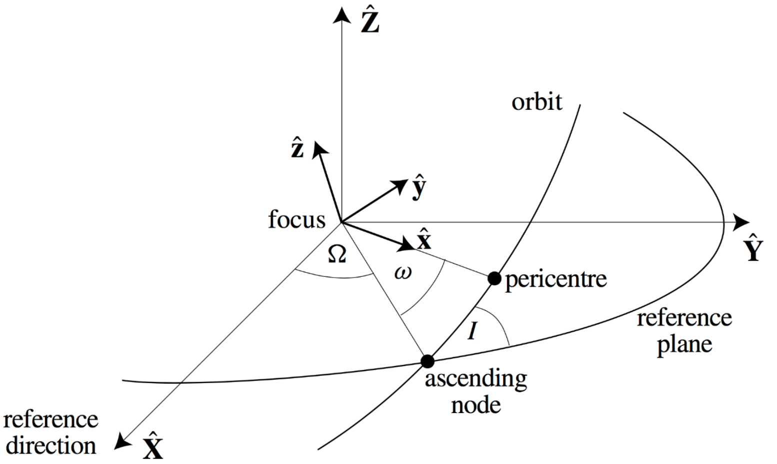

Figure 1.9: From Murray & Dermott (2000). Illustration of the Keplerian orbital elements. Here, ω is the argument of the pericentre, as well as the angle associated with the action L. Similarly, Ω is the longitude of the ascending node, and is the angle associated with the action L_z. Finally, I is the orbital inclination (w.r.t. some fixed reference plane).

$$L_{\mathrm{c}} = \sqrt{G M_\bullet a} \quad ; \quad L = L_{\mathrm{c}} \sqrt{1 - e^2} \quad ; \quad L_z = L \cos I. \tag{1.3.6}$$

In particular, this shows that L_{c} corresponds to the angular momentum for a circular orbit.

1.4 Overview

The main objective of my thesis is to characterise the long-term processes operating in stellar systems. This is of interest both astrophysically and conceptually. For the former, it provides us with means to build estimators for dark components whose impact only operates on such timescales (e.g., a measure of the clumpiness of the mass distribution near supermassive black holes). For the latter, to understand how long-range fluctuations distort orbits. Depending on the geometry and kinematics of the cluster at play, I will show that two types of contributions can drive secular evolution: the local deflections with the nearest stars, or the long-range non-local interactions with resonant orbits. This distinction will play a crucial role in the coming chapters.

In chapter 2, I will recall recent advances in kinetic theory and present the main formalisms which allow us to describe secular orbital diffusion. First, I will recover the Balescu–Lenard equation by starting from the Klimontovich description of the system. Under the assumption of small enough departures from the mean field, I will show that this equation completely captures the secular evolution of self-gravitating systems (e.g., inhomogeneity, resonant interactions and collective effects). Furthermore, I will discuss situations in which the Balescu–Lenard equation can be approximated: (i) when collective effects can be neglected,[c] giving rise to the resonant relaxation (RR) approximation; (ii) when long-range, resonant interactions can be

---

[c] It should be noted that collective effects cannot be strictly screened – as can be the case in plasma physics – due to masses always being positive. This makes collective effects a crucial feature of self-gravitating systems *a priori*.

ignored in favour of local, successive two-body deflections, giving rise to the (orbit-averaged) non-resonant relaxation (NR) approximation. I will discuss the limitations of this formalism, such as the induced large-scale and small-scale divergences.

In chapter 3, I will study the long-term evolution of the Galactic centre. Using both the NR and RR formalisms presented in chapter 2, my aim will be to probe the existence of IMBHs hidden within an unresolved dark cluster of objects orbiting around the SMBH Sgr A*. I will apply secular theory to characterise the diffusion in eccentricity of the S-stars. Here, the influence of the hidden IMBHs or faint massive star families is what accelerates the diffusion. Because its efficiency depends on the model describing them, this will allow me to determine the most likely models of IMBHs around Sgr A*.

In Chapter 4, I will apply the extended NR formalism from chapter 2 to study globular clusters with an anisotropic distribution of velocities. These objects (Fig. 1.10) are known to undergo core collapse. Recent numerical works (see, e.g., Breen et al., 2017) have shown that an initial tangential anisotropy can accelerate the rate of core collapse in isolated globular clusters. I will show how the NR formalism explains this observation. In particular, I will study orbital reshuffling and how anisotropy impacts it. This analysis will be complemented with tailored sets of N-body simulations to validate my results. Their confrontation to predictions will show how accurate the NR formalism can be. Additionally, a comparative analysis of the RR predictions against the NR ones will allow me to discuss the importance of resonances in dynamically hot systems, as well as the origin of the Coulomb logarithm of the NR theory.

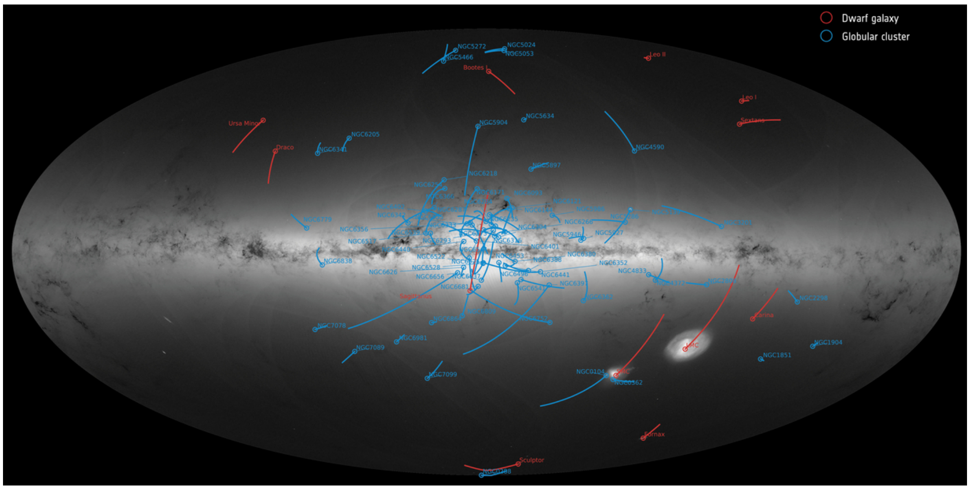

Figure 1.10: An all-sky view of 75 globular clusters (blue) and 12 nearby dwarf galaxies (red) as viewed by ESA's Gaia satellite using information from the mission's second data release. Recent observations were able to detail the kinematic richness of these objects, including velocity anisotropies and inner rotation. Acknowledgement: Gaia Data Processing and Analysis Consortium (DPAC).

Chapter 5 will extend the study to a wider class of rotating clusters. These systems are dynamically colder, hence more prone to amplified resonant interactions because of the coherence in the motion of the co-rotating stars. This will provide me with the opportunity to quantify the limitations of the NR formalism. I will apply the NR formalism developed in chapter 2 to predict the impact of rotation on both the in-plane diffusion and the out-of-plane one. When compared to my N-body simulations, I will show that the NR theory gives a satisfying prediction for the former, but fails to deliver for the latter, highlighting the shortcomings of the NR assumptions.

In chapter 6, I will study the specific secular process of bar formation from a different angle. Rather than focussing on the impact of shot noise, I will explore which subsets of geometric configurations can be subject to bi-symmetric instabilities. I will adapt the method used by Aoki et al. (1979) to describe razor-thin gaseous galactic discs with a dark halo (DH) and a bulge. Using linear response theory, I will quantify the growth mode of the disc w.r.t. to the bulge and DH fraction. I will use this formalism to provide a tentative explanation regarding the low number of bars observed in the NewHorizon simulation (Reddish et al., 2022).

In chapter 7, I will conclude by discussing the state-of-the-art for the secular evolution of self-gravitating integrable clusters displaying kinematic diversity. I will also list possible extensions of the present work.

Chapter 2

The theory of secular relaxation

2.1 Introduction

In the previous chapter, I presented a few tools from Hamiltonian mechanics, which I will use to describe the typical fate of self-gravitating systems. In particular, I highlighted two phenomena inherent to these N-body systems. First, they are subject to phase mixing, a process during which their angle dependency is washed out over a few dynamical times (Hénon, 1964). Second, they are subject to a violent relaxation, which also quickly brings out-of-equilibrium systems towards quasi-stationary states (QSS) (Lynden-Bell, 1967). These two processes efficiently virialise the system, whose potential then follows from its mean field. As a result, stellar orbits are mainly set by this mean field, while stellar positions are uniformly distributed in angles. It follows that the system can then only evolve through fluctuations, i.e. the departure from the mean field coming from the finite number of stars or external perturbations (Fig. 2.1).

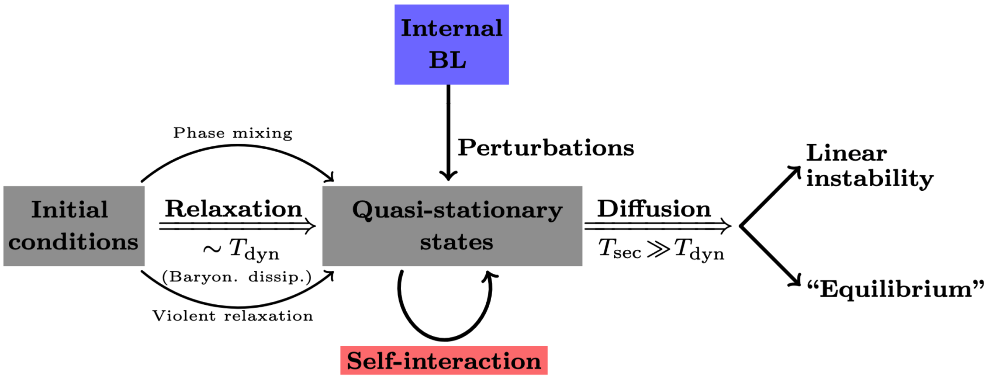

Figure 2.1: Courtesy of J.-B. Fouvry. A self-gravitating system first undergoes: (i) a violent relaxation due to abrupt variations of its mean potential; (ii) a phase-mixing due to the action-dependent frequencies of its orbits. Then, after a few dynamical times, it reaches a QSS. From there on, it can only evolve on long timescales under the effects of either external (for example, fly-bys of satellites) of internal fluctuations (e.g., of its own potential), as described by the inhomogeneous Balescu–Lenard equation. This induces a secular diffusion of its orbits, which either leads to a linear instability or a series of QSS.

Because gravity is a long-range interaction, it has the ability to amplify perturbations (see, e.g., Kalnajs, 1976; Hernquist & Ostriker, 1992; Weinberg, 1993, 1998). This phenomenon can lead to the spontaneous growth of dynamical instabilities, such as the radial orbit instability (see, e.g., Maréchal & Perez, 2011, for a review), or it can lead to a strong amplification of the potential fluctuations. This is particularly relevant in cold dynamical systems such as galactic discs (see, e.g., Toomre, 1981; Sellwood, 2012; Fouvry et al., 2015d), where the velocity dispersion is low. Collective effects are expected to have less impact on hotter stellar systems, such as globular clusters (see, e.g., Theuns, 1996; Sellwood, 2015; Hamilton et al., 2018) or the Galactic nucleus (Rauch & Tremaine, 1996; Bar-Or & Fouvry, 2018). If potential fluctuations are small, then their impact on short timescale is limited. Yet, recurrent effects operating repetitively through resonances may still reshuffle the orbital structure of the system. Under these conditions, orbital evolution can only occur over long timescales (provided the considered systems do not undergo any instability). This is what the theory of secular evolution aims at describing.

For simplicity, I shall be focused on internal fluctuations coming specifically from the finite number N of particles. These specific types of fluctuations are known as finite-N effects, or equivalently as *Poisson shot noise fluctuations*. In this regime, the graininess of the potential is what drives an irreversible, long-term relaxation in the system (see, e.g., Weinberg, 1998, 2001a,b). The existence of a mass spectrum of components – a generic situation in realistic astrophysical systems – can in particular also boost finite-N effects, and diffusion can then be dominated by the most massive components.

In this chapter, I shall sketch a derivation of the secular evolution of self-gravitating systems, in the shot noise-driven limit. I will first discuss the derivation of the generic Balescu–Lenard equation in section 2.2. This equation predicts the amplification of the fluctuations induced by self-gravity (Heyvaerts, 2010; Chavanis, 2012). Because such effects can be ignored in some conditions – this will be the case in most of this thesis – the Balescu–Lenard equation can be simplified into the inhomogeneous Landau equation (section 2.3.1). Then, in section 2.3.2, I will describe secular relaxation in systems where small-scale interactions (NR) dominate over long-range effects. In this case, the inhomogeneous Landau equation reduces to the locally homogeneous Landau equation. This is at the cost of small- and large-scale divergences regularised by a cutoff, giving rise to a Coulomb logarithm (see, e.g., Chavanis, 2013b, for a review). Nonetheless, it is computationally more accessible, and appears to give satisfactory results for some stellar systems (see, e.g., Hamilton et al., 2018, and chapter 4). Finally, I will derive an extension of the isotropic, non-rotating NR description of globular clusters to the study of anisotropic and rotating systems (section 2.3.3).

2.2 Collisional dynamics of an N-body system

The derivation of the general Balescu–Lenard equation, which I sketch below, is based on Chavanis (2012), if not stated otherwise.

2.2.1 The Klimontovich equation

Let me consider an isolated system of N stars with identical masses m, interacting with one another under the influence of gravity. Their dynamics can be described by Hamilton equations

$$m\frac{\mathrm{d}\boldsymbol{r}_i}{\mathrm{d}t} = \frac{\partial H_N}{\partial \boldsymbol{v}_i} \quad ; \quad m\frac{\mathrm{d}\boldsymbol{v}_i}{\mathrm{d}t} = -\frac{\partial H_N}{\partial \boldsymbol{r}_i}, \tag{2.2.1}$$

where H_N is the Hamiltonian of the system. It is given by

$$H_N = \frac{1}{2}\sum_{i=1}^{N} m v_i^2 + m^2 \sum_{i<j} U(|\boldsymbol{r}_i - \boldsymbol{r}_j|), \tag{2.2.2}$$

where $U(r)$ is the interaction potential. For $3D$ gravity, the Newtonian interaction potential reads $U(r) = -G/r$, where G is the gravitational constant. This system conserves its total energy $E = H_N$, its total mass $M_{\mathrm{tot}} = Nm$ and its total angular momentum $\boldsymbol{L} = \sum_i m_i \, \boldsymbol{r}_i \times \boldsymbol{v}_i$. The purpose of my work is to understand how such a system evolves over long timescales, e.g., by redistributing angular momentum and mass within the system. Such an evolution I will call secular relaxation, to make a distinction w.r.t. violent relaxation and phase mixing.

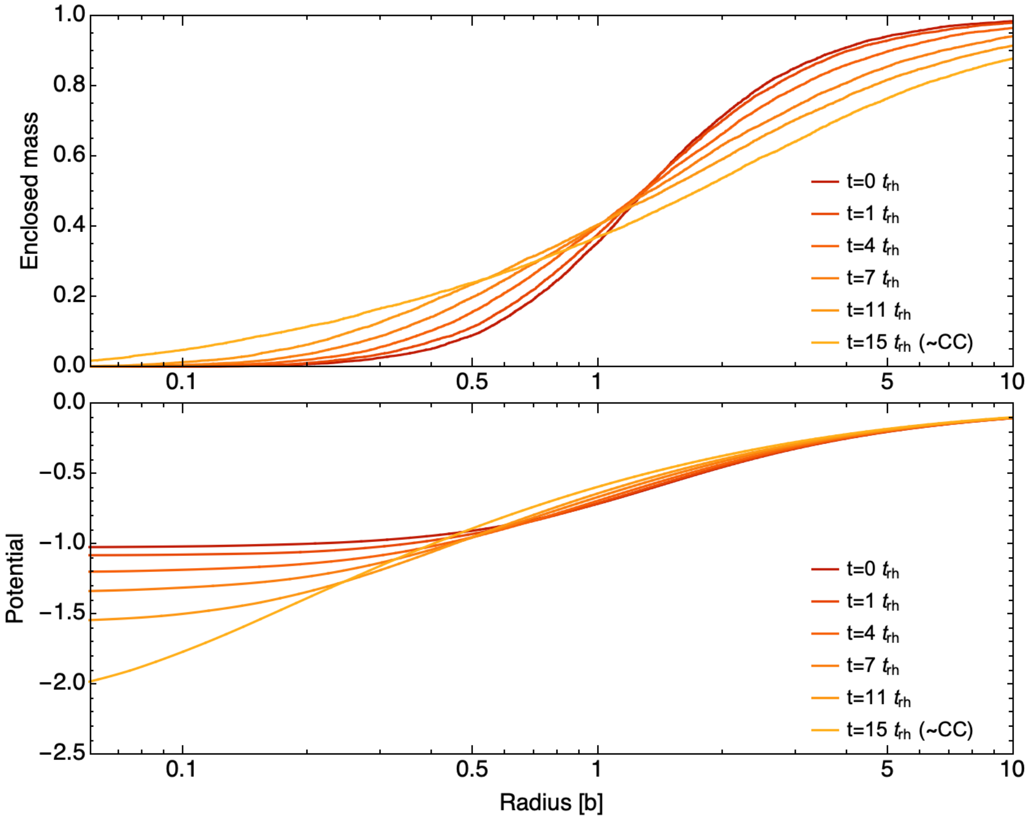

Figure 2.2: Illustration of the core collapse of an isotropic, non-rotating cluster, as measured in my N-body simulation with $N = 10^4$. The top panel shows the evolution of the enclosed mass of the cluster, while the bottom panel shows that of the cluster potential. Each colour corresponds to a different time in the evolution of the cluster, in initial half-mass radius time units (defined in eq. 5.2.1). Here, CC stands for *core collapse*. The limits on the left of the curves correspond to the location of the most central particle. As time advances, mass becomes more concentrated in the centre.

Already, Hénon (1964) noticed that self-gravitating systems were predetermined to undergo two successive types of relaxation. First, they would experience a quick, collisionless – i.e. subject only to the mean field – relaxation towards a quasi-stationary state (QSS). By this, I mean a virialised state in dynamical equilibrium in the mean field limit, but which is not in a thermodynamical equilibrium. Second, even in isolation, if N is sufficiently large, they would experience a slow, long-term collisional relaxation – i.e. sourced by finite-N effects. However, the permanent escape of high energy stars (evaporation) and the gravothermal catastrophe (core collapse, see Fig. 2.2) imply that the system may never reach a true statistical equilibrium (Hénon, 1961; Aarseth, 1963). Moreover, Lynden-Bell (1967) tried to predict the QSS resulting from the first relaxation by developing a statistical mechanics of the collisionless Vlasov equation. However, when coupled to the Poisson equation, the DF he obtained ended up having an infinite mass, reflecting the fact that the Vlasov–Poisson system has no maximum entropy state (Spitzer, 1975). His solution was later disregarded by Arad & Lynden-Bell (2005) as not satisfying transitivity in evolution. Yet it remains of interest to study how the QSS state evolves secularly through the deflection of its orbital structure via recurrent shot noise-driven perturbations. This is the topic of kinetic theory, the core topic of this thesis.

Following Chavanis (2012), let me now sketch a derivation of the Balescu–Lenard equation – first obtained by Heyvaerts (2010) – which fully describes the secular evolution of these systems. First, I consider the discrete DF of the system

$$F_{\mathrm{d}}(\boldsymbol{w},t) = m \sum_{i=1}^{N} \delta_{\mathrm{D}}(\boldsymbol{r}-\boldsymbol{r}_i[t])\, \delta_{\mathrm{D}}(\boldsymbol{v}-\boldsymbol{v}_i[t]), \tag{2.2.3}$$

where I introduced $\boldsymbol{w} = (\boldsymbol{r},\boldsymbol{v})$ the (specific) phase space coordinate. This DF describes exactly the N-body system where the particle i has position $\boldsymbol{r}_i[t]$ and velocity $\boldsymbol{v}_i[t]$ at time t. I can recover its associated potential using Poisson equation

$$\Phi_{\mathrm{d}} = \int \mathrm{d}\boldsymbol{w}'\, U(|\boldsymbol{r}-\boldsymbol{r}'|) F_{\mathrm{d}}(\boldsymbol{w}',t). \tag{2.2.4}$$

Using Hamilton eqs. (2.2.1) with the Hamiltonian given in eq. (2.2.2), the discrete DF obeys the *Klimontovich equation* (Klimontovich, 1967)

$$\boxed{\frac{\partial F_{\mathrm{d}}}{\partial t} + [F_{\mathrm{d}}, H_{\mathrm{d}}] = 0,} \tag{2.2.5}$$

where $H_{\mathrm{d}} = v^2/2 + \Phi_{\mathrm{d}}(\boldsymbol{r},t)$ is the specific Hamiltonian of an individual particle. Because I am interested in the evolution of the system driven by the fluctuations of its mean field, I define the smooth DF, $F(\boldsymbol{w},t) = \langle F_{\mathrm{d}}(\boldsymbol{w},t)\rangle$, where the average $\langle\cdot\rangle$ is to be understood as the average over a large number of initial conditions.[a] I can then introduce the quasilinear decomposition

$$F_{\mathrm{d}} = F + \delta F,$$

where δF denotes the fluctuations of the DF around its mean value. In the same fashion, I can decompose the discrete potential

$$\Phi_{\mathrm{d}} = \Phi + \delta\Phi,$$

where $\delta\Phi$ describes the fluctuations around the mean potential. I then inject these decompositions into the Klimontovich eq. (2.2.5), and obtain

$$\frac{\partial F}{\partial t} + \frac{\partial \delta F}{\partial t} + [F,H] + [\delta F, H] + [F,\delta\Phi] + [\delta F,\delta\Phi] = 0, \tag{2.2.6}$$

where I have decomposed the exact Hamiltonian $H_{\mathrm{d}} = H + \delta\Phi$, with $H = v^2/2 + \Phi$ the mean field Hamiltonian. Now, taking the ensemble average $\langle\cdot\rangle$ of eq. (2.2.6) yields

$$\frac{\partial F}{\partial t} + [F,H] = -\langle[\delta F,\delta\Phi]\rangle, \tag{2.2.7}$$

---

[a] Specifically, sets of distributions of positions and velocities which are drawn from the initial DF.

which describes the evolution of the mean field DF. If I neglect the non-linear terms, and inject eq. (2.2.7) into eq. (2.2.6), I obtain the evolution equation for the fluctuations

$$\frac{\partial \delta F}{\partial t} + [\delta F, H] + [F, \delta\Phi] = 0. \tag{2.2.8}$$

The linearisation of eq. (2.2.7) is called the *quasilinear approximation* (see, e.g., Diamond et al., 2010). Due to the non-linear term, the orbital diffusion undergone by the averaged DF only occurs only at second order in the perturbations.

2.2.2 The Balescu–Lenard equation for self-gravitating systems

Now, as I discussed in section 1.2, orbits in N-body self-gravitating systems are intricate. This is because of the (unshielded) long-range interaction operating in these systems, which makes them inherently inhomogeneous. Therefore, their description by the phase space coordinates $(\boldsymbol{r}, \boldsymbol{v})$ is not optimal to capture the mean field motion in a simple fashion. To remedy this issue, it is much more convenient to use angle-action coordinates $(\boldsymbol{\theta}, \boldsymbol{J})$ (Goldstein, 1980). Although their existence might be of concern for clusters of arbitrary geometry, I am interested in this thesis in spherically symmetric systems (on average). Under these conditions, I have access to a set of angle-action coordinates, as introduced in section 1.3. Because fluctuations are of order $1/\sqrt{N}$, the relaxation timescale of the system is of order $t_{\mathrm{R}} \sim N t_{\mathrm{D}}$ (Chandrasekhar, 1942) with t_{D} the dynamical time. Due to this timescale separation, the DF will evolve through a sequences of QSS solutions of the Vlasov equation (eq. 1.2.10) – hence depending only on the actions $\boldsymbol{J}$ – while changing slowly under the impact of finite-N effects (which are called *collisions*). Therefore, I can approximate the mean field DF by

$$\boxed{F(\boldsymbol{w}, t) \simeq F(\boldsymbol{J}, t).} \tag{2.2.9}$$

By construction, the average (mean field) Hamiltonian of the system $H = H(\boldsymbol{w}) = H(\boldsymbol{J})$ does not depend on the angles. Therefore, Hamilton equations for the averaged Hamiltonian become

$$\frac{\mathrm{d}\boldsymbol{\theta}}{\mathrm{d}t} = \frac{\partial H}{\partial \boldsymbol{J}} = \boldsymbol{\Omega}(\boldsymbol{J}) \quad ; \quad \frac{\mathrm{d}\boldsymbol{J}}{\mathrm{d}t} = -\frac{\partial H}{\partial \boldsymbol{\theta}} = 0, \tag{2.2.10}$$

where I defined the angular frequency $\boldsymbol{\Omega}(\boldsymbol{J})$ of the orbits with actions $\boldsymbol{J}$. In this space, the angles evolve ballistically as $\boldsymbol{\theta} = \boldsymbol{\Omega}(\boldsymbol{J})t + \boldsymbol{\theta}_0$. Of course, the complexity has not simply vanished. Instead, it has been relocated in the relation between the position-velocity $(\boldsymbol{r}, \boldsymbol{v})$ and angle-action coordinates $(\boldsymbol{\theta}, \boldsymbol{J})$. Most notably, the expression of the interaction potential $U(|\boldsymbol{r} - \boldsymbol{r}'|)$ has become much more intricate than in position-velocity.

Because the mapping $(\boldsymbol{r}, \boldsymbol{v}) \mapsto (\boldsymbol{\theta}, \boldsymbol{J})$ is a canonical transformation, it conserves phase space volume and Poisson brackets. I can express these in the new coordinates

$$[F, H] = \frac{\partial F}{\partial \boldsymbol{\theta}} \cdot \frac{\partial H}{\partial \boldsymbol{J}} - \frac{\partial F}{\partial \boldsymbol{J}} \cdot \frac{\partial H}{\partial \boldsymbol{\theta}} = 0, \tag{2.2.11}$$

since $H = H(\boldsymbol{J})$ and $F = F(\boldsymbol{J})$. Therefore, eqs. (2.2.7) and (2.2.8) become

$$\frac{\partial F}{\partial t} = \frac{\partial}{\partial \boldsymbol{J}} \cdot \left\langle \delta F \frac{\partial \delta\Phi}{\partial \boldsymbol{\theta}} \right\rangle, \tag{2.2.12a}$$

$$\frac{\partial \delta F}{\partial t} + \boldsymbol{\Omega}(\boldsymbol{J}) \cdot \frac{\partial \delta F}{\partial \boldsymbol{\theta}} - \frac{\partial \delta\Phi}{\partial \boldsymbol{\theta}} \cdot \frac{\partial F}{\partial \boldsymbol{J}} = 0, \tag{2.2.12b}$$

where the first equation was obtained after averaging over the angles $\boldsymbol{\theta}$ assuming phase mixing (eq. 2.2.9). Note that this angle averaging effectively erases any dependence on the initial phases. This is a generic feature of kinetic theory which aims to capture *on average* the impact of non-linearities which operate over long timescales. Thus, kinetic theory forfeits the detailed knowledge of stellar positions so as to predict the mean evolution of the stellar distribution.

From this point, if N is sufficiently large, I shall assume that the fluctuations evolve quickly compared to the evolution of the mean field. This is motivated by the observation that the evolution timescale of δF is given by the mean advection $\boldsymbol{\Omega}(\boldsymbol{J})$, hence evolves on a dynamical timescale, while F has no mean advection. This assumption of *timescale separation* is known as *Bogoliubov's ansatz*. As a consequence of this hypothesis, mean field quantities – namely the DF $F(\boldsymbol{J})$ and the orbital frequencies $\boldsymbol{\Omega}(\boldsymbol{J})$ – involved in eq. (2.2.12b) are considered as time-independent at this level of approximation. Additionally, I assume that the system does not undergo any dynamical instability, meaning that it is only sourced by *collisions*. Finally I assume that initial perturbations have had time to damp away.[b] Therefore, the system does not have too weakly damped modes (Hamilton & Heinemann, 2020, 2023). Following these assumptions, I solve eqs. (2.2.12) by using the Fourier–Laplace transform formalism. This will allow me to compute explicitly the collision term in the Vlasov eq. (2.2.12a).

First, let me express the Fourier–Laplace transform of the fluctuations

$$\delta\widetilde{F}_{\boldsymbol{k}}(\boldsymbol{J},\omega) = \int \frac{\mathrm{d}\boldsymbol{\theta}}{(2\pi)^d} \int_0^{\infty} \mathrm{d}t\, \mathrm{e}^{-\mathrm{i}(\boldsymbol{k}\cdot\boldsymbol{\theta}-\omega t)}\delta F(\boldsymbol{\theta},\boldsymbol{J},t), \tag{2.2.13}$$

where d is the dimension of the physical space. This expression is well-defined for large enough values of $\mathrm{Im}(\omega)$. Nonetheless, analytic continuation can be used to recover the remaining part of the complex ω-plane (see, e.g., Churchill & Brown, 2009). Finally, this transformation can be inversed using the *Bromwich–Mellin transform*

$$\delta F(\boldsymbol{\theta},\boldsymbol{J},t) = \sum_{\boldsymbol{k}\in\mathbb{Z}^d} \int_{\mathcal{C}} \frac{\mathrm{d}\omega}{2\pi} \mathrm{e}^{\mathrm{i}(\boldsymbol{k}\cdot\boldsymbol{\theta}-\omega t)}\delta\widetilde{F}_{\boldsymbol{k}}(\boldsymbol{J},\omega), \tag{2.2.14}$$

where $\mathcal{C}$ is a contour in the complex ω-plane which passes above all poles of the integrand, i.e. for $\mathrm{Im}(\omega)$ large enough. I apply the Fourier–Laplace transform to eq. (2.2.12b) and obtain (Chavanis, 2012)

$$-\,\delta\widetilde{F}_{\boldsymbol{k}}(\boldsymbol{J},0) - \mathrm{i}\omega\delta\widetilde{F}_{\boldsymbol{k}}(\boldsymbol{J},\omega) + \mathrm{i}\boldsymbol{k}\cdot\boldsymbol{\Omega}\,\delta\widetilde{F}_{\boldsymbol{k}}(\boldsymbol{J},\omega) - \mathrm{i}\boldsymbol{k}\cdot\frac{\partial F}{\partial \boldsymbol{J}}\delta\widetilde{\Phi}_{\boldsymbol{k}}(\boldsymbol{J},\omega) = 0. \tag{2.2.15}$$

Rearranging this expression, I can express the fluctuations as

$$\delta\widetilde{F}_{\boldsymbol{k}}(\boldsymbol{J},\omega) = \frac{\boldsymbol{k}\cdot\frac{\partial F}{\partial \boldsymbol{J}}}{\boldsymbol{k}\cdot\boldsymbol{\Omega}-\omega}\delta\widetilde{\Phi}_{\boldsymbol{k}}(\boldsymbol{J},\omega) + \frac{\delta\widetilde{F}_{\boldsymbol{k}}(\boldsymbol{J},0)}{\mathrm{i}(\boldsymbol{k}\cdot\boldsymbol{\Omega}-\omega)}. \tag{2.2.16}$$

The first term of the r.h.s. corresponds to the impact of *collective effects*. As the system gets closer to a resonance $\omega = \boldsymbol{k}\cdot\boldsymbol{\Omega}$, the fluctuations $\delta\widetilde{\Phi}$ are amplified by the resonant denominator. The second term of the r.h.s. is driven by the initial condition $\delta\widetilde{F}_{\boldsymbol{k}}(\boldsymbol{J},0)$. In particular, the $1/(\boldsymbol{k}\cdot\boldsymbol{\Omega}-\omega)$ term captures its phase mixing (Fig. 1.7).

Now, I want to compute the r.h.s. of eq. (2.2.12a). Using Poisson equation, the fluctuations

---

[b] There exist examples of systems which exhibit algebraic damping instead of the classical exponential damping (see, e.g., Barré et al., 2010, 2011).

$\delta\Phi$ of the potential Φ are related to the fluctuations δF of the DF F (eq. 2.2.4) by

$$\delta\Phi(\boldsymbol{r},t) = \int \mathrm{d}\boldsymbol{w}'\, U(|\boldsymbol{r}-\boldsymbol{r}'|)\, \delta F(\boldsymbol{w}',t). \tag{2.2.17}$$

Therefore, it is useful to expand the pairwise interaction potential in angle-action space as

$$U(|\boldsymbol{r}[\boldsymbol{\theta},\boldsymbol{J}]-\boldsymbol{r}'[\boldsymbol{\theta}',\boldsymbol{J}']|) = \sum_{\boldsymbol{k},\boldsymbol{k}'} \psi_{\boldsymbol{k}\boldsymbol{k}'}(\boldsymbol{J},\boldsymbol{J}')\, \mathrm{e}^{\mathrm{i}(\boldsymbol{k}\cdot\boldsymbol{\theta}-\boldsymbol{k}'\cdot\boldsymbol{\theta}')}, \tag{2.2.18}$$

where I introduced (following Fouvry, 2020) the *coupling coefficients*

$$\boxed{\psi_{\boldsymbol{k}\boldsymbol{k}'}(\boldsymbol{J},\boldsymbol{J}') = \int \frac{\mathrm{d}\boldsymbol{\theta}}{(2\pi)^d}\frac{\mathrm{d}\boldsymbol{\theta}'}{(2\pi)^d} U(|\boldsymbol{r}[\boldsymbol{\theta},\boldsymbol{J}]-\boldsymbol{r}'[\boldsymbol{\theta}',\boldsymbol{J}']|)\, \mathrm{e}^{-\mathrm{i}(\boldsymbol{k}\cdot\boldsymbol{\theta}-\boldsymbol{k}'\cdot\boldsymbol{\theta}')}.} \tag{2.2.19}$$

Here, these coefficients are said to be *bare* because they do not capture any self-gravitating amplification. Their role is to capture the strength of the coupling between orbits $\boldsymbol{J}$ and $\boldsymbol{J}'$ through the pair of resonance vectors $(\boldsymbol{k},\boldsymbol{k}')$. Using this decomposition, I can rewrite the self-consistency relation (eq. 2.2.17) between δF and $\delta\Phi$ as

$$\delta\widetilde{\Phi}_{\boldsymbol{k}}(\boldsymbol{J},\omega) = (2\pi)^d \sum_{\boldsymbol{k}'} \int \mathrm{d}\boldsymbol{J}' \psi_{\boldsymbol{k}\boldsymbol{k}'}(\boldsymbol{J},\boldsymbol{J}')\delta\widetilde{F}_{\boldsymbol{k}'}(\boldsymbol{J}',\omega). \tag{2.2.20}$$

I can now inject this expression into eq. (2.2.16). Ultimately, this yields

$$\delta\widetilde{\Phi}_{\boldsymbol{k}}(\boldsymbol{J},\omega) = -(2\pi)^d \sum_{\boldsymbol{k}'} \int \mathrm{d}\boldsymbol{J}' \frac{\delta\widetilde{F}_{\boldsymbol{k}'}(\boldsymbol{J}',0)}{\mathrm{i}(\omega-\boldsymbol{k}'\cdot\boldsymbol{\Omega}')} \psi^{\mathrm{d}}_{\boldsymbol{k}\boldsymbol{k}'}(\boldsymbol{J},\boldsymbol{J}',\omega), \tag{2.2.21}$$

where I have introduced the *dressed coupling coefficients* $\psi^{\mathrm{d}}_{\boldsymbol{k}\boldsymbol{k}'}(\boldsymbol{J},\boldsymbol{J}',\omega)$. It can be shown that these coefficients satisfy the self-consistency relations (Fouvry & Bar-Or, 2018)

$$\psi^{\mathrm{d}}_{\boldsymbol{k}\boldsymbol{k}'}(\boldsymbol{J},\boldsymbol{J}',\omega) = (2\pi)^d \sum_{\boldsymbol{k}''} \int \mathrm{d}\boldsymbol{J}'' \frac{\boldsymbol{k}''\cdot\partial F/\partial\boldsymbol{J}''}{\boldsymbol{k}''\cdot\boldsymbol{\Omega}''-\omega} \psi_{\boldsymbol{k}\boldsymbol{k}''}(\boldsymbol{J},\boldsymbol{J}'')\psi^{\mathrm{d}}_{\boldsymbol{k}''\boldsymbol{k}'}(\boldsymbol{J}'',\boldsymbol{J}',\omega) + \psi_{\boldsymbol{k}\boldsymbol{k}'}(\boldsymbol{J},\boldsymbol{J}'). \tag{2.2.22}$$

Because this relation only involves the mean field properties from the background, it captures the efficiency with which the underlying collisionless system can amplify perturbations through self-gravity. On the contrary, if collective effects do not occur or are neglected, then the dressed coupling coefficients reduce to the bare coupling coefficients defined in eq. (2.2.19).

Let me assume now that I have access to a complete bi-orthogonal set of basis functions $(\psi^{(p)}[\boldsymbol{r}],\rho^{(p)}[\boldsymbol{r}])$ (Kalnajs, 1976) which satisfy

$$\psi^{(p)}(\boldsymbol{r}) = \int \mathrm{d}\boldsymbol{r}'\, U(|\boldsymbol{r}-\boldsymbol{r}'|)\rho^{(p)}(\boldsymbol{r}'), \tag{2.2.23a}$$

$$\int \mathrm{d}\boldsymbol{r}\, \psi^{(p)*}(\boldsymbol{r})\rho^{(q)}(\boldsymbol{r}) = -\delta_{pq}. \tag{2.2.23b}$$

The first equation corresponds to Poisson equation. The second equation describes the mutual orthogonality between potential and density basis functions. Therefore, using this set of functions allows me to convert easily the potential fluctuations into the associated density fluctuations

$$\delta\Phi(\boldsymbol{r},t) = \sum_p A_p(t)\psi^{(p)}(\boldsymbol{r}) \quad \leftrightarrow \quad \delta\rho(\boldsymbol{r},t) = \sum_p A_p(t)\rho^{(p)}(\boldsymbol{r}), \tag{2.2.24}$$

where

$$A_p(t) = -\int \mathrm{d}\boldsymbol{r}\, \delta\Phi(\boldsymbol{r},t)\rho^{(p)*}(\boldsymbol{r}). \tag{2.2.25}$$

By construction, the basis elements satisfy Poisson equation (eq. 2.2.17). Therefore, it is immediate to go from potentials to densities. Furthermore, the temporal and spatial parts in the fluctuations have been separated in eq. (2.2.24).

Let me now express the interaction potential with the potential basis functions as

$$U(|\boldsymbol{r}-\boldsymbol{r}'|) = -\sum_p \psi^{(p)}(\boldsymbol{r})\psi^{(p)*}(\boldsymbol{r}'). \tag{2.2.26}$$

It follows that the bare coupling coefficients read as

$$\psi_{\boldsymbol{k}\boldsymbol{k}'}(\boldsymbol{J},\boldsymbol{J}') = -\sum_p \psi_{\boldsymbol{k}}^{(p)}(\boldsymbol{J})\psi_{\boldsymbol{k}'}^{(p)*}(\boldsymbol{J}'), \tag{2.2.27}$$

where $\psi_{\boldsymbol{k}}^{(p)}(\boldsymbol{J})$ is the Fourier transform of the corresponding basis element

$$\psi_{\boldsymbol{k}}^{(p)}(\boldsymbol{J}) = \int \frac{\mathrm{d}\boldsymbol{\theta}}{(2\pi)^d}\psi^{(p)}(\boldsymbol{r}[\boldsymbol{\theta},\boldsymbol{J}])\,\mathrm{e}^{-\mathrm{i}\boldsymbol{k}\cdot\boldsymbol{\theta}}. \tag{2.2.28}$$

After a lengthy computation (Chavanis, 2012), the dressed coupling coefficients can be expressed as

$$\boxed{\psi_{\boldsymbol{k}\boldsymbol{k}'}^{\mathrm{d}}(\boldsymbol{J},\boldsymbol{J}',\omega) = -\sum_{p,q} \psi_{\boldsymbol{k}}^{(p)}(\boldsymbol{J})\mathbf{E}_{pq}^{-1}(\omega)\psi_{\boldsymbol{k}'}^{(q)}(\boldsymbol{J}'),} \tag{2.2.29}$$

where I introduced the *dielectric matrix* $\mathbf{E}(\omega) = \mathbf{I} - \mathbf{M}(\omega)$. Here, $\mathbf{M}(\omega)$ is the *response matrix* defined by

$$\boxed{\mathbf{M}_{pq}(\omega) = (2\pi)^d \sum_{\boldsymbol{k}} \int \mathrm{d}\boldsymbol{J} \frac{\boldsymbol{k}\cdot\partial F/\partial \boldsymbol{J}}{\omega - \boldsymbol{k}\cdot\boldsymbol{\Omega}(\boldsymbol{J})}\psi_{\boldsymbol{k}}^{(p)*}(\boldsymbol{J})\psi_{\boldsymbol{k}}^{(q)}(\boldsymbol{J}).} \tag{2.2.30}$$

This reponse matrix is central in describing how perturbations can be amplified via the self-gravity of the system. For orbits for which ω is close to the frequency $\boldsymbol{k}\cdot\boldsymbol{\Omega}(\boldsymbol{J})$, the denominator $1/(\omega - \boldsymbol{k}\cdot\boldsymbol{\Omega}[\boldsymbol{J}])$ in eq. (2.2.30) becomes very large. The behaviour of the numerator, $\boldsymbol{k}\cdot\partial F/\partial \boldsymbol{J}$, will impact the contribution of the resonance $\boldsymbol{k}$: when many orbits accumulate near it, i.e. if it corresponds to a broad extremum, these orbits will be given more time to torque each other. I will refer to this as *coherent motion*. This is typically what happens for cold centrifugally supported systems, for which the dielectric matrix $\mathbf{E}(\omega)$ can have eigenvalues close to zero. This has the effect of amplifying the fluctuations in the system by changing the bare coupling coefficients (eq. 2.2.28) into the dressed ones (eq. 2.2.29). However, a supplementary complexity arises, because eq. (2.2.30) is only defined for values of $\mathrm{Im}(\omega)$ large enough. In order to compute $\mathbf{M}(\omega)$ for any frequency ω, I need to obtain its analytic continuation over the whole complex plane. This can be done by using the *Landau prescription* (see, e.g., section 5.2.4 of Binney & Tremaine, 2008).

Having access to the dressed coupling coefficients, it is now possible to recover – in principle – the potential fluctuation $\delta\widetilde{\Phi}_{\boldsymbol{k}}(\boldsymbol{J},\omega)$ given in eq. (2.2.21), as well as its time-dependent equivalent $\delta\Phi_{\boldsymbol{k}}(\boldsymbol{J},t)$ by taking an inverse Fourier transform (eq. 2.2.14). In practice however, the treatment of the resonant denominator in $\mathbf{M}(\omega)$ makes this computation an arduous task. Notwithstanding, Chavanis (2012) expresses eq. (2.2.12a) w.r.t. the system fluctuations, to get

$$\boxed{\begin{aligned}\frac{\partial F}{\partial t}(\boldsymbol{J},t) = \pi(2\pi)^d m \frac{\partial}{\partial \boldsymbol{J}} \cdot \sum_{\boldsymbol{k},\boldsymbol{k}'} \boldsymbol{k} \int \mathrm{d}\boldsymbol{J}' |\psi^{\mathrm{d}}_{\boldsymbol{k}\boldsymbol{k}'}(\boldsymbol{J},\boldsymbol{J}',\boldsymbol{k}\cdot\boldsymbol{\Omega})|^2 \, \delta_{\mathrm{D}}(\boldsymbol{k}\cdot\boldsymbol{\Omega} - \boldsymbol{k}'\cdot\boldsymbol{\Omega}') \\ \times\left(\boldsymbol{k}\cdot\frac{\partial}{\partial \boldsymbol{J}} - \boldsymbol{k}'\cdot\frac{\partial}{\partial \boldsymbol{J}'}\right) F(\boldsymbol{J},t)F(\boldsymbol{J}',t),\end{aligned}} \tag{2.2.31}$$

where $\boldsymbol{\Omega} = \boldsymbol{\Omega}(\boldsymbol{J})$, $\boldsymbol{\Omega}' = \boldsymbol{\Omega}(\boldsymbol{J}')$ and I reintroduced explicitely the (secular) time dependence in the DF. This is the self-consistent, inhomogeneous *Balescu–Lenard equation* first derived by Heyvaerts (2010). It convenient to rewrite eq. (2.2.31) as the continuity equation

$$\frac{\partial F}{\partial t} = -\frac{\partial}{\partial \boldsymbol{J}} \cdot \boldsymbol{\mathcal{F}}, \tag{2.2.32}$$

where $\boldsymbol{\mathcal{F}}(\boldsymbol{J},t)$ is the diffusion flux in action space. It can be expressed in the form

$$\boldsymbol{\mathcal{F}}(\boldsymbol{J}) = \mathbf{A}(\boldsymbol{J})F(\boldsymbol{J}) - \frac{\mathbf{D}(\boldsymbol{J})}{2} \cdot \frac{\partial F}{\partial \boldsymbol{J}}, \tag{2.2.33}$$

where the friction coefficient $\mathbf{A}(\boldsymbol{J})$ and the diffusion tensor $\mathbf{D}(\boldsymbol{J})$ can be identified from the Balescu–Lenard eq. (2.2.31) as

$$\mathbf{A}(\boldsymbol{J}) = \pi(2\pi)^d m \sum_{\boldsymbol{k},\boldsymbol{k}'} \boldsymbol{k} \int \mathrm{d}\boldsymbol{J}' |\psi^{\mathrm{d}}_{\boldsymbol{k}\boldsymbol{k}'}(\boldsymbol{J},\boldsymbol{J}',\boldsymbol{k}\cdot\boldsymbol{\Omega})|^2 \, \delta_{\mathrm{D}}(\boldsymbol{k}\cdot\boldsymbol{\Omega} - \boldsymbol{k}'\cdot\boldsymbol{\Omega}') \, \boldsymbol{k}'\cdot\frac{\partial F}{\partial \boldsymbol{J}'}, \tag{2.2.34a}$$

$$\mathbf{D}(\boldsymbol{J}) = 2\pi(2\pi)^d m \sum_{\boldsymbol{k},\boldsymbol{k}'} \boldsymbol{k}\otimes\boldsymbol{k} \int \mathrm{d}\boldsymbol{J}' |\psi^{\mathrm{d}}_{\boldsymbol{k}\boldsymbol{k}'}(\boldsymbol{J},\boldsymbol{J}',\boldsymbol{k}\cdot\boldsymbol{\Omega})|^2 \, \delta_{\mathrm{D}}(\boldsymbol{k}\cdot\boldsymbol{\Omega} - \boldsymbol{k}'\cdot\boldsymbol{\Omega}') F(\boldsymbol{J}'). \tag{2.2.34b}$$

As it is the master equation describing the full secular relaxation of self-gravitating systems, let me take a moment to describe each of its components. First, note that as expected, the Balescu–Lenard eq. (2.2.31) is quadratic in F. As such it retains the non-linear nature of orbital diffusion, where the system operates on itself to self-diffuse its orbital structure (Fig. 2.1). The collision term of eq. (2.2.34) is proportional to $m = M/N$, because relaxation is sourced by finite-N effects. It involves a summation over the resonance vectors $(\boldsymbol{k},\boldsymbol{k}')$, as well as a resonance condition $\boldsymbol{k}\cdot\boldsymbol{\Omega}(\boldsymbol{J}) = \boldsymbol{k}'\cdot\boldsymbol{\Omega}(\boldsymbol{J}')$, i.e. relaxation is sourced by non-local interactions between sets of orbits captured in mutual resonance. In addition, the strength of these interactions is captured by the dressed coupling coefficients $\psi^{\mathrm{d}}_{\boldsymbol{k}\boldsymbol{k}'}(\boldsymbol{J},\boldsymbol{J}',\boldsymbol{k}\cdot\boldsymbol{\Omega}[\boldsymbol{J}])$ (eq. 2.2.29). Not only do these describe the efficiency of orbital interaction, but they are also amplified by self-gravity through the response matrix $\mathbf{M}(\omega)$ defined in eq. (2.2.30). Interestingly this motivates linear response theory: the Balescu–Lenard theory simply dresses up the linear response (Hamilton, 2021). This was not obvious a priori. Furthermore, the collision term involves the mean field quantities $F(\boldsymbol{J})$ and $\boldsymbol{\Omega}(\boldsymbol{J})$, because relaxation occurs as a series of QSS (Lynden-Bell, 1967). Finally, this equation involves an integration over action space, in order to scan over all stars of the background.

One can straightforwardly transpose the derivation of the Balescu–Lenard eq. (2.2.31) to the case of a multi-mass system, which is undoubtedly astrophysically more relevant. Following

Fouvry (2020), the corresponding Balescu–Lenard equation reads

$$\boxed{\begin{aligned}\frac{\partial F_\alpha}{\partial t}(\boldsymbol{J},t) = \pi(2\pi)^d \frac{\partial}{\partial \boldsymbol{J}} \cdot \sum_{\boldsymbol{k},\boldsymbol{k}'} \boldsymbol{k} \int \mathrm{d}\boldsymbol{J}' |\psi^{\mathrm{d}}_{\boldsymbol{k}\boldsymbol{k}'}(\boldsymbol{J},\boldsymbol{J}',\boldsymbol{k}\cdot\boldsymbol{\Omega})|^2 \, \delta_{\mathrm{D}}(\boldsymbol{k}\cdot\boldsymbol{\Omega} - \boldsymbol{k}'\cdot\boldsymbol{\Omega}') \\ \times \sum_\beta \left(m_\beta \, \boldsymbol{k}\cdot\frac{\partial}{\partial \boldsymbol{J}} - m_\alpha \, \boldsymbol{k}'\cdot\frac{\partial}{\partial \boldsymbol{J}'} \right) F_\alpha(\boldsymbol{J},t) F_\beta(\boldsymbol{J}',t).\end{aligned}} \tag{2.2.35}$$

Here, m_α is the individual mass associated to the family α with DF F_α such that

$$\int \mathrm{d}\boldsymbol{\theta}\mathrm{d}\boldsymbol{J}\, F_\alpha = M_\alpha,$$

where M_α is the total mass of the family. Furthermore, the computation of the susceptibility coefficients (eq. 2.2.29) involves all the family components, i.e. one has to make the change $F \to \sum_\beta F_\beta$. In chapter 3, I will use eq. (2.2.35) to describe the secular evolution of the S-cluster under the effect of a family of stars and a family of IMBHs. Note that the multi-mass formulation captures a mass segregation of the different massive components due to the $(m_\alpha \ldots - m_\beta \ldots)$ term in eq. (2.2.35). However, I will not discuss this mechanism in this thesis.

2.2.3 Previous applications of the Balescu–Lenard equation

The previous sections showed how the Balescu–Lenard equation (eq. 2.2.31) could be used – in theory – to describe any kind of self-gravitating system. However, its structure shows how difficult both its theoretical and its numerical applications are expected to be. Let me now highlight some of the previous applications of the Balescu–Lenard formalism.

As mentioned in chapter 1, the Balescu–Lenard equation was first applied to *tepid discs* (Fouvry et al., 2015a). In this setup, a few approximations were needed. First, an explicit mapping $(\boldsymbol{x},\boldsymbol{v}) \mapsto (\boldsymbol{\theta},\boldsymbol{J})$ between physical space and angle-action space was required. Generically, such a mapping can be challenging to obtain, and is one of the main difficulties one encounters when applying the Balescu–Lenard theory (as discussed in section 2.2.2). To obtain this mapping, the authors considered a disc which is sufficiently cold so as to be able to rely on the *epicyclic approximation* (see, e.g., Binney & Tremaine, 2008). Having obtained a mapping between physical and angle-action spaces, there remains the need to use the appropriate basis elements (eq. 2.2.23). By assuming that only *tightly wound spirals* occur in the disc, a WKB basis was used. These approximations allow one to compute the initial variation of the DF in action space. In particular, one can highlight the importance of a few key resonances, such as the inner Lindblad resonance (Fouvry et al., 2015b). Overall, the Balescu–Lenard eq. (2.2.31) is able to predict the formation of ridges in action space (Fig. 2.3), already observed in simulations (Sellwood, 2012). Taking into account swing amplifications induced by self-gravity (Fouvry et al., 2015c), and using the matrix method of Kalnajs (1977), these authors were able to explain the amplification of the secular evolution by a factor ~ 1000 as a result of collective effects in the Balescu–Lenard equation.

While the cold tepid disc case highlights nicely the resonant structure of the Balescu–Lenard equation, as well as its ability to greatly amplify initially small fluctuations, there exist systems in which its application can yield quite distinct results. A particular example is that of spherically symmetric systems. This symmetry induces a degeneracy w.r.t. L_z the z-component of the angular momentum $\boldsymbol{L}$, which makes the Balescu–Lenard prediction more intricate than expected. Additional steps are required to solve the degeneracy, such as integrating over L_z, and

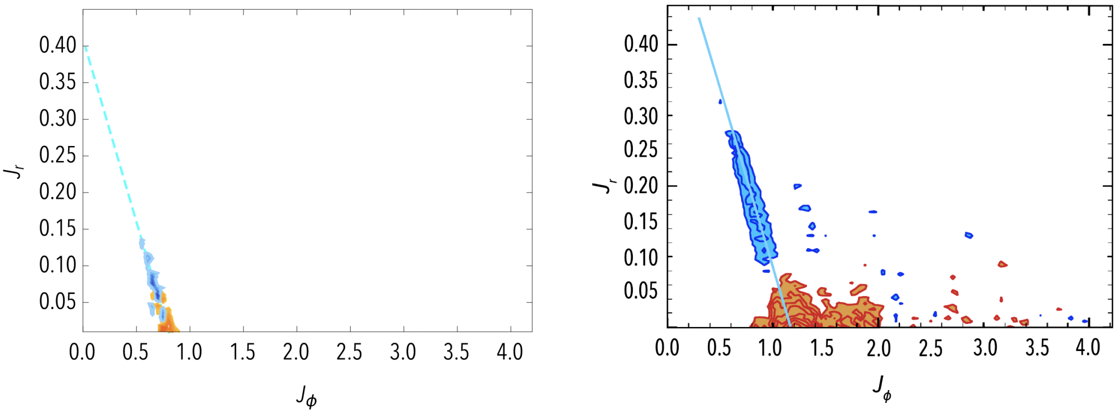

Figure 2.3: From fig. 4 of Fouvry et al. (2015c). The left panel is a map of the diffusion rate $\partial F/\partial t$ in a Mestel disc using the Balescu–Lenard equation (see eq. 2.2.31). The red contours correspond to depleted regions, while the blue contours correspond to regions where the DF is increased. The right panel is the measurement of Sellwood (2012) using N-body simulations. The Balescu–Lenard equation is able to predict the leftmost resonant ridge observed in N-body simulations.

developing the potential using a multipole expansion. This applies in particular to two systems of astrophysical interest: the Galactic nucleus (Bar-Or & Fouvry, 2018) and the isotropic isochrone globular cluster (Hamilton et al., 2018; Lau & Binney, 2019; Fouvry et al., 2021).

In the first system, the Balescu–Lenard equation can be used to predict the existence of the so-called *Schwarzschild barrier* observed numerically by Merritt et al. (2011), which prevents the orbital diffusion of stars close to the central SMBH. Furthermore, using a fixed background isotropic distribution, one can compute a Fokker–Planck equation describing the evolution of the eccentricity of test stars in the quasi-Keplerian system, as well as an associated stochastic Langevin equation which can be used to incorporate other processes.

For globular clusters (Hamilton et al., 2018; Fouvry et al., 2021), the Balescu–Lenard equation yields yet again qualitatively and quantitatively different predictions w.r.t. the previous systems. First, the multipole expansion of the Balescu–Lenard equation diverges logarithmically on small scales. Second, the resonant effects which were observed in tepid discs do not play a significant role in isotropic globular clusters. In fact, the Balescu–Lenard prediction makes quantitative predictions which are paradoxically very close to Chandrasekhar's prediction. Therefore, resonances, which had a strong impact on secular relaxation in cold systems (e.g., the tepid disc), are not as impactful in hotter systems (e.g., the non-rotating globular cluster). Additionally, collective effects do not impact strongly the system: the Balescu–Lenard prediction matches the prediction one would obtain when setting the response matrix (eq. 2.2.30) to zero. This will be investigated in more details in chapter 4.

2.3 Limiting cases of the Balescu–Lenard equation

It is also of interest to simplify the problem by neglecting collective effects (Fig. 2.4). This is the topic of the next section.

2.3.1 The inhomogeneous Landau equation

Neglecting collective effects amounts to setting the response matrix $\mathbf{M}$ (eq. 2.2.30) to zero, i.e. replacing the dressed coupling coefficients (eq. 2.2.29) by the bare ones (eq. 2.2.27). Then,

Figure 2.4: Schematic representation of the successive limiting cases of the Balescu–Lenard equation. Neglecting collective effects, i.e. setting the response matrix $\mathbf{M}$ (eq. 2.2.30) to zero, yields the inhomogeneous Landau equation (eq. 2.3.1) describing the RR theory (section 2.3.1). Imposing local homogeneity on top of the RR formalism yields the NR theory, which is dominated by non-resonant, local interactions (section 2.3.2).

the Balescu–Lenard equation (eq. 2.2.31) reduces to the *inhomogeneous Landau equation* (Polyachenko & Shukhman, 1982; Chavanis, 2013a)

$$\boxed{\begin{aligned}\frac{\partial F}{\partial t} = \pi(2\pi)^d m \frac{\partial}{\partial \boldsymbol{J}} \cdot \sum_{\boldsymbol{k},\boldsymbol{k}'} \boldsymbol{k} \int \mathrm{d}\boldsymbol{J}' |\psi_{\boldsymbol{k}\boldsymbol{k}'}(\boldsymbol{J},\boldsymbol{J}',\boldsymbol{k}\cdot\boldsymbol{\Omega})|^2\, \delta_{\mathrm{D}}(\boldsymbol{k}\cdot\boldsymbol{\Omega} - \boldsymbol{k}'\cdot\boldsymbol{\Omega}') \\ \times \left(\boldsymbol{k}\cdot\frac{\partial}{\partial \boldsymbol{J}} - \boldsymbol{k}'\cdot\frac{\partial}{\partial \boldsymbol{J}'}\right) F(\boldsymbol{J},t) F(\boldsymbol{J}',t),\end{aligned}} \tag{2.3.1}$$

where the bare coupling coefficients are the Fourier coefficients of the interaction potential, given by eq. (2.2.19).

Let me consider next the relaxation of a test star[c] – a particle which does not induce any back-reaction from the background – under the effect of a steady distribution of field stars. The effect of this background distribution, which I call $F_0(\boldsymbol{J})$, is to impose a stochastic force field on the test star. This allows me to simply transform the quadratic differential Landau eq. (2.3.1) into the linear, differential *Fokker–Planck equation*

$$\begin{aligned}\frac{\partial F}{\partial t} = \pi(2\pi)^d m \frac{\partial}{\partial \boldsymbol{J}} \cdot \sum_{\boldsymbol{k},\boldsymbol{k}'} \boldsymbol{k} \int \mathrm{d}\boldsymbol{J}' |\psi_{\boldsymbol{k}\boldsymbol{k}'}(\boldsymbol{J},\boldsymbol{J}',\boldsymbol{k}\cdot\boldsymbol{\Omega})|^2\, \delta_{\mathrm{D}}(\boldsymbol{k}\cdot\boldsymbol{\Omega} - \boldsymbol{k}'\cdot\boldsymbol{\Omega}') \\ \times \left(\boldsymbol{k}\cdot\frac{\partial}{\partial \boldsymbol{J}} - \boldsymbol{k}'\cdot\frac{\partial}{\partial \boldsymbol{J}'}\right) F(\boldsymbol{J},t) F_0(\boldsymbol{J}'),\end{aligned} \tag{2.3.2}$$

where the distribution of field stars $F_0(\boldsymbol{J})$ is fixed. Of course, I can express this equation under the form given in eq. (2.2.32). Then, the diffusion coefficients are those given in eq. (2.2.34), where I replace the self-consistent DF $F(\boldsymbol{J}',t)$ by the background distribution $F_0(\boldsymbol{J}')$.

Application to the Galactic centre

Now, let me use this Fokker–Planck approximation to a stellar system dominated by a central object, e.g., a galactic nucleus with a central SMBH. Its Hamiltonian takes the form (see, e.g., Bar-Or & Fouvry, 2018)

$$H(\boldsymbol{J}) = H_{\mathrm{Kep}}(L_{\mathrm{c}}) + \Phi_{\mathrm{GR}}(L_{\mathrm{c}}, L) + \Phi_{\star}(L_{\mathrm{c}}, L) + \delta\Phi, \tag{2.3.3}$$

where I have used the suitable Delaunay angle-action coordinates (see section 1.3.2). The first term, H_{Kep}, describes the interaction between the stars and the central SMBH. The second term, Φ_{GR}, describes the (relativistic) precession induced by the SMBH. The third term, $\Phi_{\star}$, describes the (non-relativistic) precession induced by the mass of the stellar background. Finally, the

---

[c] While the concept of test star is borrowed from theoretical physics and may seem contrived, in astrophysics it corresponds to a two-species situation where one very hot component does not react to the other thanks to its own inertia.

fourth term, $\delta\Phi$, describes the finite-N effects induced by the mutual interactions between the stars. Now, because of the overwhelming predominance of the SMBH, the most important term of the Hamiltonian is the Keplerian term. Comparing the two non-vanishing orbital frequencies yields the ratio $\Omega_{\rm Kep}/\Omega_{\rm P} \sim M_\bullet/M_\star \gg 1$, where $M_\star = Nm$ is the total stellar mass within the system and $\Omega_{\rm P}$ is the in-plane precession frequency. As a consequence, stars follow a fast, quasi-Keplerian motion around the SMBH.

This prompts me to perform an orbit-averaged over the fast Keplerian motion, which means averaging over the mean anomaly M (see, e.g., Murray & Dermott, 2000, for a more complete description of the orbital anomalies). This yields the orbit-averaged SRR Hamiltonian (Fouvry & Bar-Or, 2018)

$$\overline{H}(\boldsymbol{J}) = \overline{\Phi}_{\rm GR} + \overline{\Phi}_\star + \overline{\delta\Phi} = \overline{H}_0 + \overline{\delta\Phi}. \tag{2.3.4}$$

As a result of orbit-averaging, the circular angular momentum $L_{\rm c}$ is adiabatically conserved. In addition, instead of considering the dynamics of stars, I now consider the (orbit-averaged) dynamics of Keplerian wires (Fig. 2.5). Hence, the semi-major axis of a wire cannot be impacted by orbit-averaged dynamics. Therefore, secular theory applied to eq. (2.3.4) will describe the secular relaxation of the angular momentum of wires alone (or equivalently, of their eccentricity).

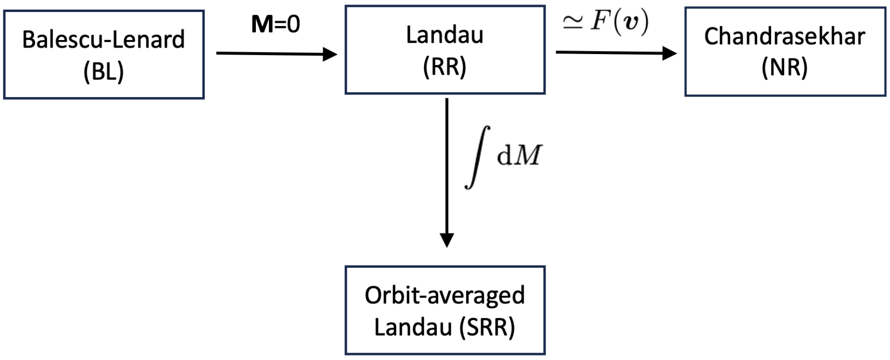

Figure 2.5: Schematic representation of the orbit-averaged Landau equation, applied to the Galactic nucleus. Due to the overwhelming presence of the central SMBH, I observe a timescale separation between the diffusion in $L_{\rm c}$ and in L. This prompts averaging over the fast Keplerian motion to study the orbit-averaged dynamics of the S-cluster.

If I restrict my analysis to an isotropic background distribution of stars $F_0(L_{\rm c})$, its gradient $\partial F_0/\partial L$ vanishes. Because the response matrix $\mathbf{M}$ in eq. (2.2.30) involves the gradient of the background DF, the response matrix naturally exactly vanishes in this case (Bar-Or & Fouvry, 2018). In practice, as stated above, this means that an isotropic background does not feel any back-reaction from the test particle. Therefore, this system sources no dynamical friction and its dressed coupling coefficients (eq. 2.2.29) reduce to the bare ones (eq. 2.2.19). It follows that the Balescu–Lenard equation for such isotropic Keplerian systems reduces to the Fokker–Planck equation given by eq. (2.3.2). Moreover, integrating eq. (2.3.1) over L_z yields the diffusion equation (Bar-Or & Fouvry, 2018)

$$\frac{\partial F(\boldsymbol{J},t)}{\partial t} = \frac{1}{2}\frac{\partial}{\partial L}\left[L D^{\rm RR}_{LL}(\boldsymbol{J}) \frac{\partial}{\partial L}\left(\frac{F(\boldsymbol{J},t)}{L}\right)\right], \tag{2.3.5}$$

where $\boldsymbol{J} = (L_{\rm c}, L)$ are the in-plane actions. In this equation, the diffusion coefficient from eq. (2.2.34b) becomes

$$D_{LL}^{\mathrm{RR}}(\boldsymbol{J}) = 4\pi \sum_{k,k'} k \int \mathrm{d}\boldsymbol{J}' |\overline{\psi}_{kk'}(\boldsymbol{J},\boldsymbol{J}')|^2 \, \delta_{\mathrm{D}}(k\Omega_{\mathrm{P}}[\boldsymbol{J}] - k'\Omega_{\mathrm{P}}[\boldsymbol{J}']) \, F_{\mathrm{tot}}(\boldsymbol{J}), \tag{2.3.6}$$

where $\Omega_{\mathrm{P}} = \partial \overline{H}_0/\partial L$ is the in-plane precession frequency and $\overline{\psi}_{kk'}(\boldsymbol{J},\boldsymbol{J}')$ are the bare in-plane orbit-averaged coupling coefficients between a set of resonant wires (Fig. 2.6). This equation applies for a multi-mass background family described by the (L_z-averaged) distribution function, $F_{\mathrm{tot}}(L_{\mathrm{c}}, L) = 2LF_0(L_{\mathrm{c}})$. Changing variables to the reduced angular momentum $j = L/L_{\mathrm{c}} = \sqrt{1-e^2}$ and semi-major axis (sma) a, the Fokker–Planck eq. (2.3.5) becomes

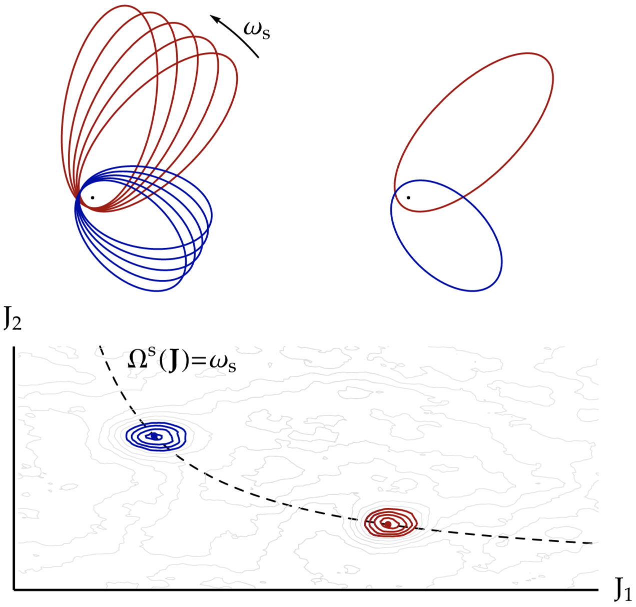

Figure 2.6: From fig. 1 of Fouvry et al. (2017). Illustration of the process of eccentricity relaxation in a galactic nucleus. In the vicinity of a SMBH, Keplerian wires undergo an in-plane pericentre precession (top left panel) due to relativistic corrections and the stellar mean potential. Additionally, two wires can resonate with each other (top right panel): they are then correlated and can efficiently couple together. To that end, they must satisfy a resonance condition between their precession frequencies. In the bottom panel are illustrated the fluctuations of the DF in action space. The resonant line is represented by the dashed black line, while the two stars are located at the blobs of their respective colours. Because they are located on the same resonance line, they can efficiently couple to one another.

$$\frac{\partial F(j,a,t)}{\partial t} = \frac{1}{2}\frac{\partial}{\partial j}\left[j D_{jj}^{\mathrm{RR}}(a,j) \frac{\partial}{\partial j}\left(\frac{F(j,a,t)}{j} \right) \right]. \tag{2.3.7}$$

Because the smas of Keplerian wires are not impacted by orbit-averaged dynamics, I can decompose the DF into $F(j,a,t) = P(j,t\,|\,a)N(a)$. This yields the simple Fokker–Planck equation (Bar-Or & Alexander, 2016)

$$\boxed{\frac{\partial P(j,t\,|\,a)}{\partial t} = \frac{1}{2}\frac{\partial}{\partial j}\left[j D_{jj}^{\mathrm{RR}}(a,j) \frac{\partial}{\partial j}\left(\frac{P(j,t\,|\,a)}{j} \right) \right],} \tag{2.3.8}$$

which describes the diffusion of j given the sma a. I will use this formulation in chapter 3 to probe the presence of IMBHs in the background cluster $F_{\mathrm{tot}}(L_{\mathrm{c}}, L)$ of the Galactic nucleus. Figure 2.7 illustrates schematically the impact of their presence in the Galactic nucleus. A few hundred years are sufficient to distribute effectively each star along its orbit (*angle averaging*), while the differential precession rate induces *phase mixing*. These two phenomena are followed by a slow relaxation of the S-cluster's eccentricity though the orbit-averaged RR formalism, whose efficiency is driven by the background families of the cluster.

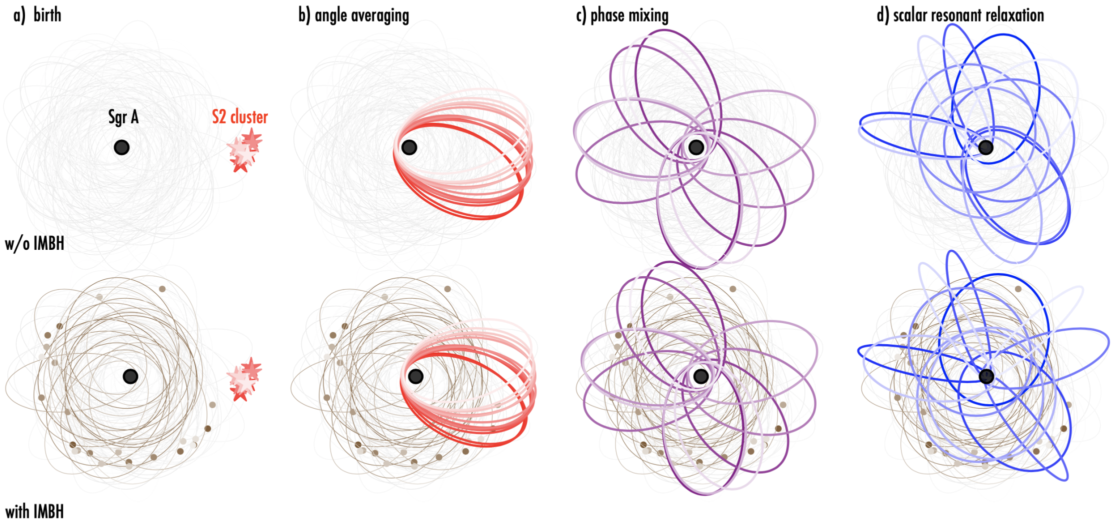

Figure 2.7: Sketch of the impact of IMBHs on the rate of diffusion of a recently formed cluster, courtesy of C. Pichon. Brown dots on the bottom represent IMBHs. From left to right: a) the time of formation of the S-cluster; b) after a few hundred years, each star is effectively distributed along its quasi-Keplerian orbit; c) because of the differential precession rates, the different orbits phase mix; d) through scalar resonant relaxation (SRR), they diffuse in eccentricity. The S-cluster on the bottom right panel contains more eccentric orbits because the IMBHs accelerate the scalar resonant relaxation.

2.3.2 The homogeneous Landau equation

In the previous section, I argued that in some systems, collective effects could be expected not to play a significant role. This allowed me to simplify the Balescu–Lenard equation into the inhomogeneous Landau equation. Yet, its implementation – while simplified compared to that of the Balescu–Lenard equation – is still convolved. This prompts me to further simplify it following Chandrasekhar (1942). Because as a first approximation, diffusion can be decomposed into a succession of local deflections, I will ignore long-range, resonant interactions and focus here on these local deflections (Chandrasekhar, 1943; Cohn, 1979). This is what is called NR theory. In this context, the test particle is only impacted by its nearest environment (Fig. 2.8). Therefore, I can enforce the additional assumption of *local homogeneity*. This can be done because in that regime, the distribution of the gravitational force is assumed to be dominated by the nearest neighbour's contribution (Chandrasekhar & von Neumann, 1942).

Let me discuss the impact of these assumptions on the inhomogeneous Landau equation (eq. 2.3.1). First, the cluster is assumed to be locally homogeneous, hence a test star locally follows a straight orbit in physical space as long as it is not deflected. Thus, orbital structure is best described in velocity space, which prompts the transformation $(\boldsymbol{\theta}, \boldsymbol{J}) \mapsto (\boldsymbol{r}, \boldsymbol{v})$. In addition, the cluster is assumed (for simplicity) to have infinite extent. Therefore, the resonance vectors form a continuum, which transforms the summation $\sum_{\boldsymbol{k}}$ into an integral $\int \mathrm{d}\boldsymbol{k}$. Finally, the coupling coefficients $\psi_{\boldsymbol{k}\boldsymbol{k}'}(\boldsymbol{J}, \boldsymbol{J}')$ reduce to the Fourier transform in physical space of the interaction potential, which reads $\delta_{\mathrm{D}}(\boldsymbol{k} - \boldsymbol{k}')/|\boldsymbol{k}|^2$ up to some prefactor. This simple form arises because the basis functions (eq. 2.2.23a) are simply Fourier basis functions as a result of translation invari-

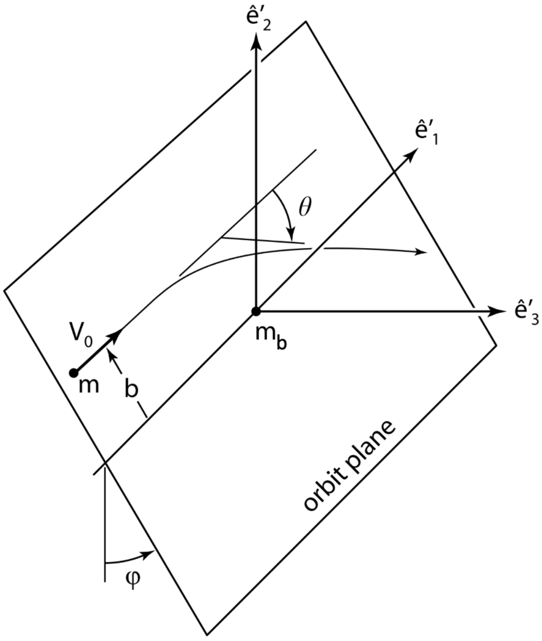

Figure 2.8: From Binney & Tremaine (2008). Geometry of one of the successive two-body encounters which source NR relaxation. The test star coming from infinity is deflected under the gravitational influence of one fixed background star, before going back to infinity. The successive deflections of the test star by background stars along its orbit, induce a secular diffusion of its orbital parameters. This method is the historical formalism used by Chandrasekhar to obtain the NR theory. This is equivalent to the method obtained from the Balescu–Lenard equation described in this chapter.

ance. In particular, orbital couplings become independent of the actions, i.e. independent of the particles' velocities. Ultimately, the inhomogeneous Landau equation (eq. 2.3.1) reduces to the *homogeneous Landau equation* (Chavanis, 2013b)

$$\frac{\partial F}{\partial t} = \pi(2\pi)^3 m \frac{\partial}{\partial v_i} \int \mathrm{d}\boldsymbol{v}'\mathrm{d}\boldsymbol{k}\, k_i k_j\, \delta_{\mathrm{D}}(\boldsymbol{k}\cdot\boldsymbol{w})\, \widehat{u}^2(k) \left(F' \frac{\partial F}{\partial v_j} - F \frac{\partial F'}{\partial v'_j} \right), \tag{2.3.9}$$

where I defined $\boldsymbol{w} = \boldsymbol{v} - \boldsymbol{v}'$, let $F = F(\boldsymbol{r}, \boldsymbol{v}, t)$ and $F' = F(\boldsymbol{r}, \boldsymbol{v}', t)$, and defined $\widehat{u}(k) = -G/(2\pi^2 k^2)$ the Fourier transform of the gravitational potential. In this formulation, the system's evolution is subject to the resonance condition $\boldsymbol{k}\cdot\boldsymbol{v} = \boldsymbol{k}\cdot\boldsymbol{v}'$ in $(\boldsymbol{r}, \boldsymbol{v})$-space. This condition can be understood as the conservation of energy during the two-body deflections (see Fig. 2.8 and Chavanis, 2013b). Equivalently, using Einstein notations, I can rewrite eq. (2.3.9) in the form (see, e.g., appendix C of Chavanis, 2013b)

$$\frac{\partial F}{\partial t} = \frac{\partial}{\partial v_i} \int \mathrm{d}\boldsymbol{v}' K_{ij} \left(F' \frac{\partial F}{\partial v_j} - F \frac{\partial F'}{\partial v'_j} \right) \quad ; \quad K_{ij} = 2\pi m G^2 \ln\Lambda \frac{w^2 \delta_{ij} - w_i w_j}{w^3}. \tag{2.3.10}$$

Here, I have explicitly introduced the *Coulomb logarithm*

$$\ln\Lambda = \int_{k_{\min}}^{k_{\max}} \frac{\mathrm{d}k}{k} = \ln\left(\frac{k_{\max}}{k_{\min}}\right) = \ln\left(\frac{b_{\max}}{b_{\min}}\right), \tag{2.3.11}$$

with some cutoffs at small scales and large scales to regularise strong collisions and far-away encounters.

The r.h.s. of eq. (2.3.10) is the original form of the collision operator given by Landau (1936) for the Coulomb interaction. It was derived under the assumption of weak deflections for a generic potential. Because of the assumption of local homogeneity, Chandrasekhar (1943) introduced a logarithmic divergence at large scales in eq. (2.3.10). In plasma physics, this divergence is taken care of by Debye shielding (see, e.g., Ichimaru, 1973). In that context, a polarisation cloud of opposite charges effectively reduces the range of interaction, making it short range in practice. This cutoff arises naturally when taking into account collective effects in the Balescu–Lenard equation of plasma physics (Balescu, 1960; Lenard, 1960). One can then use the Landau equation with the Debye length as a large-scale cutoff. However, there is no such shielding for the gravitational interaction, because only positive masses exist. Instead, the large-scale divergence is cured because two-star interactions are limited by the finite extent of the system. Taking spatial inhomogeneities into account ensures that no divergence at large scale occurs, such as in the inhomogeneous Landau equation (see, e.g., Chavanis, 2013a). In practice, I can use eq. (2.3.10) with a large scale cutoff taken at, e.g., the Jeans length λ_{J} (fixed by the size of the system).

Nevertheless, a small-scale divergence may still persist in the inhomogeneous Landau equation (eq. 2.3.1). This is the result of neglecting strong collisions at small impact parameters. In that regime, the linearisation to first-order perturbations cannot describe accurately the dynamics. Therefore, one must solve the exact two-body problem (see, e.g., appendix H in Chavanis, 2013a). Heuristically, this means imposing a small scale cutoff at the gravitational Landau length λ_{L}, which is the impact parameter for 90° deflections given by

$$b_{90} = \frac{G(m + m_{\mathrm{b}})}{w^2}, \tag{2.3.12}$$

where $w = |\boldsymbol{w}|$, m is the test star's mass and m_{b} the background star's mass. This cutoff is imposed by the fact that linear perturbation theory cannot predict deflections that are too strong (i.e. which fail to obey $\Delta\boldsymbol{v} \ll \boldsymbol{v}$). Overall, one can compute the Coulomb parameter from these cutoffs as

$$\ln\Lambda \sim \ln\frac{\lambda_{\mathrm{J}}}{\lambda_{\mathrm{L}}} \sim \ln N, \tag{2.3.13}$$

where N is the number of stars in the cluster. In effect, I shall take $\ln\Lambda = \ln(\lambda N)$ with λ being some parameter depending on the geometry of the cluster. For a globular cluster, I will take $\lambda = 0.11$ (Giersz & Heggie, 1994; Heggie & Hut, 2003).

Now, let me consider the non-resonant relaxation of a test star under the effect of a steady distribution of field stars. Following the discussion in section 2.3.1, this means changing $F(\boldsymbol{r}, \boldsymbol{v}', t)$ into $F_0(\boldsymbol{r}, \boldsymbol{v}')$ the steady distribution of the field stars in eq. (2.3.10). This allows me to simplify a quadratic differential equation (eq. 2.3.10) into the *linear* differential equation

$$\frac{\partial F}{\partial t} = \pi(2\pi)^3 m \frac{\partial}{\partial v_i} \int \mathrm{d}\boldsymbol{v}' \mathrm{d}\boldsymbol{k}\, k_i k_j\, \delta_{\mathrm{D}}(\boldsymbol{k}\cdot\boldsymbol{w})\, \widehat{u}^2(k) \left(F_0 \frac{\partial F}{\partial v_j} - F \frac{\partial F_0}{\partial v'_j} \right). \tag{2.3.14}$$

This equation is in fact once again a Fokker–Planck equation of the form

$$\frac{\partial F}{\partial t} = -\frac{\partial}{\partial v}\cdot \boldsymbol{\mathcal{F}}, \tag{2.3.15}$$

where the components of the flux $\boldsymbol{\mathcal{F}}$ are given by

$$\mathcal{F}_i = -\langle \Delta v_i \rangle F + \frac{1}{2} \sum_j \frac{\partial}{\partial v_j} \Big(\langle \Delta v_i \Delta v_j \rangle F \Big), \tag{2.3.16}$$

with (Chavanis, 2013a)

$$\langle \Delta v_i \rangle = -8\pi m G^2 \ln\Lambda \int \mathrm{d}\boldsymbol{v}' \frac{w_i}{w^3} F_0, \tag{2.3.17a}$$

$$\langle \Delta v_i \Delta v_j \rangle = 4\pi m G^2 \ln\Lambda \int \mathrm{d}\boldsymbol{v}' \frac{w^2\delta_{ij} - w_i w_j}{w^3} F_0. \tag{2.3.17b}$$

From these coefficients, I can recover the (local) friction coefficient $\mathbf{A}$ (see eq. 2.2.34 for the general self-gravitating case) by letting $A_i = \langle \Delta v_i \rangle - \frac{1}{2}\partial\langle \Delta v_i \Delta v_j\rangle/\partial v_j$, and the (local) diffusion tensor $\mathbf{D}$ by letting $D_{ij} = \langle \Delta v_i \Delta v_j \rangle$.

As I showed in the previous sections, when N is sufficiently large, the secular evolution of self-gravitating systems happens on timescales much longer than the dynamical time (Chandrasekhar, 1942). Hence, I expect that the orbital deflections induced by fluctuations occurring over a single orbit will be small. Furthermore, because the physical system is far from homogeneous, I want to reinstate the impact of some of the inhomogeneities in the NR picture. These two observations motivate me to phase-average the local diffusion coefficients over the star's orbit, and therefore to follow the secular evolution of this orbit instead of the precise location of the star on it. To that end, it is necessary to do a canonical transformation from phase space $(\boldsymbol{r}, \boldsymbol{v})$ to angle-action space $(\boldsymbol{\theta}, \boldsymbol{J})$, as was done in section 2.2.2. Under this canonical transformation, eq. (2.3.15) becomes

$$\frac{\partial F}{\partial t} = -\frac{\partial}{\partial \boldsymbol{J}} \cdot \boldsymbol{\mathcal{F}}. \tag{2.3.18}$$

Orbit-averaging eq. (2.3.18) yields the phase averaged *Fokker–Planck equation* (Cohn, 1979)

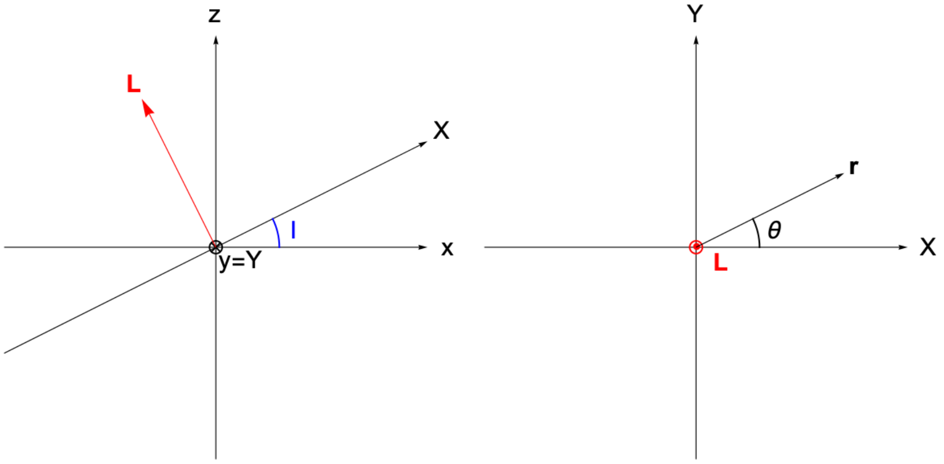

Figure 2.9: Illustration of the various parameters used to describe the dynamics of the system. In the left panel, the cluster is seen from the side, with (Oxy) being the equatorial plane of the cluster. In the right panel, the (OXY)-plane is the orbital plane of the test star, seen from above.

$$\frac{\partial F}{\partial t} = -\sum_i \frac{\partial (D_{J_i} F)}{\partial J_i} + \frac{1}{2}\sum_{i,j} \frac{\partial^2 (D_{J_i J_j} F)}{\partial J_i J_j}, \tag{2.3.19}$$

where I defined the *orbit-averaged diffusion coefficients*

$$D_{J_i} = \frac{1}{(2\pi)^3}\int \mathrm{d}\boldsymbol{\theta}\, \langle \Delta J_i \rangle \quad ; \quad D_{J_i J_j} = \frac{1}{(2\pi)^3}\int \mathrm{d}\boldsymbol{\theta}\, \langle \Delta J_i \Delta J_j \rangle. \tag{2.3.20}$$

These action diffusion coefficients can be deduced from the velocity deflection coefficients given in eq. (2.3.17) (see section 2.3.3). I will do so in this thesis in the context of the Galactic nucleus (chapter 3) and of anisotropic globular clusters (chapters 4 and 5).

Now, recall that I assumed the system to be spherically symmetric. This means that unperturbed orbits stay confined within a plane perpendicular to the angular momentum $\boldsymbol{L}$. I parametrise the star's location on this plane by r the radius and θ the angle variable (Fig. 2.9). Recall that $\boldsymbol{\theta} = (\theta_r, \theta_L, \theta_z)$ are the angles associated with the three actions (J_r, L, L_z). Using the angles defined in eqs. (1.3.3), I obtain the relation $\mathrm{d}\theta_1\mathrm{d}\theta_2 = (\Omega_r/v_r)\mathrm{d}r\mathrm{d}\theta$ with Ω_r being the radial frequency. At fixed r, the angles θ and θ_L differ by a constant r-dependent phase, hence I can average over either of them between 0 and 2π with the same end-result (Fig. 2.10). Therefore, the orbit-averaging of the local deflection coefficient $\langle \Delta X \rangle$ in X can generically be rewritten as

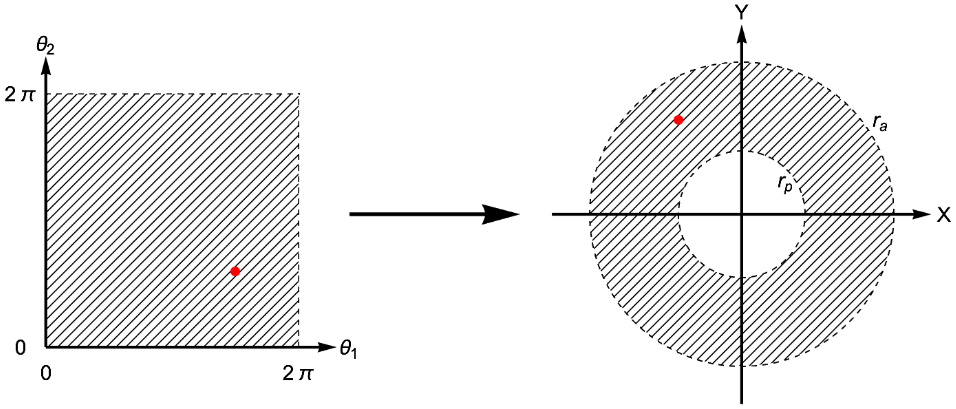

Figure 2.10: Illustration of orbit-averaging in angle-action space (left panel) and in physical space (right panel). While expressing the physical quantities w.r.t. to orbital angles can prove difficult, using physical coordinates (r, θ) in the orbital plane is straightforward. The latter can be used for orbit-averaging, at the cost of a Jacobian $1/|v_r|$ (see eq. 2.3.21). The red dot represents the location in angle space and physical space of the test star on its orbit.

$$D_X(\boldsymbol{J}) = \frac{\Omega_r}{\pi} \int_{r_\mathrm{p}}^{r_\mathrm{a}} \frac{\mathrm{d}r}{|v_r|} \int_0^{2\pi} \frac{\mathrm{d}\theta}{2\pi} \langle \Delta X \rangle (r, \theta, \boldsymbol{J}), \tag{2.3.21}$$

As it is now, eq. (2.3.21) displays an integrable singular integrand, whose behaviour is of order $|r - r_\mathrm{p,a}|^{-1/2}$ at the boundaries of motion $r_\mathrm{p,a}$ because of the factor $1/|v_r|$. On a practical level, this makes the numerical integration of eq. (2.3.21) complicated. On a theoretical level, this makes the computation of the gradient of any quantities involving $1/v_r$ impossible by simply differentiating the integrand. It is therefore better to define some *effective anomaly* u (Hénon, 1971) such that $\mathrm{d}r/v_r = \mathrm{d}u\,\Theta(u)$, where $\Theta(u) = (\mathrm{d}r/\mathrm{d}u)\,1/v_r$ is well-defined and analytical everywhere (including at the radial boundaries). In addition, $r = r(u)$ should be relatively easy to compute. In the case of a galactic nucleus dominated by a SMBH, I can use the eccentric anomaly as the effective anomaly (section 3.3.2). As for globular clusters, other effective anomalies can be calculated depending the potential. In chapter 3, I will derive an explicit effective anomaly for the Plummer potential.

2.3.3 Applications of the NR theory

I can now apply the NR formalism I have re-derived in the previous section to a variety of cases. To that aim, let me first compute the local diffusion coefficients in E and L from which I can obtain all the J_r and L diffusion coefficients. These coefficients can be deduced from the velocity coefficients by computing the changes in energy and angular momentum at second order in $\Delta v/v$ (see appendix 2.B). They read (Bar-Or & Alexander, 2016)

$$\begin{aligned}
\langle \Delta E \rangle &= \frac{1}{2}\langle (\Delta v_{\parallel})^2 \rangle + \frac{1}{2}\langle (\Delta v_{\perp})^2 \rangle + v\langle \Delta v_{\parallel} \rangle, && \text{(2.3.22a)}\\
\langle (\Delta E)^2 \rangle &= v^2 \langle (\Delta v_{\parallel})^2 \rangle, && \text{(2.3.22b)}\\
\langle \Delta L \rangle &= \frac{L}{v}\langle \Delta v_{\parallel} \rangle + \frac{r^2}{4L}\langle (\Delta v_{\perp})^2 \rangle, && \text{(2.3.22c)}\\
\langle (\Delta L^2) \rangle &= \frac{L^2}{v^2}\langle (\Delta v_{\parallel})^2 \rangle + \frac{1}{2}\frac{r^2 v_r^2}{v^2}\langle (\Delta v_{\perp})^2 \rangle, && \text{(2.3.22d)}\\
\langle \Delta E \Delta L \rangle &= L\langle (\Delta v_{\parallel})^2 \rangle. && \text{(2.3.22e)}
\end{aligned}$$

The coefficients $\langle \Delta v_{\parallel} \rangle$, $\langle (\Delta v_{\parallel})^2 \rangle$ and $\langle (\Delta v_{\perp})^2 \rangle$ can be obtained from eqs. (2.3.17) using the appropriate velocity coordinate system, and are the first- and second-order local velocity deflections. Here, $\Delta v_{\parallel}$ stands for the velocity increment along the initial trajectory, while $\Delta \boldsymbol{v}_{\perp}$ stands for the velocity increment perpendicular to the initial trajectory. In particular, they obey the relation

$$\Delta \boldsymbol{v} = \Delta v_{\parallel} \hat{\boldsymbol{v}} + \Delta \boldsymbol{v}_{\perp}, \qquad \text{(2.3.23)}$$

where $\Delta \boldsymbol{v}$ is the change in velocity of the test particle during a local encounter. Using the frame represented in Fig 2.11, the following relations hold

$$\begin{aligned}
\langle \Delta v_{\parallel} \rangle &= \langle \Delta v_1 \rangle, && \text{(2.3.24a)}\\
\langle (\Delta v_{\parallel})^2 \rangle &= \langle (\Delta v_1)^2 \rangle, && \text{(2.3.24b)}\\
\langle (\Delta v_{\perp})^2 \rangle &= \langle (\Delta v_2)^2 \rangle + \langle (\Delta v_3)^2 \rangle. && \text{(2.3.24c)}
\end{aligned}$$

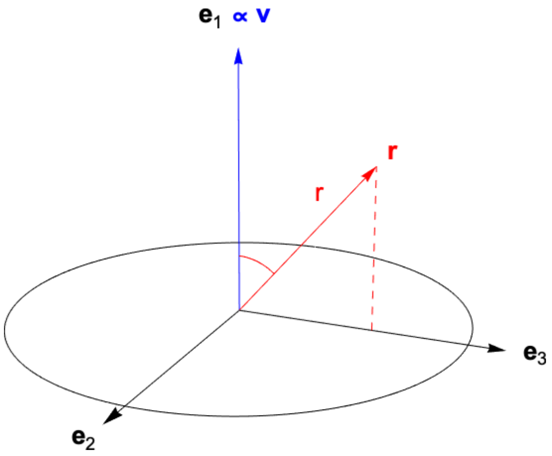

Figure 2.11: Tailored frame used to compute the parallel and perpendicular local velocity deflections in eq. (2.3.24). By construction, the test star's angular momentum $\boldsymbol{L}$ is along the axis $\mathbf{e}_2$.

Isotropic background

The simplest case to which I apply the NR theory is that of an isotropic background. Let me compute the associated velocity deflection coefficients (eqs. 2.3.17). They can be rewritten under the form (Chavanis, 2013a)

$$\langle \Delta v_i \rangle = 8\pi m G^2 \ln \Lambda \frac{\partial h}{\partial v_i}(\boldsymbol{v}), \tag{2.3.25a}$$

$$\langle \Delta v_i \Delta v_j \rangle = 4\pi m G^2 \ln \Lambda \frac{\partial^2 g}{\partial v_i \partial v_j}(\boldsymbol{v}), \tag{2.3.25b}$$

where the *Rosenbluth potentials* (Rosenbluth et al., 1957) are defined by

$$g(\boldsymbol{v}) = \int \mathrm{d}\boldsymbol{v}'\, F_{\mathrm{tot}}(\boldsymbol{v}')|\boldsymbol{v} - \boldsymbol{v}'| \quad ; \quad h(\boldsymbol{v}) = \int \mathrm{d}\boldsymbol{v}'\, \frac{F_{\mathrm{tot}}(\boldsymbol{v}')}{|\boldsymbol{v} - \boldsymbol{v}'|}. \tag{2.3.26}$$

For an isotropic distribution $F_{\mathrm{tot}}(r, \boldsymbol{v}) = F_{\mathrm{tot}}(r, v)$, it can be shown (see, e.g., appendix L of Binney & Tremaine, 2008) that the Rosenbluth potentials depend on r and v only. After computation,

$$\langle \Delta v_{\|} \rangle = -\frac{32\pi^2 m G^2 \ln \Lambda}{v^2} \int_0^v \mathrm{d}v' \frac{v'^2}{v^2} F_{\mathrm{tot}}(r, v'), \tag{2.3.27a}$$

$$\langle (\Delta v_{\|})^2 \rangle = \frac{32\pi^2 m G^2 \ln \Lambda}{3} \left[\int_0^v \mathrm{d}v' \frac{v'^4}{v^3} F_{\mathrm{tot}}(r, v') + \int_v^{\infty} \mathrm{d}v' v' F_{\mathrm{tot}}(r, v') \right], \tag{2.3.27b}$$

$$\langle (\Delta v_{\perp})^2 \rangle = \frac{32\pi^2 m G^2 \ln \Lambda}{v^2} \left[\int_0^v \mathrm{d}v' \left(\frac{3v'^2}{v} - \frac{v'^4}{v^3} \right) F_{\mathrm{tot}}(r, v') + 2 \int_v^{\infty} \mathrm{d}v' v' F_{\mathrm{tot}}(r, v') \right]. \tag{2.3.27c}$$

Since the cluster is assumed to be spherically symmetric and non-rotating, all these quantities depend only on the radius r, making the θ-orbit-average in eq. (2.3.21) trivial.

The Galactic nucleus

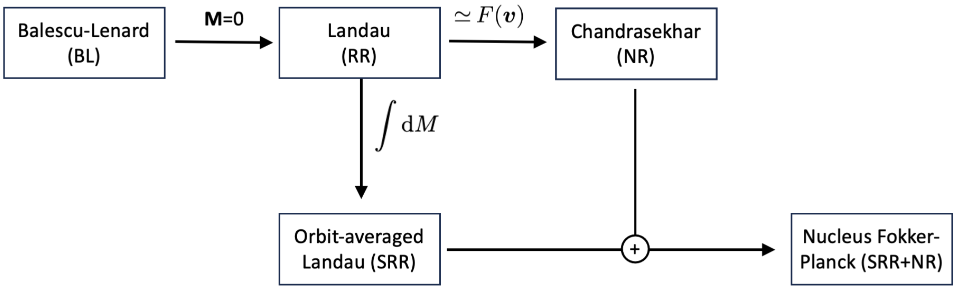

Figure 2.12: Schematic representation of the Fokker–Planck equation describing the secular evolution of the Galactic nucleus. The orbit-averaged RR dynamics (SRR) describes the secular relaxation of Keplerian wires, but can be very damped near the SMBH. In these regions, the NR formalism, which complements the orbit-averaged RR dynamics, drives the diffusion.

In section 2.3.1, I presented an equation describing the relaxation of eccentricity in the case where it is sourced by long-range, resonant interactions between precessing wires. However, there exist regions in orbital space where the RR prediction is considerably damped. In these regions, relaxation is therefore sourced by the NR theory described in section 2.3.2 (Fig. 2.12).

Due to the timescale separation between the diffusion in L_{c} and in L discussed in section 2.3.1, I can approximate the Fokker–Planck equation by setting all the L_{c} diffusion coefficients of the $3D$-Fokker Planck equation (eq. 2.3.19) to zero (Bar-Or & Alexander, 2016). Figure 2.13 represents the (L_{c}, L)-NR diffusion flux in a typical galactic nucleus, and clearly shows the separation between both diffusions. Using this observation, the Fokker–Planck eq. (2.3.19)

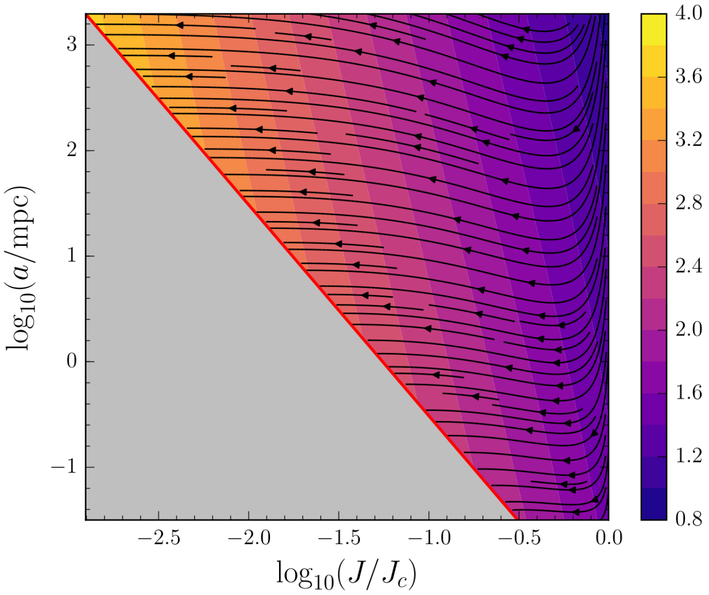

Figure 2.13: From fig. 5 of Bar-Or & Alexander (2016). Illustration of the NR diffusion flux in (j, a)-space. The streamlines mostly follow the j-direction. This shows a separation between the diffusion timescales in a and j, and motivates the study of j-relaxation at fixed a. The color map describes the strength of the diffusion coefficient.

reduces to the 1D Fokker Planck equation

$$\frac{\partial F(L_\mathrm{c}, L, t)}{\partial t} = -\frac{\partial (D_L F)}{\partial L} + \frac{1}{2}\frac{\partial^2 (D_{LL} F)}{\partial L^2}. \tag{2.3.28}$$

Then, I can change variables $(L_\mathrm{c}, L) \mapsto (a, j)$ using $L_\mathrm{c} = \sqrt{GMa}$ and $j = L/L_\mathrm{c}(E)$. Under this transformation, eq. (2.3.28) reads

$$\boxed{\frac{\partial P(j, t\,|\,a)}{\partial t} = \frac{1}{2}\frac{\partial}{\partial j}\left[j D_{jj} \frac{\partial}{\partial j}\left(\frac{P(j,t|a)}{j}\right)\right],} \tag{2.3.29}$$

where $D_{jj} = D_{LL}/L_\mathrm{c}^2$ and $F(a, j, t) = N(a) P(j, t\,|\,a)$ owing to timescale separation. Equation (2.3.29) requires the computation of the j diffusion coefficient D_{jj}, hence the L-coefficient D_{LL}, which are given in eqs. (2.3.22). I will come back to the computation of D_{jj} in chapter 3.

Anisotropic clusters

Let me consider a stellar system of N stars embedded in a background distribution of stars with spherical symmetry. Let me denote its potential by $\psi(r)$. I drop the assumption of isotropy: this means that the diffusion coefficients cannot be computed by the previous Rosenbluth isotropic formulae (eqs. 2.3.27). Instead, it is useful to start from eq. (2.3.17). To benefit from the straightforward relations given in eqs. (2.3.24), I define the velocity frame to be the one from Fig. 2.11. The spherical coordinates read

$$w_1 = w\cos\varphi \quad ; \quad w_2 = w\sin\varphi\cos\phi \quad ; \quad w_3 = w\sin\varphi\sin\phi, \tag{2.3.30}$$

where $\boldsymbol{w} = \boldsymbol{v} - \boldsymbol{v}_1$ as defined for eq. (2.3.1), $v_1 = v$, and $v_2 = v_3 = 0$. I may plug these expressions in eq. (2.3.17). I therefore obtain the new expressions (see appendix 2.A for my complete derivation of these coefficients)

$$\boxed{\begin{aligned}\langle\Delta v_{\parallel}\rangle &= -8\pi m G^2 \ln\Lambda \int_0^{\pi}\mathrm{d}\varphi \int_0^{2\pi}\mathrm{d}\phi \int_0^{w_{\max}}\mathrm{d}w\, \sin\varphi\cos\varphi\, F_{\mathrm{tot}}(r,E',L'), && \text{(2.3.31a)}\\ \langle(\Delta v_{\parallel})^2\rangle &= 4\pi m G^2 \ln\Lambda \int_0^{\pi}\mathrm{d}\varphi \int_0^{2\pi}\mathrm{d}\phi \int_0^{w_{\max}}\mathrm{d}w\, w\sin^3\varphi F_{\mathrm{tot}}(r,E',L'), && \text{(2.3.31b)}\\ \langle(\Delta v_{\perp})^2\rangle &= 4\pi m G^2 \ln\Lambda \int_0^{\pi}\mathrm{d}\varphi \int_0^{2\pi}\mathrm{d}\phi \int_0^{w_{\max}}\mathrm{d}w\, w\sin\varphi(1+\cos^2\varphi) F_{\mathrm{tot}}(r,E',L'), && \text{(2.3.31c)}\end{aligned}}$$

where the arguments of the DF, $F_{\mathrm{tot}}(E,L)$, normalised such that $\int \mathrm{d}\boldsymbol{r}\mathrm{d}\boldsymbol{v}\, F_{\mathrm{tot}} = M$ the total cluster's mass, read

$$\boxed{\begin{aligned} E'(r,\boldsymbol{v},\boldsymbol{v}') &= \psi(r) + \frac{v^2}{2} + \frac{w^2}{2} - vw\cos\varphi, && \text{(2.3.32a)}\\ L'(r,\boldsymbol{v},\boldsymbol{v}') &= r\sqrt{(w\sin\varphi\cos\phi)^2 + \left(v_{\mathrm{t}} + \frac{v_r}{v} w\sin\varphi\sin\phi - \frac{v_{\mathrm{t}}}{v} w\cos\varphi\right)^2}. && \text{(2.3.32b)}\end{aligned}}$$

The w-integrand originally ranges from 0 to $+\infty$. However, I can limit this interval to cover only the region within which $E' < 0$, i.e. for bound background stars. Solving $E' < 0$ gives me the upper bound $w_{\max} = v\cos\varphi + \sqrt{v^2\cos^2\varphi - 2E}$, where E is the energy of the test star. As the w-bound $w_{\max}$ involves φ, I can push the w-integration in eqs. (2.3.31) inside. Furthermore, in all these expressions, the non-negativity of the second-order velocity deflection coefficients is ensured.

I now orbit-average the coefficients given in eqs. (2.3.22) (using the anisotropic velocity deflection coefficients) as described in section 2.3.2. Then, I obtain the diffusion coefficients in (J_{r}, L) from the (E, L) ones (eqs. 2.3.22)

$$\begin{aligned} D_{J_{\mathrm{r}}} &= \frac{\partial J_{\mathrm{r}}}{\partial E} D_E + \frac{\partial J_{\mathrm{r}}}{\partial L} D_L + \frac{1}{2}\frac{\partial^2 J_{\mathrm{r}}}{\partial E^2} D_{EE} + \frac{1}{2}\frac{\partial^2 J_{\mathrm{r}}}{\partial L^2} D_{LL} + \frac{\partial^2 J_{\mathrm{r}}}{\partial E \partial L} D_{EL}, && \text{(2.3.33a)}\\ D_{J_{\mathrm{r}}L} &= \frac{\partial J_{\mathrm{r}}}{\partial E} D_{EL} + \frac{\partial J_{\mathrm{r}}}{\partial L} D_{LL}, && \text{(2.3.33b)}\\ D_{J_{\mathrm{r}}J_{\mathrm{r}}} &= \left(\frac{\partial J_{\mathrm{r}}}{\partial E}\right)^2 D_{EE} + 2\frac{\partial J_{\mathrm{r}}}{\partial E}\frac{\partial J_{\mathrm{r}}}{\partial L} D_{EL} + \left(\frac{\partial J_{\mathrm{r}}}{\partial L}\right)^2 D_{LL}. && \text{(2.3.33c)}\end{aligned}$$

Here, I need to compute a few energy- and angular momentum-derivatives of the radial action J_{r}. This prompts the need to obtain an easily computable formula for it. This is presented in section 4.5.1. Finally, I recover the Fokker–Planck eq. (2.3.19) in action space. By defining $\boldsymbol{J} = (J_{\mathrm{r}}, L)$, it may be rewritten in a flux form as

$$\boxed{\frac{\partial F(\boldsymbol{J})}{\partial t} = -\frac{\partial}{\partial \boldsymbol{J}}\cdot \boldsymbol{\mathcal{F}}(\boldsymbol{J}) = -\frac{\partial}{\partial \boldsymbol{J}}\cdot\left[\boldsymbol{D}_1(\boldsymbol{J})\, F(\boldsymbol{J}) - \frac{1}{2}\frac{\partial}{\partial \boldsymbol{J}}\cdot\Big(\boldsymbol{D}_2(\boldsymbol{J})\, F(\boldsymbol{J})\Big)\right],} \tag{2.3.34}$$

where $\boldsymbol{\mathcal{F}}(\boldsymbol{J})$ is the (orbit-averaged) two-dimensional diffusion flux in the (J_{r}, L)-action space, and the first- and second-order diffusion coefficients read

$$\boldsymbol{D}_1(\boldsymbol{J}) = \begin{pmatrix} D_{J_{\mathrm{r}}} \\ D_L \end{pmatrix}, \quad \boldsymbol{D}_2(\boldsymbol{J}) = \begin{pmatrix} D_{J_{\mathrm{r}}J_{\mathrm{r}}} & D_{J_{\mathrm{r}}L} \\ D_{J_{\mathrm{r}}L} & D_{LL} \end{pmatrix}. \tag{2.3.35}$$

These coefficients will be used in chapter 4.

Rotating clusters

As observations have shown, rotation in stellar clusters appears to be the norm rather than the exception. Because it impacts linear response, it also impacts the secular fate of these systems. In order to predict the evolution of the distribution of L_z, or that of $\cos I$ – the cosine of the orbital inclination – I need to compute the $3D$ diffusion tensors involved in the local $3D$ Fokker–Planck equation. For simplicity, I apply the Lynden–Bell demon (LBD) boost (Lynden-Bell, 1960; Rozier et al., 2019) and consider the DF

$$F_{\mathrm{rot}}(J_{\mathrm{r}},L,L_z)=F_{\mathrm{tot}}(J_{\mathrm{r}},L)\big(1+\alpha\,\mathrm{sgn}[L_z/L]\big), \tag{2.3.36}$$

where $F_{\mathrm{tot}}(J_{\mathrm{r}},L)$ is a DF for a non-rotating cluster and $\alpha\in[-1,1]$ a rotation parameter. Using formulae (C.52) and (C.53) from Bar-Or & Alexander (2016), I can construct the $\cos I$ diffusion coefficients in $(J_{\mathrm{r}},L,\cos I)$-space from those in (J_{r},L,L_z)-space (the other coefficients are given in eqs. 2.3.22). These new coefficients read (see appendix 2.C for my derivation of these expressions)

$$\begin{aligned}
\langle\Delta L_z\rangle &= \frac{L_z}{v}\langle\Delta v_{\parallel}\rangle, && (2.3.37\text{a})\\
\langle(\Delta L_z^2\rangle &= \left(\frac{L_z}{L}\right)^2\left[\frac{L^2}{v^2}\langle(\Delta v_{\parallel})^2\rangle+\frac{1}{2}\frac{r^2v_r^2}{v^2}\langle(\Delta v_{\perp})^2\rangle\right]+\frac{r^2\sin^2\theta}{2}\left(1-\frac{L_z^2}{L^2}\right)\langle(\Delta v_{\perp})^2\rangle, && (2.3.37\text{b})\\
\langle\Delta E\Delta L_z\rangle &= L_z\langle(\Delta v_{\parallel})^2\rangle, && (2.3.37\text{c})\\
\langle\Delta L\Delta L_z\rangle &= \frac{L_z}{L}\left(\frac{L^2}{v^2}\langle(\Delta v_{\parallel})^2\rangle+\frac{1}{2}\frac{r^2v_r^2}{v^2}\langle(\Delta v_{\perp})^2\rangle\right). && (2.3.37\text{d})
\end{aligned}$$

Because the local diffusion terms (eqs. 2.3.31 and 2.3.37) now depend on the physical angle θ (see Fig. 2.9 and appendix 2.C), the orbit-average discussed in section 2.3.2 cannot be reduced to a simple radial integral. Therefore, I must compute a non-trivial θ-integral (eq. 2.3.21). All in all, the 3D orbit-averaged Fokker–Planck equation reads

$$\frac{\partial F_{\mathrm{rot}}(\boldsymbol{J})}{\partial t}=-\frac{\partial}{\partial\boldsymbol{J}}\cdot\boldsymbol{\mathcal{F}}(\boldsymbol{J})=-\frac{\partial}{\partial\boldsymbol{J}}\cdot\left[\boldsymbol{D}_1(\boldsymbol{J})\,F_{\mathrm{rot}}(\boldsymbol{J})-\frac{1}{2}\frac{\partial}{\partial\boldsymbol{J}}\cdot\Big(\boldsymbol{D}_2(\boldsymbol{J})\,F_{\mathrm{rot}}(\boldsymbol{J})\Big)\right], \tag{2.3.38}$$

where $\boldsymbol{\mathcal{F}}(\boldsymbol{J})$ is the corresponding $3D$ diffusion flux in action space, and the first- and second-order diffusion coefficients read

$$\boldsymbol{D}_1(\boldsymbol{J})=\begin{pmatrix}D_{J_{\mathrm{r}}}\\ D_L\\ D_{L_z}\end{pmatrix},\quad \boldsymbol{D}_2(\boldsymbol{J})=\begin{pmatrix}D_{J_{\mathrm{r}}J_{\mathrm{r}}} & D_{J_{\mathrm{r}}L} & D_{J_{\mathrm{r}}L_z}\\ D_{J_{\mathrm{r}}L} & D_{LL} & D_{LL_z}\\ D_{J_{\mathrm{r}}L_z} & D_{LL_z} & D_{L_zL_z}\end{pmatrix}. \tag{2.3.39}$$

Converting the Fokker–Planck equation into $(J_{\mathrm{r}},L,\cos I)$-space yields

$$\frac{\partial F}{\partial t}=-\frac{\partial}{\partial\boldsymbol{J}}\cdot\boldsymbol{\mathcal{F}}(\boldsymbol{J})=-\frac{\partial}{\partial\boldsymbol{J}}\cdot\left[\boldsymbol{D}_1(\boldsymbol{J})\,F-\frac{1}{2}\frac{\partial}{\partial\boldsymbol{J}}\cdot\Big(\boldsymbol{D}_2(\boldsymbol{J})\,F\Big)\right], \tag{2.3.40}$$

where $\boldsymbol{\mathcal{F}}(\boldsymbol{J})$ is the new $3D$ diffusion flux in action space, $F(J_{\mathrm{r}},L,\cos I)=LF_{\mathrm{rot}}(J_{\mathrm{r}},L,L\cos I)$, and the first- and second-order diffusion coefficients read

$$\boldsymbol{D}_1(\boldsymbol{J})=\begin{pmatrix}D_{J_{\mathrm{r}}}\\ D_L\\ D_{\cos I}\end{pmatrix},\quad \boldsymbol{D}_2(\boldsymbol{J})=\begin{pmatrix}D_{J_{\mathrm{r}}J_{\mathrm{r}}} & D_{J_{\mathrm{r}}L} & 0\\ D_{J_{\mathrm{r}}L} & D_{LL} & 0\\ 0 & 0 & D_{\cos I\cos I}\end{pmatrix}, \tag{2.3.41}$$

since computation (presented in appendix 2.D) shows that $D_{J_\mathrm{r}\cos I} = D_{L\cos I} = 0$. In particular, I can obtain the expressions of the flux components for the $3D$ $(J_\mathrm{r}, L, \cos I)$-Fokker–Planck equation as

$$\mathcal{F}_{J_\mathrm{r}} = D_{J_\mathrm{r}} F - \frac{1}{2}\frac{\partial (D_{J_\mathrm{r}J_\mathrm{r}} F)}{\partial J_\mathrm{r}} - \frac{1}{2}\frac{\partial (D_{J_\mathrm{r}L} F)}{\partial L}, \tag{2.3.42a}$$

$$\mathcal{F}_{L} = D_{L} F - \frac{1}{2}\frac{\partial (D_{J_\mathrm{r}L} F)}{\partial J_\mathrm{r}} - \frac{1}{2}\frac{\partial (D_{LL} F)}{\partial L}, \tag{2.3.42b}$$

$$\mathcal{F}_{\cos I} = D_{\cos I} F - \frac{1}{2}\frac{\partial (D_{\cos I\cos I} F)}{\partial I}. \tag{2.3.42c}$$

Note that I can simplify the expressions for the $\cos I$ coefficients (see eqs. 2.D.1), which become

$$D_{\cos I} = -\left\langle \frac{r^2\cos I}{4L^2}\langle(\Delta v_\perp)^2\rangle \right\rangle_{r,\theta}, \tag{2.3.43a}$$

$$D_{\cos I\cos I} = \left\langle \frac{r^2\sin^2 I\sin^2\theta}{2L^2}\langle(\Delta v_\perp)^2\rangle \right\rangle_{r,\theta}. \tag{2.3.43b}$$

In that expression, all θ-dependencies except for the $\sin^2\theta$ term disappear, and I obtain the fluctuation-dissipation relation

$$D_{\cos I} - \frac{1}{2}\frac{\partial D_{\cos I\cos I}}{\partial \cos I} = -\left\langle \frac{r^2\cos I}{4L^2}\langle(\Delta v_\perp)^2\rangle \right\rangle_{r} - \frac{1}{2}\left\langle \frac{-2r^2\cos I}{4L^2}\langle(\Delta v_\perp)^2\rangle \right\rangle_{r} = 0. \tag{2.3.44}$$

It follows that $\mathcal{F}_{\cos I} = 0$ if F does not depend on $\cos I$ (e.g., for a non-rotating cluster). In that case, I can then integrate the Fokker–Planck equation and recover exactly the $2D$ (J_r, L)-space eq. (2.3.34). This is a pleasant self-consistency check.

Let me now integrate the $3D$ Fokker–Planck equation in $(J_\mathrm{r}, L, \cos I)$ over L. It reduces to the Fokker–Planck equation in $(J_\mathrm{r}, \cos I)$ space

$$\frac{\partial F}{\partial t}(J_\mathrm{r}, \cos I) = -\frac{\partial}{\partial \boldsymbol{J}}\cdot \overline{\boldsymbol{\mathcal{F}}}, \tag{2.3.45}$$

where $\boldsymbol{J} = (J_\mathrm{r}, L)$ and the components of the 2D-flux $\overline{\boldsymbol{\mathcal{F}}}$ are

$$\overline{\mathcal{F}}_{J_\mathrm{r}} = \int_0^\infty \mathrm{d}L \left(D_{J_\mathrm{r}} F - \frac{1}{2}\frac{\partial (D_{J_\mathrm{r}J_\mathrm{r}} F)}{\partial J_\mathrm{r}} \right), \tag{2.3.46a}$$

$$\overline{\mathcal{F}}_{\cos I} = \int_0^\infty \mathrm{d}L \left(D_{\cos I} F - \frac{1}{2}\frac{\partial (D_{\cos I\cos I} F)}{\partial \cos I} \right). \tag{2.3.46b}$$

Finally, integrating over J_r, I obtain

$$\frac{\partial F}{\partial t}(\cos I) = -\frac{\partial \overline{\overline{\mathcal{F}}}_{\cos I}}{\partial \cos I}, \tag{2.3.47}$$

where the $1D$-flux in $\cos I$ reads

$$\overline{\overline{\mathcal{F}}}_{\cos I} = \int_0^\infty \mathrm{d}J_\mathrm{r} \int_0^\infty \mathrm{d}L \left(D_{\cos I} F - \frac{1}{2}\frac{\partial (D_{\cos I\cos I} F)}{\partial I} \right). \tag{2.3.48}$$

I should not separate the two terms in the last integrand, because while the difference is well-behaved, the same cannot be said for each term individually, whose asymptotic behaviour for $L \to 0^+$ behaves like $1/L$ (as can be seen from eqs. 2.3.43). In particular, when there is no rotation (hence no dependency on $\cos I = L_z/L$), $\overline{\overline{\overline{\mathcal{F}}}}_{\cos I} = 0$, hence $F(\cos I)$ does not change. All these expressions will be useful when studying the relaxation of globular clusters in chapter 5.

2.4 Concluding remarks

In this chapter, I showed how intrinsic shot noise driven fluctuations in isolated self-gravitating systems drive orbital diffusion. The master equation which describes this process is the Balescu–Lenard eq. (2.2.31). Given its theoretical complexity, I also presented two complementary approaches based on approximations of it. The first approach, presented in section 2.3.1, is the RR theory. It is captured by the inhomogeneous Landau eq. (2.3.1). It is sourced by non-local orbital resonances and depends on long-range orbital torques. In particular, it neglects collective effects. The second formalism, presented in section 2.3.2, is the NR theory. It is captured by the homogeneous Landau eq. (2.3.9), which relies on the further assumption of local homogeneity. In this formalism, only local interactions are considered – though orbit-averaging is used to recover global inhomogeneities. In all cases, orbital diffusion is driven by the graininess of the potential, i.e. finite-N effects.

In the next chapters – chapters 3, 4 and 5 – I will implement these two methods in two distinct stellar systems. In chapter 3, I will apply the NR and RR formalisms to the Galactic centre. In particular, I will show how secular evolution can be used to constrain the parameters of an eventual hidden dark cluster. In chapter 4, I will apply the NR formalism to describe the secular evolution of Plummer globular clusters, complemented by N-body simulations. I will determine the impact of initial velocity anisotropies on orbital reshuffling, and discuss the resonant structure of the RR formalism in dynamically hot systems. In chapter 5, I will extend this analysis to rotating clusters and highlight the limits of the NR formalism in cold systems to predict azimuthal diffusion (Fig. 2.14).

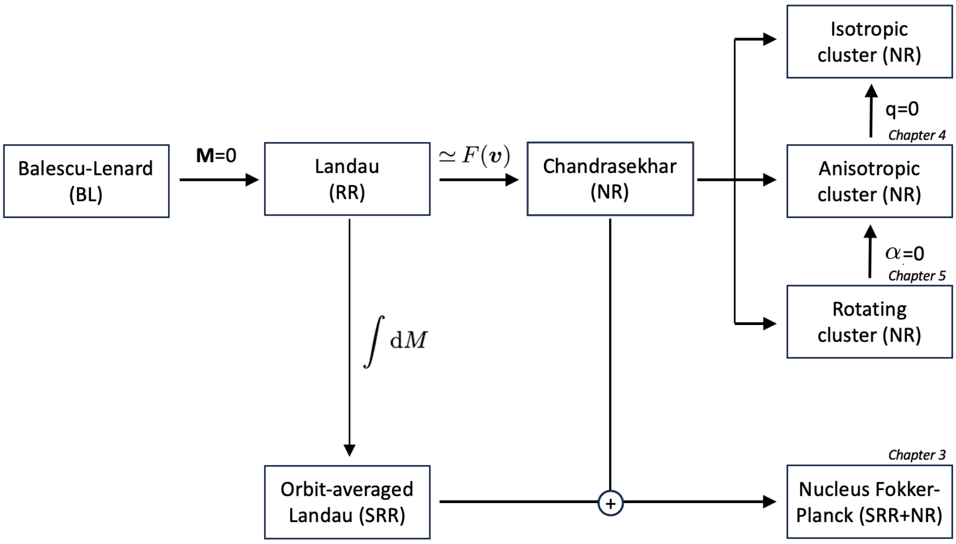

Figure 2.14: Schematic representation of the different approximations of the Balescu–Lenard equation. Applying the NR theory to globular cluster yields a kinetic theory for anisotropic, rotating clusters. These can be compared to N-body measurements to determine the respective importance of large-scale interactions and small-scale relaxation.

2.4.1 Perspectives

During the derivation of the formalisms described in this chapter, I relied on a few simplifying assumptions. These could be lifted in future works, which I discuss now.

The theory of secular orbital diffusion with collective effects has only recently been developed generically (Heyvaerts, 2010; Chavanis, 2012). However, its complexity has made difficult its applications to astrophysical systems. The case of galactic discs (Fouvry et al., 2015d), isotropic clusters (Hamilton et al., 2018; Fouvry et al., 2021) and galactic nuclei (Bar-Or & Fouvry, 2018; Fouvry et al., 2022) have been studied, and their extension to anisotropic systems is still accessible with some work. However, its extension to rotating systems – more generally, in systems depending explicitly on three integrals of motion – has yet to be achieved. Nonetheless, part of the work has been done in developing the associated linear response theory (Rozier et al., 2019). In particular, in section 2.3.1, I neglected collective effects to obtain the inhomogeneous Landau eq. (2.3.1). This simplification has been shown to be justified qualitatively in systems such as isotropic globular clusters (Theuns, 1996; Sellwood, 2015; Hamilton et al., 2018). This motivates a similar study to anisotropic systems, eventually with rotation. This is the topic of chapters 4 and 5.

Furthermore, the long-term evolution of non-spherically symmetric systems is still an open question, owning to both its computational difficulty (an additional action dependency) and its theoretical difficulty (lack of analytical angle-action for generic spheroidal potential). Relaxation in chaotic systems is yet again an open question, as they lack parametrisation of the mean field trajectories. Finally, one could of course consider the impact of the environment on the secular behaviour of isolated anisotropic clusters, with or without rotation. While some work has been initiated on the subject (Palmer et al., 1990; Kuijken & Dubinski, 1994; Sellwood & Valluri, 1997; Breen et al., 2021), a comprehensive theoretical study has yet to be developed.

Appendices of chapter 2

2.A Local velocity deflections for an anisotropic cluster

Let me compute the formulae of eqs. (2.3.31) as well as the expressions of its arguments given in eqs. (2.3.32). To begin, I consider eqs. (2.3.17). In the frame described in Fig. 2.11, the local velocity deflections are related to the coefficients in eqs. (2.3.31) by the relations given in eqs. (2.3.24). Therefore, I have to compute the coefficients given in eqs. (2.3.17).

Starting from these equations, I let $\boldsymbol{w} = \boldsymbol{v} - \boldsymbol{v}'$ and change the integration variables from $\boldsymbol{v}'$ to $\boldsymbol{w}$ to obtain

$$\langle \Delta v_i \rangle = -8\pi m G^2 \ln\Lambda \int \mathrm{d}\boldsymbol{w}\, \frac{w_i}{w^3} F_{\mathrm{tot}}(E', L'), \tag{2.A.1a}$$

$$\langle \Delta v_i \Delta v_j \rangle = 4\pi m G^2 \ln\Lambda \int \mathrm{d}\boldsymbol{w}\, \frac{w^2\delta_{ij} - w_i w_j}{w^3} F_{\mathrm{tot}}(E', L'). \tag{2.A.1b}$$

These expressions can be expressed using polar coordinates

$$w_1 = w\cos\varphi \quad ; \quad w_2 = w\sin\varphi\cos\phi \quad ; \quad w_3 = w\sin\varphi\sin\phi, \tag{2.A.2}$$

and yield

$$\langle \Delta v_1 \rangle = -8\pi m G^2 \ln\Lambda \int \mathrm{d}\boldsymbol{w}\, \frac{w_1}{w^3} F_{\mathrm{tot}}(E', L'), \tag{2.A.3a}$$

$$\langle \Delta (v_1)^2 \rangle = 4\pi m G^2 \ln\Lambda \int \mathrm{d}\boldsymbol{w}\, \frac{w^2 - w_1^2}{w^3} F_{\mathrm{tot}}(E', L'), \tag{2.A.3b}$$

$$\langle \Delta (v_2)^2 \rangle = 4\pi m G^2 \ln\Lambda \int \mathrm{d}\boldsymbol{w}\, \frac{w^2 - w_2^2}{w^3} F_{\mathrm{tot}}(E', L'), \tag{2.A.3c}$$

$$\langle \Delta (v_3)^2 \rangle = 4\pi m G^2 \ln\Lambda \int \mathrm{d}\boldsymbol{w}\, \frac{w^2 - w_3^2}{w^3} F_{\mathrm{tot}}(E', L'). \tag{2.A.3d}$$

Therefore, injecting eqs. (2.A.2) into eqs. (2.A.3), I obtain

$$\langle \Delta v_1 \rangle = -8\pi m G^2 \ln\Lambda \int \mathrm{d}w\mathrm{d}\varphi\mathrm{d}\phi \sin\varphi\cos\varphi F_{\mathrm{tot}}(E', L'), \tag{2.A.4a}$$

$$\langle \Delta (v_1)^2 \rangle = 4\pi m G^2 \ln\Lambda \int \mathrm{d}w\mathrm{d}\varphi\mathrm{d}\phi\, w\sin^3\varphi\, F_{\mathrm{tot}}(E', L'), \tag{2.A.4b}$$

$$\langle \Delta (v_2)^2 \rangle = 4\pi m G^2 \ln\Lambda \int \mathrm{d}w\mathrm{d}\varphi\mathrm{d}\phi\, w\sin\varphi\, (1 - \sin^2\varphi\cos^2\phi) F_{\mathrm{tot}}(E', L'), \tag{2.A.4c}$$

$$\langle \Delta (v_3)^2 \rangle = 4\pi m G^2 \ln\Lambda \int \mathrm{d}w\mathrm{d}\varphi\mathrm{d}\phi\, w\sin\varphi\, (1 - \sin^2\varphi\sin^2\phi) F_{\mathrm{tot}}(E', L'). \tag{2.A.4d}$$

Through the relations given by eqs. (2.3.24), I obtain

$$\langle \Delta v_{\parallel} \rangle = -8\pi m G^2 \ln \Lambda \int \mathrm{d}w \mathrm{d}\varphi \mathrm{d}\phi w \, \sin\varphi \cos\varphi \, F_{\mathrm{rot}}(E', L'), \tag{2.A.5a}$$

$$\langle (\Delta v_{\parallel})^2 \rangle = 4\pi m G^2 \ln \Lambda \int \mathrm{d}w \mathrm{d}\varphi \mathrm{d}\phi w \, w \sin^3 \varphi F_{\mathrm{rot}}(E', L'), \tag{2.A.5b}$$

$$\langle (\Delta v_{\perp})^2 \rangle = 4\pi m G^2 \ln \Lambda \int \mathrm{d}w \mathrm{d}\varphi \mathrm{d}\phi w \, w \sin\varphi (1 + \cos^2 \varphi) F_{\mathrm{rot}}(E', L'). \tag{2.A.5c}$$

Now, I have to compute the arguments E' and L' in the background distribution function. First, let me compute E'. It is given by

$$\begin{aligned} E' &= \psi(r) + \frac{(\boldsymbol{v}')^2}{2} = \psi(r) + \frac{(\boldsymbol{v} - \boldsymbol{w})^2}{2} \\ &= \psi(r) + \frac{v^2 + w^2 - 2\boldsymbol{w} \cdot \boldsymbol{v}}{2} \\ &= \psi(r) + \frac{v^2 + w^2 - 2wv\cos\varphi}{2} \\ &= E + \frac{w^2}{2} - wv\cos\varphi, \end{aligned} \tag{2.A.6}$$

since $\boldsymbol{v} = v\,\mathbf{e}_1$. On the other hand, the computation of L' needs some work. Following Figs. 2.9 and 2.11, I can relate the frame $(1, 2, 3)$ to the frame (X, Y, Z) through the relations

$$\mathbf{e}_1 = \left(\frac{v_r}{v} \cos\theta - \frac{v_{\mathrm{t}}}{v} \sin\theta \right) \mathbf{e}_X + \left(\frac{v_r}{v} \sin\theta + \frac{v_{\mathrm{t}}}{v} \cos\theta \right) \mathbf{e}_Y, \tag{2.A.7a}$$

$$\mathbf{e}_2 = \mathbf{e}_Z, \tag{2.A.7b}$$

$$\mathbf{e}_3 = \left(\frac{v_r}{v} \sin\theta + \frac{v_{\mathrm{t}}}{v} \cos\theta \right) \mathbf{e}_X + \left(\frac{v_{\mathrm{t}}}{v} \sin\theta - \frac{v_r}{v} \cos\theta \right) \mathbf{e}_Y. \tag{2.A.7c}$$

I can also relate the frame (X, Y, Z) to the frame (x, y, z) through the relations

$$\mathbf{e}_X = \cos I \, \mathbf{e}_x + \sin I \, \mathbf{e}_z, \tag{2.A.8a}$$

$$\mathbf{e}_Y = \mathbf{e}_y, \tag{2.A.8b}$$

$$\mathbf{e}_Z = -\sin I \, \mathbf{e}_x + \cos I \, \mathbf{e}_z. \tag{2.A.8c}$$

Now, let me compute L, the norm of $\boldsymbol{L}$. As it is a norm, I can freely choose any frame for its computation. I choose the frame $(1, 2, 3)$, as it is used in the computation of the integrands. I have

$$L'^2 = (r_1 v_2' - r_2 v_1')^2 + (r_1 v_3' - r_3 v_1')^2 + (r_2 v_3' - r_3 v_2')^2, \tag{2.A.9}$$

where (r_1, r_2, r_3) are the coordinates of $\boldsymbol{r}$ in the frame $(1, 2, 3)$. Using the above relations, I can compute those directly using linear algebra. I obtain

$$r_1 = \frac{v_r}{v} r \quad ; \quad r_2 = 0 \quad ; \quad r_3 = \frac{v_{\mathrm{t}}}{v} v. \tag{2.A.10}$$

Therefore,

$$\begin{aligned} L' &= r\sqrt{v_2'^2 + \left(\frac{v_r}{v}v_3' - \frac{v_\mathrm{t}}{v}v_1'\right)^2} \\ &= r\sqrt{(w\sin\varphi\cos\phi)^2 + \left(v_\mathrm{t} + \frac{v_r}{v}w\sin\varphi\sin\phi - \frac{v_\mathrm{t}}{v}w\cos\varphi\right)^2}, \end{aligned} \tag{2.A.11}$$

by using $\boldsymbol{v}' = \boldsymbol{v} - \boldsymbol{w}$.

2.B Local deflection coefficients in E and L

Following closely appendix C of Bar-Or & Alexander (2016), let me compute the E and L diffusion coefficients given in eqs. (2.3.22). Let me consider a star located at position $\boldsymbol{r}$ in the potential $\psi(r)$, with the velocity $\boldsymbol{v}$. Its specific energy and angular momentum are given by

$$E = \psi(r) + \frac{\boldsymbol{v}^2}{2} \quad ; \quad \boldsymbol{L} = \boldsymbol{r} \times \boldsymbol{v}. \tag{2.B.1}$$

Suppose that it is deflected by a field star. Therefore, its velocity changes from $\boldsymbol{v}$ to $\boldsymbol{v}' = \boldsymbol{v} + \Delta\boldsymbol{v}$. Now, I consider the frame described in Fig. 2.11. By construction, its units vectors $\mathbf{e}_1, \mathbf{e}_2, \mathbf{e}_3$ can be related to the unit vectors $\hat{\mathbf{r}}, \hat{\boldsymbol{v}}, \hat{\boldsymbol{L}}$ through

$$\mathbf{e}_1 = \hat{\boldsymbol{v}} \quad ; \quad \mathbf{e}_2 = \hat{\boldsymbol{L}} \quad ; \quad \mathbf{e}_3 = \frac{v\hat{\mathbf{r}} - v_r\hat{\boldsymbol{v}}}{v_\mathrm{t}}. \tag{2.B.2}$$

I can then decompose the velocity deflection vector into

$$\Delta\boldsymbol{v} = \Delta v_\parallel \hat{\boldsymbol{v}} + \Delta\boldsymbol{v}_\perp \quad ; \quad \Delta\boldsymbol{v}_\perp = \sqrt{(\Delta v_2)^2 + (\Delta v_3)^2}. \tag{2.B.3}$$

The change in energy due to the deflection is therefore given by

$$\Delta E = \frac{1}{2}(v'^2 - v^2) = \frac{1}{2}(\Delta v)^2 + \boldsymbol{v}\cdot\Delta\boldsymbol{v} = \frac{1}{2}(\Delta v_\parallel)^2 + \frac{1}{2}(\Delta v_\perp)^2 + v\Delta v_\parallel. \tag{2.B.4}$$

Let me now compute the change in the angular momentum vector. First, I can straightforwardly decompose the position vector onto my reference frame

$$\boldsymbol{r} = \frac{rv_r}{v}\mathbf{e}_1 + \frac{rv_\mathrm{t}}{v}\mathbf{e}_3. \tag{2.B.5}$$

Therefore, I can compute the change in the angular momentum vector

$$\Delta\boldsymbol{L} = \boldsymbol{r}\times\Delta\boldsymbol{v} = \left(\frac{\Delta v_\parallel}{v} - \frac{v_r}{v_\mathrm{t}^2}\Delta v_3\right)\boldsymbol{L} + \frac{\Delta v_2 L}{v}\left(\frac{v_r}{v_\mathrm{t}}\hat{\boldsymbol{w}} - \hat{\boldsymbol{v}}\right). \tag{2.B.6}$$

The change in the norm of the angular momentum is slightly trickier to compute. First, I evaluated the change in the radial velocity

$$\Delta v_r = \Delta\boldsymbol{v}\cdot\hat{\mathbf{r}} = \frac{v_r}{v}\Delta v_\parallel + \frac{v_\mathrm{t}}{v}\Delta v_3. \tag{2.B.7}$$

From this expression, the change in the transverse velocity (at second order in $\Delta v/v$) reads (Bar-Or & Alexander, 2016)

$$\Delta v_\mathrm{t} = \frac{v_\mathrm{t}}{v}\Delta v_\parallel + \frac{1}{2v_\mathrm{t}}\Delta v_2^2 - \frac{v_r}{v}\Delta v_3. \tag{2.B.8}$$

It follows that

$$\Delta L = r\Delta v_\mathrm{t} = \frac{L}{v}\Delta v_\parallel + \frac{r^2}{2L}\Delta v_2^2 - \frac{r v_r}{v}\Delta v_3, \tag{2.B.9}$$

at second order. Now, averaging over all orbital inclinations yields $\langle \Delta v_2 \rangle = \langle \Delta v_3 \rangle = 0$ while $\langle \Delta v_2^2 \rangle = \langle \Delta v_3^2 \rangle = \langle \Delta v_\perp^2 \rangle/2$. This yields eqs. (2.3.22).

2.C Local deflection coefficients for a rotating cluster

If I consider a rotating cluster, the local velocity coefficients given in eq. (2.3.31) keep the same form. However, the DF of the background must be evaluated at (E', L', L'_z). Let me compute this last argument. It is expressed in the (x, y, z) frame as

$$L'_z = x v'_y - y v'_x. \tag{2.C.1}$$

First, the position components are obtained using the change of frame $(X, Y, Z) \mapsto (x, y, z)$, and read

$$\begin{aligned} x &= X\cos I &&= r\cos\theta\cos I, \\ y &= Y &&= r\sin\theta, \\ z &= X\sin I &&= r\cos\theta\sin I, \end{aligned} \tag{2.C.2}$$

using $X = r\cos\theta$ and $Y = r\sin\theta$. Let me now compute the background velocity components. First,

$$\begin{pmatrix} v'_x \\ v'_y \\ v'_z \end{pmatrix} = \begin{pmatrix} \cos I & 0 & -\sin I \\ 0 & 1 & 0 \\ \sin I & 0 & \cos I \end{pmatrix} \begin{pmatrix} v'_X \\ v'_Y \\ v'_Z \end{pmatrix}. \tag{2.C.3}$$

Second,

$$\begin{pmatrix} v'_X \\ v'_Y \\ v'_Z \end{pmatrix} = \begin{pmatrix} \frac{v_r}{v}\cos\theta - \frac{v_\mathrm{t}}{v}\sin\theta & 0 & \frac{v_r}{v}\sin\theta + \frac{v_\mathrm{t}}{v}\cos\theta \\ \frac{v_r}{v}\sin\theta + \frac{v_\mathrm{t}}{v}\cos\theta & 0 & \frac{v_\mathrm{t}}{v}\sin\theta - \frac{v_r}{v}\cos\theta \\ 0 & 1 & 0 \end{pmatrix} \begin{pmatrix} v'_1 \\ v'_2 \\ v'_3 \end{pmatrix}. \tag{2.C.4}$$

Therefore

$$\begin{pmatrix} v'_x \\ v'_y \\ v'_z \end{pmatrix} = \begin{pmatrix} \cos I(\frac{v_r}{v}\cos\theta - \frac{v_\mathrm{t}}{v}\sin\theta) & -\sin I & \cos I(\frac{v_r}{v}\sin\theta + \frac{v_\mathrm{t}}{v}\cos\theta) \\ \frac{v_r}{v}\sin\theta + \frac{v_\mathrm{t}}{v}\cos\theta & 0 & \frac{v_\mathrm{t}}{v}\sin\theta - \frac{v_r}{v}\cos\theta \\ \sin I(\frac{v_r}{v}\cos\theta - \frac{v_\mathrm{t}}{v}\sin\theta) & \cos I & \sin I(\frac{v_r}{v}\sin\theta + \frac{v_\mathrm{t}}{v}\cos\theta) \end{pmatrix} \begin{pmatrix} v'_1 \\ v'_2 \\ v'_3 \end{pmatrix}. \tag{2.C.5}$$

From there, I can compute L'_z

$$\begin{aligned} L'_z &= r\left(\frac{v'_1 v_\mathrm{t}}{v} - \frac{v'_3 v_r}{v}\right)\cos I + r v'_2 \sin\theta\sin I \\ &= r\left(v_\mathrm{t} - \frac{v_\mathrm{t}}{v} w\cos\varphi + \frac{v_r}{v} w\sin\varphi\sin\phi\right)\cos I - r w\sin\varphi\cos\phi\sin\theta\sin I. \end{aligned} \tag{2.C.6}$$

In order to compute the 3D Fokker–Planck equation, I need to obtain the local diffusion coefficients involving L_z. Following eqs. (2.B.2) and (2.B.6), and using the expressions given in appendix 2.C, I obtain

$$\widehat{w}_z = \sin I \bigg(\frac{v_r}{v} \sin\theta + \frac{v_{\mathrm{t}}}{v} \cos\theta \bigg). \tag{2.C.7}$$

It follows that

$$\frac{v_r}{v} \hat{w}_z - \frac{v_z v_{\mathrm{t}}}{v^2} = \sin\theta \sin I, \tag{2.C.8}$$

hence

$$\langle \Delta L_z \rangle = \frac{L_z}{v} \langle \Delta v_{\|} \rangle, \tag{2.C.9a}$$

$$\langle (\Delta L_z^2 \rangle = \bigg(\frac{L_z}{L} \bigg)^2 \bigg(\frac{L^2}{v^2} \langle (\Delta v_{\|})^2 \rangle + \frac{1}{2} \frac{r^2 v_r^2}{v^2} \langle (\Delta v_{\perp})^2 \rangle \bigg) + \frac{r^2 \sin^2\theta}{2} \bigg(1 - \frac{L_z^2}{L^2} \bigg) \langle (\Delta v_{\perp})^2 \rangle, \tag{2.C.9b}$$

$$\langle \Delta E \Delta L_z \rangle = L_z \langle (\Delta v_{\|})^2 \rangle, \tag{2.C.9c}$$

$$\langle \Delta L \Delta L_z \rangle = \frac{L_z}{L} \bigg(\frac{L^2}{v^2} \langle (\Delta v_{\|})^2 \rangle + \frac{1}{2} \frac{r^2 v_r^2}{v^2} \langle (\Delta v_{\perp})^2 \rangle \bigg). \tag{2.C.9d}$$

2.D Computing the $\cos I$ diffusion coefficients

Let me compute the $\cos I$-matrix elements involved in eq. (2.3.41). Using the change of variables $(J_{\mathrm{r}}, L, L_z) \mapsto (J_{\mathrm{r}}, L, \cos I)$, I obtain the transformations (Risken, 1996)

$$D_{\cos I} = -\frac{\cos I}{L} D_L + \frac{1}{L} D_{L_z} + \frac{\cos I}{L^2} D_{LL} - \frac{1}{L^2} D_{LL_z}, \tag{2.D.1a}$$

$$D_{J_{\mathrm{r}} \cos I} = -\frac{\cos I}{L} D_{J_{\mathrm{r}} L} + \frac{1}{L} D_{J_{\mathrm{r}} L_z} = 0, \tag{2.D.1b}$$

$$D_{L \cos I} = -\frac{\cos I}{L} D_{LL} + \frac{1}{L} D_{LL_z} = 0, \tag{2.D.1c}$$

$$D_{\cos I \cos I} = \frac{\cos^2 I}{L^2} D_{LL} - \frac{2\cos I}{L^2} D_{LL_z} + \frac{1}{L^2} D_{L_z L_z}, \tag{2.D.1d}$$

while the other coefficients stay unchanged. Injecting eqs. (2.3.37) into eqs. (2.D.1) yields the desired coefficients. In particular, the vanishing of the off-diagonal terms is due to the two relations $D_{LL_z} = \cos I \, D_{LL}$ and $D_{EL_z} = \cos I \, D_{EL}$.

Chapter 3

The Galactic centre and IMBHs

Unless stated otherwise, the work presented in this chapter is based on Tep et al. (2021).

3.1 Introduction

Observations of the Galactic centre of our own Milky Way reveal the presence of a cluster of bright young stars, called the *S-cluster*, whose behaviour appears to be very peculiar. Indeed, these stars follow quasi-Keplerian orbits around an invisible object – Sgr A*, see Fig. 3.1.1 – which is strongly believed to be a SMBH (Genzel & Eckart, 1999; Melia & Falcke, 2001; Ghez et al., 2008; Gillessen et al., 2017). The existence of such a massive object is one of the keys to our understanding of galaxy formation (Haehnelt & Rees, 1993). On one hand, we know that stellar mass black holes (BHs) exist (see, e.g., Abbott et al., 2016, 2017), while on the other hand, we strongly believe that SMBHs exist (Event Horizon Telescope Collaboration et al., 2019, 2022) within every galactic centre (Kormendy & Richstone, 1995; Magorrian et al., 1998; Richstone

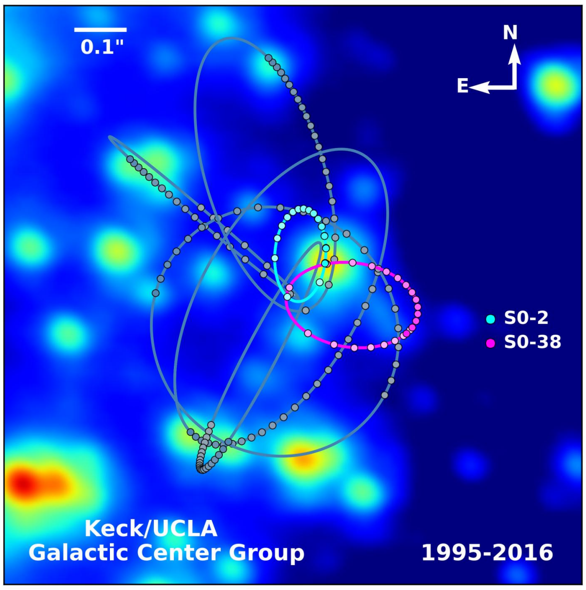

Figure 3.1.1: From Hees et al. (2017). Stars of the S-clusters orbit around the SMBH at the centre of the Milky Way. As such, they follow quasi-Keplerian orbits. On longer timescales, relativistic effects due to the central SMBH induce a precession of their pericentre.

et al., 1998). It is therefore legitimate to ask ourselves the question of their formation, that is how they came to be so massive.

A wide range of scenarii have been proposed to explain the formation of these cosmic behemoths. A SMBH could have been the result of the collapse of the first generation of stars. As these stars were formed out of metal-free gas with no efficient cooling mechanism, this may have led to a very top-heavy initial stellar mass distribution (Carr et al., 1984; Larson, 1998). Numerical simulations tend to reach the same conclusions (Bromm et al., 1999; Abel et al., 2000; Bromm et al., 2002) and predict the formation of BHs of mass $10-100M_\odot$ through this mechanism. Another formation scenario points to the collapse of supermassive objects formed out of dense gas in the early Universe (Haehnelt & Rees, 1993; Umemura et al., 1993; Loeb & Rasio, 1994; Koushiappas et al., 2004). However, both these models struggle with the disposal of angular momentum (Eisenstein & Loeb, 1995). To remedy this issue, more exotic mechanisms have been explored, such as the existence of early *quasi-stars* – extremely massive objects in which accretion from the envelope surrounding the collapsed core can build up a substantial black hole mass very rapidly, at a highly super-Eddington rate (Begelman et al., 2006, 2008). Finally, one of the possibilities is that SMBHs arose from the merger of IMBHs, that is, BHs with a mass range of $\sim 100M_\odot$. However, their existence has yet to be proven with certainty (Portegies Zwart & McMillan, 2002) and is an ongoing investigation (The LIGO Scientific Collaboration et al., 2019). If those were to exist, then galactic centres are among the best locations to look for intermediate mass objects. Because they tend to migrate there via mass segregation, they would then merge together to increase the mass of the central BH.

Astrometric data from the satellite GAIA (see, e.g., Jindal et al., 2019), coupled with spectral data from the Very Large Telescope (VLT)'s instrument GRAVITY (see, e.g., Gravity Collab. et al., 2020, 2023), give us access to a very well-furnished catalogue of the Milky Way, including in particular precise information on the dynamics of the S-cluster (Ghez et al., 2008; Habibi et al., 2017; Gillessen et al., 2017), i.e. the stellar cluster within the very core of the Galactic centre. As $\mathrm{Sgr\ A}^\star$ overwhelmingly dominates the gravitational potential of the region, with a mass $M_\bullet = 4.3\times10^6 M_\odot$ (Gillessen et al., 2017), the stars follow quasi-Keplerian orbits with a very fast period, of order $T_\star = 10-10^3\,\mathrm{yr}$ (Kocsis & Tremaine, 2011). This is very short compared to that of the Sun around the Milky Way ($T_\odot \sim 200\,\mathrm{Myr}$). More generally, the Keplerian orbital frequency is given by

$$\Omega_{\mathrm{Kep}} = \sqrt{GM_\bullet/a^3}, \tag{3.1.1}$$

with a the orbit's semi-major axis. Finally, astrometric data from the VLT (Boehle et al., 2016; Gillessen et al., 2017) show that these stars are close to being thermalised, in the sense that their angular momentum distribution is the equilibrium distribution of the associated diffusion process (see sections 2.3.1 and 2.3.3).

In this chapter, I will constrain the presence of unresolved background stellar families made of faint stellar objects or IMBHs (Fig. 3.1.2). I will use tools from kinetic theory to that end, as there is a high density of stars ($N\sim10^6$) within $1\mathrm{pc}^3$, the region of influence where the SMBH predominates. To describe the evolution of the stellar cluster, I will use the gravitational Landau eq. (2.3.8) developed in chapter 2. First, I will describe the dynamics driving secular relaxation in the Galactic centre in section 3.2. Then I will compute the associated diffusion coefficients. While this is relatively straightforward within the NR formalism, it is (much) more difficult for the RR formalism, as one has to solve a resonance condition and compute the strength of orbital couplings (section 3.3). Finally, in section 3.4, I will constrain the parameters of $\mathrm{Sgr\ A}^\star$'s unresolved background cluster by doing a likelihood analysis in parameter space.

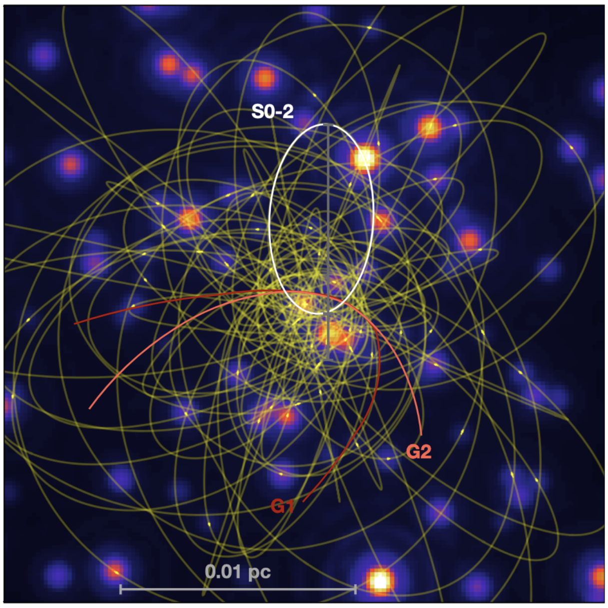

Figure 3.1.2: From Do et al. (2019). Simulated image of the S cluster in the Galactic centre as it will be seen by the TMT (Thirty Meter Telescope) in a couple of years. Today, only one star (S2) has the astrometric and radial velocity precision to constrain GR (Gravity Collab. et al., 2020). With ELTs, it should be possible to use about 100 stars jointly for GR tests (Gravity Collab. et al., 2021; Gravity+ Collab. et al., 2022).

3.2 Dynamics of the Galactic nucleus

Following closely Fouvry et al. (2017), let me present the dynamics occurring in the S-cluster of the Galactic nucleus. The most important feature is the presence of the SMBH $\mathrm{Sgr\ A}^\star$. Because the SMBH dominates the gravitational potential, these stars – in particular the S-stars – follow quasi-Keplerian orbits, with orbital periods ranging from $7.6\mathrm{yr}$ for S4711 to $3580\mathrm{yr}$ for S85 (Gillessen et al., 2017; Gravity Collab. et al., 2020; Peißker et al., 2020; Gravity Collab. et al., 2021). Nevertheless, because there is a finite number of stars in the cluster, the stars are also subjected to stochastic Poisson fluctuations, which have a definite impact on secular times as described in section 2.3.1.

I can model this system by a set of N stars of mass m orbiting a SMBH of mass $M_\bullet$. As is the case in the Galactic nucleus, I assume that $M_\bullet$ is much bigger that the total stellar mass $M_\star = Nm$. Following section 2.3.1, I can describe the secular relaxation of this system by averaging over the fast quasi-Keplerian motion of the stars. This yields a specific, orbit-averaged Hamiltonian (eq. 2.3.4) describing the secular evolution of Keplerian wires. The principal contribution to the relativistic correction induced by the SMBH is the 1PN contribution, called the Schwarzschild precession (Merritt, 2013). It drives an in-plane precession of the stars' pericentre, hence a precession of the Keplerian wires. The associated precession frequency reads (see, e.g., Touma et al., 2009)

$$\Omega_{\mathrm{GR}}(a,e) = \frac{\partial \overline{\Phi}_{\mathrm{GR}}}{\partial L} = \frac{3GM_\bullet \Omega_{\mathrm{Kep}}(a)}{c^2 a(1-e^2)}. \tag{3.2.1}$$

It is prograde (i.e. has positive frequency) and does not depend on the wire's inclination. Another source of in-plane precession comes from the background stellar distribution. Because this distribution is spherically symmetric on average, it generates a precession of the test's wire with frequency (Tremaine, 2005)

$$\Omega_\star(a,e) = \frac{\partial \overline{\Phi}_\star}{\partial L} = \frac{\Omega_{\rm Kep}(a)}{\pi M_\bullet e} \int_0^\pi \mathrm{d}f\, M_\star(r[f]) \cos f, \tag{3.2.2}$$

where f is the true anomaly and $M_\star(r)$ the enclosed mass profile. For the background family which I will consider in this chapter, this precession is retrograde (see appendix 3.B) and independent of the wire's inclination.

As discussed in section 2.3.1, the response matrix (eq. 2.2.30) of this system exactly vanishes for an isotropic background distribution of the form $F_0(L_{\rm c})$. Therefore, the secular relaxation of a Keplerian wire in that system is fully described by the inhomogeneous Landau eq. (2.3.1).

3.3 Eccentricity relaxation of the Keplerian wires

Now, the unresolved background cluster is expected to be old, i.e. has been orbiting around Sgr A* for a time much longer than the SRR relaxation time. As such, I may assume that it has already fully relaxed in all its orbital elements. I therefore assume that it has a spherically symmetric distribution of orientations, and, importantly, follows a thermal distribution of eccentricities. As such, it corresponds to a background for the subset of observed stars.

In that limit, as shown in section 2.3.1, the eccentricities of the test particles, i.e. the eccentricities of the S-stars, diffuse according to the Fokker–Planck equation given by eq. (2.3.8), where $P(j,t\,|\,a)$ describes the probability distribution function (PDF) of the test stars' eccentricities, j, for a given sma a, as a function of time, normalised so that $\int \mathrm{d}j\, P(j,t\,|\,a) = 1$. Let me already note that eq. (2.3.8) can be rewritten under the more classical Fokker–Planck (FP) form as

$$\frac{\partial P(j,t\,|\,a)}{\partial t} = -\frac{\partial}{\partial j}\bigg[D_j(a,j)\, P(j,t\,|\,a)\bigg] + \frac{1}{2}\frac{\partial^2}{\partial j^2}\bigg[D_{jj}(a,j)\, P(j,t\,|\,a)\bigg]. \tag{3.3.1}$$

The structure of eq. (3.3.1) is useful to perform Monte-Carlo integrations of the stochastic dynamics, as presented in section 3.4.2.

In eq. (2.3.8), the diffusion coefficient involves only a RR contribution at the moment. However, as will be discussed in the next section, there exist regions of orbital space where the RR contribution is considerably damped. If I introduce the diffusion coefficient in angular momentum, $D_{jj}(a,j)$, it is the sum of two contributions

$$\boxed{D_{jj}(a,j) = D_{jj}^{\rm RR}(a,j) + D_{jj}^{\rm NR}(a,j),} \tag{3.3.2}$$

where $D_{jj}^{\rm RR}(a,j)$ captures the contribution from the RR theory, while $D_{jj}^{\rm NR}(a,j)$ is associated with the contribution from the NR theory. Together, the RR and NR contributions drive the Fokker–Planck equation

$$\frac{\partial P(j,t\,|\,a)}{\partial t} = \frac{1}{2}\frac{\partial}{\partial j}\bigg[j\, D_{jj}(a,j)\, \frac{\partial}{\partial j}\bigg(\frac{P(j,t\,|\,a)}{j}\bigg)\bigg]. \tag{3.3.3}$$

At this point, one may be worried about adding together the NR and the RR contributions aforementioned. Indeed, I argued in section 2.3.2 that the NR theory is contained in the RR theory, in the sense that it is a limiting case of the latter one. However, the resonant contribution (which I still call RR in this section) is not exactly the one described in section 2.3.1.

Indeed, consider the summation over resonances involved in eq. (2.3.1). This inhomogeneous Landau equation describes the RR formalism of secular evolution. First, because the Keplerian potential is degenerate w.r.t. L_z (meaning that $\Omega_3 = 0$), eq. (2.3.1) must be integrated over L_z to obtain a well-defined evolution equation (Hamilton et al., 2018). This integration reduces the 3D summation of resonances over (k_1, k_2, k_3) to a 2D summation over (k_1, k_2). Second, due to the presence of a SMBH in the centre of the Galactic nucleus, I remarked that $\Omega_1 \gg \Omega_2$. Therefore, I considered the orbit-averaged dynamics of Keplerian wires, reducing the 2D summation to a 1D summation over the resonances k_2 (associated to the slow motion). The successive dimension reductions can be summed up as follows

$$\sum_{k_1,k_2,k_3} \xrightarrow{\int \mathrm{d}L_z} \sum_{k_1,k_2} \xrightarrow{\int \mathrm{d}M} \sum_{k_2} .$$

The *true* dynamics of the stars is described by the RR theory involving the 2D summation. The 1D summation can be understood as the *mean field* term $k_1 = 0$ of the 2D summation. Therefore, higher resonances have been neglected due to the SMBH's influence. Because high order resonances correspond to small-scale interactions, it is natural to supplement the 1D-RR summation with the NR theory.

Additionally, because of the influence of the SMBH, I expect that the orbit-averaged RR part contributes the most to the relaxation. This can be understood roughly through the following argument. Let me recall that $(\Omega_1, \Omega_2) = (\Omega_{\mathrm{Kep}}, \Omega_{\mathrm{P}})$ where $\Omega_{\mathrm{P}} = \Omega_{\mathrm{GR}} + \Omega_{\star}$. As mentioned above, because of the much larger mass of the SMBH, $\Omega_{\mathrm{P}} = \epsilon \Omega_{\mathrm{Kep}}$, where $\epsilon \sim M_{\star}/M_{\bullet} \ll 1$. Hence, the overall contribution of the resonances to the relaxation is roughly given by

$$\begin{aligned} \sum_{\boldsymbol{k},\boldsymbol{k}'} \delta_{\mathrm{D}}(\boldsymbol{k}\cdot\boldsymbol{\Omega} - \boldsymbol{k}'\cdot\boldsymbol{\Omega}') \simeq \; & \frac{1}{|\epsilon|} \sum_{k_2,k_2'} \delta_{\mathrm{D}}(k_2\Omega_{\mathrm{Kep}} - k_2'\Omega_{\mathrm{Kep}}') \quad && (\mathrm{RR}) \\ & + \sum_{|\boldsymbol{k}|,|\boldsymbol{k}'|\gg 1} \delta_{\mathrm{D}}(\boldsymbol{k}\cdot\boldsymbol{\Omega} - \boldsymbol{k}'\cdot\boldsymbol{\Omega}'), \quad && (\mathrm{NR}) \end{aligned}$$

where I used the relation $\delta_{\mathrm{D}}(\epsilon x) = \delta_{\mathrm{D}}(x)/|\epsilon|$. From this decomposition, the first part of the summation ($k_1 = k_1' = 0$) corresponds to the orbit-averaged RR contribution (SRR), and is of order $1/\epsilon \gg 1$. This dominates the second part – which contains higher resonances, hence local interactions described by NR theory – in regions that are not too close to the SMBH.[a]

I now detail the content of each of these coefficients.

3.3.1 RR diffusion coefficients

A first source of eccentricity relaxation stems from the long-range resonant couplings between the in-plane precessing wires. Following Bar-Or & Fouvry (2018), the SRR diffusion coefficients read

$$\boxed{D_{jj}^{\mathrm{RR}}(a,j) = \frac{4\pi G^2}{L_{\mathrm{c}}^2} \sum_{k=1}^{+\infty} \sum_{\substack{k'=-\infty \\ k'\neq 0}}^{+\infty} \frac{k^2}{|k'|} \int \mathrm{d}a' \, F_{\mathrm{tot}}(a',j') \frac{|\psi_{kk'}(a,j,a',j')|^2}{|\partial_j \Omega_{\mathrm{P}}(a',j')|},} \tag{3.3.4}$$

---

[a] In these regions, the precession frequency diverges, hence ϵ becomes much bigger than 1 and the NR part dominates over the RR part (Fig. 3.3.5).

where $L_\mathrm{c} = L_\mathrm{c}(a)$ was defined in section 1.3.2, and j' is the implicit solution of the resonance condition

$$k'\Omega_\mathrm{P}(a',j') = k\Omega_\mathrm{P}(a,j), \tag{3.3.5}$$

where the in-plane precession frequency $\Omega_\mathrm{P}(a,j)$ is defined by

$$\Omega_\mathrm{P} = \Omega_\mathrm{GR} + \Omega_\star. \tag{3.3.6}$$

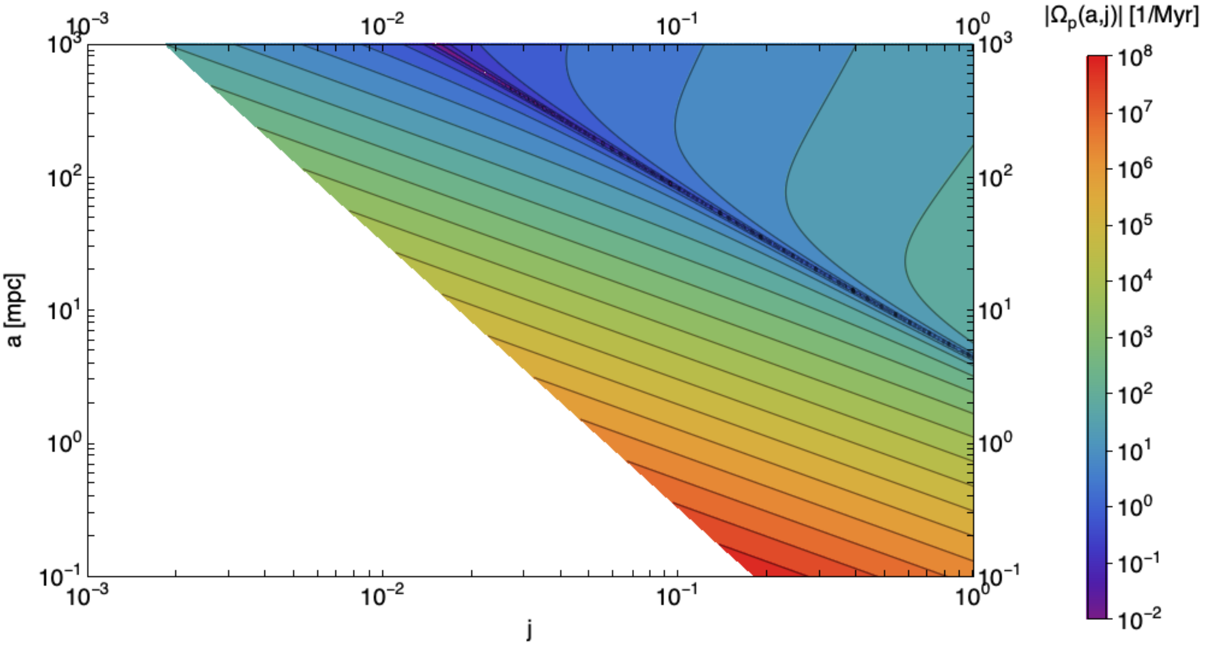

Figure 3.3.1: Illustration of precession frequencies, $|\Omega_\mathrm{P}(a,j)|$, in orbital space for the Top-Heavy model (eq. 3.4.2). For circular orbits and large sma, i.e. $j \to 1$ and large a, the precession is dominated by the mass precession and is therefore retrograde ($\Omega_\mathrm{P} < 0$). For small j and small a, the precession is dominated by the relativistic precession and is therefore prograde ($\Omega_\mathrm{P} > 0$).

In eq. (3.3.4), I introduced the DF, $F_\mathrm{tot}(a',j')$. It is defined as

$$F_\mathrm{tot}(a,j) = \sum_i m_i^2 N_i(a)\, f_i(j\,|\,a), \tag{3.3.7}$$

where the sum over i runs over all the sub-populations of the background cluster. Each population is characterised by an individual mass, m_i, while $N_i(a)$ is the number of stars per unit sma a, and $f_i(j\,|\,a)$ is the conditional PDF of j for a given a, normalised so that $\int \mathrm{d}j\, f_i(j\,|\,a) = 1$. In practice, in order to ease the numerical resolution of the resonance condition (see appendix 3.B) and the computation of the NR diffusion coefficients, I assume that each population follows a power law distribution in smas and is also fully relaxed in eccentricity, i.e. $f_i(j|a) = 2j$, owing to their old dynamical age. I further detail all my normalisation conventions in section 3.4.1.

The resonant diffusion coefficients from eq. (3.3.4) involve the coupling coefficients $|\psi_{kk'}|^2$, which describe the efficiency of the resonant coupling between two wires. In the present case, they read (Bar-Or & Fouvry, 2018)

$$\left|\psi_{kk'}(a,j,a',j')\right|^2 = 16\pi^2 \sum_\ell \frac{|y_\ell^k|^2 |y_\ell^{k'}|^2}{(2\ell+1)^3} \left|K_{kk'}^\ell(a,j,a',j')\right|^2, \tag{3.3.8}$$

with the constant coefficients $y_\ell^k = Y_\ell^k(\frac{\pi}{2}, \frac{\pi}{2})$, where the spherical harmonics are defined with the convention $\int \mathrm{d}\hat{\mathbf{r}}\, |Y_\ell^k(\hat{\mathbf{r}})|^2 = 1$. This equation involves the pairwise in-plane coupling coefficients $K_{kk'}^\ell$ that read

$$K_{kk'}^\ell(a, j, a', j') = \left\langle \cos(kf)\cos(k'f') \frac{\min(r, r')^\ell}{\max(r, r')^{\ell+1}} \right\rangle_{\circlearrowleft}, \tag{3.3.9}$$

where f is the true anomaly, while $\langle \cdot \rangle_{\circlearrowleft}$ stands for the orbit-average over both radial oscillations.

Let me already emphasise that the coupling coefficients from eq. (3.3.8) satisfy various symmetry properties. First, as imposed by the symmetries of $|y_\ell^k|^2$ and $|y_\ell^{k'}|^2$, these coefficients are non-zero only when $|k|, |k'| \leq \ell$, as well as $(\ell - k)$ and $(\ell - k')$ even. In addition, I note that $|\psi_{kk'}|^2 = |\psi_{\pm k \pm k'}|^2$, i.e. the strength of the (k, k') coupling, is independent of the sign of the resonance numbers. These are all important features which allow me to reduce the number of evaluations of the coupling coefficients required. Finally, in practice, in eq. (3.3.8), I truncate the harmonics up to some given $\ell_{\max}$.

In eq. (3.3.9), the $\min - \max$ terms stem from the usual Legendre expansion of the Newtonian interaction potential. The computation of $K_{kk'}^\ell$ is the overall bottleneck of the whole calculation of the SRR diffusion coefficients which I therefore have to address. A naive inspection of eq. (3.3.9) would lead me to believe that its computational complexity scales like $\mathcal{O}(K^2)$, with K the number of sampling points used to discretise both anomalies. Fortunately, I can take inspiration from multipole methods (see, e.g., Fouvry et al., 2022) to compute them much more efficiently, yielding a computational complexity scaling like $\mathcal{O}(K)$. This is detailed in appendix 3.A.

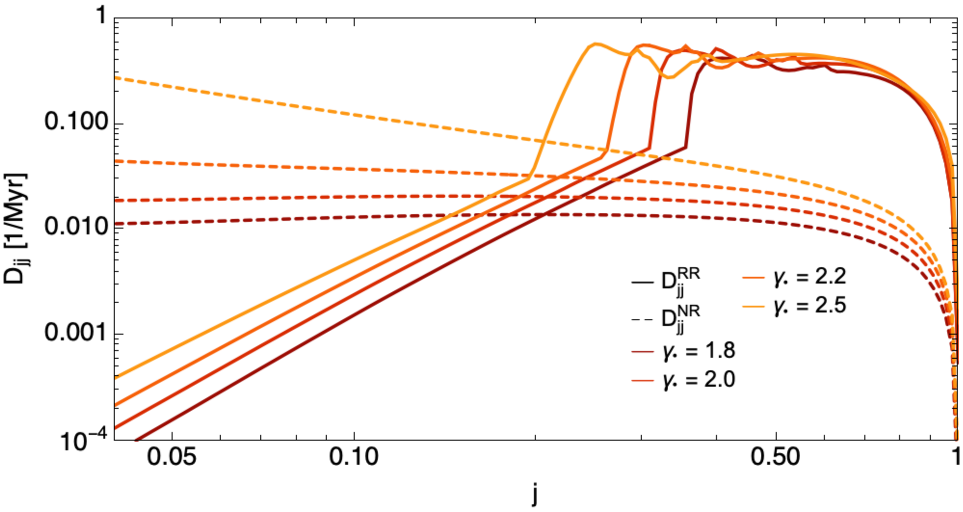

Figure 3.3.2: Illustration of the RR (full line, see section 3.3.1) and NR (dashed line, see section 3.3.2) diffusion coefficients D_{jj}. For the Top-Heavy model (eq. 3.4.2), I vary the cusp parameter $\gamma_\bullet$ for a given value of semi-major axis $a = 10$ mpc and the harmonic cutoff $\ell_{\max} = 10$. The diffusion coefficients go to 0 as $j \to 1$ (circular orbits), while the RR ones get drastically reduced for very eccentric orbits due to the Schwarzschild precession. As such, for small enough j, the NR coefficients dominate over the RR ones.

Once the coupling coefficients have been estimated, I rely on eq. (3.3.4) to evaluate the diffusion coefficients. This requires in particular to solve for the resonance condition from eq. (3.3.5). For a given wire (a, j) and a given resonance pair (k, k'), this amounts to finding all the wires (a', j') for which the resonance condition $k\Omega_{\mathrm{P}}(a, j) = k'\Omega_{\mathrm{P}}(a', j')$ is satisfied (see Fig. 3.3.1 for a representation of the iso-contours of precession frequencies). I detail in appendix 3.B my approach to solve the resonance condition, improving upon the method from Bar-Or & Fouvry

(2018).

Figure 3.3.2 gives an example of a computation of the RR diffusion coefficients for a fixed value of the sma. Furthermore, I represent in Fig. 3.3.3 the contribution to the total RR diffusion coefficient D_{jj}^{RR} from the first lowest resonance vectors. In particular, I recover the drastic damping of the RR diffusion coefficients for very eccentric orbits. This is due to the divergence of the relativistic precession frequencies for ever more eccentric wires, which prevents these wires from resonating with the bulk of the other wires (Merritt et al., 2011; Bar-Or & Alexander, 2016). This is the so-called *Schwarzschild barrier*, for which I give a schematic representation in Fig. 3.3.4. As can be noted in Fig. 3.3.2, very eccentric wires ($j \sim 0$) are then immune to the RR diffusion, and can only keep diffusing under the effect of the NR contributions.

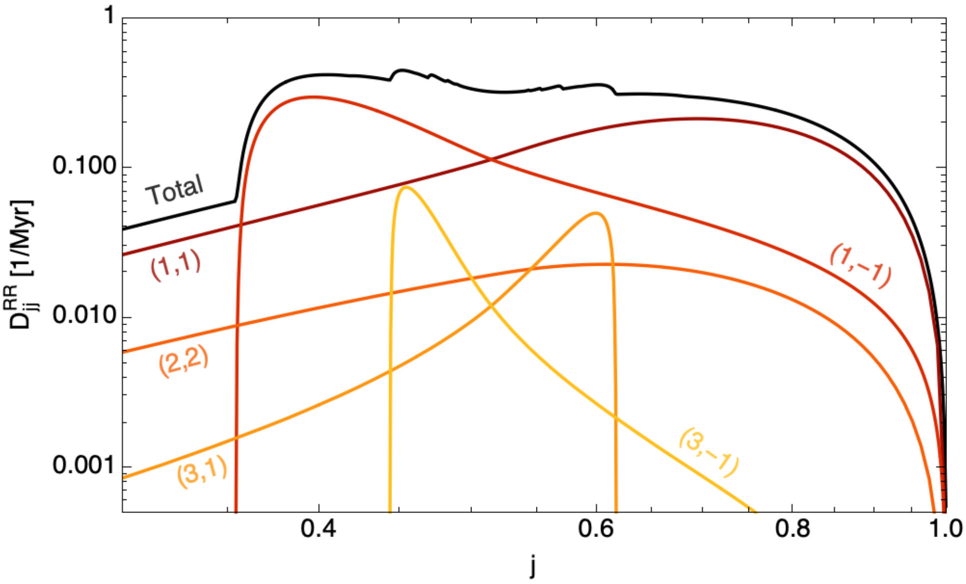

Figure 3.3.3: Illustration of the contribution to the RR diffusion coefficients (eq. 3.3.4) of the different resonances (k,k'), for a given sma $a = 10$ mpc and the cutoff $\ell_{\mathrm{max}} = 10$. The RR coefficients are typically dominated by the resonances $(k,k')=(1,1)$ (for small and large j) and $(k,k')=(1,-1)$ (for intermediate j). For intermediate eccentricities, higher-order resonances also contribute to the fine structure of D_{jj} (i.e. the bumps on the black curve).

3.3.2 NR diffusion coefficients

A second process through which test stars relax in eccentricities originates from the NR theory (see section 2.3.3). In order to evaluate the associated diffusion coefficient, $D_{jj}^{\mathrm{NR}}(a,j)$, I used the approach detailed in section 2.3.3. In practice, I define the Coulomb logarithm of a family as $\ln \Lambda_i = \ln(M_\bullet/m_i)$ (see eq. 7.84 of Binney & Tremaine, 2008). Because they do not involve any resonance condition, these NR diffusion coefficients are numerically much less demanding to compute than the RR ones.

The computation of the orbit-averaged version of these coefficients (section 2.3.2) relies on the particular form of the Keplerian potential. Here, r_{p} (resp. r_{a}) is the pericentre (resp. apocentre) of the Keplerian orbit with energy E and angular momentum L. These two values are the two solutions of the radial equation $v_r = 0$ in the equation

$$E = -\frac{M_\bullet}{r} + \frac{v_r^2}{2} + \frac{L^2}{2r^2} = -\frac{GM_\bullet}{2a}. \tag{3.3.10}$$

For the Keplerian potential, this orbit-average can be done using the eccentric anomaly u, such

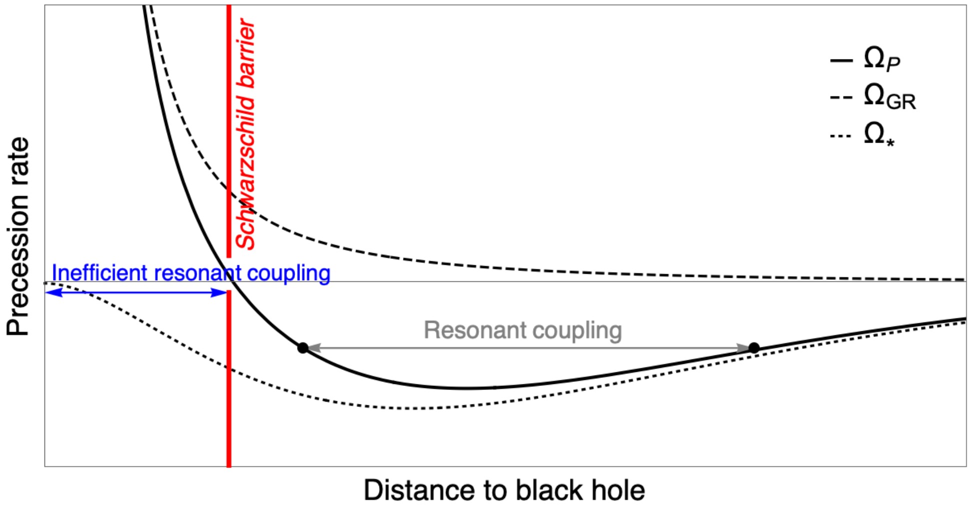

Figure 3.3.4: Schematic representation of the precession frequency of a Keplerian wire. Far away from the SMBH, the retrograde mass precession dominates, and orbits can resonate with each other. However, near the SMBH, relativistic effects – the prograde Schwarzschild precession – induced by the SMBH dominate. Therefore, in that region, no resonant couplings can occur. This is the so-called Schwarzschild barrier (Merritt et al., 2011), which leads to a sharp drop of the resonant diffusion coefficients near the SMBH.

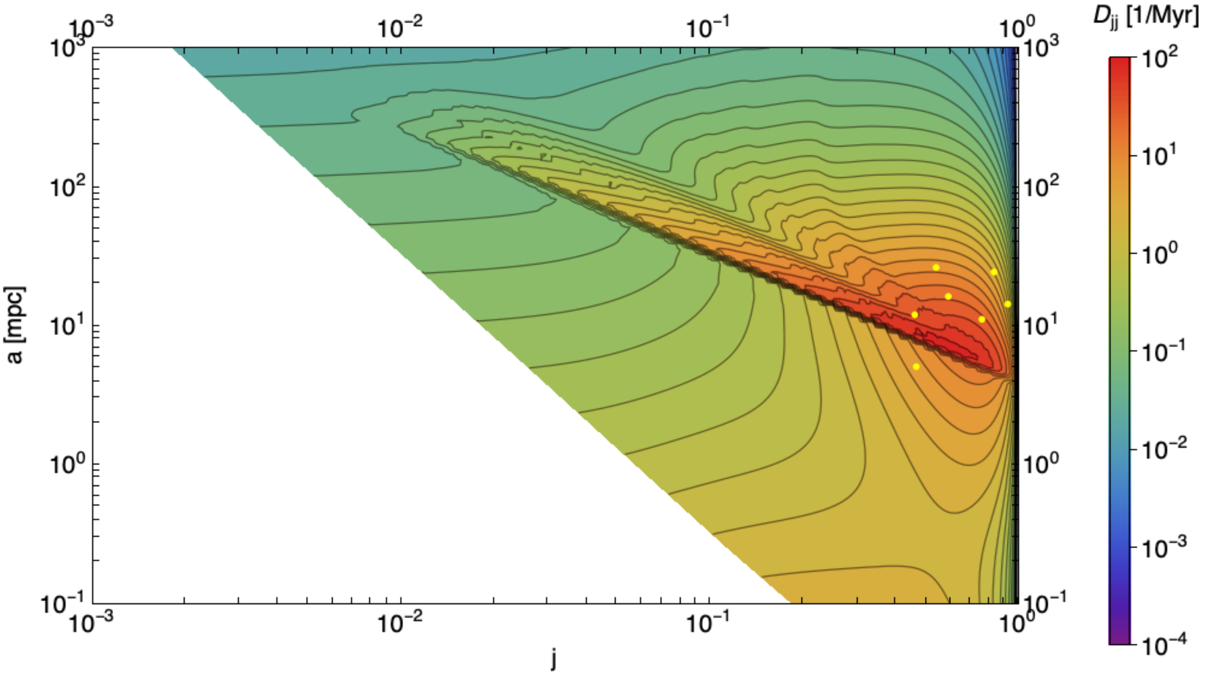

Figure 3.3.5: Illustration of the total diffusion coefficients, D_{jj}, in the (a, j)-orbital space for the Top-Heavy model defined in eq. (3.4.2). Here are also represented in yellow the seven S-stars which I used to constrain the properties of the underlying unresolved stellar cluster. The white region on the left represents the location in orbital space of the central BH's loss cone. In the centre of the figure, resonant couplings due to RR create this rugged but accurate aspect, that can be linked to the iso-contours of the precession frequencies. The sharp drop of amplitude beyond this structure is due to the Schwarzschild barrier (see section 3.3.1 and Fig. 3.3.4).

that

$$r(u) = a(1 + e\cos u). \tag{3.3.11}$$

The orbit-average (eq. 2.3.21) becomes

$$D_X = \frac{1}{\pi}\int_0^{\pi} \mathrm{d}u \, \langle \Delta X \rangle (r[u]) \, (1 + e\cos u). \tag{3.3.12}$$

In the end, I obtain through this method the diffusion coefficients D_j and D_{jj} sourced by the NR theory (see, e.g., Cohn, 1979, for a detailed description of the computation of these coefficients). As discussed in section 2.3.3, they are the components of the Fokker–Planck eq. (3.3.1) describing the secular evolution of the PDF, $P(j, t \,|\, a)$. In Fig. 3.3.2, I illustrate the NR diffusion coefficients. In practice, contrary to the RR ones, the NR diffusion coefficients are mostly independent of the stars' eccentricities.

Finally, in Fig. 3.3.5, I illustrate the overall dependence of the total diffusion coefficients from eq. (3.3.2), i.e. both the RR and NR contributions, in the whole (a, j)-space. In that figure, I can clearly note the presence of resonance lines associated with RR. In addition, the bulk of the currently observed S-stars lie in a region of orbital space, where the diffusion of eccentricities is dominated by resonant effects. As a consequence, it is essential to account for these resonant mechanisms in order to accurately describe the dynamical fate of the S-stars' eccentricities. Finally, I note that the diffusion coefficient varies significantly as a function of j and stalls dramatically for $j \to 1$. As a result, it takes a much shorter amount of time for initially low eccentricity orbits to thermalise, or equivalently for a given age, it requires less massive unresolved perturbers (see also Fig. 3.4.4 below).

3.3.3 Diffusion time

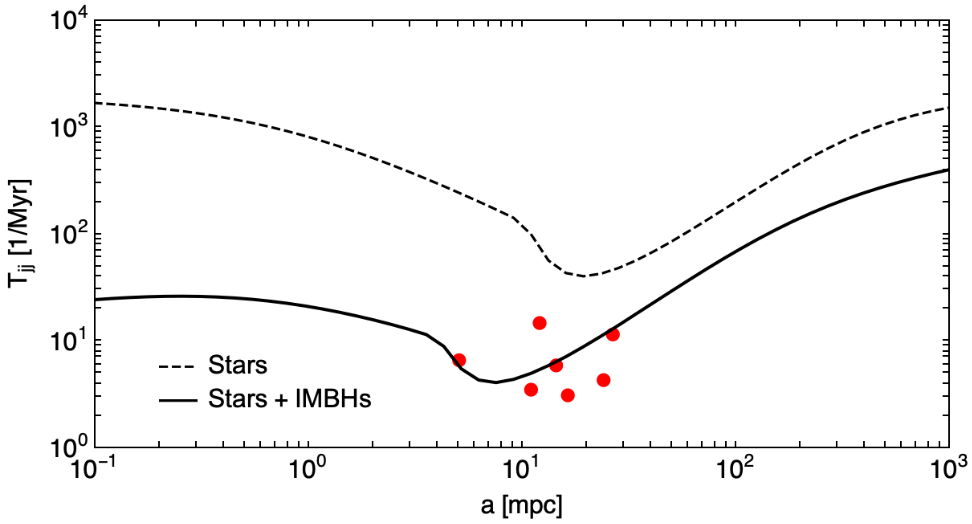

Figure 3.3.6: Representation of the diffusion time for two different families: a one-family model with solar-mass stars (dashed), and a two-family model with solar-mass stars and IMBHs (full lines) of mass $m_\bullet = 50 M_\odot$. Adding black holes in the model sharply increases the efficiency of this diffusion process. The seven S-stars used to constrain the models are represented in red dots. In particular, this two-family model fails to pass the zeroth order criterion described in section 3.3.3.

Observations of the Galactic centre show that the S-cluster has nearly relaxed in eccentricity (Eisenhauer, 2019; Gillessen et al., 2017; Peißker et al., 2020). Therefore, I can define the *diffusion* *time* by setting

$$\boxed{T_{jj}(a) = \frac{1}{D_{jj}^{\mathrm{iso}}(a)} \quad ; \quad D_{jj}^{\mathrm{iso}}(a) = \int_0^1 \mathrm{d}j\, f(j;a) D_{jj}(a,j),} \tag{3.3.13}$$

which in this context is of order of the relaxation timescale (Bar-Or & Fouvry, 2018). I compute this timescale for a model with a single family of stellar masses, as well as a model composed of a stellar family and an IMBH family. The results are shown in Fig. 3.3.6. The family of IMBHs accelerates the system's relaxation. Indeed, as I discussed in section 2.2, secular relaxation is sourced by finite-N effects. The presence of IMBHs impacts the granularity of the potential, and impacts the efficiency of the diffusion. The diffusion time can be used to probe this effect, and thus gives a rough criterion to determine which background families can induce an efficient enough eccentricity diffusion of the S-stars.

Let me detail a simple zeroth order criterion which will tell me whether one model is acceptable or not. To that end, I have access to the sma, the angular momentum and the main-sequence age for 7 stars of the S-cluster around $\mathrm{Sgr\,A}^\star$, which I reproduce in Table 3.1 (Habibi et al., 2017; Gillessen et al., 2017). I also know the distance to the SMBH $\mathrm{Sgr\,A}^\star$, $R_\bullet = 8.32 \times 10^6\,\mathrm{mpc}$ (Gillessen et al., 2017), which allows me to convert the smas from arcsec to mpc. The criterion goes as follows. Consider a set S of parameters $\{\boldsymbol{\alpha}\}_{\alpha \in S}$.

Star	S1	S2	S4	S6	S8	S9	S12
Semi-major axis (")	0.595	0.1255	0.3570	0.6574	0.4047	0.2724	0.2987
Semi-major axis (mpc)	24.00	5.062	14.40	26.52	16.32	10.99	12.05
Eccentricity	0.556	0.8839	0.3905	0.8400	0.8031	0.644	0.8883
Main-sequence age (Myr)	4.3	6.6	5.9	11.5	3.1	3.5	14.7

Table 3.1: Table of orbital parameters of the 7 stars used to constrain the parameters of the unresolved background families of the Galactic nucleus. Taken from Habibi et al. (2017) and Gillessen et al. (2017).

1. Compute $T_{jj}(a_k)$ (eq. 3.3.13) for $\boldsymbol{\alpha} \in S$, where a_k is the sma of those 7 stars.
2. If $T_{jj}(a_k) < T_k$ with T_k the main-sequence age of star k for more than half the stars (here, at least 4), I say that $\boldsymbol{\alpha}$ is a valid set of parameters and that the stars had enough time to diffuse to their current eccentricity distribution.

I apply this criterion to the Top-Heavy model (defined in eq. 3.4.2) in Fig. 3.3.7, where I varied the individual masses of the families' components. First, I observe that the diffusion is not efficient enough for IMBH masses that are too low, as expected. Second, I cannot give an upper bound on these masses, which is a problem. Indeed, on a practical level, observations show that the S-stars have almost relaxed. In particular, some deviation from the thermal equilibrium can be observed. In order to put an upper bound on the family's parameters, I therefore have to go beyond this zeroth order criterion.

3.4 Application to the search for IMBHs

3.4.1 Parametrisation of the unresolved cluster

For observational data, I use the orbital parameters listed in Tab. 3.1. The main sequence ages are a measure of the total time that the diffusion equation has had to operate. For simplicity, I assume that on these timescales, the NR relaxation did not drive any significant diffusion of the S-stars' energies, so that the stars' smas are kept fixed. Regarding the initial conditions for

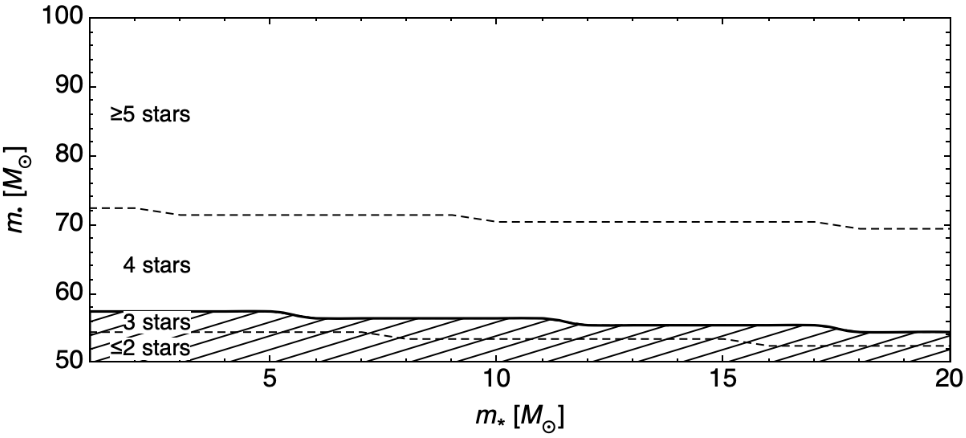

Figure 3.3.7: Zeroth order criterion in the space of mass parameters of the Top-Heavy families. The dashed region corresponds to models which fail to pass the criterion. The number of stars satisfying the criterion is written in the figure. Increasing the individual mass of the IMBH background family increases the efficiency of diffusion. However, this criterion fails to impose an upper mass bound on the models.

the stars' eccentricities, I investigate two possibles scenarii, either originating from binary tidal disruptions (Hills, 1988; Gould & Quillen, 2003; Alexander, 2017), i.e. large initial eccentricities, or from an episode of disc formation (Alexander, 2005; Levin, 2006; Koposov et al., 2019), i.e. small initial eccentricities. In practice, I assume that the S-stars are initialised following a Gaussian distribution centred at $j(t = 0) = 0.2$ – with width 0.02 – to mimic the eccentricity distribution of binary disruptions (Generozov & Madigan, 2020), or $j(t=0)=0.9$ to mimic an in-situ disc formation (see, e.g., Perets et al., 2007; Madigan et al., 2009, for alternative scenarii).

Now, let me also make key assumptions regarding the background old stellar cluster. I assume that it is composed of various sub-populations of different individual masses m_i with a total mass $M_i(< a_0)$ enclosed within a physical radius a_0. In addition, I also assume that each population follows a thermal distribution in eccentricity, and infinite power-law distribution in smas, that is

$$M_i(< a) = M_i(< a_0)(a/a_0)^{3-\gamma_i}. \tag{3.4.1}$$

This eases the resolution of the resonance condition in eq. (3.3.5). I finally assume that throughout their eccentricity diffusion, the S-stars are treated as test stars. As such, they do not contribute to the system's mean potential, and do not interact with one another. Since I expect the background to be thermal, the RR dynamical friction vanishes exactly (section 2.3.1). Conversely, I also neglect the NR part of dynamical friction, since energy diffusion is inefficient in quasi-Keplerian systems on SRR timescale (Bar-Or & Alexander, 2016). Assuming a two-family background composed of stars and an other heavy sub-population (e.g., IMBHs), I then have a total of 7 free parameters for the available models, namely the power indices $(\gamma_\star, \gamma_\bullet)$, the individual masses $(m_\star, m_\bullet)$, the total enclosed masses $(M_\star[< a_0], M_\bullet[< a_0])$ as well as the initial eccentricity of the S-stars, $j_0 = j(t=0)$. These models are complemented with the observed constraints on the seven considered S-stars, namely their main-sequence age, as well as their observed sma and eccentricity (Table 3.1).

In practice, I started my investigation from the two-family Top-Heavy model of Generozov & Madigan (2020). Using $a_0 = 0.1$ pc, the fiducial model contains both stars and IMBHs

$$\begin{cases} m_\star = 1 M_\odot, \\ m_\bullet = 50 M_\odot, \end{cases} \begin{cases} M_\star(< a_0) = 7.9\times 10^3 M_\odot, \\ M_\bullet(< a_0) = 38\times 10^3 M_\odot, \end{cases} \begin{cases} \gamma_\star = 1.5, \\ \gamma_\bullet = 1.8, \end{cases} \tag{3.4.2}$$

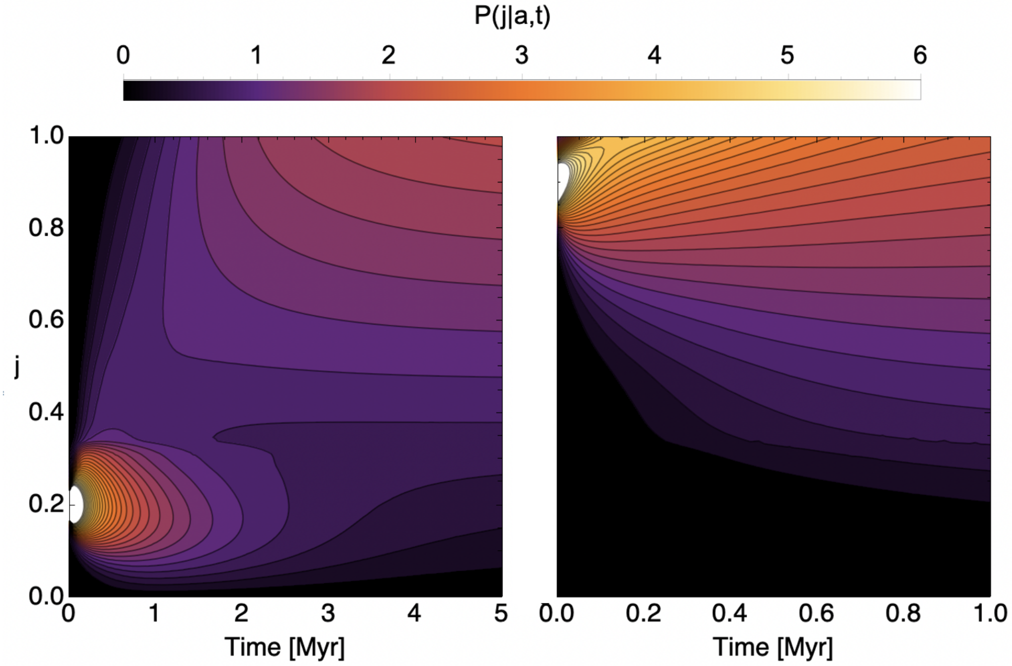

Figure 3.4.1: Solution of the diffusion equation (as given by eq. 3.4.3) at fixed sma $a = 10$ mpc. The initial j-distribution is a Gaussian with width $\sigma = 0.02$. On the left, the Gaussian is centred at $j = 0.2$, which corresponds to the binary's tidal disruption formation scenario. On the right, the Gaussian is centred at $j = 0.9$, which corresponds to more circular orbits (in-situ star formation). The time after which I observe thermalisation depends on the initial conditions. In particular, an in-situ star formation yields a faster thermalisation of the S-cluster.

where the star parameters follow Schödel et al. (2017). Such a model is compatible with the current constraints associated with S2's pericentre shift (Gravity Collab. et al., 2020), since $M_\bullet(<r_{\rm apo}^{\rm S2})+M_\star(<r_{\rm apo}^{\rm S2})\simeq 2500 M_\odot$.

3.4.2 Time evolution and stochastic process

Under the effect of the background stellar families, the test stars of the S-cluster undergo a diffusion, the efficiency of which depends on the profile of the background, as could be seen in a first rough approach in section 3.3.3. However, if I want to obtain a more precise description of eccentricity diffusion, I have to integrate the Fokker–Planck equation (eq. 3.3.3) forward in time.

There are two methods to obtain the evolution of this PDF. The first one is to directly integrate the smooth partial differential equation (eq. 3.3.3) in time, using an initial condition in j depending on the formation scenario (see section 3.4.1). In Fig. 3.4.1, I show the time-evolution for the Fokker–Planck equation from the two initial conditions discussed previously with a Top-Heavy model background.

In order to determine whether or not a model is compatible with the observational constraints of a significant eccentricity relaxation of the S-stars, I proceed as follows. I first compute the RR and NR diffusion coefficients for the semi-major axis of the S-stars considered. The total diffusion coefficients are then interpolated and I integrate the diffusion equation forward in time using finite elements. More precisely, I rely on the so-called method-of-lines implemented in the `Mathematica NDSolve` function, which discretises the j dimension and integrates the semi-discrete problem as a system of Cauchy's ODEs. As the smas are conserved, they can be integrated separately. As such, I integrate eq. (3.3.3) for each of the seven considered S-stars, for a total time equal to the age of each star. In order to ensure that the PDF stays normalised during the integration, it is useful to rewrite eq. (3.3.3) under the form

$$j^2 \frac{\partial P}{\partial t} = \frac{j^2}{2} \frac{\partial}{\partial j} \left(D_{jj} \frac{\partial P}{\partial j} \right) - \frac{1}{2} \left[j \frac{\partial (D_{jj} P)}{\partial j} \right] + \frac{D_{jj}}{2}. \tag{3.4.3}$$

This form is more stable and avoid any $1/j$ singularity. This form is more stable numerically and ensures the conservation of the PDF norm.

The second method is to consider the equivalent Langevin process. Following Risken (1996), I can mimic the dynamics of a given test star through the stochastic Langevin equation

$$\Delta j = D_j \, \Delta t + \sqrt{D_{jj} \, \Delta t} \, \xi(t). \tag{3.4.4}$$

In that expression, Δt is my chosen (fixed) timestep, and $\xi(t)$ follows a normal distribution of unit variance, uncorrelated in time. I can then use a large sample of test particles to recover the time evolution of their smooth underlying PDF. In Fig. 3.4.2, I illustrate some examples of random walks in eccentricities.

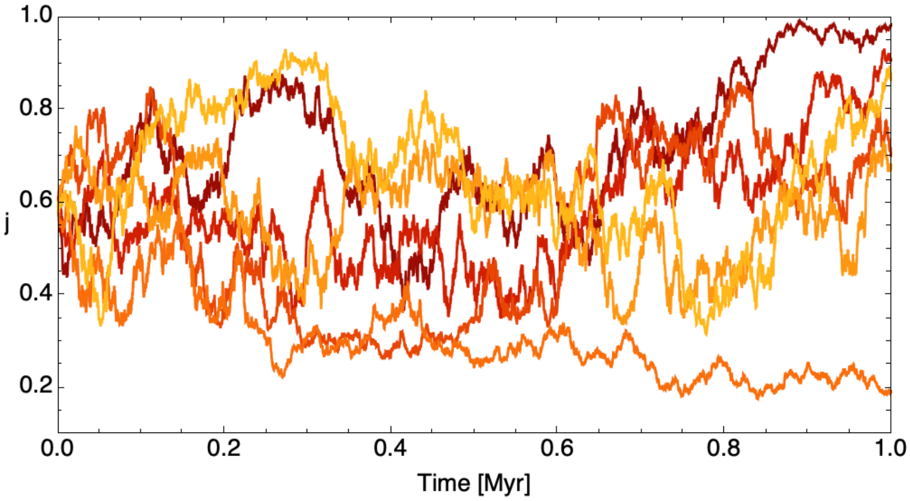

Figure 3.4.2: Illustration of stochastic random walks in eccentricities as driven by eq. (3.4.4) with a timestep $\Delta t = 0.1$ kyr. Here, the test particles all have $a = 10$ mpc, are initialised with $j = 0.6$, and evolve within the same background model as in Fig. 3.4.1. These random walks are not physical – in particular, they are uncorrelated – but their average over realisations follows the physically relevant Fokker–Planck equation (eq. 3.3.1).

To ensure that the random walks do not wander off the range $j \in [0, 1]$, I introduce a reflective barrier at $j = 0, 1$. Let me note that the stochastic walks from Fig. 3.4.2 do not describe any physically realistic random walks on their own, but only in an average sense. Indeed, here I have supposed that the $\xi(t)$ are uncorrelated in time, whereas they are in fact correlated (at least on the fluctuations' coherence time) in a real physical process. However, their average over realisations accurately describes the evolution of the corresponding FP eq. (3.3.1).

Consequently, in Fig. 3.4.3, I use $N = 10^6$ test particles to recover the PDF at various times and compare it with that obtained from the direct integration of the diffusion eq. (3.3.3). It is reassuring to note that both approaches are in precise agreement.

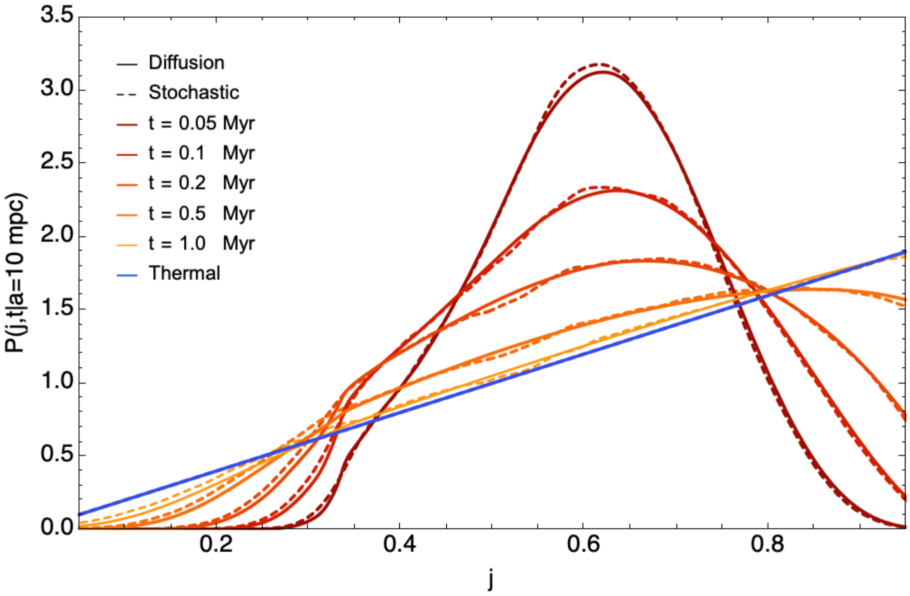

Figure 3.4.3: Comparison between the direct integration of the diffusion eq. (3.4.3) (full lines) and its stochastic realisation through eq. (3.4.4) (dashed lines), as a function of time, and using the same initial conditions as in Fig. 3.4.2. For the stochastic evolution, I considered a total of $N = 10^6$ test particles, evolved with the timestep $\Delta t = 0.1$ kyr. Some of its realisations are represented in Fig. 3.4.2. Both approaches are found to be in very good agreement, and ultimately relax to the thermal distribution.

3.4.3 Likelihood analysis

Using the aforementioned approaches, I am now able to predict the time evolution of a variety of models, parametrised by their individual masses, cusps, total masses and mass spectra. In order to determine which one is best to understand the Galactic centre's observations, let me define a model's *likelihood* as

$$L(\boldsymbol{\alpha}) = \prod_k P(j_k, T_k \,|\, a_k), \tag{3.4.5}$$

where $k = 1, ..., 7$ go through the seven S-stars mentioned before. Here, T_k is the main-sequence age of star k at which the PDF is evaluated. Relying on eq. (3.4.5), I can then explore the space of parameters $\boldsymbol{\alpha}$ and compare the various models to one another. To that end, I use the likelihood ratio (LR) test through

$$\lambda_{\mathrm{R}}(\boldsymbol{\alpha}) = 2 \ln \big(L_{\max} / L[\boldsymbol{\alpha}] \big) \geq 0, \tag{3.4.6}$$

where $L_{\max}$ is the maximum likelihood in the domain of explored models.

When $\boldsymbol{\alpha}$ maximises the likelihood, it minimises by definition this likelihood ratio (as would a χ^2 analysis for Gaussian statistics), such that $\lambda_{\mathrm{R}}(\boldsymbol{\alpha}) = 0$. Then, I can reject a model $\boldsymbol{\alpha}$ with confidence $0 \leq p \leq 1$, if the corresponding LR, $\lambda_{\mathrm{R}}(\boldsymbol{\alpha})$, lies above a certain (explicit) value η_p.

As an illustration of the present method, I first consider the Top-Heavy model defined in eq. (3.4.2), and let the individual masses $m_\star$ and $m_\bullet$ vary, with the natural constraint $m_\bullet \geq m_\star$ while fixing the total enclosed masses $M_\bullet(<a_0)$ and $M_\star(<a_0)$. This is presented in Fig. 3.4.4. In that figure, a model outside of the region of confidence $n\sigma$ means that it can be discarded with confidence $n\sigma$, as it would not allow the diffusion process to be fast enough to reach the observed eccentricity distribution of the S-cluster. As expected, in Fig. 3.4.4 (top-left panel), I recover that the larger the individual masses, the larger the underlying Poisson shot noise. Therefore, the more efficient the diffusion process, and the faster the relaxation of the S-stars. Conversely, Fig. 3.4.4 shows that models with small individual masses cannot explain the current

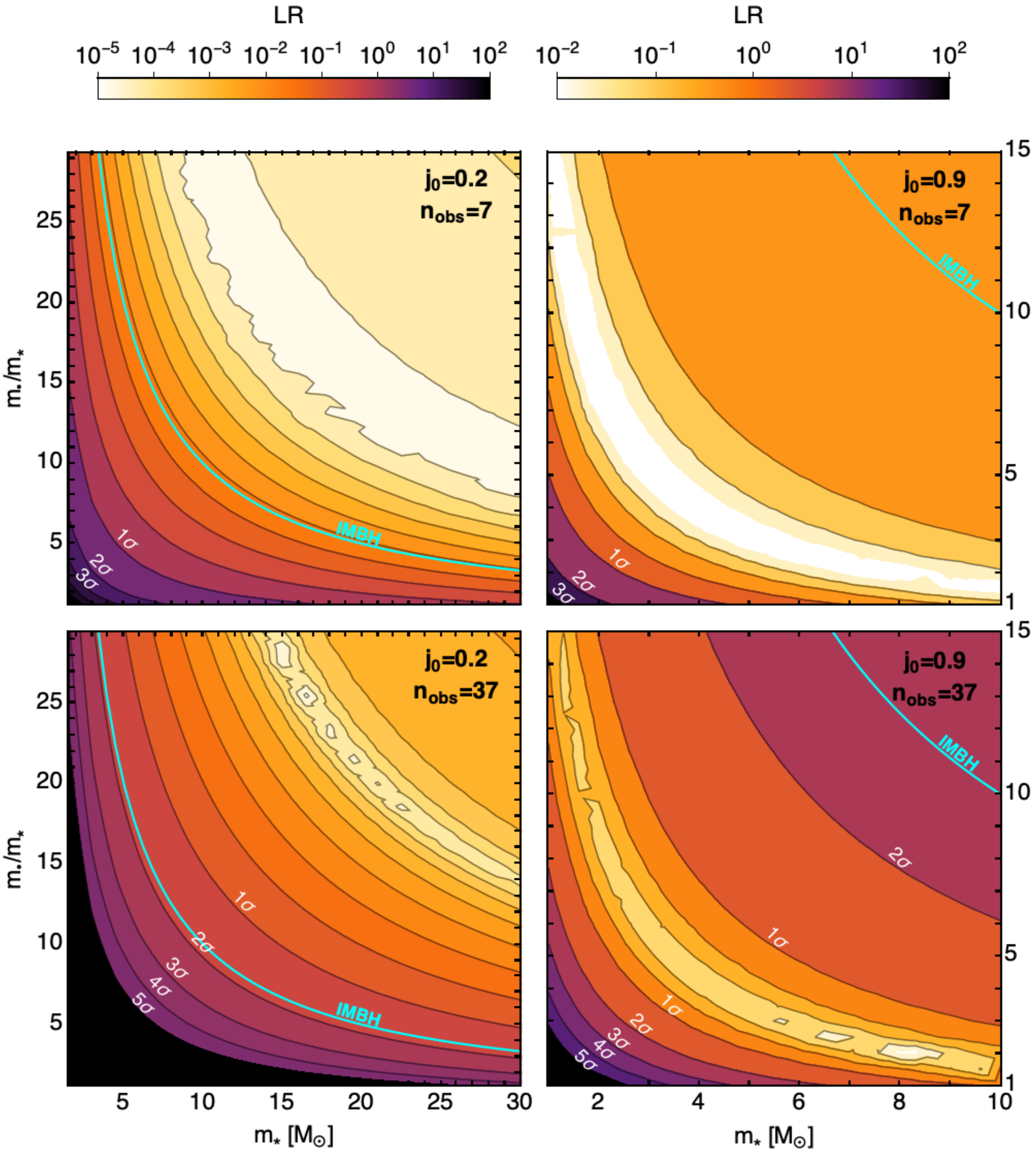

Figure 3.4.4: Confidence regions for the Top-Heavy model defined in eq. (3.4.2) using the maximum likelihood method applied to the observed S-stars, assuming a large initial eccentricity ($j_0 = 0.2$, the canonical value, left panels), or a small initial eccentricity ($j_0 = 0.9$, right panels). The cyan line corresponds to $m_\bullet = 100M_\odot$, above which heavy objects are usually considered as IMBHs. The cusp's indices and the total enclosed masses are fixed to their fiducial values (see eq. 3.4.2), but I let the individual masses vary. Confidence levels are inferred from the LR test, see eq. (3.4.6). The top panels only used the seven S-stars with known orbital parameters and stellar ages (see Tab. 3.1), while the bottom ones expanded this observed sample using the other thirty S-stars (Gillessen et al., 2017), assuming a common age $T = 7.1$ Myr, i.e. the average age of the constrained seven S-stars. As expected, the smaller j_0, i.e. the more eccentric the stellar initial conditions, the slower the relaxation of the S-stars. Similarly, the larger the observed sample, the tighter the constraints on the background clusters.

S-cluster's angular momentum PDF. As such, a relatively massive set of background sources orbiting within the S-cluster is required to trigger a fast enough orbital diffusion of the observed stars over their lifetime. Using the same data, in Fig. 3.4.4 (top-right panel), I also change the initial eccentricity of the S-stars to $j_0 = 0.9$, to mimic an episode of disc formation. As already observed in Fig. 3.3.5, I note that the diffusion coefficient is larger at smaller eccentricities, so that the diffusion proceeds more swiftly, hence enhancing the overall efficiency of the relaxation of the S-stars.

The global shape of the likelihood contours presented in Fig. 3.4.4 clearly illustrates the known dynamical degeneracy in flipping IMBHs and stars of the same mass, as the efficiency of eccentricity relaxation is directly connected to the amplitude of the Poisson fluctuations generated by the background clusters as a whole. Interestingly, I note that all likelihood landscapes presented in the top panels present an absolute minimum. This suggests that, having only diffused a finite time, the observed eccentricity distribution of the S-stars is not fully thermal.

In order to increase the observed stellar sample, and tighten the inferred model constraints, I present in the bottom panels of Fig. 3.4.4 the same measurement but using 30 additional S-stars (as in fig. 13 of Gillessen et al., 2017). Their individual ages was fixed to $T = 7.1\,\mathrm{Myr}$, i.e. the average age of the seven S-stars, whose ages have been measured (Habibi et al., 2017). As expected, I recover that a larger sample of observed stars leads to narrower contours around the likelihood extremum, making the presence of a second population of massive objects all the more mandatory. Finally, I also note that since the expanded sample of 37 stars contains stars with smas larger than that of the initial seven S-stars, i.e. stars whose eccentricity relaxation time is longer, the location of the likelihood maximum gets displaced to larger masses as I increase the observed stellar sample.

From these considerations, Fig. 3.4.4 can be used to determine the presence or not of IMBHs. Indeed, at fixed cusp indexes and fixed enclosed masses, increasing the individual masses of the background's families increases the efficiency of the eccentricity diffusion. Hence, I can determine which values of the mass parameters are the most likely parameters to fit the observations of the S-cluster today. Using this method, I could ultimately study the impact of the initial condition for eccentricity on the likelihood of a model. Depending on the model – in-situ formation of near-circular orbits or binary disruptions resulting in eccentric stars – the presence of IMBHs can be either strengthened (binary disruptions, left panels of Fig. 3.4.4) or discarded (in-situ formation, right panels of Fig. 3.4.4). Of course, this requires the knowledge of the other parameters, arbitrarily fixed in this example. Fortunately, a study of the full parameter space is certainly numerically accessible for future works.

3.4.4 Impact of the data sample size

Let me now carry out a fiducial experiment where I vary the number of stars for which orbital parameters are available, i.e. a prospective experiment appropriate for future surveys (Do et al., 2019).

I consider a model similar to the one in eq. (3.4.2) where I set $m_\star = 5\,M_\odot$ and $m_\bullet = 20\,M_\odot$. I now wish to probe how the number of observed stars impacts my constraints on the determination of the background cluster's parameters. To that end, I take the same seven S-stars as in Fig. 3.4.4, and consider their smas and main-sequence ages. For each of the seven smas, I evolve the PDF from eq. (3.3.3) for $j_0 = 0.2$ for the entire star's observed lifetime. From the resulting PDFs, I draw N stars for each sma. In total, I therefore assume that my observation sample is composed of a total of $n_{\rm obs}=7N$ stars. This sample constitutes my mock data, to which I apply the previous likelihood analysis.

Following this approach, Fig. 3.4.5 shows the ability of the method to constrain the parameters of the IMBHs' population given a larger mock sample. While the stellar parameters $(m_\star, \gamma_\star)$ are observables, I illustrate in that figure how the maximum likelihood approach indeed allows me to constrain the parameters of the invisible dark cluster $(m_\bullet, \gamma_\bullet)$, which cannot be directly observed. As $(m_\bullet, \gamma_\bullet)$ are not degenerate with one another, an increase in the number of measured eccentricities (from $N=1$ to $N=100$ from top to bottom panels) narrows the confidence contours around the extremum of the likelihood, which itself converges to a specific pair $(m_\bullet, \gamma_\bullet)$ close to the fiducial one (green dot).

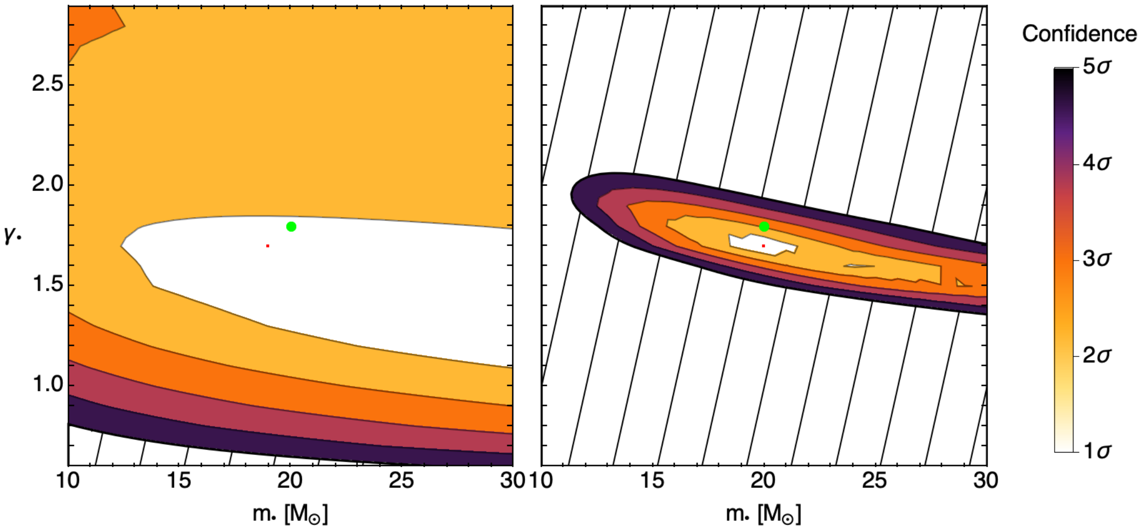

Figure 3.4.5: Same analysis as in Fig. 3.4.4, but applied to mock data, as detailed in section 3.4.4, as I vary the parameters $(m_\bullet, \gamma_\bullet)$ of the IMBHs' population (keeping the total enclosed mass fixed). The left panel corresponds to mock data with $n_{\rm obs}=7$ stars, while the right panel uses $n_{\rm obs}=700$ stars. As expected, increasing the observed sample narrows the confidence contours around the maximum likelihood estimator (red dot) which converges towards the fiducial model (green dot).

I further pursue this experiment in Fig. 3.4.6, where I investigate the expected improvements in the inferred constraints as a function of the number of observed stars, $n_{\rm obs}$. For a given mock realisation, I compute the uncertainty $\sigma_{m_\bullet}$, defined as the width of the LR w.r.t. $m_\bullet$ at the 3σ height and fixed $\gamma_\bullet=1.8$. This is represented in Fig. 3.4.6 as a function of $n_{\rm obs}$. Since the maximum likelihood estimator is asymptotically normal and efficient (see, e.g., Wasserman, 2004) it reaches the Cramér–Rao bound in the large $n_{\rm obs}$ limit, so that $\sigma_{m_\bullet}(n_{\rm obs})=\sigma_3/\sqrt{n_{\rm obs}}$, with $\sigma_3\simeq 220\,M_\odot$. Assuming crudely that the number of resolved stellar orbits is proportional to the survey's bolometric limit, one can directly connect a target accuracy with the survey's limiting magnitude. Indeed, the survey's magnitude would simply read $M=-2.5\log_{10}[(\sigma_{m_\bullet}/\sigma_3)^{-2}]$. Gaining a factor two in the accuracy of the mass (i.e. $\sigma_{m_\bullet}\to\sigma_{m_\bullet}/2$) would require a survey that is at least $\Delta M=-5\log_{10}(2)\simeq-1.5$ magnitudes fainter. Undoubtedly, upcoming surveys of Sgr A*'s stellar neighbourhood, such as GRAVITY+ (Eisenhauer, 2019; Gravity Collab. et al., 2021), TMT (Do et al., 2019), and ELT/MICADO (Davies et al., 2018; Pott et al., 2018) are on the verge of putting ever more stringent dynamical constraints on the unresolved dark cluster. Indeed, the central stellar cusp around Sgr A* is strongly confusion-limited for current observations on 8-meter class telescopes with adaptive optics. This limits in effect the reliable detection and measurement of positions of stars to K magnitudes $\sim 16-17.5$, i.e. main-sequence B stars.

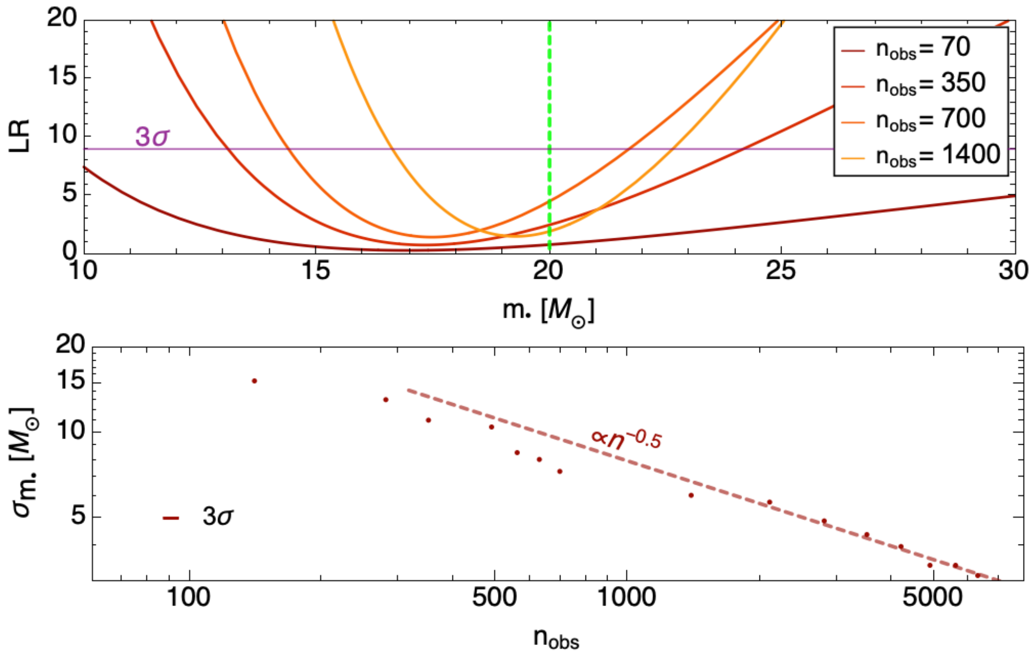

Figure 3.4.6: Same as in Fig. 3.4.5, using the same mock data, but with varying numbers of observed stars, $n_{\rm obs}$. The top panel shows the evolution of the LR at fixed $\gamma_\bullet = 1.8$, as a function of $m_\bullet$, for various values of $n_{\rm obs}$. The vertical green line represents the fiducial parameters of the model, $m_\bullet = 20\,M_\odot$. The horizontal line represents the value of the LR for a 3σ confidence contour. The bottom panel illustrates the evolution of the accuracy, $\sigma_{m_\bullet}$, of the inferred IMBH mass as a function of the $n_{\rm obs}$, and for the 3σ confidence levels. For the modified Top-Heavy model I used, I expect $\sim 10^3$ stars within 5 and $20\,\mathrm{mpc}$. Of course one does not expect to observe so many stars around SgrA*, i.e. the asymptote $1/\sqrt{n_{\rm obs}}$ will not be attained, because of crowding and, more importantly, because the total number of observed S-stars will be much smaller than 5000.

The combination of MICADO and the ELT will push the effective stellar detection sensitivity by $\gtrsim 5$ magnitudes with modest integration times (Fiorentino et al., 2019).

3.5 Concluding remarks

In this chapter, I showed how eccentricity diffusion in galactic nuclei can be used to put constraints on the stellar and putative dark clusters present therein. To that end, I used the NR and RR formalisms developed in chapter 2, and applied them in the context of the Galactic centre. Due to the overwhelming presence of the SMBH, the system is quasi-Keplerian. This defines a set of convenient angle-action coordinates which can be used to describe the secular evolution of the system (section 3.3). The recent observations of the (quasi-)thermal distribution of eccentricities of the S-stars orbiting Sgr A*, in conjunction with updated computations of the eccentricity diffusion coefficients, can now be leveraged to this purpose. Investigating a simple two-population model (section 3.4.1), I showed how the presence of a heavy sub-population, e.g., IMBHs, can be mandatory to source an efficient enough relaxation of the S-stars' eccentricities. I jointly showed how only some ranges of dark cusp's power law indices and masses are compatible with that same dynamical constraint. Indeed, preliminary observations – such as the study of the typical diffusion time – had motivated the existence of a heavy unresolved population (section 3.3.3). In section 3.4, I refined this study by directly integrating forward in time the Fokker–Planck equation describing the S-cluster's orbital diffusion. I then applied a likelihood approach to constrain the background families' parameters. Assuming that upcoming experiments will better quantity the properties of the visible cluster, kinetic theory will allow for dynamical dark matter experiment to constrain both the typical mass and geometry of the IMBH cluster.

Finally, a simple fiducial experiment allowed me to quantify the depth that upcoming surveys should achieve in order to, e.g., double the accuracy on the IMBHs' mass required to match the data. More generally, my investigation suggests that it will be of interest to lift some of these dynamical degeneracies, both by increasing the number of measured stellar ages and better quantifying the mass function and shape of the observed stellar cluster and initial eccentricity distribution. Then, kinematic modelling will be able to further focus on dynamically quantifying the properties of the dark cluster.

3.5.1 Future works

Let me now discuss some venues for future developments. As shown in section 3.4.1, my investigation relied on various assumptions, some of which one could hope to partially lift. My models for the old stellar and dark cluster remain simplistic, and it will be worthwhile to investigate possible contributions from other populations such as a dark matter dominated component, or additional populations of IMBHs. Similarly, as already emphasised in eq. (3.3.3), I assumed that the background cluster is spherically symmetric. Yet, Szölgyén & Kocsis (2018) recently showed that in systems with a large mass spectrum, e.g., containing IMBHs, one could expect vector resonant relaxation (VRR) to lead to equilibria distribution where the massive components follow a strongly anisotropic structure, i.e. aligned within the same disc. Such a structure could definitely affect the efficiency of eccentricity relaxation within it. Any additional non-trivial structures present in that PDF, e.g., non-spherically symmetric distributions or dearth of stars in orbital space, would also have to be explained by the present diffusion processes. Similarly, on scales even closer to the central BH, one would also have to account for additional relativistic corrections stemming from it, e.g., effects associated with its spin such as the Lense-Thirring process (see, e.g., Kocsis & Tremaine, 2015).

Observations show that 7-10% of the stars may have originated from an infalling population. These stars display significant rotation (Do et al., 2020) and likely populate a disc. The most direct impact of that disc would be to induce a mean field torquing on the orbital planes, but it might also impact later on the eccentricities within the cluster. Recently, Szölgyén et al. (2021) have investigated this effect numerically and found that the timescale for the eccentricity decrease is much shorter than Chandrasekhar's dynamical friction timescale. This supports previous findings by Madigan & Levin (2012) that RR dynamical friction, driven by orbit-averaged torques, dominates over ordinary NR dynamical friction, driven by nearby encounters, and leads to eccentricity decrease for a co-rotating disc.

The mass in the S-star cluster is only a small fraction of the total enclosed mass within 1 arcsec of the central black hole. As such, it is unlikely that the S-cluster itself strongly disturbs the background stellar distribution. I also assumed here that this background cluster was thermal (i.e. $f(j;a)=2j$) hence fully relaxed. In that limit, it does not drive any RR dynamical friction (Bar-Or & Fouvry, 2018). Should one lift this assumption, a more accurate modelling would include the coupling between both components of the cluster as a two-population model. This would require integrating the coupled set of kinetic equations in time (eq. 2.2.35), rather than relying on a frozen Fokker–Planck approximation for the diffusion coefficient. While this might be a worthwhile endeavour for upcoming data sets, it is clearly beyond the scope of this first investigation.

When modelling the S-stars' dynamics, I assumed that the smas of the stars were fixed throughout the diffusion, owing to the orbit-average. While accounting for the contributions from the NR diffusion coefficients in a, it could be interesting to investigate whether any additional diffusion in a-space would affect the present constraints. As already noted, the initial conditions of the S-stars, e.g., very eccentric vs. quasi-circular, strongly affect the efficiency of their eccentricity relaxation (see Fig. 3.4.4). In particular, I expect that the distribution of the S-stars in smas also carries some information on their initial formation mechanism.

Here, I focused my interest on the innermost S-stars ($a \simeq 5\,\mathrm{mpc}$), which are known to have partially relaxed in eccentricity (Gillessen et al., 2017). This allowed me to place constraints on cluster models so that admissible clusters have to source an eccentricity diffusion that is fast enough. One could use a similar approach to investigate the relaxation of S-stars further out. These outer stars have only very partially relaxed in eccentricity, so that any admissible cluster model must source a diffusion that is slow enough for these outer regions not to have fully relaxed. Leveraging both constraints, one should be in a position to effectively bracket cluster models, given that their induced diffusion must be both efficient enough in the inner regions, and inefficient enough in the outer ones. A same double-sided investigation could also be carried out in the context of the VRR of the same S-stars. Indeed, it has been observed that the innermost stars follow a spherically symmetric distribution, while the outer ones tend to be aligned within a disc (Bartko et al., 2009; Yelda et al., 2014), i.e. orientation neighbours have not been separated (Giral Martínez et al., 2020). Once again, simultaneously accounting for all these dynamical constraints will allow for better characterisations of Sgr A*'s dark and visible structures. Recently, Fouvry et al. (2022) used the VRR formalism to constrain the parameter space of the class of Top-Heavy families studied in this chapter. They found constraints roughly corresponding with those presented in this chapter (Fig. 3.5.1). The survival of the observed

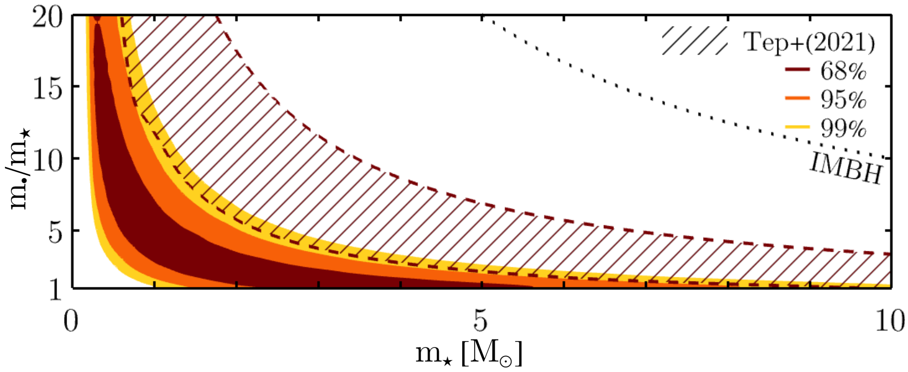

Figure 3.5.1: From fig. 5 of Fouvry et al. (2023). The constraints obtained through the use of the VRR formalism (coloured contours) roughly correspond to those obtained by the orbit-averaged RR prediction (hashed region) in Fig. 3.4.4 (see bottom right panel). The offset between the two predictions could be linked, for example, to the differences between the hypotheses of the two formalisms. Here, the existence of IMBHs is very unlikely, as objects that massive in the background would drive a relaxation incompatible with the observations of Sgr A*'s disc.

Sgr A*'s stellar disc enforces a background population with very small individual masses. This rejoins the observation made in Fig. 3.4.4 (right panels) for an in-situ formation scenario, and seems to disfavour the possible presence of IMBHs in the Galactic centre. A recent study of S2's orbit seems to go in the same direction, showing that the presence of a large IMBH within S2's orbit is unlikely (Gravity Collab. et al., 2023).

Finally, future observations will undoubtedly prove useful in placing these investigations on firmer grounds. A possible observation from GRAVITY of stars on scales even smaller than S2 would carry essential information on Sgr A*'s stellar structure on smaller scales, i.e. closer to the central BH (Gravity+ Collab. et al., 2022). On larger scales, one expects that observations from upcoming thirty-meter telescopes (Do et al., 2019) will allow for a finer characterisation of the S-stars' current distribution, $P(a, j, t)$, a very valuable dynamical information as shown in section 3.4.4. In particular, the dependence of P w.r.t. a is strongly dependent on the formation mechanism of these stars. Regarding the dependence w.r.t. j, one could in particular hope to measure the scale, i.e. the a, at which the S-stars diffuse less and less efficiently towards a thermal distribution of eccentricities, hence strongly constraining the efficiency of the diffusion mechanisms. I note that the present maximum likelihood formalism can naturally be extended to account for the measurement uncertainties, such as uncertainties on stellar ages. Eventually, this line of investigation should prove useful in constraining SMBH formation scenarii, possibly jointly with core collapse predictions for massive stellar clusters as investigated in the next chapter.

Appendices of chapter 3

3.A Numerical implementation of the RR coupling coefficients $K^{\ell}_{kk'}$

Let me detail the numerical implementation of the pairwise in-plane coupling coefficients from eq. (3.3.9). The naive implementation has a quadratic complexity in $\mathcal{O}(K^2)$, where K is the number of sampling nodes. Indeed, its expression reads

$$K^{\ell}_{kk'}(a,L,a',L') = \int_0^{2\pi} \frac{\mathrm{d}M}{2\pi} \int_0^{2\pi} \frac{\mathrm{d}M'}{2\pi} \, \frac{\min(r,r')^{\ell}}{\max(r,r')^{\ell+1}} \, \cos(kf)\, \cos(k'f'), \tag{3.A.1}$$

where f is the Keplerian true anomaly and M the mean anomaly. First, I note that since $M \mapsto r(M)$ and $M \mapsto f(M)$ are even functions, the ranges of the angular integrals can be reduced to $M, M' \in [0,\pi]$. Moreover, in order not to have to invert Kepler's equation of motion, it is appropriate to perform the average from eq. (3.A.1) w.r.t. the true anomaly. I recall that the radius r is obtained from the true anomaly f (see, e.g., Murray & Dermott, 2000, for a more complete description of the Keplerian anomalies) as

$$r = \frac{a(1-e^2)}{1+e\cos f}. \tag{3.A.2}$$

Finally, the mapping $M \mapsto f$ is characterised by the Jacobian

$$\frac{\mathrm{d}M}{\mathrm{d}f} = \left(\frac{R}{a}\right)^2 \frac{1}{\sqrt{1-e^2}}. \tag{3.A.3}$$

Following these changes, I can rewrite eq. (3.A.1) as

$$K^{\ell}_{kk'}(a,L,a',L') = \int_0^{\pi} \frac{\mathrm{d}f}{\pi} \int_0^{\pi} \frac{\mathrm{d}\,f'}{\pi} \, \frac{\mathrm{d}M}{\mathrm{d}f} \, \frac{\mathrm{d}M'}{\mathrm{d}f'} \, \frac{\min(r,r')^{\ell}}{\max(r,r')^{\ell+1}} \, \cos(kf)\, \cos(k'f'). \tag{3.A.4}$$

Computing efficiently the interaction coefficients involves computing efficiently the double integral from eq. (3.A.4).

Let me now detail this approach. I sample uniformly the integration interval from eq. (3.A.4) using K nodes. Specifically, I sample the true anomaly with

$$f_n = \delta f \, (n - \tfrac{1}{2}) \quad \text{with} \quad \delta f = \frac{\pi}{K} \quad \text{and} \quad 1 \leq n \leq K. \tag{3.A.5}$$

Following this discretisation, eq. (3.A.4) becomes

$$K^{\ell}_{kk'} = \frac{1}{K^2} \sum_{i,j} g(r_i)\, g(r_j) \, \frac{\min(r_i,r_j)^{\ell}}{\max(r_i,r_j)^{\ell+1}} \quad ; \quad \text{with} \quad g(r) = \frac{\mathrm{d}M}{\mathrm{d}f} \cos(kf). \tag{3.A.6}$$

A naive glance at eq. (3.A.6) would suggest that computing eq. (3.A.6) requires the evaluation of $\mathcal{O}(K^2)$ terms. Luckily, I can use the particular structure of the terms summed in eq. (3.A.6) to drastically accelerate this computation. To do so, I sort the set of radii $\{r_i, r_j\}$ by increasing order. I note that this can be done in $\mathcal{O}(K)$ steps, provided that the sets $\{r_i\}$ and $\{r_j\}$ are already ordered, so that it only remains to merge the two lists.

Following this ordering, I can then construct the array w_j, for $1 \leq j \leq K$, defined as

$$w_j = \text{Number of radii } r_i \text{ that satisfy } r_i \leq r_j. \tag{3.A.7}$$

where the boundary terms are given by $w_0 = 0$ and $w_{K+1} = K$. The double sum from eq. (3.A.6) can then be rewritten as

$$K^{\ell}_{kk'} = \frac{1}{K^2} \sum_{j=1}^{K} g_j \left\{ P_j + Q_j \right\}, \tag{3.A.8}$$

where I used the shortened notation $g_i = g(r_i)$ and $g_j = g(r_j)$, and introduced the reduced sums P_j and Q_j, with $1 \leq j \leq K$, as

$$P_j = \sum_{i=1}^{w_j} g_i \, \frac{r_i^{\ell}}{r_j^{\ell+1}} \quad ; \quad Q_j = \sum_{i=w_j+1}^{K} g_i \, \frac{r_j^{\ell}}{r_i^{\ell+1}}. \tag{3.A.9}$$

Interestingly, the sum P_j (resp. Q_j) can be computed linearly in time, through an increasing (resp. decreasing) recurrence. To highlight this property, let me define the partial sums, for $1 \leq j \leq K$,

$$\delta P_j = \sum_{i=w_{j-1}+1}^{w_j} g_i \, \frac{r_i^{\ell}}{r_j^{\ell+1}} \quad ; \quad \delta Q_j = \sum_{i=w_j+1}^{w_{j+1}} g_i \, \frac{r_j^{\ell}}{r_i^{\ell+1}}. \tag{3.A.10}$$

It is then important to note that the sum P satisfies the increasing recurrence relation

$$P_1 = \delta P_1 \quad ; \quad P_{j+1} = z_j^{\ell+1} \, P_j + \delta P_{j+1} \, , \quad \text{for} \quad 1 \leq j < K, \tag{3.A.11}$$

where I introduced the ratio

$$z_j = \frac{r_j}{r_{j+1}} \, , \quad \text{for} \quad 1 \leq j < K. \tag{3.A.12}$$

Similarly, the sum Q satisfies the decreasing recurrence relation

$$Q_K = \delta Q_K \quad ; \quad Q_{j-1} = z_{j-1}^{\ell} \, Q_j + \delta Q_{j-1} \quad \text{for} \quad 1 < j \leq K. \tag{3.A.13}$$

As a conclusion, owing to these recurrence relations, the discrete sum from eq. (3.A.8) can be computed in $\mathcal{O}(K)$ operations. Moreover, I note that the prefactors appearing in the recurrence relations from eqs. (3.A.11) and (3.A.13) are always smaller than unity, which helps making the recurrence relations numerically stable. Finally, in eq. (3.A.8), having the discrete samples separated by a constant step allows me to benefit from the very fast convergence of the trapezoidal rule for the computation of periodic functions (Trefethen & Weideman, 2014).

3.B Resonance condition

In the vicinity of a supermassive BH, Keplerian wires undergo an in-plane precession of their pericentres, as described by eq. (3.3.6). In that relation, the relativistic precession is given by (see, e.g., Hartle, 2003)

$$\Omega_{\mathrm{GR}}(a,j) = 3\frac{r_{\mathrm{g}}}{a}\frac{1}{j^2}\Omega_{\mathrm{Kep}}(a), \tag{3.B.1}$$

where I introduced the (fast) Keplerian frequency, $\Omega_{\mathrm{Kep}}(a)$, in eq. (3.1.1), as well as the gravitational radius $r_{\mathrm{g}} = GM_\bullet/c^2$. In practice, this precession is said to be prograde as one always has $\Omega_{\mathrm{GR}}(a,j) > 0$. The gravitational radius allows me to introduce a maximal eccentricity

$$j_{\mathrm{lc}}(a) = 4\sqrt{r_{\mathrm{g}}/a}, \tag{3.B.2}$$

so that wires with $j \leq j_{\mathrm{lc}}(a)$ are assumed to be within the loss cone (Merritt, 2013), and as such are unavoidably absorbed by the central BH.

In order to compute $\Omega_\star(a,j)$, I assume that the stellar cluster follows an infinite power-law distribution of the form $M(<a) \propto a^{3-\gamma}$, where $M(<a)$ stands for the total stellar mass physically enclosed within the radius a (see section 3.4.1). In that limit, following appendix A of Kocsis & Tremaine (2015), the mass precession frequency reads

$$\Omega_\star(a,j) = \overline{\Omega}_\star(a)\, h_{\mathrm{M}}(j), \tag{3.B.3}$$

where the dimensional dependence w.r.t. a is captured by

$$\overline{\Omega}_\star(a) = \Omega_{\mathrm{Kep}}(a)\,\frac{M(<a)}{M_\bullet}, \tag{3.B.4}$$

while the dimensionless eccentricity dependence is given by

$$h_{\mathrm{M}}(j) = \frac{j^{4-\gamma}}{1-j^2}\left[P_{1-\gamma}(1/j) - \frac{1}{j}P_{2-\gamma}(1/j)\right], \tag{3.B.5}$$

with P_α the Legendre function of order α. In practice, near the edge $j=1$, I note that $h_{\mathrm{M}}(j)$ can be advantageously replaced with its Taylor expansion

$$h_{\mathrm{M}}(j) \simeq \tfrac{1}{2}(-3+\gamma) - \tfrac{1}{8}(-12+\gamma+4\gamma^2-\gamma^3)(1-j), \tag{3.B.6}$$

to avoid singularities.

Importantly, note that the function $h_{\mathrm{M}}(j)$ is always negative for $\gamma < 3$. Indeed, following eq. (A2) of Kocsis & Tremaine (2015), I can rewrite eq. (3.B.5) with the alternative integral form

$$\begin{aligned} h_{\mathrm{M}}(j) &= \frac{j^{2(3-\gamma)}}{\pi\sqrt{1-j^2}}\int_0^\pi \mathrm{d}\psi\, \frac{\cos\psi}{(1+e\cos\psi)^{3-\gamma}} \\ &= \frac{j^{2(3-\gamma)}}{\pi\sqrt{1-j^2}}\int_0^{\pi/2} \mathrm{d}\psi\, \cos\psi\left(\frac{1}{(1+e\cos\psi)^{3-\gamma}} - \frac{1}{(1-e\cos\psi)^{3-\gamma}}\right), \end{aligned} \tag{3.B.7}$$

which is explicitly negative for any potential satisfying $3-\gamma > 0$. As a consequence, the mass precession is generically retrograde, i.e. one has $\Omega_\star(a,j) \leq 0$.

Now, in order to compute the resonant diffusion coefficients from eq. (3.3.4), I must solve the resonance condition from eq. (3.3.5). For a given wire (a,j), and a given resonance pair (k,k'), this involves characterising all the wires (a',j') such that $k'\Omega_{\mathrm{P}}(a',j') = k\Omega_{\mathrm{P}}(a,j)$, i.e. identifying the appropriate level lines in Fig. 3.3.1.

Let me briefly detail my implementation for the search of the resonant lines. Here, the key remark is to note that, following eqs. (3.B.1) and (3.B.5), I always have $\partial\Omega_{\mathrm{P}}/\partial j < 0$. As a consequence, for a given value of a', it is straightforward to determine whether or not there exists a j', with $j_{\mathrm{lc}}(a') \leq j' \leq 1$, and $k'\Omega_{\mathrm{P}}(a',j') = k\Omega_{\mathrm{P}}(a,j)$. Using this approach, I may then identify a domain $a'_{\mathrm{min}} \leq a' \leq a'_{\mathrm{max}}$, within which the resonance condition can be satisfied, by solving appropriately the resonance conditions along the critical lines $j = j_{\mathrm{lc}}(a)$ as well as along $j = 1$. At this stage, I also enforce that $16\, r_{\mathrm{g}} \leq a'_{\mathrm{min}}$ (see eq. 3.B.2) as well as $a'_{\mathrm{max}} \leq r_{\mathrm{h}}$, with r_{h} the considered influence radius (e.g., $r_{\mathrm{h}} = 2\mathrm{pc}$ for $\mathrm{Sgr\ A}^{\star}$), to ensure that I limit myself only to meaningful resonant regions of orbital space.

Once the range $[a'_{\mathrm{min}}, a'_{\mathrm{max}}]$ has been determined, to emphasise the system's partial scale-invariance, I sample this domain of smas linearly in $\log$-space, using $K_{\mathrm{res}} = 100$ points. Finally, for a given value a' such that $a'_{\mathrm{min}} \leq a' \leq a'_{\mathrm{max}}$, the associated resonant value j' is directly obtained by bisection. For models with $\gamma < 1.5$, it may happen that $a \mapsto \Omega_{\mathrm{P}}(a,j)$ is not monotonic anymore for j close to 1 (circular orbit), leading to the appearance of a second range of smas over which the resonance condition is satisfied. When this is the case, I accordingly sample this domain using the same method.

Chapter 4

Core collapse of anisotropic spheres

The work presented in this chapter is based on Tep et al. (2022).

4.1 Introduction

Understanding the long-term evolution of globular clusters is a long-standing problem in stellar dynamics (Hénon, 1961; Harris & Racine, 1979; Spitzer, 1987). Not only is the dynamics of globular clusters (Fig. 4.1.1) interesting per se (see, e.g., Lightman & Shapiro, 1978; Harris, 1991; Meylan & Heggie, 1997; Brodie & Strader, 2006), but it is also the archetype for the relaxation of a (weakly) collisional self-gravitating system with a simple integrable configuration (see, e.g., Chavanis, 2013a, for a review). Historically, their study is often done under a set of very crude approximations, including in particular isotropy, spherical symmetry and lack of rotation. In Chandrasekhar (1943)'s picture, the velocity of a given test star undergoes a series of weak, local, and uncorrelated kicks from each field star it encounters, a process that I coined NR theory (see section 2.3.2). Once these deflections accumulated along the stars' underlying unperturbed orbits, the NR theory yields the classical picture for long-term relaxation in spherical clusters (Heggie & Hut, 2003). In practice, the NR theory is straightforward to implement for isotropic clusters and has been extensively used to describe their long-term evolution (see, e.g., Vasiliev, 2015, for a review). This approach was recently generalised via the (inhomogeneous) Balescu–Lenard equation (Heyvaerts, 2010; Chavanis, 2012) to account for gravitational wakes and large-scale resonances within globular clusters (Hamilton et al., 2018; Fouvry et al., 2021). Overall these non-local effects were, somewhat surprisingly, found to be of small importance for such isotropic spheres.

However, with the development of more realistic numerical simulations, as well as detailed observations, it has become apparent that the dynamical evolution of collisional systems can be affected by anisotropy (Baumgardt et al., 2004), which may be both evolutionary or primordial (Vesperini et al., 2014), and rotation (see, e.g., Hachisu, 1979). In addition, anisotropy can be naturally generated by a star cluster's evolution (Hénon, 1971; Spitzer & Shapiro, 1972), with the formation of an isotropic core and an anisotropic stellar halo (see, e.g., Breen et al., 2017, for further references). Afternatively, Longaretti & Lagoute (1997), Kim et al. (2008) and Hong et al. (2013) studied the impact of rotation on globular clusters using N-body simulations and Fokker–Planck models. They concluded that core collapse was accelerated in clusters with a non-zero total angular momentum. This phenomenon, analogous to the *gravothermal catastrophe* of non-rotating globular clusters, is known as the *gravo-gyro catastrophe*. I will discuss this

Figure 4.1.1: Photography of the heart of the globular cluster NGC 6638, taken by the HST. Globular clusters contain hundreds of thousands of stars held together tightly by gravity in a very small region of order $1\mathrm{pc}^3$. One can observe a high concentration of stars in that region.

phenomenon in more details in chapter 5.

As one moves away from isotropy, one could expect that more coherent motions within the cluster could affect its long-term evolution. In this chapter, I wish to quantify the extent to which the NR theory still applies for such systems. For non-rotating, but anisotropic clusters, Hénon (1973) devised an orbit-averaged Fokker–Planck equation to integrate self-consistently the evolution of a spherical star cluster. In that approach, the velocity diffusion coefficients are computed using a pseudo-isotropic distribution function: at a fixed radius, the test star is scattered by a locally isotropic background of perturbers. This approach was further refined in the Fokker–Planck simulations of Drukier et al. (1999) to carefully treat the effects of velocity-space anisotropy. More recently, Breen et al. (2017) used direct N-body simulations to investigate the relaxation of isolated equal-mass star clusters, primarily focusing on the effects of primordial velocity anisotropies. Interestingly, core collapse is found to be swifter as the model becomes more and more tangentially anisotropic. This can be probed by following the evolution of the core radius R_c (Fig. 4.1.2), defined by

$$R_\mathrm{c}^2 = \sum_{i=1}^{N} \rho_i^2 \boldsymbol{r}_i^2 \bigg/ \sum_{i=1}^{N} \rho_i^2, \tag{4.1.1}$$

where ρ_i is the stellar density at the position $\boldsymbol{r}_i$ of the star i.

In this chapter, I will apply the NR formalism presented in chapter 2 to spherically symmetric, anisotropic isolated globular clusters. I will be faced with a few new difficulties to overcome in order to numerically compute the rate of orbital diffusion. First, I will describe the Plummer cluster in section 4.2 and detail the computation of the useful orbital parameters in section 4.3. Then, I will perform a series of N-body simulations in section 4.4 and solve various technicali-

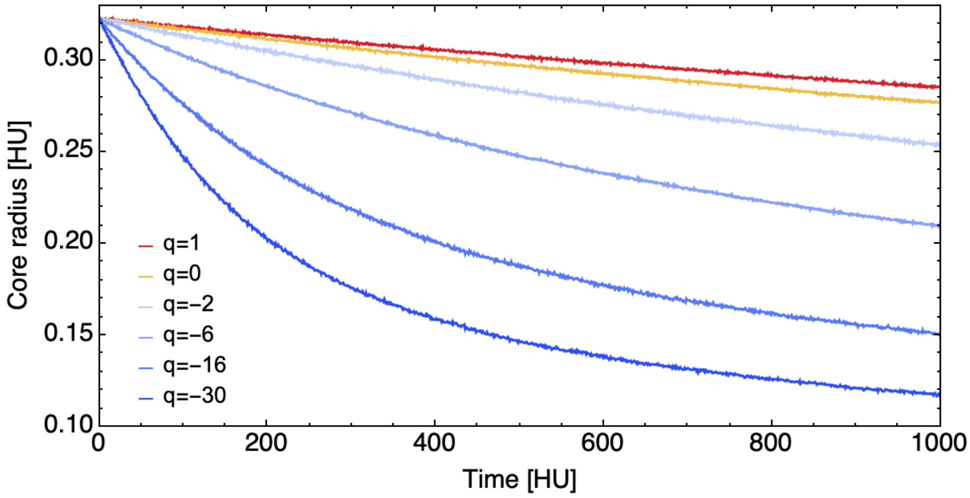

Figure 4.1.2: Ensemble-averaged evolution of the cluster's core radius (eq. 4.1.1) as a function of time from direct N-body simulations, where I varied the anisotropy parameter q (present in the DF , see eq. 4.2.3). Larger negative values of q, i.e. more tangentially anisotropic clusters, are unambiguously associated with a faster initial evolution.

ties arising from their treatment. I will also compute in section 4.5 the NR prediction for the rate of orbital diffusion. To achieve this goal, I will define a well-chosen anomaly to perform a numerically stable orbit-averaging and compute the NR diffusion rate in an action space tailored for this self-gravitating system. When compared to the N-body measurements, I will show how the two predictions match relatively well, up to some limits that I shall discuss in section 4.5.3. In addition, in section 4.6, I will compare the fully anisotropic prediction to a *pseudo-isotropic* prediction proposed by Cohn (1979), and show the limitations of this approach. Finally, I will explore the links between the RR and the NR approximations in section 4.7, and discuss the physical meaning of the *Coulomb logarithm*.

4.2 The Plummer cluster

Various models have been used to model globular clusters (see, e.g., King, 1966; Wilson, 1975). In my work, I will use the Plummer model (Plummer, 1911), which was shown in the past to provide a good match to observations. Even though better suited models have been used since then (see, e.g., Bertin & Varri, 2008; Webb et al., 2023), the Plummer model retains a theoretical interest. As will be apparent later on, it will allow me to compute numerically stable predictions for the NR theory, by allowing for numerous analytical formulae.

The gravitational potential of the Plummer model reads

$$\psi(r) = -\frac{GM}{\sqrt{r^2+b^2}}, \tag{4.2.1}$$

with M the cluster's total mass and b the Plummer scale radius. In the following, if not specified, I will use physical units, so that $G = M = b = 1$. I consider a cluster composed of $N = 10^5$ stars. Following Giersz & Heggie (1994), the value of the Coulomb logarithm is set to $\ln\Lambda = \ln(0.11\,N)$ (see chapter 2).

One of the main difficulties of the NR theory is to obtain the DF associated with the potential $\psi(r)$. For an isotropic cluster, this can be done by using Eddington's inversion (Eddington, 1916). The analytical computation yields the unique associated isotropic DF

$$F_{\mathrm{tot}}(E) = \frac{3}{7\pi^3} \frac{M}{(GMb)^{3/2}} (2\widetilde{E})^{7/2}, \tag{4.2.2}$$

where $\widetilde{E} = -bE/(GM) = E/E_0$ is a reduced energy. However, for anisotropic clusters, the inversion is more challenging. In my work, I will consider the family of DFs derived by Dejonghe (1987). They read

$$F_{\mathrm{tot}}(E, L; q) = \frac{M}{L_0^3} \frac{3\,\Gamma(6-q)\,\widetilde{E}^{7/2-q}}{2(2\pi)^{5/2}}\, \mathbb{H}_q\!\left(\frac{\widetilde{L}^2}{2\widetilde{E}}\right), \tag{4.2.3}$$

where q controls the flavour and degree of anisotropy in the cluster (see Fig. 4.2.1) and I introduced a reduced angular momentum $\widetilde{L} = L/\sqrt{GMb} = L/L_0$. This parametrisation allows me to study all types of anisotropies (from radial $q > 0$ to tangential $q < 0$) by simply varying the continuous parameter q, as shown by the anisotropy parameter (Fig. 4.2.1) defined by (Breen et al., 2017)

$$\beta(r) = 1 - \frac{\sigma_{\mathrm{t}}^2}{2\sigma_{\mathrm{r}}^2} = \frac{q}{2} \frac{r^2}{r^2 + b^2}. \tag{4.2.4}$$

While Plummer clusters are always isotropic at their centre, their velocity anisotropy is felt as one gets further away from it. I also introduced the function

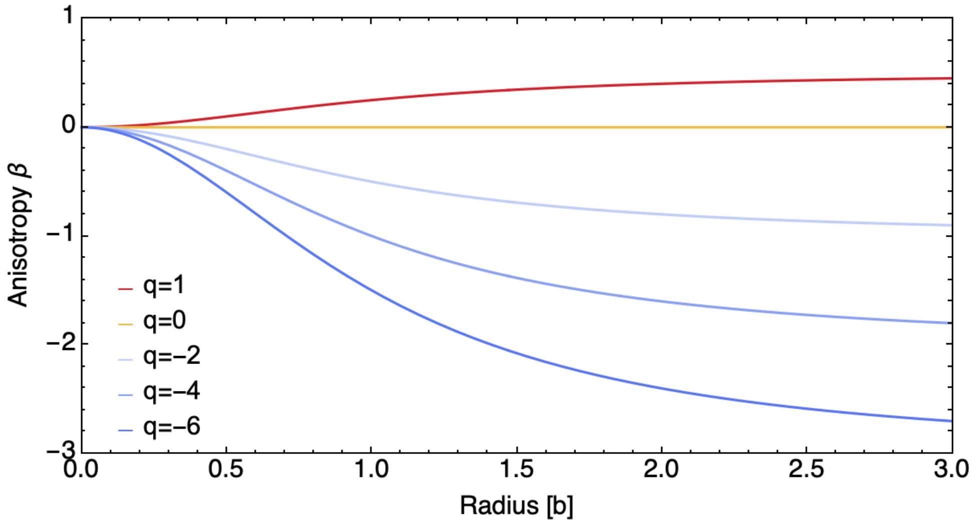

Figure 4.2.1: Anisotropy parameter $\beta(r)$ (eq. 4.2.4) of the considered equilibrium DFs as a function of the radius, in physical units $b = 1$. Here, $q = 0$ stands for the isotropic equilibrium while $q < 0$ (resp. $q > 0$) are tangentially (resp. radially) anisotropic equilibria. Plummer clusters are isotropic in their centre, and velocity anisotropy begins to appear as one gets away from it. If a cluster is more anisotropic, then its anisotropy will be felt closer to the centre.

$$\mathbb{H}_q(x) = \begin{cases} \dfrac{{}_2F_1(\frac{1}{2}q, q-\frac{7}{2}, 1; x)}{\Gamma(\frac{9}{2}-q)} & \text{if } x \leq 1, \\[2ex] \dfrac{{}_2F_1(\frac{1}{2}q, \frac{1}{2}q, \frac{1}{2}(9-q); 1/x)}{\Gamma(1-\frac{1}{2}q)\Gamma(\frac{1}{2}(9-q))} \dfrac{1}{x^{q/2}} & \text{if } x \geq 1, \end{cases} \tag{4.2.5}$$

with ${}_2F_1$ the hypergeometric function and Γ the Gamma function. In Fig. 4.2.2, I illustrate the reduced DF, $F = \int \mathrm{d}L_z\, F_{\mathrm{tot}} = 2LF_{\mathrm{tot}}$, in action space for various anisotropies.

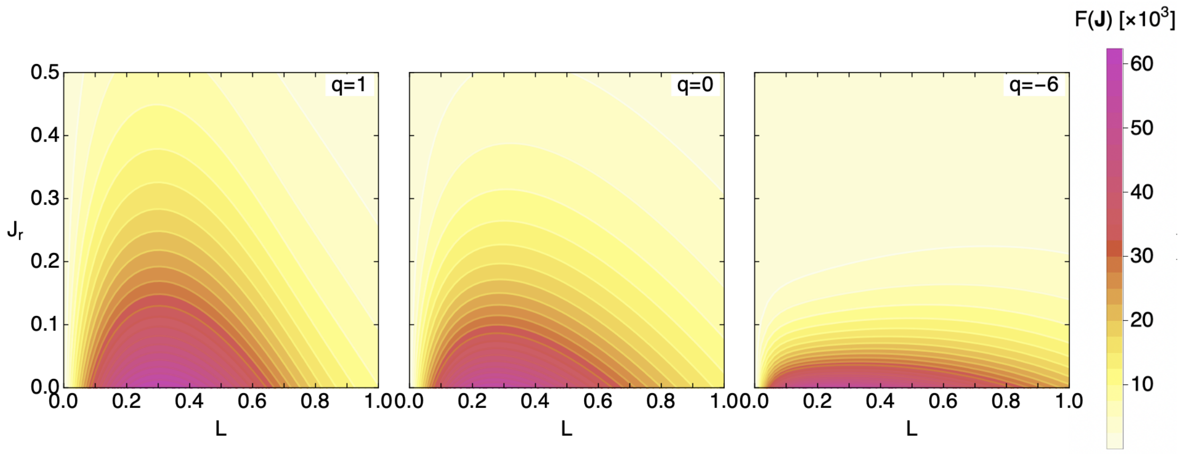

Figure 4.2.2: Illustration of the reduced DF, $F = 2LF_{\rm tot}$, for a radially anisotropic distribution ($q = 1$, left), an isotropic one ($q = 0$, middle), and a tangentially anisotropic one ($q = -6$, right). The radially (resp. tangentially) anisotropic DF shows a higher concentration of radial (resp. tangential) orbits, i.e. orbits with small L (resp. small $J_{\rm r}$).

4.3 Computing the orbital parameters

Before turning to the study of any NR prediction (section 2.3.3) or N-body measurement, let me present in this section the relevant orbital parameters. Indeed, the velocity diffusion coefficients are functions of the local parameters r, v_r and $v_{\rm t}$ (eqs. 2.3.31 and 2.3.32). The Fokker–Planck equation is also a function of the integrals of motion $J_{\rm r}$ and L (eq. 2.3.34). Thus, I need to relate these two sets of parameters.

4.3.1 Position-velocity space to/from energy-angular momentum space

Let me consider a bound orbit with energy $E < 0$ and angular momentum L. Its radial motion is given by the conservation equation

$$E = \psi(r) + \frac{v_r^2}{2} + \frac{L^2}{2r^2}, \tag{4.3.1}$$

where its radius r is contained between its boundaries – pericentre and apocentre $r_{\rm p}, r_{\rm a}$ – set by $v_r = 0$. Now, define the radial coordinate s through the relation $s^2 = 1 + (r/b)^2$. Equation (4.3.1) can be easily expressed w.r.t. the s-coordinate, whose inverse is given by $r^2 = b^2(s^2 - 1)$. Therefore, it is equivalent to look for the s-boundaries $(s_{\rm p}, s_{\rm a})$, which are solution to the equation of conservation

$$E = \frac{E_0}{s} + \frac{L^2}{2b^2(s^2 - 1)}. \tag{4.3.2}$$

Equation (4.3.2) is equivalent to the polynomial equation

$$\widetilde{E}s^3 - s^2 + \left(\frac{\widetilde{L}^2}{2} - \widetilde{E}\right)s + 1 = 0. \tag{4.3.3}$$

The two roots can then be found by bisection. Additionally, I can compute analytically the value of the circular angular momentum $L_{\rm c}(E)$. This is done in appendix 4.B. It is then straightforward to recover (E,L) from $(r_\mathrm{p},r_\mathrm{a})$ (Lynden-Bell, 2015)

$$E = \frac{r_\mathrm{p}^2\psi(r_\mathrm{p}) - r_\mathrm{a}^2\psi(r_\mathrm{a})}{r_\mathrm{p}^2 - r_\mathrm{a}^2} \quad ; \quad L = \sqrt{\frac{2(\psi[r_\mathrm{a}] - \psi[r_\mathrm{p}])}{r_\mathrm{p}^{-2} - r_\mathrm{a}^{-2}}}, \tag{4.3.4}$$

which in the specific case of a Plummer sphere can be simplified into the expressions

$$E = \frac{E_0}{s_\mathrm{p}} + \frac{E_0(s_\mathrm{a}^2-1)}{s_\mathrm{a}s_\mathrm{p}(s_\mathrm{a}+s_\mathrm{p})} \quad ; \quad L = L_0\sqrt{\frac{2(s_\mathrm{p}^2-1)(s_\mathrm{a}^2-1)}{s_\mathrm{a}s_\mathrm{p}(s_\mathrm{a}+s_\mathrm{p})}}. \tag{4.3.5}$$

These two expressions are well-posed and numerically stable, even for circular and/or radial orbits.

4.3.2 Energy-angular momentum space to/from action space

Computing the radial action is straightforward for any spherically symmetric potential. In practice, it can be rewritten in terms of an effective anomaly u

$$J_\mathrm{r}(E,L) = \frac{1}{\pi}\int_{r_\mathrm{p}}^{r_\mathrm{a}} \mathrm{d}r\, v_r = \frac{1}{\pi}\int_{r_\mathrm{p}}^{r_\mathrm{a}} \frac{\mathrm{d}r}{v_r}\, v_r^2 = \frac{1}{\pi}\int_{-1}^{1} \mathrm{d}u\, \Theta(u)\, v_r^2(r[u]), \tag{4.3.6}$$

where $v_r^2(r) = 2(E-\psi[r]) - L^2/r^2$ and $\Theta(u) = (\mathrm{d}r/\mathrm{d}u)(1/v_r)$ is the Jacobian of the change of variables $r \mapsto u$ (computed explicitly in eq. 4.5.1 for the Plummer cluster). However, the computation of the derivatives of J_r w.r.t. E and L is more subtle. One can write

$$\frac{\partial J_\mathrm{r}}{\partial E} = \frac{1}{\pi}\int_{r_\mathrm{p}}^{r_\mathrm{a}} \frac{\mathrm{d}r}{v_r} = \frac{1}{\pi}\int_{-1}^{1} \mathrm{d}u\, \Theta(u), \tag{4.3.7a}$$

$$\frac{\partial J_\mathrm{r}}{\partial L} = -\frac{L}{\pi}\int_{r_\mathrm{p}}^{r_\mathrm{a}} \frac{\mathrm{d}r}{r^2 v_r} = -\frac{L}{\pi}\int_{-1}^{1} \mathrm{d}u\, \frac{\Theta(u)}{r^2(u)}. \tag{4.3.7b}$$

While the first expression is well-defined for any kind of orbits, the second one appears to be ill-defined for radial orbits, though one can infer that it tends to $-1/2$ when $L \to 0^+$ (Binney & Tremaine, 2008). For this reason, I must take extra care when computing the L-derivative – even with the effective anomaly – by using a particular integration scheme when L is too close to 0 (see appendix 4.C for more details).

Taking the second derivative within the integral is – in both cases – not possible for the radial expression of eqs. (4.3.7), because the derivative of the integrand is not integrable. However, using the effective anomaly makes it possible to differentiate the integrand and still obtain an integrable expression (see appendix 4.C).

Now, it remains to invert the transformation $(E,L) \mapsto (J_\mathrm{r},L)$. This is done using a bisection method with some restrictions to stay within the authorised (E,L) region (see appendix 4.A).

4.4 N-body simulations

I performed the numerical simulations presented throughout this chapter using the direct N-body code `NBODY6++GPU` (Wang et al., 2015), version 4.1. The initial conditions I used for the anisotropic Plummer spheres (see eq. 4.2.3 and Fig. 4.2.2) were generated from `PlummerPlus.py` (Breen et al., 2017), while I used the same input file as in appendix H1 of Fouvry et al. (2021).

q	1	0	-6	-16	-30
N_{run}	100	100	100	50	50
$t_{\mathrm{last}}\,[\mathrm{HU}]$	1000	1000	100	100	100
$(N_{J_{\mathrm{r}}}, N_L)$	(20,15)	(20,20)	(20,20)	(70,70)	(70,70)
$(J_{\mathrm{r}}^{\mathrm{min}}, J_{\mathrm{r}}^{\mathrm{max}})$	(0, 0.55)	(0, 0.55)	(0, 0.6)	(0, 0.6)	(0, 0.6)
$(L^{\mathrm{min}}, L^{\mathrm{max}})$	(0,1.05)	(0,1.05)	(0,1.1)	(0,1.1)	(0,1.1)

Table 4.1: Detailed parameters for the N-body simulations and the associated binning of action space. Following eq. (4.4.12), I bin the $\boldsymbol{J} = (J_{\mathrm{r}}, L)$ action space in $N_{J_{\mathrm{r}}} \times N_L$ uniform bins within the domain $J_{\mathrm{r}}^{\mathrm{min}} \leq J_{\mathrm{r}} \leq J_{\mathrm{r}}^{\mathrm{max}}$ (similarly for L). All quantities are in physical units $G = M = b = 1$ if not stated otherwise.

Internally, `NBODY6++GPU` uses Hénon units (HU) (Hénon, 1971), defined such that the physical constants are set to $G = M = R_{\mathrm{v}} = 1\,\mathrm{HU}$, with R_{v} the cluster's virial radius.

For the Plummer potential from eq. (4.2.1), one readily finds $R_{\mathrm{v}}/b = 16/(3\pi)$ (see, e.g., tab. 1 p. 81 in Heggie & Hut, 2003). Each N-body realisation is composed of $N = 10^5$ stars and integrated up to $t_{\mathrm{max}} = 1\,000\,\mathrm{HU}$ with a dump every $\Delta t = 1\,\mathrm{HU}$. On a 40-core node with a single V100 GPU, one simulation typically required $\sim 24\,\mathrm{h}$ of computation. In practice, I consider anisotropies set by $q = 1, 0, -6, -16, -30$ and, depending on the values of q, performed either $N_{\mathrm{run}} = 50, 100$ independent realisations, as spelled out in Tab. 4.1. This was made possible thanks to my continuous access to the Infinity cluster which hosts seven such GPUs. In the end, it allowed me to compare the ensemble averaged kinetic theory to the ensemble average of N_{run} simulations.

4.4.1 Finding the cluster's centre

N-body simulations give me access to the time evolution of a self-gravitating system. However, various technical difficulties come with their analysis. In this chapter, I am interested in the evolution of the DF in action space. Therefore, I need to compute the radial action J_{r} and the angular momentum L of every star. These quantities require the computation of the instantaneous potential of the system $\psi(r)$, as well as the positions and velocities $(\boldsymbol{r}, \boldsymbol{v})$ of every star.

In practice, I need to define a frame to compute the numerical values of the position-velocities of the stars. The computation of $\psi(r)$ supposes that I have set this frame so that $\boldsymbol{r} = 0$ is at the centre of the cluster. In addition, I also need to centre the velocity of the cluster, which is trivially done by subtracting from the velocity the barycentre velocity.

Therefore, I must centre the cluster. Because I expect that the centre of the cluster should correspond the location with maximum density, I must build an estimator biased by star density. Following Casertano & Hut (1985), let me first define a density estimator. Consider a star in the cluster. I label "1" its nearest neighbour, "2" its second nearest, ..., k its k-th nearest, and so on (see Fig. 4.4.1). I let r_k be the distance between star k and the considered star. Then, the enclosed volume up to star k is given by $V(r_k) = 4\pi r_k^3/3$. I can now define the *density estimator of order k*

$$\rho_k = \frac{k-1}{V(r_k)} m. \tag{4.4.1}$$

It can be shown that $\langle \rho_k \rangle(\boldsymbol{r}) = \rho(\boldsymbol{r})$, and that this estimator is unbiased (Casertano & Hut, 1985). The average is to be understood in the sense that this estimator gets better as one increases the number of stars N. On the one hand, increasing the number of neighbours k reduces fluctu-

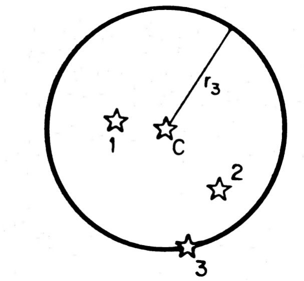

Figure 4.4.1: From fig. 3 of Casertano & Hut (1985). Representation of the sphere used in the local density estimator. The centre C might or might not coincide with a star. Distance to the third-nearest neighbour of C defines here the radius of the sphere.

ations. On the other hand, in order to retain locality, k should not be too large w.r.t. N. The compromise that is usually taken is the value $k = 6$. Using this estimator, I can now define the *density centre*

$$\boldsymbol{r}_{\mathrm{d}} = \sum_{i=1}^{N} \boldsymbol{r}_i \rho_k^{(i)} \bigg/ \sum_{i=1}^{N} \rho_k^{(i)}, \tag{4.4.2}$$

where $\rho_k^{(i)}$ is the density estimator of order k for the i^{th} star. In order to centre the positions of the cluster, I can now subtract the density centre from the stars' positions.

4.4.2 Evolution of the potential

In Fig. 4.4.2, I represent the *sphericality* for a variety of anisotropic clusters w.r.t. time. As detailed in appendix 4.D, this quantity is the ratio between the eigenvalues of an inertia-like tensor, and therefore is used to probe how spherical the cluster is. In particular, the closer it is to 1, the more spherical the cluster is. Using these properties, Fig. 4.4.2 shows that the systems stay spherically symmetric. Therefore, I can assume that the density and the gravitational potential depend only on radius. In particular, these two quantities are related through the relation

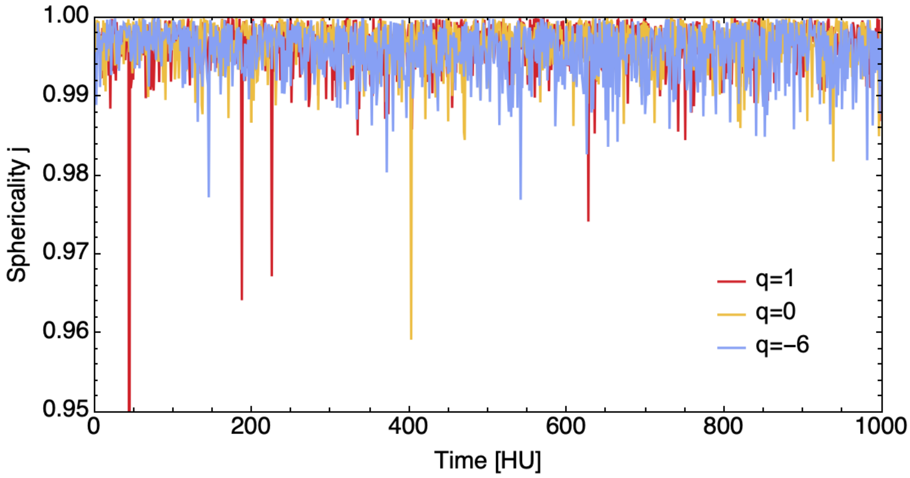

Figure 4.4.2: Time dependence of the cluster sphericality j for various anisotropies. As detailed in appendix 4.D, the closer to 1 the sphericality, the more spherical the cluster is. The typical value of j is ~ 0.996, i.e. the clusters stay close to spherical symmetry throughout their relaxation.

(Hénon, 1971)

$$\psi(r,t) = -4\pi G \int_0^{\infty} \mathrm{d}r' \, \frac{r'^2 \rho(r',t)}{\max(r,r')} = -\frac{GM(<r)}{r} - 4\pi G \int_r^{\infty} \mathrm{d}r' \, r' \rho(r',t), \tag{4.4.3}$$

where $M(<r)$ is the mass within the sphere of radius r. For a discrete system of N stars of individual mass $m = M/N$, its instantaneous radial mass density is given by

$$n(r) = \sum_{i=1}^{N} m_i \delta_{\mathrm{D}}(r - r_i), \tag{4.4.4}$$

where the i^{th} particle is at radius r_i and has mass m_i and I have ordered the particle radii $r_1 \leq r_2 \leq ... \leq r_N$. Therefore, for $r_k \leq r < r_{k+1}$, I have

$$\psi(r) = G\bigg(-\frac{1}{r} \sum_{i=1}^{k} m_i - \sum_{i=k+1}^{N} \frac{m_i}{r_i} \bigg), \tag{4.4.5}$$

with the conventions $r_0 = 0$ and $r_{N+1} = \infty$. This formula allows me to compute the potential by recursion (Fig. 4.4.3) using the formulae (Hénon, 1971)

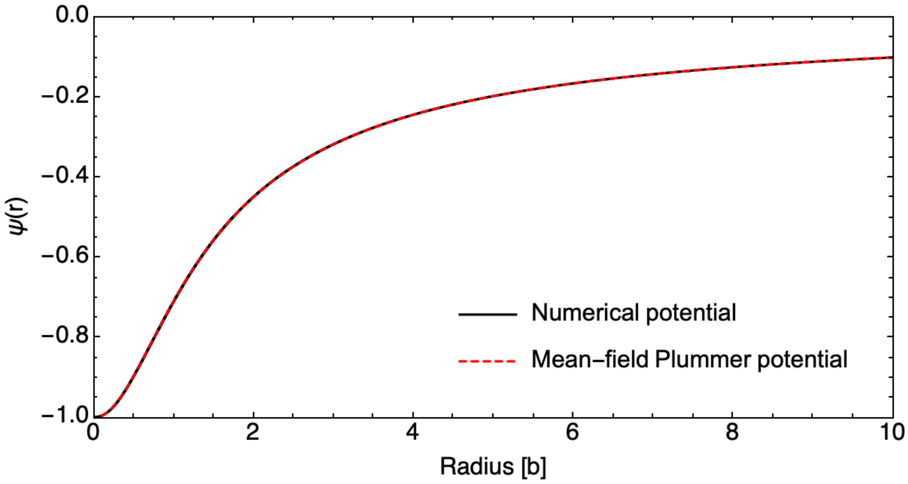

Figure 4.4.3: Comparison between the mean field Plummer potential $\psi(r)$ as given by eq. (4.2.1) (full black line) to the numerical reconstruction of its N-body realisation (dashed red line) at the initial time for a single realisation. The reconstruction of the potential is in close agreement with the theoretical value.

$$\begin{cases} \psi_{N+1} &= 0, \\ M_N &= M, \end{cases} \qquad \begin{cases} \psi_k &= \psi_{k+1} - GM_k(1/r_k - 1/r_{k+1}), \\ M_{k-1} &= M_k - m_k, \end{cases} \tag{4.4.6}$$

where ψ_k is the potential at r_k, $M_k = M(\leq r_k)$ the mass within the sphere of radius r_k. It follows that the potential is given by

$$\psi(r) = \psi_k + \frac{1/r_k - 1/r}{1/r_k - 1/r_{k+1}} (\psi_{k+1} - \psi_k), \tag{4.4.7}$$

where $r_k < r \leq r_{k+1}$.

4.4.3 Computing the simulation's actions

Now that I can evaluate the cluster's potential $\psi(r)$ at any time, I can compute the stars' orbital parameters to study their evolution. Let me consider a star with the (centred) position $\boldsymbol{r}$ and velocity $\boldsymbol{v}$. Its energy is given by $E = \psi(r) + v^2/2$ and the norm of its angular momentum is given by $L = |\boldsymbol{r} \times \boldsymbol{v}|$. In order to determine the bounds of its radial motion, I must solve the radial equation

$$E = \psi(r) + \frac{L^2}{r^2}. \tag{4.4.8}$$

This has two solutions r_{p} and r_{a} (see section 4.3.1). I can compute the radial actions with the expression

$$J_{\mathrm{r}} = \int_{r_{\mathrm{p}}}^{r_{\mathrm{a}}} \mathrm{d}r' \, \sqrt{2(E - \psi[r']) - L^2/r'^2}. \tag{4.4.9}$$

Finally, I can estimate the discrete DF in action space of one simulation by taking

$$F_{\mathrm{d}}(\boldsymbol{J}, t) = \frac{M n(\boldsymbol{J}, t)}{(2\pi)^3 \delta J_{\mathrm{r}} \delta L}. \tag{4.4.10}$$

Here, I defined δJ_{r} the size of the J_{r} bins and δL the size of the L, while the star number density is given by

$$n(\boldsymbol{J}, t) = \frac{\text{stars in } [J_{\mathrm{r}} - \frac{1}{2}\delta J_{\mathrm{r}}, J_{\mathrm{r}} + \frac{1}{2}\delta J_{\mathrm{r}}] \times [L - \frac{1}{2}\delta L, L + \frac{1}{2}\delta L]}{\text{total number of bound stars}}. \tag{4.4.11}$$

Then, I estimate the time derivative via

$$\frac{\partial F_{\mathrm{d}}}{\partial t}(\boldsymbol{J}, t = 0) \simeq \frac{F_{\mathrm{d}}(\boldsymbol{J}, t_{\mathrm{last}}) - F_{\mathrm{d}}(\boldsymbol{J}, t = 0)}{t_{\mathrm{last}}}. \tag{4.4.12}$$

Increasing the number of realisations and averaging over them, I can estimate the DF by using the discrete one, since the ensemble average obeys $\langle F_{\mathrm{d}} \rangle = F$.

4.5 Non-resonant relaxation

As a result of the cluster's finite number of constituents, a given test star of mass m and velocity $\boldsymbol{v}$, embedded in such a noisy environment will irreversibly see its velocity diffuse. This long-term relaxation is driven by pairwise encounters, which I called NR theory in section 2.3.2. Both assumptions (local and uncorrelated encounters) used in the NR theory are strictly speaking not satisfied, as can be seen within the RR framework (section 2.3.1). It turns out to be nonetheless a fairly good approximation in practice.

4.5.1 Orbit averaging and diffusion coefficients

Assuming that the deflection is local and following section 2.3.2, the test star's velocity will locally diffuse according to the first- and second-order velocity diffusion coefficients given by eqs. (2.3.17). While fully generic, eqs. (2.3.17) are typically further simplified by assuming spherical symmetry and a locally isotropic velocity distribution (see, e.g., Hénon, 1958). In that limit, one imposes $F_{\mathrm{tot}}(\boldsymbol{r}, \boldsymbol{v}) = F_{\mathrm{tot}}(r, v)$, with $v = |\boldsymbol{v}|$, $r = |\boldsymbol{r}|$, and all the integrals from eq. (2.3.17) become one-dimensional. In this chapter, following section 2.3.3, I will consider the fully anisotropic case. This will allow me to compute a theoretical prediction of the relaxation in anisotropic Plummer spheres.

Because I consider a system without rotation, the angle-dependency in eq. (2.3.21) can be integrated over, and I am left with an average over the radial motion of the form

$$D_X(\boldsymbol{J}) = \frac{2}{T_r} \int_{r_\mathrm{p}}^{r_\mathrm{a}} \frac{\mathrm{d}r}{v_r} \langle \Delta X \rangle (r, \boldsymbol{J}). \tag{4.5.1}$$

Now, let me introduce an effective anomaly u in order to rewrite the orbit-average into the form

$$D_X(\boldsymbol{J}) = \frac{2}{T_r} \int_{-1}^{1} \mathrm{d}u \, \Theta(u, \boldsymbol{J}) \langle \Delta X \rangle (r[u, \boldsymbol{J}], \boldsymbol{J}), \tag{4.5.2}$$

where $r = r(u)$, $\Theta(u, \boldsymbol{J}) = (\mathrm{d}r/\mathrm{d}u)\, 1/v_r$ and T_r is the radial period. My motivation is the existence of such a nicely behaved anomaly in other types of stellar systems, including the Keplerian system or the isochrone cluster (Fouvry et al., 2021). Taking inspiration from Hénon (1971) and Fouvry et al. (2021), I chose an effective anomaly of the form $r(u) = b\sqrt{s^2(u) - 1}$, where

$$s(u) = a\big(1 + e f[u]\big), \quad \text{with} \quad f[u] = u\big(\tfrac{3}{2} - \tfrac{1}{2}u^2\big). \tag{4.5.3}$$

Here, I have defined an effective semi-major axis a and an effective eccentricity e by

$$a = \frac{s_\mathrm{a} + s_\mathrm{p}}{2}, \quad e = \frac{s_\mathrm{a} - s_\mathrm{p}}{s_\mathrm{a} + s_\mathrm{p}}. \tag{4.5.4}$$

I provide a way to compute the bounds $(s_\mathrm{p}, s_\mathrm{a})$ in section 4.3, along with other useful orbital parameters.

Using these formulae and feeding them into the $\Theta(u)$, I obtain after simplification

$$\boxed{\Theta(u) = \frac{\mathrm{d}r}{\mathrm{d}u}\frac{1}{v_r} = \frac{1}{\Omega_0}\frac{3}{4\sqrt{2}} \frac{\sqrt{s_\mathrm{a} s_\mathrm{p}(s_\mathrm{a} + s_\mathrm{p})}}{\sqrt{4 - u^2}} \frac{\mathcal{A}(u)^{3/2}}{\sqrt{s_\mathrm{a} s_\mathrm{p} \mathcal{A}(u) + \mathcal{B}(u)}},} \tag{4.5.5}$$

where I defined the frequency scale $\Omega_0 = \sqrt{GM/b^3}$ and the functions

$$\mathcal{A}(u) = s_\mathrm{p}(u+2)(u-1)^2 - s_\mathrm{a}(u-2)(u+1)^2, \tag{4.5.6a}$$
$$\mathcal{B}(u) = s_\mathrm{p}(u^3 - 3u + 6) - s_\mathrm{a}(u^3 - 3u - 6), \tag{4.5.6b}$$

which are always positive. Under this form, $\Theta(u)$ is not singular, and neither are the orbit-averaging integrands. Similarly, the radial half-period is now given by

$$\frac{T_r(\boldsymbol{J})}{2} = \int_{-1}^{1} \mathrm{d}u \, \Theta(u, \boldsymbol{J}). \tag{4.5.7}$$

Using this effective anomaly allows me to replace any expression involving $\mathrm{d}r/v_r$ with its regular counterpart $\mathrm{d}u\,\Theta(u)$. While the radial integrand (r-integral of eqs. 4.3.7) is not differentiable, the u-one is (u-integral of eqs. 4.3.7). This is important as it allows me to differentiate these expressions (see appendix 4.C).

4.5.2 Global relaxation

In this chapter, my goal is to investigate the impact of velocity anisotropy on a cluster's relaxation. Using direct N-body simulations, detailed in section 4.4, I illustrated this dependence in Fig. 4.1.2 with the evolution of the cluster's core radius as I vary q. As already pointed out

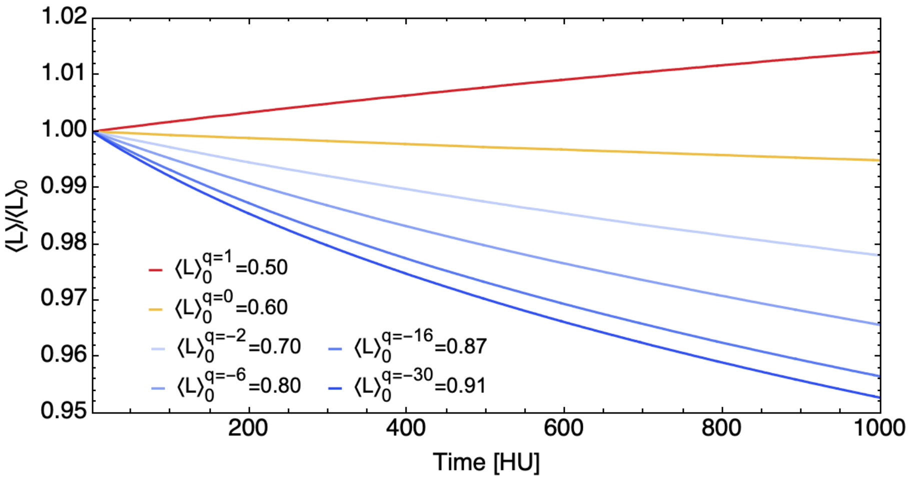

Figure 4.5.1: Ensemble-averaged evolution of the mean angular momentum norm, $\langle L\rangle$ (eq. 4.5.8), rescaled by its initial value $\langle L\rangle(0)$, as one varies the anisotropy parameter q, from N-body measurements. Clusters isotropise throughout their relaxation, i.e. $\langle L\rangle$ increases for radially anisotropic clusters and decreases for tangentially anisotropic ones. In addition, for $q<0$, the stronger the tangential anisotropy, the faster the initial isotropisation.

in Breen et al. (2017) (fig. 4 therein), the more tangentially anisotropic the cluster, the faster its initial contraction.

Using the same simulations, I also investigate the time evolution of the clusters' average angular momentum modulus

$$\langle L\rangle = \frac{(2\pi)^3}{M}\int \mathrm{d}\boldsymbol{J}\, L\, F(\boldsymbol{J}), \tag{4.5.8}$$

as illustrated in Fig. 4.5.1. Similarly to fig. 7 of Breen et al. (2017), I recover here that the clusters' relaxations drive them towards more isotropic distributions. Indeed, radially anisotropic clusters (i.e. $q>0$) see their average angular momentum grow, i.e. orbits become on average more circular, while tangentially anisotropic clusters (i.e. $q<0$) see their average angular momentum decrease, i.e. orbits become more radial. Finally, similarly to Fig. 4.1.2, I recover that the more tangentially anisotropic a cluster, the faster its initial isotropisation.

4.5.3 Diffusion rate

Let me now assess how well the anisotropic NR theory from section 2.3.3 can predict these trends. In the limit where nearby deflections drive the cluster's relaxation, its long-term evolution is governed by the Fokker–Planck eq. (2.3.38), which predicts the rate of change, $\partial F/\partial t$, in action space.

In Fig. 4.5.2, I compare the contours of $\partial F/\partial t$ as predicted by the anisotropic NR theory from eq. (2.3.34) with those measured in N-body simulations, for various initial velocity anisotropies. It is remarkable that the NR maps and the N-body measurements are so similar, up to an overall prefactor which appears to weakly depend on the considered actions. This prefactor reflects the fact that NR theory poorly accounts for far-away encounters, that only RR captures (see, e.g., Fouvry et al., 2021).

In order to better quantify the overall amount by which the NR prediction overestimates the

N-body prediction, I define the average ratio

$$\frac{\text{NR}}{N\text{-BODY}} = \frac{\displaystyle\int \mathrm{d}\boldsymbol{J}\, F(\boldsymbol{J})\, |\partial F/\partial t|_{\text{NR}}}{\displaystyle\int \mathrm{d}\boldsymbol{J}\, F(\boldsymbol{J})\, |\partial F/\partial t|_{N\text{-BODY}}}, \tag{4.5.9}$$

where the rates of change, $\partial F/\partial t$, are inferred from Fig. 4.5.2.

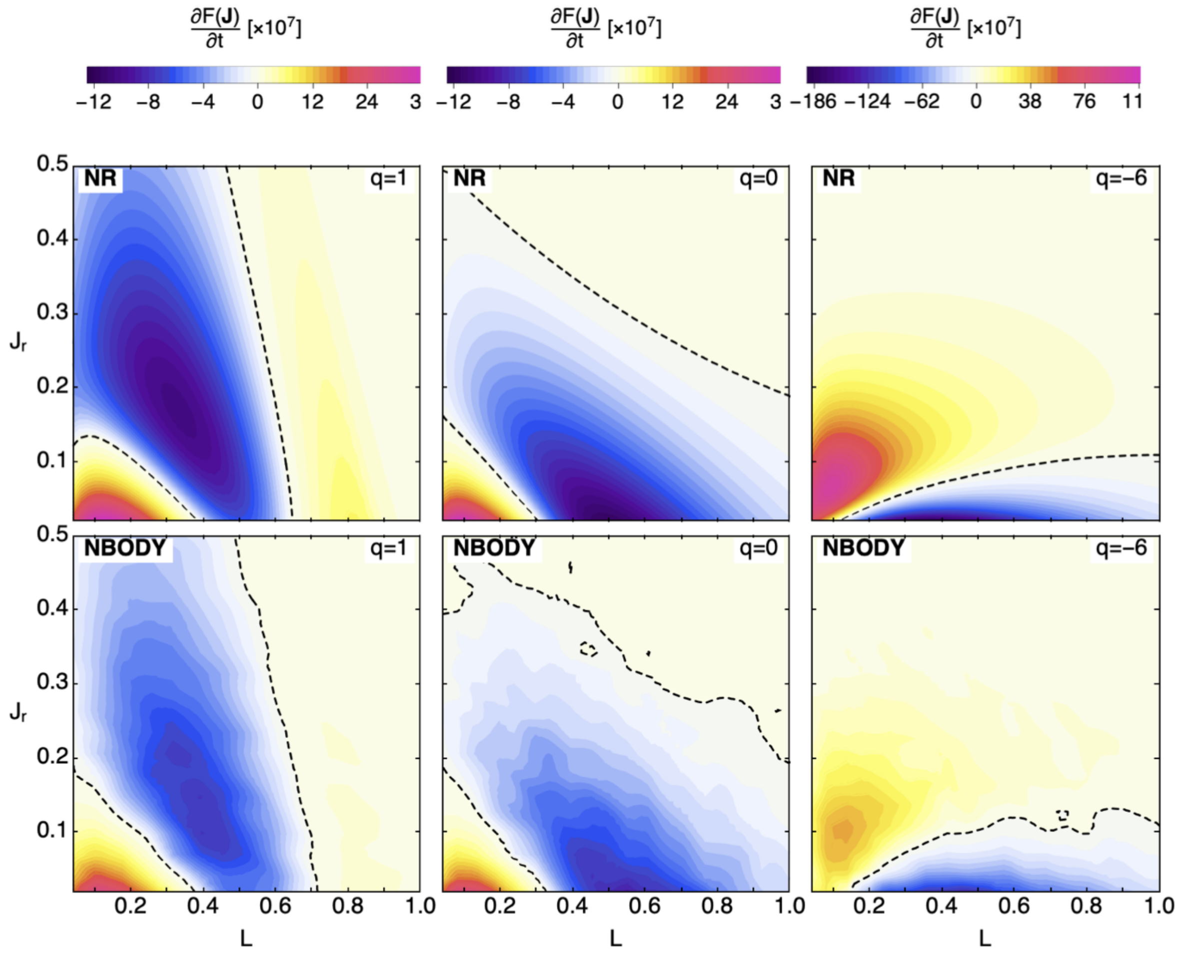

Figure 4.5.2: Illustration of the relaxation rate, $\partial F/\partial t$, for various values of the anisotropy parameter q (left to right), as predicted by the anisotropic NR prediction (top panels) and measured in direct numerical simulations (bottom panels). There is a qualitative agreement between the NR predictions and the N-body measurements. Because globular clusters are hot systems, resonances between orbits do not play a role as important as one might expect from the Balescu–Lenard formulation. However, this is up to an overall prefactor depending on the level of anisotropy q (see Fig. 4.5.3). This can be the result of long-range interactions, which the NR formalism does not capture accurately.

In that figure, I find that for an isotropic velocity distribution, i.e. $q = 0$, NR overestimates the N-body measurement by a factor ~ 1.4. This is compatible with the previous measurements from Theuns (1996) and Fouvry et al. (2021) that observed ratios of order $\sim 1.5 - 2$ in isotropic King spheres and isotropic isochrone clusters respectively. Interestingly, in Fig. 4.5.3, I show that the ratio from eq. (4.5.9) worsens as the cluster gets more tangentially anisotropic: for $q = -30$, the NR theory overestimates the diffusion rate by a factor ~ 3. To complete this observation, I compute the same ratio over different regions in the clusters, as defined in Fig. 4.5.4. The closer to the cluster's centre, the more the NR theory overestimates the diffusion rate. Due

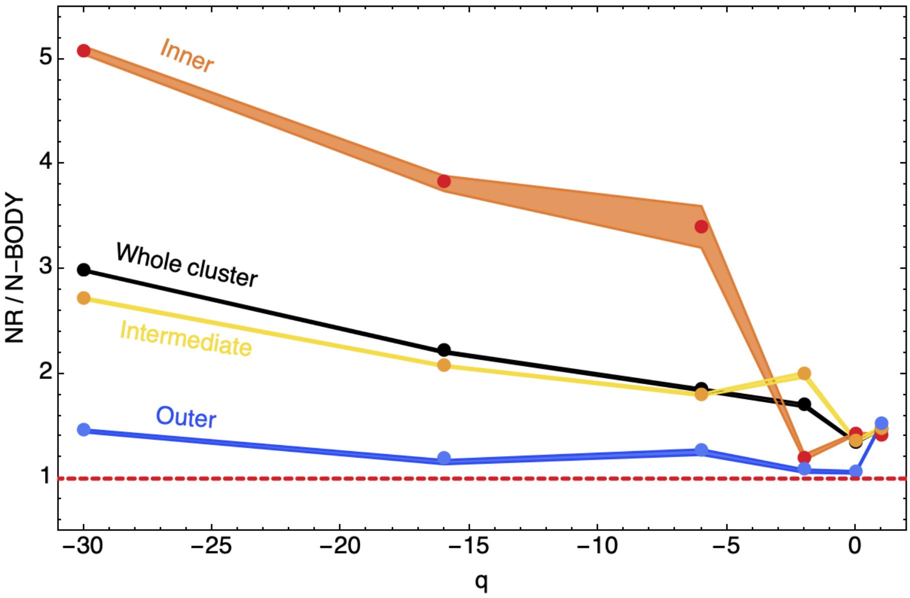

Figure 4.5.3: Ratio of the diffusion rate of the NR theory and N-body predictions (eq. 4.5.9) as a function of the cluster's anisotropy parametrised by q and computed over the whole cluster (black line). The dots correspond to anisotropies for which N-body simulations were performed, and the contours correspond to the 16% and 84% level lines over the available realisations. For the isotropic cluster ($q = 0$), the NR theory overestimates the diffusion rate by a factor ~ 1.4, which worsens as the cluster becomes more anisotropic. The coloured lines illustrate the ratios when computed over different regions in the clusters (see Fig. 4.5.4). As one gets closer to the cluster's centre, the NR theory overestimates more and more the diffusion rate.

to the high stellar density in the cluster's centre, strong deflections might impact more the relaxation occurring in that region than in external regions. Because the NR approximation neglects these interactions (with a small-scale cutoff), a large discrepancy is expected to occur. Furthermore, in all regions, the ratio of the diffusion rate increases as one increases the cluster's anisotropy. Indeed, as I increase tangential anisotropy, more and more stars follow circular orbits. The respective motions of the stars become more coherent w.r.t. one another. This facilitates long-range resonant interactions, which the NR theory fails to account for accurately.

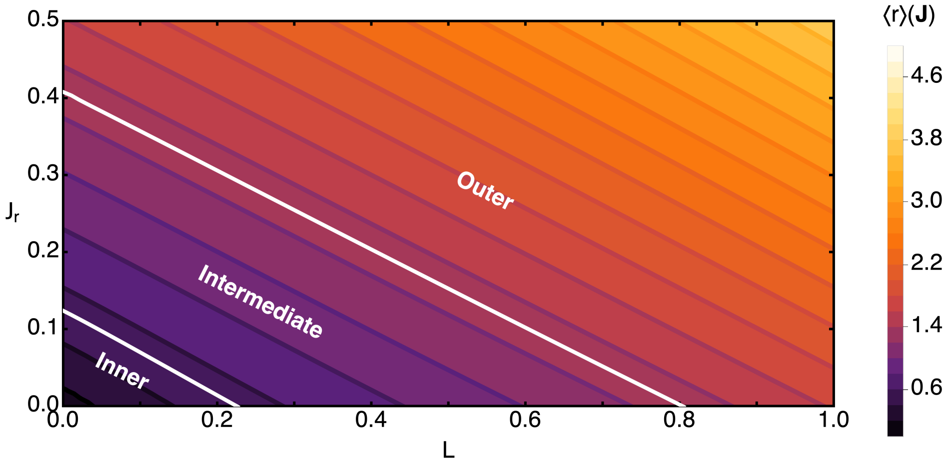

Figure 4.5.4: Average radius $\langle r \rangle$ as a function of the orbital parameters. I divide the cluster into three regions: (i) the inner region ($\langle r \rangle < 0.52b$) contains 10% of the total cluster's mass; (ii) the intermediate one ($0.52b < \langle r \rangle < 1.30b$) comprises 40% of the total mass; (iii) and the outer one ($\langle r \rangle > 1.30b$) the remaining 50%.

Figure 4.5.5 provides an alternative representation of the diffusion predicted by the NR theory. In that figure, I represent the field lines of the diffusion flux sourced by eq. (2.3.38), i.e. the direction along with orbits flow in action space. Here, I recover that the NR diffusion flux reshuffles the system towards a more isotropic distribution. In particular, the field lines show a clear flow from radial orbits (resp. circular orbits) in initially radially (resp. tangentially) anisotropic clusters towards circular orbits (resp. radial orbits).

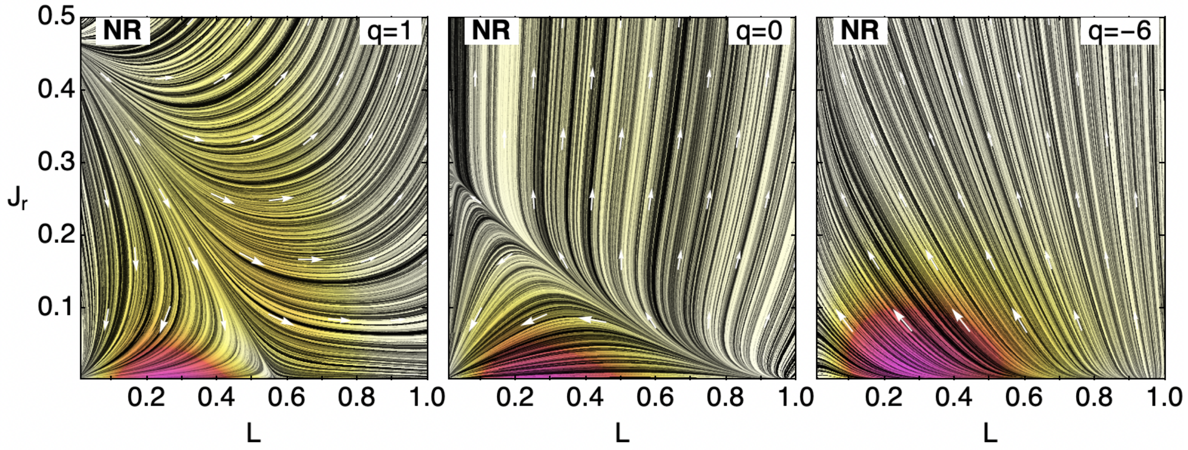

Figure 4.5.5: Illustration of the field lines of the diffusion flux, $\boldsymbol{\mathcal{F}}(\boldsymbol{J})$ (see eq. 2.3.34), as predicted by the NR theory for various anisotropies. The arrows give the average direction along which orbits flow in action space, while red colours are associated with larger flux amplitudes. For anisotropic clusters, i.e. $q \neq 0$, these flows reflect the expected redistribution of orbits towards a more isotropic distribution.

4.6 Pseudo-isotropic diffusion

The anisotropic diffusion coefficients involve three-dimensional integrals (see eq. 2.3.31). This is numerically more demanding than the isotropic ones which involve one-dimensional integrals (see eq. 2.3.27). In the view of benefiting from these simpler expressions, Cohn (1979) introduced the concept of a locally isotropised DF. Following eq. (16) of Cohn (1979), I introduce the pseudo-isotropic (P-Iso) DF[a]

$$\boxed{F_{\mathrm{tot}}^{\text{P-Iso}}(r,E) = \int_0^{\frac{\pi}{2}} \mathrm{d}x \, \sin x \, F_{\mathrm{tot}}\big(E, \sin x \, L_{\max}\big),} \tag{4.6.1}$$

with $L_{\max}(r,E) = \sqrt{2r^2(E-\psi[r])}$ the maximum angular momentum possible for a bound orbit of energy E going through the radius r. Importantly, following this local average, the pseudo-isotropic DF, $F_{\mathrm{tot}}^{\text{P-Iso}}$, only depends on the energy E. In appendix 4.E, I justify the form of this P-Iso DF.

In Fig. 4.6.1, I compare the cluster's anisotropic and pseudo-isotropic DFs for various radii and various anisotropies. As already highlighted in Fig. 4.2.1, for a fixed value of q, as one moves closer to the cluster's centre, the local anisotropy diminishes so that the anisotropic and pseudo-isotropic DFs closely follow one another. For a fixed radius r, as the anisotropy parameter q gets away from $q=0$, the local anisotropy increases, hence increasing the differences between the two DFs.

---

[a] Equation (4.6.1) follows from eq. (16) of Cohn (1979) via the change of variable $R = \sin^2 x \, R_{\max}$, with R and $R_{\max}$ defined in Cohn (1979).

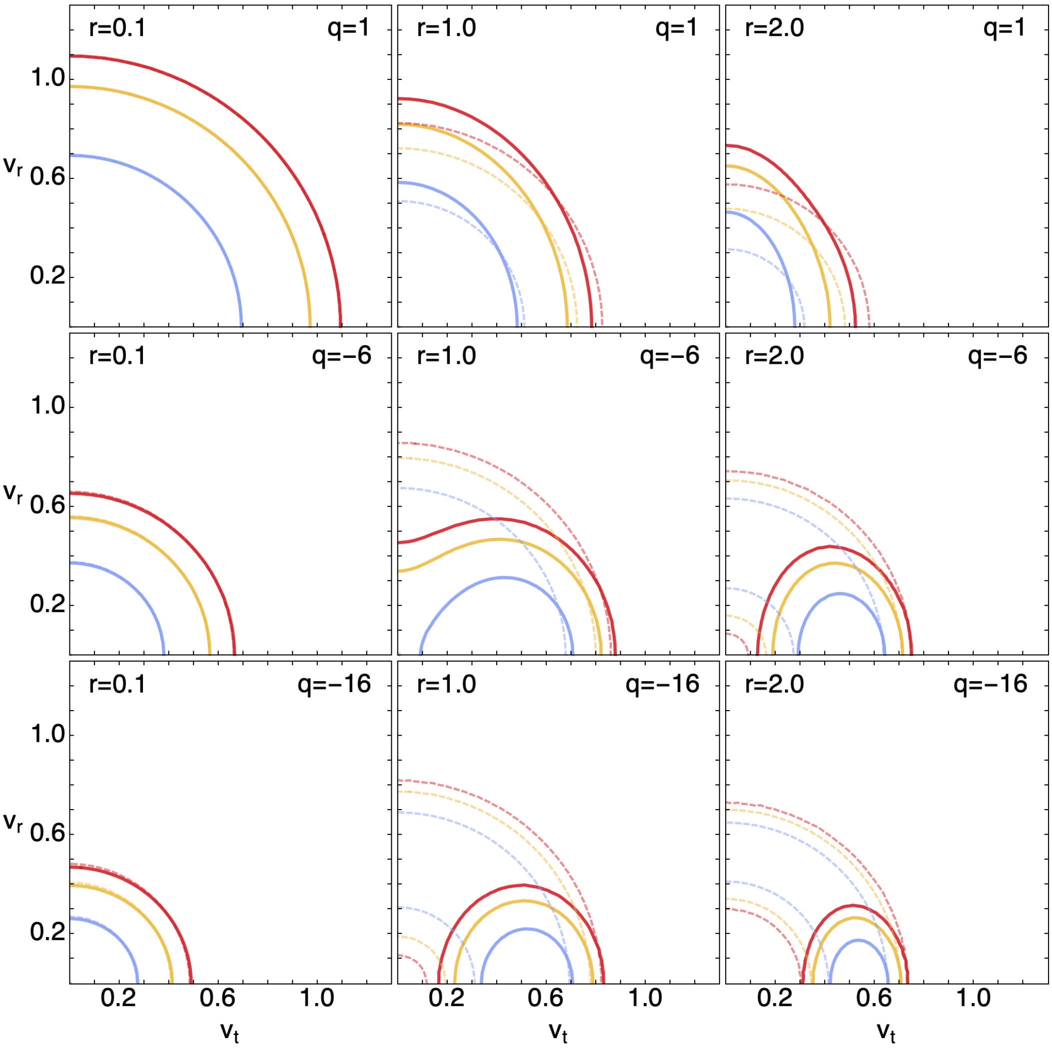

Figure 4.6.1: Contour levels of the anisotropic DF (full lines) and pseudo-isotropic DF (dashed lines) in the (v_t, v_r)-space, for various radii (left to right) and various anisotropies (top to bottom). Contours levels correspond to 50% (blue), 20% (orange) and 10% (red) of the DF's maximum at the considered radius. The closer to the cluster's centre, the weaker the anisotropy, and therefore the better the match between the two DFs.

4.6.1 Local velocity deflections

Once the pseudo-isotropic DF is known, it can straightforwardly be used in eq. (2.3.27) to estimate the velocity diffusion coefficients via (rapid) one-dimensional integrals. This is what I present in Fig. 4.6.2, where I compare the contours of $\partial F/\partial t$ as predicted by the fully anisotropic diffusion coefficients (computed via eq. 2.3.31) and their pseudo-isotropic analogues (computed via eq. 2.3.27).

In that figure, I note that, for the anisotropies considered here, the differences between the two maps are minor. This follows in fact from Fig. 4.2.1, where I noted that as one moves closer to the cluster's core, the anisotropy gets reduced, hence the similitude of the two maps reported in Fig. 4.6.2 which focuses on the cluster's central region. To strengthen this conclusion, I note that the local velocity deflections accumulated along a test star's motion in the cluster's core only marginally differ between the anisotropic and pseudo-isotropic predictions (see Fig. 4.6.3). Indeed, the anisotropy of the background Plummer cluster appears to have a weak impact on local deflections. This might be a sign of the *weak anisotropy* of this family of Plummer DFs, which I already observed in Fig. 4.6.1.

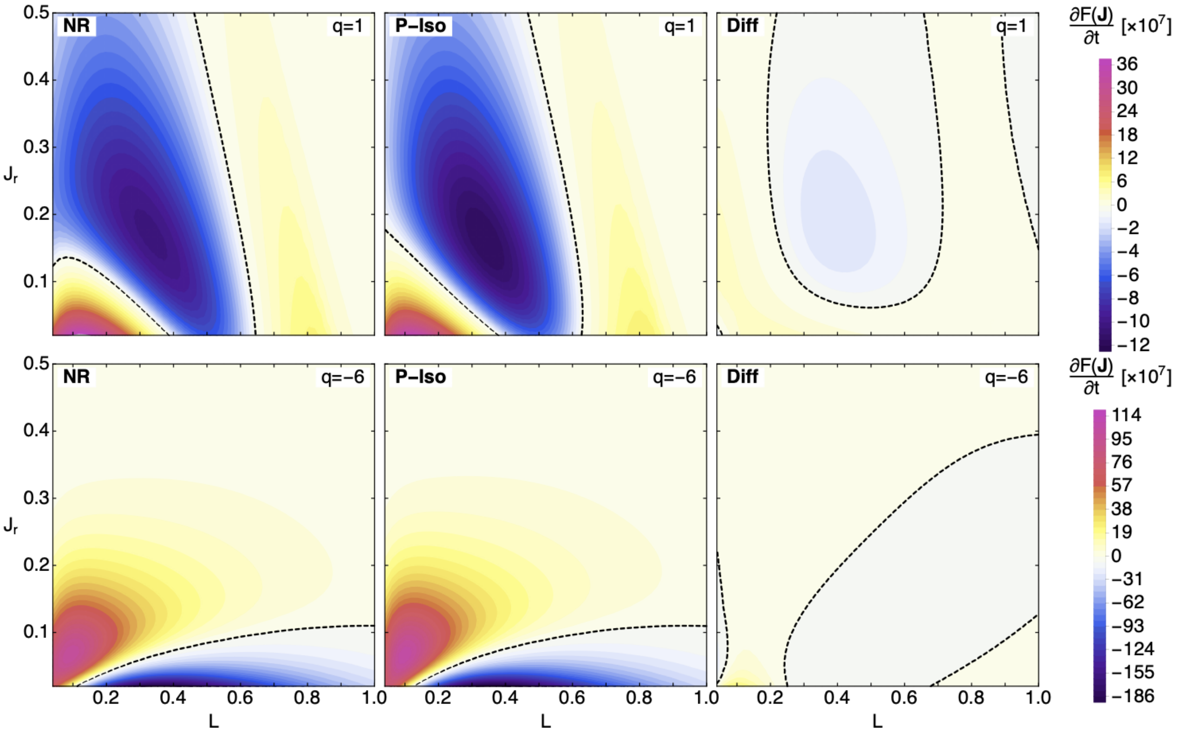

Figure 4.6.2: Illustration of the relaxation rate, $\partial F/\partial t$, for two values of the anisotropy parameter q (top and bottom), as predicted by the fully anisotropic NR diffusion coefficients (left) and the pseudo-isotropic ones (middle). The right panel illustrates the difference (NR minus P-Iso). For the level of anisotropy considered here, the difference between the two predictions is found to be, at most, $\sim 5\%$.

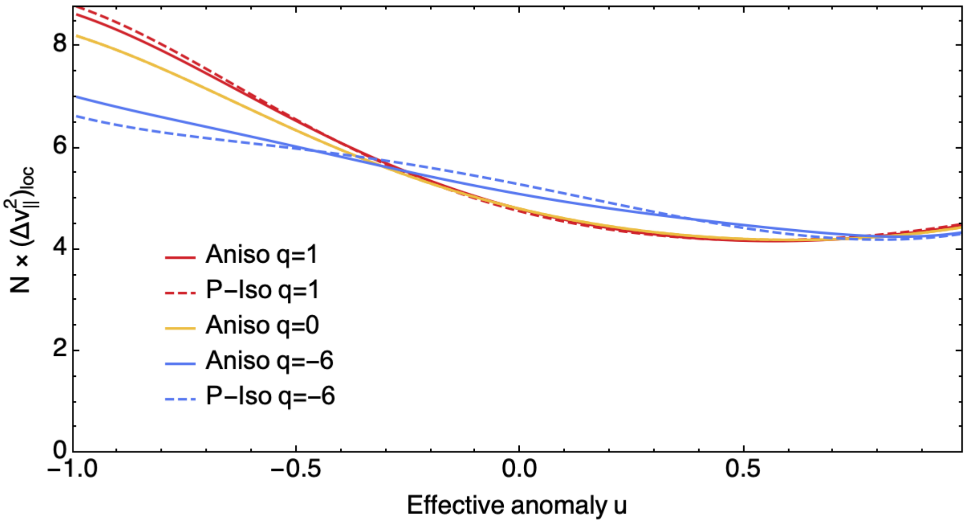

Figure 4.6.3: Illustration of the parallel velocity deflections accumulated along the motion of a test star, seen here as a function of the effective anomaly u. The full lines are the anisotropic NR predictions, while the dashed ones are the pseudo-isotropic ones. Different colours correspond to different background velocity anisotropies. The test star's orbit is $J_{\rm r} = 0.1\, L_0$ and $L = 0.5\, L_0$. As in Fig. 4.6.2, for the present levels of anisotropies, the differences between the two predictions are minor.

4.6.2 Impact of anisotropy

In order to better compare these two predictions, following eq. (4.5.9), I compute the respective ratios of the NR and P-Iso predictions through

$$\frac{\text{NR}}{\text{P-Iso}} = \frac{\displaystyle\int \mathrm{d}\boldsymbol{J}\, F(\boldsymbol{J})\, |\partial F/\partial t|_{\text{NR}}}{\displaystyle\int \mathrm{d}\boldsymbol{J}\, F(\boldsymbol{J})\, |\partial F/\partial t|_{\text{P-Iso}}}. \tag{4.6.2}$$

This is represented in Fig. 4.6.4. In that figure, I recover that for the anisotropy parameters q considered here, the two maps typically differ, at most, by $\sim 5\%$. As expected, as I increase the cluster's anisotropy, the mismatch between the two predictions increases. This similitude between NR and P-Iso is some pleasant numerical news. Indeed, rather than having to go through the three-dimensional NR integrals from eq. (2.3.31), the P-Iso prediction requires, in essence, two-dimensional integrals by computing first the pseudo-isotropic DF from eq. (4.6.1) and subsequently the associated isotropic diffusion coefficients from eq. (2.3.27).

4.7 Linking the Landau theory to the NR theory

In sections 4.5 and 4.6, I showed how the NR theory can be used to capture the secular behaviour of anisotropic globular clusters. As discussed in section 2.3, this theory comes with a few caveats. The derivation of the NR's Fokker–Planck equation (eq. 2.3.34) from the Balescu–Lenard equation (eq. 2.2.31) uses the approximation of local homogeneity, which introduces the Coulomb logarithm $\ln\Lambda$ (eq. 2.3.11). In a certain sense, this quantity is a free parameter, whose value is set by the geometry of the system. Efforts have been made to give a heuristic value to $\ln\Lambda$. In particular, Giersz & Heggie (1994) have given the fit $\ln\Lambda = \ln(0.11\, N)$ for the Plummer system. However, determining $\ln\Lambda$ directly from first principles could in principle be achieved starting from the gravitational homogeneous Landau equation (eq. 2.3.10). These two remarks – the accuracy of NR predictions and the determination of $\ln\Lambda$ – are open questions,

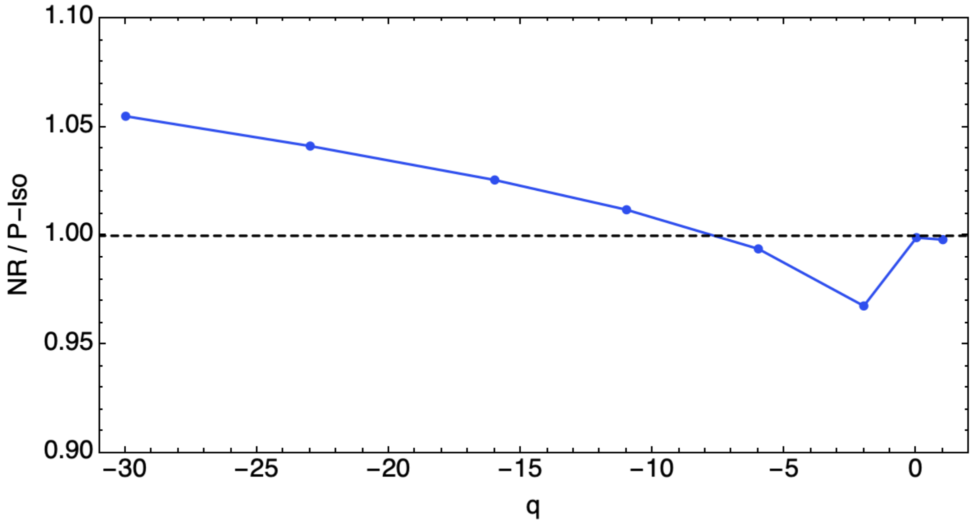

Figure 4.6.4: Ratio of the diffusion rate of the NR prediction and the P-Iso one, as defined in eq. (4.6.2). For an isotropic cluster ($q = 0$) both predictions are, naturally, in agreement, and they start to (marginally) differ as the cluster becomes more and more anisotropic.

which I explore briefly in this section.

4.7.1 The inhomogeneous Landau prediction

In order to understand these two observations, let me build upon Hamilton et al. (2018) and consider the inhomogeneous Landau equation given in eq. (2.3.1). Following these authors, I can express eq. (2.3.1) under the form

$$\frac{\partial F}{\partial t} = -\frac{\partial}{\partial \boldsymbol{J}} \cdot \boldsymbol{\mathcal{F}}(\boldsymbol{J}) = -\sum_{\ell=0}^{\infty} \frac{\partial}{\partial \boldsymbol{J}} \cdot \boldsymbol{\mathcal{F}}_{\ell}(\boldsymbol{J}) \quad ; \quad \boldsymbol{\mathcal{F}}_{\ell}(\boldsymbol{J}) = \sum_{\boldsymbol{k},\boldsymbol{k}' \in \mathbb{Z}^2} \boldsymbol{k}\, \mathcal{F}^{\ell}_{\boldsymbol{k}\boldsymbol{k}'}(\boldsymbol{J}), \tag{4.7.1}$$

where

$$\begin{aligned} \mathcal{F}^{\ell}_{\boldsymbol{k}\boldsymbol{k}'}(\boldsymbol{J}) = \frac{\pi(2\pi)^3 m}{2\ell+1} \int & \mathrm{d}\boldsymbol{J}' L L' |\psi^{\ell}_{\boldsymbol{k}\boldsymbol{k}'}(\boldsymbol{J},\boldsymbol{J}')|^2 \delta_{\mathrm{D}}(\boldsymbol{k}\cdot\boldsymbol{\Omega} - \boldsymbol{k}'\cdot\boldsymbol{\Omega}') \\ & \times \left(\boldsymbol{n}' \cdot \frac{\partial}{\partial \boldsymbol{J}'} - \boldsymbol{n} \cdot \frac{\partial}{\partial \boldsymbol{J}} \right) \frac{F(\boldsymbol{J})}{L} \frac{F(\boldsymbol{J}')}{L'}. \end{aligned} \tag{4.7.2}$$

I refer to appendix 4.F for more details on how I compute numerically eq. (4.7.2) in practice. Here, I have used in eq. (4.7.1) the spherical harmonic expansion of the interaction potential (see, e.g., eqs. 9 and 10 of Fouvry et al., 2021, for the exact expressions). This allows me to distinguish the contributions coming from different scales, in particular, between large-scale and small-scale interactions. As in the Balescu–Lenard equation (eq. 2.2.31) from which it is derived, eq. (4.7.2) contains a resonance condition $\delta_{\mathrm{D}}(\boldsymbol{k}\cdot\boldsymbol{\Omega} - \boldsymbol{k}'\cdot\boldsymbol{\Omega}')$ and a coupling coefficient $\psi^{\ell}_{\boldsymbol{k}\boldsymbol{k}'}(\boldsymbol{J},\boldsymbol{J}')$ that encodes the strength of orbital couplings. In this section, I will in particular be interested in the regime of large harmonics $\ell \gg 1$ and high-order resonances $|\boldsymbol{k}|, |\boldsymbol{k}'| \gg 1$.

Figure 4.7.1 shows the contributions of the first harmonics ℓ to the relaxation rate, $\partial F/\partial t$, for the isotropic cluster $q = 0$. Let me now comment on these various contributions.

First, let me consider the first harmonics $\ell = 0, 1, 2$. Due to the condition $|k_2|, |k_2'| \leq \ell$, only low-order resonances occur. As a result, the resonant orbits will not overlap very much during

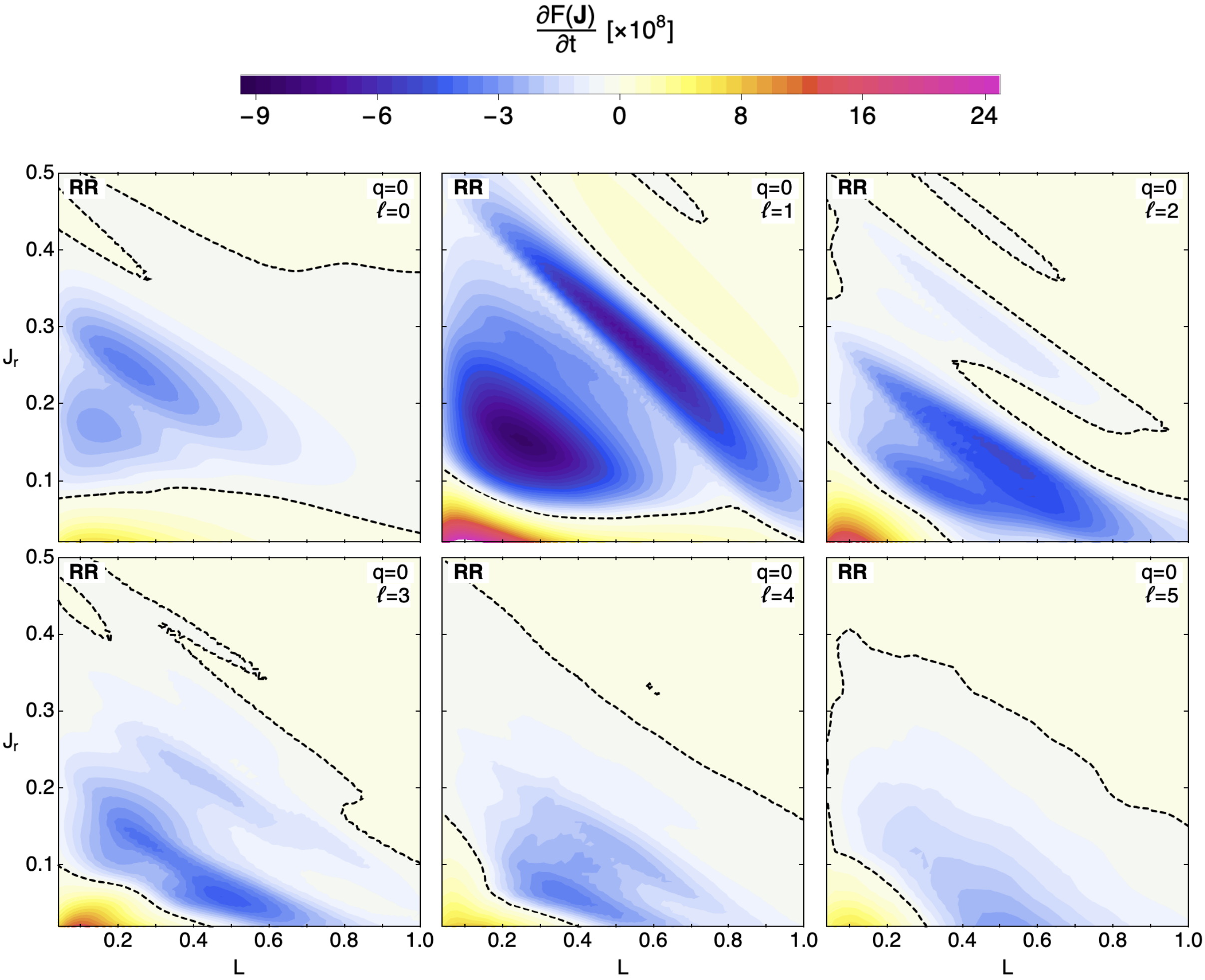

Figure 4.7.1: Computation of the relaxation rate $\partial F/\partial t$ for the isotropic Plummer cluster, as predicted by the RR theory (eq. 4.7.1). Each panel corresponds to $-\frac{\partial}{\partial \boldsymbol{J}} \cdot \boldsymbol{\mathcal{F}}_\ell(\boldsymbol{J})$, from $\ell = 0$ (large scales) to $\ell = 5$ (smaller scales). On the one hand, large scales are dominated by resonant interactions, hence need to be described by the RR theory. On the other hand, small scales predictions (from $\ell = 5$) appear to converge toward the NR prediction (Fig. 4.5.2, central panel). In that regime, the Landau theory appears not to be as resonant as the structure of the Landau equation would imply.

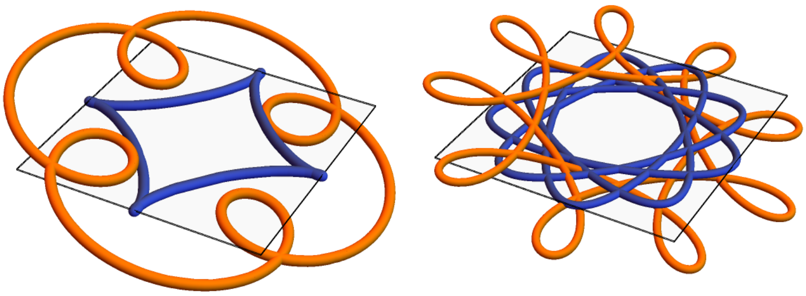

Figure 4.7.2: Inspired from fig. 10 of Fouvry et al. (2021). Schematic representation of the in-plane resonant interaction between two orbits. I represent a low-order resonance, (k, k'), in the left panel, whereas I represent a high-order resonance in the right panel. As they are much more high-order resonances than low-order ones, it surely is not obvious whether or not they contribute the most to the total Landau flux.

their motions (see the left panel of Fig. 4.7.2 for an example). This implies a large pairwise distance, hence a weak interaction between the two. Therefore, relaxation will mostly be induced by the long-term resonant interactions of the orbits over multiple orbital times. Thus, these harmonics can be understood as the contribution coming from large-scale interactions. In addition, because self-gravity plays an important role mostly on large scales (as illustrated by, e.g., the Jeans instability), collective effects are, in essence, limited only to these large-scale harmonics (top left panels of Fig. 4.7.1). As a consequence, accurately modelling these contributions requires the dressed RR theory, i.e. the Balescu–Lenard equation (eq. 2.2.31).

Then, let me consider the next harmonics $\ell = 3, 4, 5$. Due to the aforementioned condition on $|k_2|, |k_2'|$, these harmonics correspond to the contribution of resonances of a higher rank. These correspond to scales which are not small enough to be described by a local theory, but not large enough to be largely impacted by collective effects (bottom panels of Fig. 4.7.1). These contributions can therefore be described by the bare RR theory, i.e. the inhomogeneous Landau equation (eq. 2.3.1).

Finally, let me consider the harmonics $\ell = 6, 7, 8, \ldots$. In this case, high-order resonances make up the most part of the associated diffusion flux. Their high order induces a large number of overlaps in their orbits (see the right panel of Fig. 4.7.2 for an example), hence a large number of local encounters which accumulate during their motions. Heuristically, they play the role of the local deflections involved in the NR theory: they correspond to small-scale interactions. Thus, I expect that high harmonics will behave closely to the NR prediction (eq. 2.3.34).

This last remark is exactly what I observe in Fig. 4.7.3 (central panel). I observe that: (i) the relaxation rate $\partial F/\partial t|_\ell$ closely looks like the NR prediction $\partial F/\partial t$; (ii) $\ell\, \partial F/\partial t|_\ell$ does not depend on ℓ for large harmonics ℓ. Nevertheless, because high-order resonances are much more numerous than low-order ones, it is not obvious question to determine whether they may or may not dominate over the RR prediction. (Fig. 4.5.2).

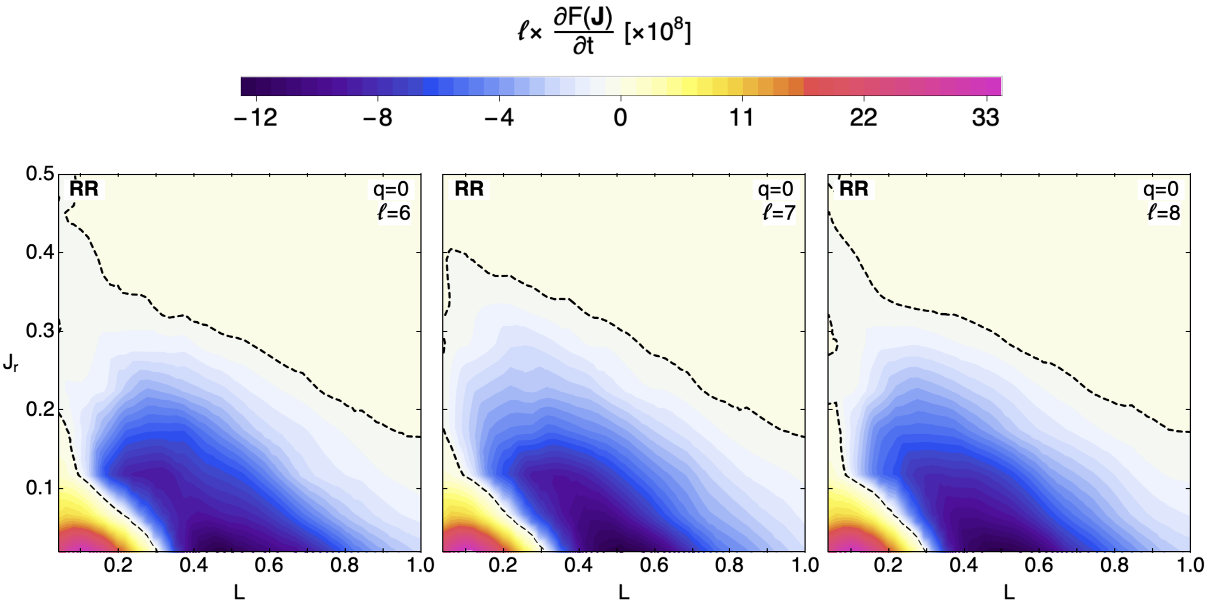

Figure 4.7.3: Relaxation rate, $\partial F/\partial t$, for the isotropic cluster, as in Fig. 4.7.1. The amplitudes have been multiplied by ℓ to emphasise the $1/\ell$ behaviour for large ℓ, so as to highlight the convergence towards the NR prediction (Fig. 4.5.2, central panel).

Figure 4.7.4 shows the dependence of $|\boldsymbol{\mathcal{F}}_\ell|$ w.r.t. ℓ for the usual anisotropies used in this thesis, namely $q=1, 0, -6$. The actions $\boldsymbol{J}$ at which the flux is evaluated is the mean action, $\langle \boldsymbol{J} \rangle_q$, defined as

$$\langle \boldsymbol{J} \rangle_q = \frac{(2\pi)^3}{M} \int \mathrm{d}\boldsymbol{J}\, \boldsymbol{J}\, F(\boldsymbol{J}). \tag{4.7.3}$$

This figure clearly shows a logarithmic small-scale divergence in $1/\ell$, which requires me to truncate the ℓ-summation in eq. (4.7.1) to some cutoff $\ell_{\max}$. As I increase ℓ, I consider encounters which are closer and closer, until they can be considered strong encounters. This is the small-scale divergence observed in the NR formalism (section 2.3.2). However, the large-scale divergence of the NR theory does not occur in the RR formalism. Fundamentally, this is because the RR formalism takes into account the cluster's inhomogeneity (section 2.3.1). Formally, this is described by the fact that the largest scales are described by the first harmonics $\ell = 0$, which is not divergent. Still, the determination of a small-scale cutoff remains an open question at the moment.

Fouvry et al. (2021) argues that $\ell_{\max}$ should be related to the $b_{\min}$ cutoff used in eqs. (2.3.11) and (2.3.13) through $\ell_{\max} = \ln(2)\, b/b_{\min}$. Indeed, consider the multipole expansion of the potential at order ℓ (see eq. 4.F.3 for the exact expression)

$$U_\ell(r, r') \propto \frac{1}{r_{\max}} \left(\frac{r_{\min}}{r_{\max}} \right)^{\ell}, \tag{4.7.4}$$

where $r_{\max} = \max(r, r')$ and $r_{\min} = \min(r, r')$. As ℓ increases, this function becomes extremely peaked, hence the interactions which matter are the local ones. Following Fouvry et al. (2021), if I consider an interaction in the core of the cluster with $r_{\max} = b$ and $r_{\min} = b(1-\epsilon)$ with $\epsilon \ll 1$, then the potential can be rewritten as $U_\ell \propto \exp(-\ell\epsilon)/b$. Taking the half-width of the potential as the typical separation of this interaction yields $\epsilon = \ln(2)/\ell$. Equating this with $b_{\min}$ the NR small-scale cutoff yields the desired heuristic prescription of $\ell_{\max}$. This sets an effective Coulomb logarithm in the RR formulation of the inhomogeneous Landau eq. (4.7.1) which is matched to the usual Coulomb logarithm prescription for the NR theory.

4.7.2 Higher-order harmonics and Chandrasekhar limit

Because the RR theory appears to behave like the NR theory asymptotically (Fig. 4.7.1), and because of the corresponding $1/\ell$ divergence (Fig. 4.7.4), let me define the (assumed to be ℓ-independent) correction ratio $\mathcal{R}(\boldsymbol{J})$ by the equation

$$D^{\ell}_{\mathrm{RR}}(\boldsymbol{J}) \sim \frac{\mathcal{R}(\boldsymbol{J})}{\ell} \frac{D_{\mathrm{NR}}(\boldsymbol{J})}{\ln \Lambda} \quad \text{when} \quad \ell \gg 1, \tag{4.7.5}$$

where I have chosen D_{NR} (resp. D_{RR}) as the LL diffusion coefficient predicted using NR theory (resp. RR theory, see appendix 4.F). This choice is motivated by the fact that this diffusion coefficient is always positive. This prevents any sign change, and hence any division by 0, when computing $\mathcal{R}(\boldsymbol{J})$. Furthermore, I have taken $\ln \Lambda = \ln(0.11\, N)$, so as to normalise by the *average Coulomb logarithm*. Hence by construction, $\mathcal{R}(\boldsymbol{J})$ is expected to be of order unity. In Fig. 4.7.5, I represent $\mathcal{R}(\boldsymbol{J})$ for $q=1, 0, -6$. Figure 4.7.5 has been made using the formula (obtained from the asymptotic behaviour given in eq. (4.7.5))

$$\mathcal{R}(\boldsymbol{J}) \sim \frac{\ell\, D^{\ell}_{\mathrm{RR}}(\boldsymbol{J})}{D_{\mathrm{NR}}(\boldsymbol{J})/\ln \Lambda}, \tag{4.7.6}$$

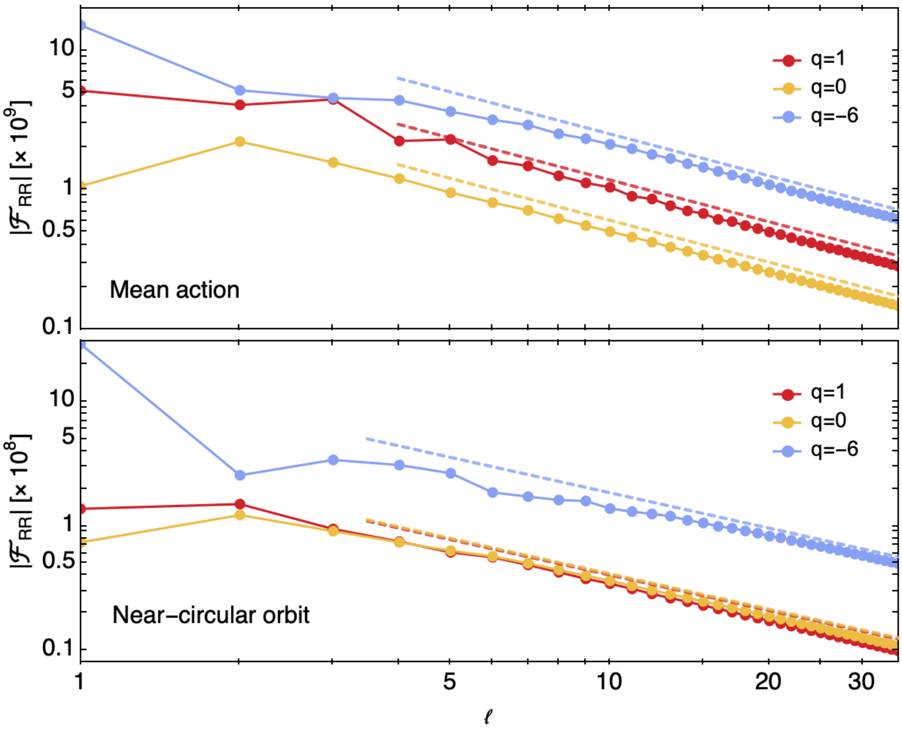

Figure 4.7.4: Illustration of $|\mathcal{F}^{\ell}_{\mathrm{RR}}|$ for $q = 1, 0, -6$. The modulus of the fluxes are computed at the mean action $\boldsymbol{J} = \langle \boldsymbol{J} \rangle_q$ for each value of q (top panel) and for $(J_{\mathrm{r}}, L) = (0.025, 0.25)$ (bottom panel). In the top panel, I observe an asymptotic behaviour in $\sim 1/\ell$ for large values of ℓ, which can be understood as the origin of the Coulomb logarithm. The relative amplitudes of the fluxes show the increasing isotropisation strength when increasing anisotropy. The bottom panel shows that the $1/\ell$ asymptotic behaviour is seen for higher harmonics for near-circular orbits.

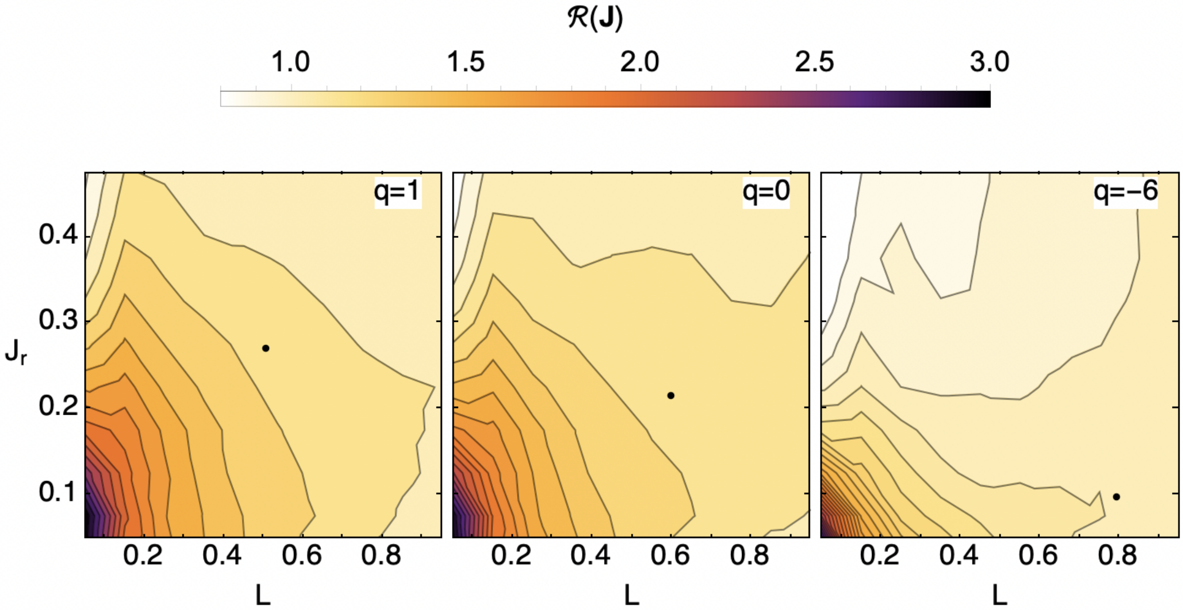

Figure 4.7.5: Computation of $\mathcal{R}(\boldsymbol{J})$, as defined by eq. (4.7.5), for Plummer clusters with anisotropies $q = 1, 0, -6$. Apart from the central region, this ratio is close to 1, hence the Coulomb logarithm stems from the $1/\ell$ summation. The black dot corresponds to the average action $\langle \boldsymbol{J} \rangle_q$ used in Fig. 4.7.4. I observe a gradient roughly along the first diagonal, with $\mathcal{R}(\boldsymbol{J})$ increasing from ~ 0.9 to ~ 2 towards the centre.

which is accurate only for ℓ large enough. This requires the computation of the r.h.s. of eq. (4.7.6) for large values of ℓ, followed by a fit with a constant. Whereas using the range of harmonics $\ell \sim 5-10$ appears to be sufficient to make this prediction for actions large enough (Fig. 4.7.4), this is not necessarily the case for smaller actions. In the end, using eq. (4.7.5) and summing over ℓ, I obtain

$$\ln \Lambda \, D_{LL}^{\mathrm{RR}} \simeq \mathcal{R}(\boldsymbol{J}) \bigg(\sum_{\ell=1}^{\ell_{\max}} \frac{1}{\ell} \bigg) D_{LL}^{\mathrm{NR}}(\boldsymbol{J}), \tag{4.7.7}$$

hence

$$\ln \Lambda \simeq \mathcal{R}(\boldsymbol{J}) \ln(\ell_{\max}). \tag{4.7.8}$$

Overall, Fig. 4.7.5 appears to show a small gradient in $\mathcal{R}(\boldsymbol{J})$ along the first diagonal in action space, with a maximum value reached for small actions. Understanding the origin of this action dependence would hopefully yield a definitive prescription for the computation of the Coulomb logarithm. To that end, I try in the following section to recover the observations of Fig. 4.7.5 using a simple model for $\ln \Lambda$.

4.7.3 Estimating the Coulomb logarithm

The physical prescription of the Coulomb logarithm which is widely used is the one given by Chandrasekhar (1943), where $b_{\min} \sim 2Gm/\sigma^2$, with $\sigma^2 = \sigma_x^2 + \sigma_y^2 + \sigma_z^2$ is the velocity r.m.s. of the system, while $b_{\max}$ is a free parameter. Nevertheless, other prescriptions exist: Chandrasekhar & von Neumann (1942) argue that one should take $b_{\max}$ as the interparticle distance. Other authors (see, e.g., Hénon, 1961; Merritt, 2013, and references within) have chosen larger values for $b_{\max}$ of the order of the size of the system, such as the core radius $(0.64b)$, the 3D half-mass radius $(1.3b)$, the 2D half-mass radius (b), the virial radius $(1.7b)$, the mean radius $(2b)$, and so on. Let me now investigate the possible impacts of these various prescriptions for $\ln \Lambda$, and compare them with my numerical measurements of $\mathcal{R}(\boldsymbol{J})$. For the Plummer potential (Dejonghe, 1987), the velocity r.m.s. σ is given by

$$\sigma^2(r) = \frac{1}{6-q} \frac{GM}{\sqrt{b^2+r^2}} \bigg(3 - q \frac{r^2}{b^2+r^2} \bigg). \tag{4.7.9}$$

In order to obtain an estimator depending only on orbital parameter, I can orbit-average the velocity r.m.s. . This provides me with a naive estimator of the Coulomb logarithm

$$\ln \Lambda_\star(\boldsymbol{J}) = \ln \frac{b \, \langle \sigma^2 \rangle(\boldsymbol{J})}{2Gm}. \tag{4.7.10}$$

I represent this estimator of $\ln \Lambda(\boldsymbol{J})$ in Fig. 4.7.6. This prediction fails to recover the action dependency I observe in Fig. 4.7.5 for the full range of q considered. First, whereas the cluster $q=0$ and $q=1$ reach a maximum at the bottom left corner of action space (left and centre panels of Fig. 4.7.6), this is not the case for $q = -6$. Additionally, the contour lines observed in Fig. 4.7.5 do not appear as simple as the seemingly straight lines of Fig. 4.7.6. Finally, whereas the range of values observed in Fig. 4.7.5 extends between 0.8 and $2-3$, the range observed for the estimator is much smaller, and typically goes from 0.9 to 1.15. Such clear qualitative and quantitive distinctions show that the prediction the Coulomb logarithm from first principles still requires more research, and goes beyond the naive prescription described in this section.

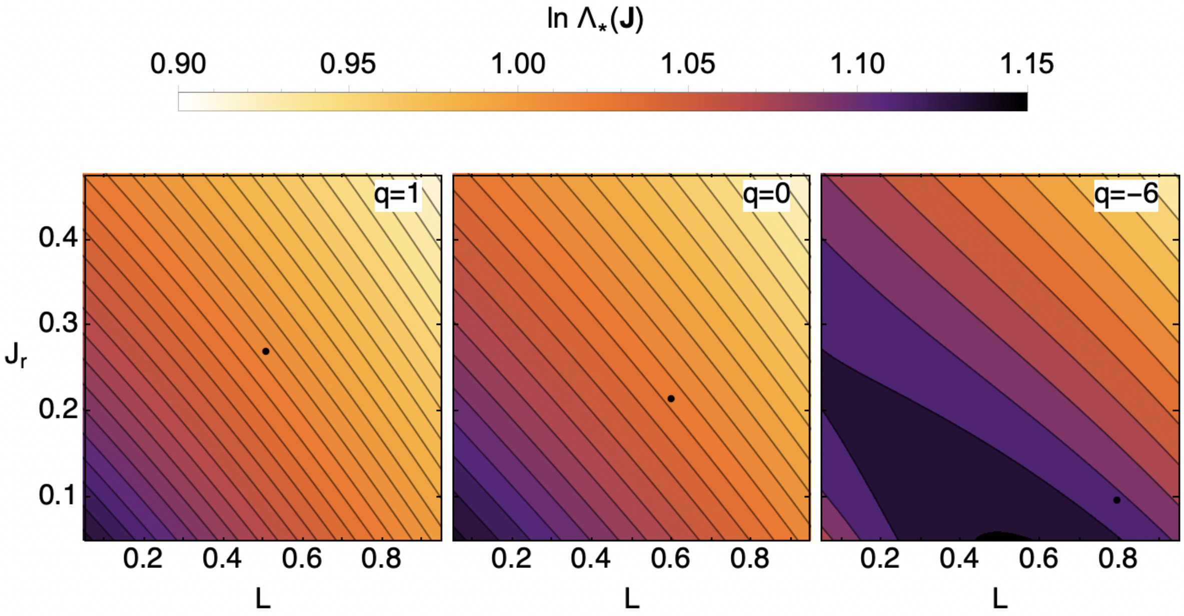

Figure 4.7.6: Illustration of the effective Coulomb logarithm, $\ln \Lambda_\star$, in action space, as defined by eq. (4.7.10). The large-scale cutoff is set by the size of the system, approximated by the Plummer length b. The small-scale cutoff is set by a rough estimator of the 90-degree deflection impact parameter b_{90}, and hence is set by the velocity dispersion of the cluster. While this Coulomb estimator appears to reproduce the diagonal gradient observed in Fig. 4.7.5 for low-anisotropy system, obvious differences occur for more tangentially systems. Furthermore, the range of the Coulomb logarithm given by this estimator is much smaller than that obtained from RR theory.

4.7.4 Asymptotics of the inhomogeneous Landau equation

In an unpublished paper, Heggie & Retterer (priv) considered the limiting case of a radial orbit near the centre of a globular cluster. They showed that its interactions with the background amounts to the orbit-averaged NR prediction, with the Coulomb logarithm coming from a cutoff on an harmonics summation similar to that of eq. (4.7.1).

Supposing that the background stars perturbing the radial star must be close to the centre, hence with a low angular momentum, they were able to obtain an expression for the diffusion coefficient in energy for the perturbed orbit

$$\langle \Delta E^2 \rangle = \frac{32\pi^2 G^2 m^2}{3} E \ln\left(\frac{b_{\max}}{b_{\min}}\right) \int \mathrm{d}E_\mathrm{p}\, F_\mathrm{tot}(E_\mathrm{p}), \tag{4.7.11}$$

at the cost of a few computation tricks such as, e.g., summation/integration exchanges (see appendix 4.G for a brief overview of the computation). Here, $b_{\max}$ is cutoff coming from the contribution of large scales, which is induced by the finite extent of the system. As for $b_{\min}$, it is a cutoff coming from the contributions of small scales, which is induced by the strong deflections which cannot be dealt with by this theory. Equation (4.7.11) can then be compared to the NR prediction

$$\langle \Delta E^2 \rangle = \frac{32\pi^2 G^2 m^2}{3} E \ln \Lambda \int \mathrm{d}E_\mathrm{p}\, F_\mathrm{tot}(E_\mathrm{p}). \tag{4.7.12}$$

Therefore, setting $\Lambda = b_{\max}/b_{\min}$, the two formulae (eqs. 4.7.12 and 4.7.11) exactly correspond to one another. This is a remarkable result. Indeed, despite the approximations needed to obtain an analytic asymptotic formula (e.g., the radial limit and only radial perturbers), Heggie & Retterer (priv) were able to obtain a formula identical to the NR limit, down to the exact multiplicative prefactor before $\ln \Lambda$. Thus, they recovered the NR theory from the RR theory in the case of radial orbits in an isotropic globular cluster.

Unfortunately, eq. (4.7.11) cannot be compared to Fig. 4.7.5 because it corresponds to a point on the J_r-axis in orbital space. Therefore, determining $\mathcal{R}$, thus the Coulomb logarithm, is a difficult numerical problem. Focussing on a different subset of orbits, one might be interested in doing a similar prediction for circular orbits, using for example an epicyclic approximation to recover analytical predictions. This alternative regime also falls in the region where a prediction is numerically difficult to make. This is a problem generic to asymptotes, and one should eventually match them to customised numerics accounting for the limiting scalings of this regime.

4.8 Concluding remarks

In this chapter, I extended Chandrasekhar's NR theory to compute the local velocity diffusion coefficients in non-rotating anisotropic spherical clusters. This allowed me to go beyond the usual isotropic and pseudo-isotropic predictions made in this context (see, e.g., Spitzer & Shull, 1975; Lightman & Shapiro, 1978; Cohn, 1979, 1980; Spitzer, 1987; Takahashi, 1993; Theuns, 1996; Quinlan, 1996; Heggie & Hut, 2003; Vasiliev, 2015; Fouvry et al., 2021). By relying on tailored N-body simulations (section 4.4), I was able to investigate the impact of anisotropy on the evolution of an anisotropic Plummer cluster. Namely, I observed a clear dependence of the core collapse rate w.r.t. the initial velocity anisotropy of the cluster, as already reported in Breen et al. (2017). To understand this trend, I measured the evolution of the core radius, a proxy for the cluster's size. In order to obtain a quantity more accessible to NR predictions, I directly measured the time evolution of the DF in action space. This allowed me to observe a reshuffling of the orbits, reflecting the isotropisation of the cluster. In section 4.5, I computed the NR prediction for this latter measurement. Overall, I reached two main conclusions. First, the NR prediction matches qualitatively direct N-body measurements (see Fig. 4.5.2) up to an overall prefactor $\sim 1.4-2$ that worsens as the initial anisotropy increases (see Fig. 4.5.3). This match between theory and simulations shows that the NR theory captures the faster compression of tangentially anisotropic globular clusters compared to radially anisotropic ones (see Fig. 4.1.2). Nonetheless, the incorrect prefactor suggests that the NR theory overestimates the relaxation rate coming from contributions from large-scale encounters. Second, I pointed out that the NR theory also drives initially an isotropisation of the cluster (see, e.g., Fig. 4.5.5).

Then, following Cohn (1979), I investigated in section 4.6 the errors introduced by locally isotropising the DF of the perturbers (see eq. 4.6.1), an approach coined *pseudo-isotropic*. For the class of anisotropic clusters considered, I emphasised that the limited extent of anisotropy in the inner regions (see Fig. 4.6.1) led to differences of order $\lesssim 5\%$ w.r.t. the fully anisotropic calculation. As such, for the clusters considered here, I confirmed that the anisotropy of the perturbers' DF, via $F_\mathrm{tot}(\boldsymbol{r}, \boldsymbol{v}')$ in eq. (2.3.31), plays a much less important role than the anisotropy in the test particles' DF, via $F(\boldsymbol{J})$ in eq. (2.3.38).

Finally, I studied the impact of resonant interactions in the secular evolution of anisotropic clusters in section 4.7. By computing the Landau prediction for the long-term relaxation of the cluster (RR theory), I was able to study the impact of low-order harmonics (large scales) and higher-order harmonics (small scales) on orbital diffusion. I found that high-order harmonics predictions converge toward the NR prediction. Furthermore, I observed a logarithmic divergence of the RR prediction, which I linked to the Coulomb logarithm parameter present in the NR theory. This overall logarithmic prefactor weakly depends on actions. However at this stage I did not manage to relate its behaviour and amplitude to simplistic prescriptions for the Coulomb logarithm.

4.8.1 Future works

Having computed $\partial F/\partial t$ from kinetic theory (Fig. 4.5.2), I could in principle predict the initial time evolution of more traditional quantities such as the anisotropy parameter $\beta(r)$ (Fig. 4.2.1) or the core radius $R_c(t)$ (Fig. 4.1.2). This would come at the cost of accounting appropriately for the self-consistent update of the cluster's mean potential. Ultimately, following for example Vasiliev (2015), one could also hope to integrate self-consistently the time evolution of the whole cluster as driven by the present NR theory (or ultimately, its RR counterpart). Figure 4.5.5 emphasised that local deflections naturally tend to isotropise the cluster's DF. Given this increased isotropy, I can expect that the pseudo-isotropic prescription from eq. (4.6.1) will become more relevant as relaxation occurs. Of course this would deserve to be investigated in more detail, following for example fig. 7 of Breen et al. (2017).

In this chapter, I restricted my analysis to Plummer potentials. Nevertheless, the generic derivation presented in section 2.3.3 should translate to any *reasonable* cored potential, provided one has access to its DF (e.g., following the method from Dejonghe, 1987). It would also be of interest to investigate truncated or cuspy spheres, since the clusters' orbital structure impacts both their linear and long-term responses. In order to alleviate some of the present numerical challenges, it would be worthwhile to find an efficient way of carrying out the orbit-averages using numerically stable effective anomalies (as in section 4.5.1) for such potentials.

As illustrated in Fig. 4.5.3, the NR theory and the N-body measurements still present an overall multiplicative discrepancy. Following Fouvry et al. (2021), it would be of interest to investigate the RR of spherical clusters with various levels of anisotropy. This should ultimately pave the way to predict ab-initio the effective Coulomb logarithm $\ln\Lambda$ in eq. (2.3.11), as was briefly discussed in section 4.7. A promising way to achieve this aim would be to capitalise on the work of Heggie & Retterer (priv) (briefly presented in section 4.7.4). As they were able to recover NR theory from RR theory in the radial orbit limit, it would be enlightening to achieve a similar result in the circular orbit limit, before moving onto a more general analytic formulation.

Appendices of chapter 4

4.A Computing energy from radial action

In any spherically symmetric system, the transformation $(E, L) \mapsto (J_\mathrm{r}, L)$ is done straightforwardly using the integral expression of $J_\mathrm{r}(E, L)$ (eq. 4.3.6). However, the inverse transformation $(J_\mathrm{r}, L) \mapsto (E, L)$ cannot be done analytically in the general case.[b] Nonetheless, because the transformation is bijective, this inverse can be done by solving the equation $J_\mathrm{r}(E, L) = J_\mathrm{r}$ w.r.t. the unknown energy E, at fixed L. This is achieved by using a classical bisection method. Yet, because the (E, L) is limited by circular orbits, i.e. is delimited by $L \leq L_\mathrm{c}(E)$, I have to be careful not to overshoot the prediction for E. To that end, I proceed as follows. Let $\epsilon > 0$ be the desired precision on E and suppose that $(J_\mathrm{r}, L) \neq (0, 0)$ (if not, then $E = E_0$). Define $\{\Delta_n\}_n$ the sequence of upper bounds on the energy error, and $\{E_n\}_n$ the sequence of energy estimators.

1. Start with an initial guess $E_1 = 0.5 E_0$. Since $E_0 < E < 0$, we have $\Delta_1 = |E_0|/2$
2. If $\Delta_1 > \epsilon$, then the energy guess is not precise enough. Set $\Delta_2 = \Delta_1/2$. If $L > L_\mathrm{c}(E_1)$, then E_1 overshoots the region and I move back to the orbital region by letting $E_2 = E_1 + \Delta_2$. Otherwise, consider $J_{\mathrm{r},1} = J_\mathrm{r}(E_1, L)$. If $J_{\mathrm{r},1} < J_\mathrm{r}$, then $E_2 = E_1 + \Delta_2$. Otherwise, I set $E_2 = E_1 - \Delta_2$. Conversely, if $\Delta_1 < \epsilon$, then the desired precision on the energy has been reached.
3. ...
4. If $\Delta_n > \epsilon$, then the energy guess is not precise enough. Set $\Delta_{n+1} = \Delta_n/2$. If $L > L_\mathrm{c}(E_n)$, then E_n overshoots the region and I move back to the orbital region by setting the energy as $E_{n+1} = E_n + \Delta_{n+1}$. Otherwise, consider $J_{\mathrm{r},n} = J_\mathrm{r}(E_n, L)$. If $J_{\mathrm{r},n} < J_\mathrm{r}$, then I set $E_{n+1} = E_n + \Delta_2$. Otherwise, I set $E_{n+1} = E_n - \Delta_2$. Conversely, if $\Delta_n < \epsilon$, then desired precision on the energy has been reached.

Finally, the last estimation E_n satisfies $J_\mathrm{r}(E_n, L) = J_\mathrm{r}$ with a precision bounded by ϵ.

4.B Computing the circular motion

The region in (E, L)-space where orbits are located is defined by the constraints $E < 0$ and $L \geq 0$ such that there exists $r \geq 0$ verifying the inequality $\psi_\mathrm{eff}(r; L) \leq E$. For $L > 0$, this function has a global minimum at some radius r_c. Increasing the value of L increases this minimum value, meaning that there exists a maximum value $L_\mathrm{c}(E)$ such that $\psi_\mathrm{eff}(r_\mathrm{c}; L_\mathrm{c}[E]) = E$.

---

[b] If one has access to an analytical expression of $J_\mathrm{r}(E, L)$, then the inversion is trivial. This is the case for the isochrone potential (see, e.g., Binney & Tremaine, 2008).

The effective potential is given by

$$\psi_{\text{eff}}(r) = -\frac{GM}{\sqrt{b^2+r^2}} + \frac{L^2}{2r^2} = E_0\left(\frac{1}{s} - \frac{\widetilde{L}^2}{2(s^2-1)}\right), \tag{4.B.1}$$

where I used the change of variable $s^2 = (r/b)^2 + 1$ and $\widetilde{L}$ is the reduced angular momentum (occurring in eq. 4.2.3). Then, let me define for convenience

$$\eta(s,E) = (s^2-1)\left(\frac{1}{s} - \widetilde{E}\right). \tag{4.B.2}$$

By definition, the circular radius r_{c}, or equivalently s_{c}, corresponding to the energy E is reached when $\eta(s,E)$ reaches its maximum value. It follows that

$$L_{\text{c}}^2(E) = 2L_0^2 \max_{s>0} \eta(s,E) = 2L_0^2 \eta(s_{\text{c}}[E], E). \tag{4.B.3}$$

Let me compute the maximum of η. Its derivative is given by

$$\frac{\mathrm{d}\eta}{\mathrm{d}s} = \frac{s^2+1}{s^2} - 2\widetilde{E}s. \tag{4.B.4}$$

It vanishes iff

$$-2\widetilde{E}s^3 + s^2 + 1 = 0. \tag{4.B.5}$$

The polynomial discriminant of eq. (4.B.5) is given by $\Delta = -4(27\widetilde{E}^2+1) < 0$, meaning that it has only one real root, which is positive. The Cardan formula gives its expression. Let me define

$$\alpha = -2\widetilde{E} \quad ; \quad \beta = 1 \quad ; \quad \gamma = 0 \quad ; \quad \delta = 1, \tag{4.B.6}$$

and let

$$p = \frac{3\alpha\gamma - \beta^2}{3\alpha^2} = -\frac{1}{12\widetilde{E}^2}, \tag{4.B.7a}$$

$$q = \frac{2\beta^3 - 9\alpha\beta\gamma + 27\alpha^2\delta}{27\alpha^3} = -\frac{1+54\widetilde{E}^2}{108\widetilde{E}^3}, \tag{4.B.7b}$$

The discriminant Δ' of the depressed cubic is that of the initial polynomial divided by α^4, hence $\Delta' = -(4p^3+27q^2) = -(27\widetilde{E}^2+1)/(4\widetilde{E}^4)$. The unique real root is given by

$$s_{\text{c}}(E) = -\frac{\beta}{3\alpha} + \sqrt[3]{-\frac{q}{2} + \sqrt{\frac{q^2}{4} + \frac{p^3}{27}}} + \sqrt[3]{-\frac{q}{2} - \sqrt{\frac{q^2}{4} + \frac{p^3}{27}}}, \tag{4.B.8}$$

or, more explicitly,

$$s_{\text{c}}(E) = \frac{1}{6\widetilde{E}} + \sqrt[3]{\frac{1+54\widetilde{E}^2}{216\widetilde{E}^3} + \frac{1}{4\widetilde{E}}\sqrt{1+\frac{1}{27\widetilde{E}^2}}} + \sqrt[3]{\frac{1+54\widetilde{E}^2}{216\widetilde{E}^3} - \frac{1}{4\widetilde{E}}\sqrt{1+\frac{1}{27\widetilde{E}^2}}}. \tag{4.B.9}$$

This expression allows me to compute $L_{\text{c}}(E)$ analytically using eq. (4.B.3).

4.C Computing the derivatives of $J_{\mathrm{r}}(E, L)$

The computation of the (J_{r}, L)-space orbit-averaged diffusion coefficients involves the first and second derivatives of $J_{\mathrm{r}}(E, L)$ w.r.t. (E, L). However, their computation is made difficult by both the presence of an integrable singularity and the lack of an integrable integrand (eqs. 4.3.7). In the latter case, one would be forced to take the numerical derivative of the integral expression. However, the existence of an effective anomaly u (with nice properties, see section 4.5.1) allows me to bypass these difficulties.

First, I consider the radial action J_{r} given by eq. (4.3.6). To obtain the equalities in that equation, I use the identity $\mathrm{d}r/v_r = \mathrm{d}u\, \Theta(u)$, which is the property that motivated the research of the effective anomaly u. Now, taking the first derivative of the radial expressions yields eqs. (4.3.7). The E-derivative can now be integrated with both precision and efficiency using a classical midpoint integration scheme. The case of the L-derivative is a bit trickier, and shall be discussed later in this appendix (see eq. 4.C.10).

Now, I observe that while the radial integrands in eqs. (4.3.7) are not differentiable, this issue does not occur in the u-integral. This allows me to differentiate these expressions once more to recover the second-order derivatives

$$\frac{\partial^2 J_{\mathrm{r}}}{\partial E^2} = \frac{1}{\pi} \int_{-1}^{1} \mathrm{d}u \, \frac{\partial \Theta}{\partial E}, \tag{4.C.1a}$$

$$\frac{\partial^2 J_{\mathrm{r}}}{\partial L \partial E} = \frac{1}{\pi} \int_{-1}^{1} \mathrm{d}u \, \frac{\partial \Theta}{\partial L}, \tag{4.C.1b}$$

$$\frac{\partial^2 J_{\mathrm{r}}}{\partial L^2} = -\frac{1}{\pi} \left[\int_{-1}^{1} \frac{\mathrm{d}u \, \Theta(u)}{r^2(u)} + L \int_{-1}^{1} \frac{\mathrm{d}u}{r^4(u)} \left(\frac{\partial \Theta}{\partial L} r^2(u) - 2b^2 \Theta(u) s(u) \frac{\partial s}{\partial L} \right) \right]. \tag{4.C.1c}$$

The derivatives that appear in the integrand can be easily obtained by the chain rule and implicit differentiations.

Now, let me discuss the u-integration of $\partial J_{\mathrm{r}}/\partial L$ (eq. 4.3.7b). As I consider $L \to 0^+$, the radius $r(u)^2$ in the denominator tends to 0 at the lower bound $u = -1$. This is in theory compensated by the L prefactor in eq. (4.3.7b), which overall allows $\partial J_{\mathrm{r}}/\partial L$ to converge to $-1/2$ as $L \to 0^+$. A naive sampling would however miss all the contributions from the lower u-bound. In order to remedy that issue, I proceed as follows. First, I consider the u-derivative of r^2

$$\frac{\mathrm{d}(r^2)}{\mathrm{d}u} = 3 \frac{s_{\mathrm{a}} + s_{\mathrm{p}}}{2} \left[1 + \frac{s_{\mathrm{a}} - s_{\mathrm{p}}}{s_{\mathrm{a}} + s_{\mathrm{p}}} u \left(\frac{3}{2} - \frac{u^2}{2} \right) \right] \frac{s_{\mathrm{a}} - s_{\mathrm{p}}}{2} (1 - u^2). \tag{4.C.2}$$

Its Taylor expansion near $u = -1$ is given by

$$\frac{\mathrm{d}(r^2)}{\mathrm{d}u} = 3(s_{\mathrm{a}} - s_{\mathrm{p}}) s_{\mathrm{p}} \left[(u+1) - \frac{(u+1)^2}{2} \right] + O[(u+1)^3], \tag{4.C.3}$$

hence

$$\frac{\mathrm{d}(1/r^2)}{\mathrm{d}u} = \frac{3(s_{\mathrm{a}} - s_{\mathrm{p}}) s_{\mathrm{p}}}{b^2 (s_{\mathrm{p}}^2 - 1)^2} \left[(u+1) - \frac{(u+1)^2}{2} \right] + O[(u+1)^3]. \tag{4.C.4}$$

Therefore, $1/r^2$ flattens near $u = -1$. I will therefore cut the integration in two parts: (i) I integrate the flat contribution near $u = -1$ linearly; (ii) I sample linearly in $\ln(u)$ the rest of the integral. I set the cutoff to be such that the slope is small with value $\varepsilon \ll 1$, i.e.

$$\frac{3(s_{\mathrm{a}} - s_{\mathrm{p}})s_{\mathrm{p}}}{b^2(s_{\mathrm{p}}^2 - 1)^2}\left[(u+1) - \frac{(u+1)^2}{2}\right] \leq \frac{\varepsilon}{b^2}. \tag{4.C.5}$$

Therefore

$$u + 1 \leq 1 - \sqrt{1 - \frac{2\,\varepsilon\,(s_{\mathrm{p}}^2 - 1)^2}{3(s_{\mathrm{a}} - s_{\mathrm{p}})s_{\mathrm{p}}}} \simeq \frac{\varepsilon\,(s_{\mathrm{p}}^2 - 1)^2}{3(s_{\mathrm{a}} - s_{\mathrm{p}})s_{\mathrm{p}}} \simeq \frac{\varepsilon\, r_{\mathrm{p}}^4}{3b^4(s_{\mathrm{a}} - 1)}, \tag{4.C.6}$$

and I choose $u_{\min} + 1 = \varepsilon\,(s_{\mathrm{p}}^2 - 1)^2/(3(s_{\mathrm{a}} - 1))$ to be the u-cutoff in the integral. Defining $v_{\min} = \ln(u_{\min} + 1)$, I can write

$$v_{\min} = \ln(\varepsilon) + 4\ln(r_{\mathrm{p}}) - \ln(3) - \ln(s_{\mathrm{a}} - 1). \tag{4.C.7}$$

Following energy conservation for $L \to 0^+$ (i.e. $r_{\mathrm{p}} \to 0^+$)

$$E = \psi(r_{\mathrm{p}}) + \frac{L^2}{2r_{\mathrm{p}}^2} = \psi(0) + \frac{L^2}{2r_{\mathrm{p}}^2} + o(L), \tag{4.C.8}$$

I obtain the asymptotic behaviour $r_{\mathrm{p}} \sim L/\sqrt{2(E - \psi[0])}$ as $L \to 0^+$. It follows that

$$v_{\min} \simeq \ln(\varepsilon) + 4\ln(L) - 2\ln(E - \psi[0]) - 2\ln(2) - \ln(3) - \ln(s_{\mathrm{a}} - 1). \tag{4.C.9}$$

I can use this approximation to avoid computing r_{p} with precision using bisection, as that method tends to give $|r_{\mathrm{p}}| \leq 10^{-16}$, hence $v_{\min} = -\infty$, due to rounding errors. Overall, I obtain the expression

$$\begin{aligned}\frac{\partial J_{\mathrm{r}}}{\partial L} &= -\frac{L}{\pi}\int_{-1}^{1}\frac{\mathrm{d}u\,\Theta(u)}{r^2(u)} = -\frac{L}{\pi}\int_{-1}^{u_{\min}}\frac{\mathrm{d}u\,\Theta(u)}{r^2(u)} - \frac{L}{\pi}\int_{u_{\min}}^{1}\frac{\mathrm{d}u\,\Theta(u)}{r^2(u)}\\ &= -\frac{(u_{\min}+1)\,L\,\Theta(\frac{u_{\min}-1}{2})}{\pi\, r^2(\frac{u_{\min}-1}{2})} - \frac{L}{\pi}\int_{v_{\min}}^{\ln 2}\frac{\mathrm{d}v\, e^v\,\Theta(e^v - 1)}{r^2(e^v - 1)}.\end{aligned} \tag{4.C.10}$$

In practice, I use $\varepsilon = 10^{-5}$.

4.D Testing the cluster's sphericity

In order to track the clusters' sphericity, I introduce the inertia-like matrix $\mathbf{I} = \{I_{ij}\}_{1\leq i,j\leq 3}$ where

$$I_{ii} = \frac{\sum_{k=1}^{N}\rho_k^2(r_k^2 - x_{i,k}^2)}{\sum_{k=1}^{N}\rho_k^2};\ I_{ij} = -\frac{\sum_{k=1}^{N}\rho_k^2 x_{i,k}x_{j,k}}{\sum_{k=1}^{N}\rho_k^2}\ (i \neq j), \tag{4.D.1}$$

with $r_k^2 = x_{1,k}^2 + x_{2,k}^2 + x_{3,k}^2$. In eq. (4.D.1), the extra ρ factor enhances the contributions from the regions close to the centre and reduces the ones from far-away stars.

The matrix $\mathbf{I}$ is symmetric and semi-definite positive. Indeed, it can be written as

$$\mathbf{I} = \sum_{k=1}^{N}\rho_k^2\left(||\boldsymbol{r}_k||^2 I_3 - \boldsymbol{r}_k\boldsymbol{r}_k^{\mathrm{T}}\right)\Big/\sum_{k=1}^{N}\rho_k^2 = \sum_{k=1}^{N}\rho_k^2\,\tilde{\mathbf{I}}_k\Big/\sum_{k=1}^{N}\rho_k^2, \tag{4.D.2}$$

from which symmetry is trivial. To prove semi-definite positiveness, I must show that $\mathbf{y}^{\mathrm{T}}\,\mathbf{I}\,\mathbf{y} \geq 0$

for any $\mathbf{y} \in \mathbb{R}^3$. Let me consider each term of the summation in eq. (4.D.2):

$$\begin{aligned} \mathbf{y}^{\mathrm{T}} \widetilde{\mathbf{I}}_k \, \mathbf{y} &= ||\boldsymbol{r}_k||^2 \, \mathbf{y}^{\mathrm{T}} \mathbf{y} - \mathbf{y}^{\mathrm{T}} \, \boldsymbol{r}_k \, \boldsymbol{r}_k^{\mathrm{T}} \, \mathbf{y} = ||\boldsymbol{r}_k||^2 \, \mathbf{y}^{\mathrm{T}} \mathbf{y} - (\boldsymbol{r}_k^{\mathrm{T}} \, \mathbf{y})^{\mathrm{T}} \, (\boldsymbol{r}_k^{\mathrm{T}} \, \mathbf{y}) \\ &= ||\boldsymbol{r}_k||^2 \, ||\mathbf{y}||^2 - |\langle \boldsymbol{r}_k, \mathbf{y} \rangle|^2 \geq 0, \end{aligned} \tag{4.D.3}$$

where the last inequality follows from Cauchy-Schwarz's inequality. Therefore it has three positive eigenvalues $\lambda_1, \lambda_2, \lambda_3$, which encapsulate the cluster's sphericality: when all eigenvalues are equal, the cluster is spherically symmetric. I generically define the cluster's sphericality with $j = \min_i \lambda_i / \max_i \lambda_i$. To reduce shot noise when estimating j, I average its value over realisations as follows. I compute the elementary symmetric polynomials $\alpha = \lambda_1 + \lambda_2 + \lambda_3$, $\beta = \lambda_1 \lambda_2 + \lambda_1 \lambda_3 + \lambda_2 \lambda_3$ and $\gamma = \lambda_1 \lambda_2 \lambda_3$ for every cluster, and average them over all realisations. From their expectation, I recover estimators for the eigenvalues λ_i as the roots of the polynomial $\lambda^3 - \langle \alpha \rangle \lambda^2 + \langle \beta \rangle \lambda - \langle \gamma \rangle$. In Fig. 4.4.2, I show the evolution of the sphericality j for various anisotropies. Its typical value is $j \simeq 0.996$, i.e. I can safely assume that the clusters remain on average spherically symmetric throughout their evolution.

4.E Pseudo-isotropic DF

Let me justify the expression of the P-Iso DF defined in eq. (4.6.1). First, I consider the energy distribution of the cluster with a DF $F_{\mathrm{tot}}(E, L)$ given by (see, e.g., Binney & Tremaine, 2008)

$$N(E) = \int \mathrm{d}\boldsymbol{r} \mathrm{d}\boldsymbol{v} \, \delta_{\mathrm{D}}(H - E) F_{\mathrm{tot}}(H, L). \tag{4.E.1}$$

Developing the integrand in eq. (4.E.1) yields

$$N(E) = 8\pi^2 \int \mathrm{d}r \, r^2 \int \mathrm{d}v_r \mathrm{d}v_{\mathrm{t}} \, v_{\mathrm{t}} \, \delta_{\mathrm{D}}(H - E) F_{\mathrm{tot}}(H, L), \tag{4.E.2}$$

where the integral is now restricted to positive values for v_r. Changing variables and resolving the Dirac yields

$$N(E) = (4\pi)^2 \int \mathrm{d}r \int_0^{L_{\max}} \mathrm{d}L \frac{L F_{\mathrm{tot}}(H, L)}{v_r}, \tag{4.E.3}$$

where $v_r^2 = 2(E - \psi[r]) - L^2/r^2$ and $L_{\max}(r, E) = 2r^2(E - \psi[r])$ is the maximum value of L which can be reached for a star with energy E and radius r. Let me define $R = L^2/L_{\mathrm{c}}^2$ and $R_{\max} = L_{\max}^2/L_{\mathrm{c}}^2$. Then $v_r = (L_{\mathrm{c}}/r)\sqrt{R_{\max} - R}$ and the energy distribution can be written as

$$N(E) = (4\pi)^2 \int \mathrm{d}r \, r L_{\mathrm{c}} \int_0^{R_{\max}} \frac{\mathrm{d}R \, F_{\mathrm{tot}}(E, L)}{\sqrt{R_{\max} - R}}. \tag{4.E.4}$$

Now, let me consider a system described by an isotropic DF, $F_{\mathrm{tot}}(E)$. Then eq. (4.E.4) becomes

$$N(E) = (4\pi)^2 \int \mathrm{d}r \, r L_{\mathrm{c}} F_{\mathrm{tot}}(E) \, 2\sqrt{R_{\max}}. \tag{4.E.5}$$

If I define the locally isotropic DF

$$F_{\mathrm{tot}}^{\text{P-Iso}}(r, E) = \frac{1}{2\sqrt{R_{\max}}} \int_0^{R_{\max}} \frac{\mathrm{d}R \, F_{\mathrm{tot}}(E, L)}{\sqrt{R_{\max} - R}}, \tag{4.E.6}$$

then eq. (4.E.4) becomes

$$N(E) = (4\pi)^2 \int \mathrm{d}r\, r L_{\mathrm{c}}\, F_{\mathrm{tot}}^{\text{P-Iso}}(r, E)\, 2\sqrt{R_{\max}}, \tag{4.E.7}$$

which is identical to the fully isotropic case. Therefore, the P-Iso distribution $F_{\mathrm{tot}}^{\text{P-Iso}}(r, E)$ corresponds to the locally isotropic DF of the anisotropic system which yields the same energy distribution as the fully anisotropic DF $F_{\mathrm{rot}}(E, L)$. Letting $R = R_{\max} \sin^2 x$, I recover the DF defined from eq. (4.6.1).

4.F Landau prediction (RR)

4.F.1 Coupling coefficients

Following Fouvry et al. (2021), the coupling coefficient $\psi^{\ell}_{\boldsymbol{k}\boldsymbol{k}'}$ (eq. 4.7.2) can be reduced to the expression

$$\psi^{\ell}_{\boldsymbol{k}\boldsymbol{k}'}(\boldsymbol{J}, \boldsymbol{J}') = y^{\ell}_{k_2}\, y^{\ell}_{k_2'}\, W^{\ell}_{\boldsymbol{k}\boldsymbol{k}'}(\boldsymbol{J}, \boldsymbol{J}'), \tag{4.F.1}$$

where $y^{\ell}_{k_2} = Y^{k_2}_{\ell}\left(\frac{\pi}{2}, 0\right)$ is a spherical harmonics, normalised such that $\int \mathrm{d}\hat{\mathbf{r}}\, |Y^{k_2}_{\ell}(\hat{\mathbf{r}})|^2 = 1$, and

$$W^{\ell}_{\boldsymbol{k}\boldsymbol{k}'}(\boldsymbol{J}, \boldsymbol{J}') = \int_0^{\pi} \frac{\mathrm{d}\theta_1}{\pi} \frac{\mathrm{d}\theta_1'}{\pi} U_{\ell}(r, r') \cos\left(k_1\theta_1 + k_2(\theta_2 - \theta)\right) \cos\left(k_1'\theta_1' + k_2'(\theta_2' - \theta')\right). \tag{4.F.2}$$

This coefficient involves the ℓ^{th} harmonics of the potential decomposition

$$U_{\ell}(r, r') = \frac{4\pi G}{2\ell + 1} \frac{\min(r, r')^{\ell}}{\max(r, r')^{\ell+1}}, \tag{4.F.3}$$

the phase angles (θ_1, θ_2) of the star with orbital parameters $\boldsymbol{J}$ and the phase angles (θ_1', θ_2') of the star with orbital parameters $\boldsymbol{J}'$. Using the effective anomaly obtained in eq. (4.5.5), I can rewrite $W^{\ell}_{\boldsymbol{k}\boldsymbol{k}'}$ and the phase angles in the more convenient forms

$$\theta_1(u) = \int_{-1}^{u} \mathrm{d}u'\, \Theta(u')\, \Omega_1, \tag{4.F.4a}$$

$$\theta_2(u) - \theta = \int_{-1}^{u} \mathrm{d}u'\, \Theta(u') \left(\Omega_2 - \frac{L}{r^2(u')}\right), \tag{4.F.4b}$$

and

$$\begin{aligned} W^{\ell}_{\boldsymbol{k}\boldsymbol{k}'}(\boldsymbol{J}, \boldsymbol{J}') = \frac{2\Omega_1}{\pi} \frac{2\Omega_1'}{\pi} \int_{-1}^{1} \frac{\mathrm{d}u}{2} \frac{\mathrm{d}u'}{2}\, \Theta(u)\Theta(u')\, U_{\ell}(r, r') \\ \times \cos\left(k_1\theta_1 + k_2(\theta_2 - \theta)\right) \cos\left(k_1'\theta_1' + k_2'(\theta_2' - \theta')\right). \end{aligned} \tag{4.F.5}$$

This multipole decomposition is very similar to the one used in chapter 3. Therefore, I can use the same method as in appendix 3.A to perform the integration. Now, contrary to the Keplerian case, I must also compute the angles θ_1, θ_2 numerically. However, because the integration variable is the same both for the coefficient $W^{\ell}_{\boldsymbol{k}\boldsymbol{k}'}$ and the phase angles, I can integrate both variables at the same time (Rozier et al., 2019). Finally, because of the $1/r^2$ term in the $\theta_2 - \theta$ integrand, the computation of $\theta_2 - \theta$ is very difficult for the effective anomaly u close to -1. This is solved by performing the integration in reverse – i.e. starting at $u = 1$.

4.F.2 Resonance condition

The final step in the computation of $\mathcal{F}^{\ell}_{\boldsymbol{k}\boldsymbol{k}'}(\boldsymbol{J})$ (eq. 4.7.2) is the integration over phase space w.r.t. the action variable $\boldsymbol{J}'$. To do so, I am constrained by a resonance condition. Following Fouvry & Prunet (2022), I define the dimensionless frequencies

$$\frac{1}{\alpha} = \frac{\Omega_1^{\max}}{\pi}\int_{r_{\mathrm{p}}}^{r_{\mathrm{a}}} \frac{\mathrm{d}r}{v_r(r,E,L)}, \quad \beta = \frac{L}{\pi}\int_{r_{\mathrm{p}}}^{r_{\mathrm{a}}} \frac{\mathrm{d}r}{r^2 v_r(r,E,L)}, \tag{4.F.6}$$

where $\Omega_1^{\max} = \max\Omega_1 = 2\Omega_0$. This defines a bijection between (J_{r}, L) and (α,β). By design, $0 \leq \alpha \leq 1$, with $\alpha = 0$ at the centre of the cluster and $\alpha = 1$ at infinity. As for the β variable, it is bound by the minimal value $1/2$ for radial orbits, and β_{c} its value for circular orbits. For the Plummer cluster, I cannot obtain the analytical formula $\beta_{\mathrm{c}} = \beta_{\mathrm{c}}(\alpha)$. However, I can compute its inverse relation

$$\alpha_{\mathrm{c}}(\beta) = \frac{1}{2}\frac{(1-\beta)^{3/4}}{3^{3/4}\beta^{5/2}}. \tag{4.F.7}$$

Letting $\omega_{\boldsymbol{k}} = \boldsymbol{k}\cdot\boldsymbol{\Omega}(\boldsymbol{J})$, I can rewrite the resonance condition in eq. (4.7.2) as

$$\omega_{\boldsymbol{k}} = \boldsymbol{k}'\cdot\boldsymbol{\Omega}(\boldsymbol{J}') = \Omega_1^{\max}(k_1'\alpha' + k_2'\alpha'\beta'). \tag{4.F.8}$$

Let me define

$$\omega_{\boldsymbol{k}}^{\min} = \min_{(\alpha,\beta)} \omega_{\boldsymbol{k}}(\alpha,\beta) = \min_{\beta} \omega_{\boldsymbol{k}}(\alpha_{\mathrm{c}}[\beta],\beta), \tag{4.F.9a}$$

$$\omega_{\boldsymbol{k}}^{\max} = \max_{(\alpha,\beta)} \omega_{\boldsymbol{k}}(\alpha,\beta) = \max_{\beta} \omega_{\boldsymbol{k}}(\alpha_{\mathrm{c}}[\beta],\beta), \tag{4.F.9b}$$

and

$$\Sigma_{\boldsymbol{k}} = \omega_{\boldsymbol{k}}^{\max} + \omega_{\boldsymbol{k}}^{\min}, \tag{4.F.10a}$$

$$\Delta_{\boldsymbol{k}} = \omega_{\boldsymbol{k}}^{\max} - \omega_{\boldsymbol{k}}^{\min}. \tag{4.F.10b}$$

I then define the change of variables

$$u = \frac{2\omega_{\boldsymbol{k}}(\alpha,\beta) - \Sigma_{\boldsymbol{k}}}{\Delta_{\boldsymbol{k}}}, \quad v = \begin{cases} \beta & \text{if } k_2 = 0, \\ \alpha & \text{if } k_2 \neq 0, \end{cases} \tag{4.F.11}$$

where $-1 \leq u \leq 1$ and $v > 0$ (since $\alpha > 0$ and $\beta \geq \frac{1}{2}$). Its inverse transformation is given by

$$\alpha = \begin{cases} \dfrac{\Sigma_{\boldsymbol{k}} + u\Delta_{\boldsymbol{k}}}{2k_1\Omega_1^{\max}} & \text{if } k_2 = 0, \\ v & \text{if } k_2 \neq 0, \end{cases} \quad \beta = \begin{cases} v & \text{if } k_2 = 0, \\ \dfrac{1}{n_2}\left(\dfrac{\Sigma_{\boldsymbol{k}} + u\Delta_{\boldsymbol{k}}}{2v\Omega_1^{\max}} - n_1\right) & \text{if } k_2 \neq 0, \end{cases} \tag{4.F.12}$$

with the Jacobians given by

$$\left|\frac{\partial(u,v)}{\partial(\alpha,\beta)}\right| = \frac{2\Omega_1^{\max}}{\Delta_{\boldsymbol{k}}} \times \begin{cases} k_1 & \text{if } k_2 = 0, \\ k_2\alpha & \text{if } k_2 \neq 0, \end{cases} \tag{4.F.13}$$

and

$$\left|\frac{\partial(\alpha,\beta)}{\partial(u,v)}\right| = \frac{\Delta_{\boldsymbol{k}}}{2\Omega_1^{\max}} \times \begin{cases} 1/k_1 & \text{if } k_2 = 0, \\ 1/(k_2 v) & \text{if } k_2 \neq 0. \end{cases} \tag{4.F.14}$$

I can then rewrite the $\boldsymbol{J}'$ integration of eq. (4.7.2) under the form

$$\mathcal{F}^{\ell}_{\boldsymbol{k}\boldsymbol{k}'}(\boldsymbol{J}) = \int \frac{\mathrm{d}\alpha'\mathrm{d}\beta'}{\alpha'^3(\Omega_1^{\max})^2}\, \frac{G(\boldsymbol{J},\boldsymbol{J}')}{|\mathrm{Hess}|}\, \delta_{\mathrm{D}}\big[\Omega_1^{\max}\alpha'(k_1' + k_2'\beta') - \omega_{\boldsymbol{k}}(\boldsymbol{J})\big]. \tag{4.F.15}$$

If a resonance line exists, then letting $\omega' = (\Delta_{\boldsymbol{k}} u' + \Sigma_{\boldsymbol{k}})/2$, eq. (4.F.15) becomes

$$\begin{aligned} \mathcal{F}^{\ell}_{\boldsymbol{k}\boldsymbol{k}'}(\boldsymbol{J}) &= \int \frac{\mathrm{d}\alpha'\mathrm{d}\beta'}{\alpha'^3(\Omega_1^{\max})^2}\, \frac{G(\boldsymbol{J},\boldsymbol{J}')}{|\mathrm{Hess}|}\, \delta_{\mathrm{D}}\left(\frac{\Delta_{\boldsymbol{k}'}u' + \Sigma_{\boldsymbol{k}'}}{2} - \omega_{\boldsymbol{k}}(\boldsymbol{J})\right) \\ &= \frac{2}{\Delta_{\boldsymbol{k}'}} \int \frac{\mathrm{d}\alpha'\mathrm{d}\beta'}{\alpha'^3(\Omega_1^{\max})^2}\, \frac{G(\boldsymbol{J},\boldsymbol{J}')}{|\mathrm{Hess}|}\, \delta_{\mathrm{D}}(u' - u_0), \end{aligned} \tag{4.F.16}$$

where $u_0 = (2\omega_{\boldsymbol{k}}[\boldsymbol{J}] - \Sigma_{\boldsymbol{k}'})/\Delta_{\boldsymbol{k}'}$, $|\mathrm{Hess}|$ is the Hessian of $J_{\mathrm{r}}(E,L)$ and

$$G(\boldsymbol{J},\boldsymbol{J}') = \frac{\pi(2\pi)^3 m}{2\ell+1} L\, L'\, |\psi^{\ell}_{\boldsymbol{k}\boldsymbol{k}'}(\boldsymbol{J},\boldsymbol{J}')|^2 \left(\boldsymbol{k}'\cdot\frac{\partial}{\partial\boldsymbol{J}'} - \boldsymbol{k}\cdot\frac{\partial}{\partial\boldsymbol{J}}\right) \frac{F(\boldsymbol{J})}{L}\frac{F(\boldsymbol{J}')}{L'}. \tag{4.F.17}$$

A final change of variable $(\alpha,\beta) \mapsto (u,v)$ transforms eq. (4.F.16) into

$$\mathcal{F}^{\ell}_{\boldsymbol{k}\boldsymbol{k}'}(\boldsymbol{J}) = \begin{cases} \dfrac{\mathrm{sgn}(k_1')k_1'^2}{\omega_{\boldsymbol{k}}(\boldsymbol{J})^3} \displaystyle\int_{u'=u_0} \mathrm{d}v'\, \frac{G(\boldsymbol{J},\boldsymbol{J}')}{|\mathrm{Hess}|} & \text{if } k_2' = 0, \\ \dfrac{1}{(\Omega_1^{\max})^3}\dfrac{1}{|k_2'|} \displaystyle\int_{u'=u_0} \frac{\mathrm{d}v'}{v'^4}\, \frac{G(\boldsymbol{J},\boldsymbol{J}')}{|\mathrm{Hess}|} & \text{if } k_2' \neq 0. \end{cases} \tag{4.F.18}$$

In the case $k_2' = 0$, then $v' = \beta'$, while in the case $k_2' \neq 0$, $v' = \alpha'$.

$k_1' + \frac{1}{2}k_2'$	ν	μ	Resonance line
$\neq 0$	> 1	×	None
$\neq 0$	$[0, 1]$	×	RC
$\neq 0$	$[\nu_{\min}, 0]$	×	CC
$\neq 0$	$< \nu_{\min}$	×	None
$= 0$	×	> 0	None
$= 0$	×	$[\mu_{\min}, 0]$	CC
$= 0$	×	$< \mu_{\min}$	None

Table 2: Nature of the resonance line depending on the resonance numbers (n_1', n_2') and action location $\boldsymbol{J}$. The resonance line can either be bound by a radial and a circular orbit (denoted as RC), by two circular orbits (CC), or might not exist.

I still have to determine the boundaries of the resonance line in order to compute these integrals. There are two types of resonance lines: (i) a radial-circular resonance line, whose boundaries are radial and circular orbits; (ii) a circular-circular resonance line, whose boundaries are both circular orbits. Let me define $\nu_{\boldsymbol{k}'} = \omega_{\boldsymbol{k}'}/[\Omega_1^{\max}(k_1' + \frac{1}{2}k_2')]$ and $\nu = \omega/[\Omega_1^{\max}(k_1' + \frac{1}{2}k_2')]$. Similarly, let me define $\mu_{\boldsymbol{k}'} = \omega_{\boldsymbol{k}'}/(\Omega_1^{\max}k_1') = \alpha(1-2\beta)$and $\mu = \omega/(\Omega_1^{\max}k_1')$. For each of these, I define their minimum value

$$\nu_{\mathrm{min}} = \min_{\beta\in[\frac{1}{2},1]} \nu_{\boldsymbol{k}'}(\alpha_{\mathrm{c}}[\beta],\beta) = \min_{\beta\in[\frac{1}{2},1]} \frac{\alpha_{\mathrm{c}}(\beta)\,(k_1'+k_2'\beta)}{k_1'+\frac{1}{2}k_2'}, \tag{4.F.19a}$$

$$\mu_{\mathrm{min}} = \min_{\beta\in[\frac{1}{2},1]} \mu_{\boldsymbol{k}'}(\alpha_{\mathrm{c}}[\beta],\beta) = \min_{\beta\in[\frac{1}{2},1]} \alpha_{\mathrm{c}}(\beta)\,(1-2\beta). \tag{4.F.19b}$$

Finally, I regroup the different cases in Tab. 2.

If $k_1'+\frac{1}{2}k_2'\neq 0$, then the radial boundary is always set by $(\alpha,\beta)=(\nu,1/2)$. In any case, if one or two circular boundaries exist, then they are given by $(\alpha,\beta)=(\alpha_{\mathrm{c}}[\beta],\beta)$, where β is a solution of $\omega_{\boldsymbol{k}'}(\alpha_{\mathrm{c}}[\beta],\beta)=\omega$.

4.G Computing the NR diffusion coefficients from Landau theory

Let me give a few key points of the derivations of eq. (4.7.11). Consider a radial star $(L=0)$ with a low energy orbit $(E\sim\psi[0])$, so that its unperturbed motion is approximately simply harmonic. Letting ϕ be an angle variable and ω be its frequency, we have

$$\boldsymbol{r}(\phi)=\boldsymbol{r}_0\cos\phi \quad ; \quad \boldsymbol{r}(t)=\boldsymbol{r}_0\cos\omega t, \tag{4.G.1}$$

where $\boldsymbol{r}_0$ is a constant vector. Because the star is located deeply within the potential, most of the stars which perturb its motion will have a much higher energy. Additionally, in order to exert substantial perturbations on the test star's motion, the perturbing star must be close to the centre, i.e. its angular momentum must be low. Suppose for simplicity that their angular momentum is $L_{\mathrm{p}}=0$. The rate of change of the perturbed star's energy is given by

$$\dot{E}=\dot{\boldsymbol{r}}\cdot\frac{\partial}{\partial\boldsymbol{r}}\bigg(\sum_{\mathrm{p}}\frac{Gm}{|\boldsymbol{r}-\boldsymbol{r}_{\mathrm{p}}|}+\psi(\boldsymbol{r},t)\bigg), \tag{4.G.2}$$

where the sum is performed over the perturbers indexed by p. Since $\boldsymbol{r}$ is a periodic function of ϕ, we can write

$$\psi(\boldsymbol{r},t)=\sum_{\ell}\psi_\ell(t)\mathrm{e}^{\mathrm{i}\ell\phi}, \tag{4.G.3}$$

hence

$$\dot{\boldsymbol{r}}\cdot\frac{\partial\psi}{\partial\boldsymbol{r}}=\dot{\phi}\cdot\frac{\partial\psi}{\partial\phi}=\mathrm{i}\omega{\sum_{\ell}}'\,\ell\,\psi_\ell\,\mathrm{e}^{\mathrm{i}\ell\phi}, \tag{4.G.4}$$

where the prime denotes the fact that the summation excludes $\ell=0$. Furthermore, we can also use the decomposition

$$\dot{\boldsymbol{r}}\cdot\frac{\partial}{\partial\boldsymbol{r}}\bigg(\frac{Gm}{|\boldsymbol{r}-\boldsymbol{r}_{\mathrm{p}}|}\bigg)=\sum_{\ell}\sum_{n}a_{\ell n}\,\mathrm{e}^{\mathrm{i}(\ell\phi+n\phi_{\mathrm{p}})}, \tag{4.G.5}$$

for certain quantities $a_{\ell n}$ using the periodicity of each angle variables. As we are interested in computing the first-order change in E, the expressions for the unperturbed motion may be substituted for ϕ and ϕ_{p} on the r.h.s. of eq. (4.G.2), that is,

$$\phi=\phi_0+\omega t;\quad \phi_{\mathrm{p}}=\phi_{\mathrm{p}0}+\omega_{\mathrm{p}}t, \tag{4.G.6}$$

where $\phi_0, \phi_{\mathrm{p}0}$ are initial values. Now, let us compute the average value of $(\Delta E)^2$, assuming that stars are randomly distributed along orbits (in the sense that ϕ_0 and $\phi_{\mathrm{p}0}$ are distributed uniformly and independently). A lengthly computation yields

$$\langle \Delta E^2 \rangle = \frac{1}{t} \sum_{\mathrm{p}} \sum_{\ell}{}' \sum_{n}{}' |a_{\ell n}|^2 \frac{\sin^2(x_{\mathrm{p}} t)}{x_{\mathrm{p}}^2}, \tag{4.G.7}$$

where $x_{\mathrm{p}} = \frac{1}{2}(\ell\omega + n\omega_{\mathrm{p}})$. Let us drop the prime notation for clarity. We shall suppose that the DF of the perturbing stars (in position-velocity space) is a function of energy alone, i.e. $F_{\mathrm{tot}}(\boldsymbol{r}_{\mathrm{p}}, \boldsymbol{v}_{\mathrm{p}}) = F_{\mathrm{tot}}(E_{\mathrm{p}})$. Then the distribution of E_{p} and L_{p} is $F_{\mathrm{tot}}(E_{\mathrm{p}}, L_{\mathrm{p}})$ where, following Spitzer & Shapiro (1972),

$$F_{\mathrm{tot}}(E_{\mathrm{p}}, L_{\mathrm{p}}) \mathrm{d}E_{\mathrm{p}} \mathrm{d}L_{\mathrm{p}} = \frac{8\pi^3}{\omega_{\mathrm{p}}} F_{\mathrm{tot}}(E_{\mathrm{p}}) \mathrm{d}E_{\mathrm{p}} \mathrm{d}L_{\mathrm{p}}. \tag{4.G.8}$$

Thus the diffusion coefficient reads

$$\langle \Delta E^2 \rangle = \frac{1}{t} \sum_{\ell} \sum_{n} \int \mathrm{d}E_{\mathrm{p}} \mathrm{d}L_{\mathrm{p}}\, F_{\mathrm{tot}}(E_{\mathrm{p}}, L_{\mathrm{p}}) \langle |a_{\ell n}|^2 \rangle \frac{\sin^2(x_{\mathrm{p}} t)}{x_{\mathrm{p}}^2}, \tag{4.G.9}$$

where $\langle |a_{\ell n}|^2 \rangle$ is an average taken over all perturbers with particular values of $E_{\mathrm{p}}, L_{\mathrm{p}}$. In the limit of large t, we substitute the sinc term with a Dirac function. This yields

$$\langle \Delta E^2 \rangle = 4\pi \sum_{\ell>0} \sum_{n<0} \frac{1}{|n|} \int \mathrm{d}L_{\mathrm{p}} \left| \frac{\partial E_{\mathrm{p}}}{\partial \omega_{\mathrm{p}}} \right| F_{\mathrm{tot}}(E_{\mathrm{p}}, L_{\mathrm{p}})\, \langle |a_{\ell n}|^2 \rangle, \tag{4.G.10}$$

where the value of E_{p} corresponds to the resonance condition $x_{\mathrm{p}} = 0$, i.e. a perturber such that $n\omega_{\mathrm{p}} + \ell\omega = 0$. After computation, the contribution from all resonances yields eq. (4.7.11).

Chapter 5

Rotating globular clusters

5.1 Introduction

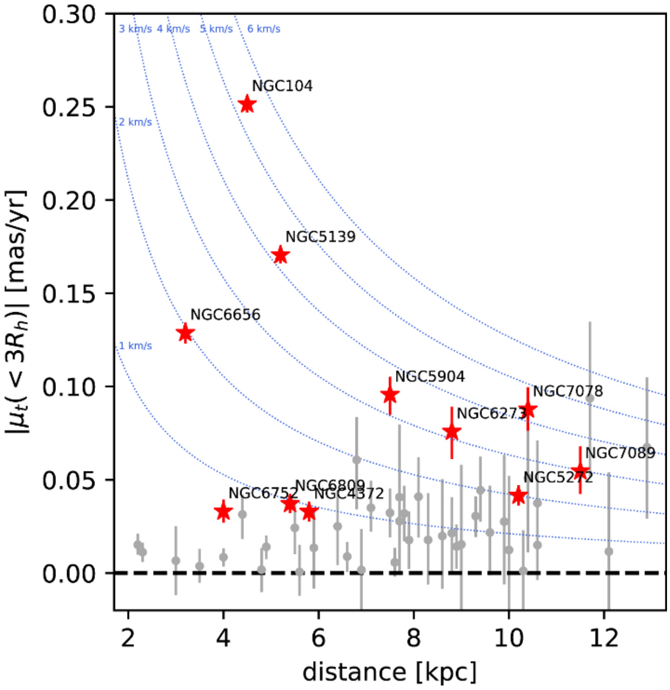

Figure 5.1.1: From fig. 2 of Bianchini et al. (2018). Representation of the mean proper motion along the tangential component measured in a 3 half-light radii field-of-view around a large sample of globular clusters using proper motions from Gaia DR2. Red stars indicate clusters for which rotation is detected at least with a 3-sigma confidence level. Overall, a significant fraction of globular clusters have been shown to be rotating.

Rotation is ubiquitous. I showed in chapter 2 that kinetic theory involves the gradient of the distribution function w.r.t. to angular momentum, both explicitly (eq. 2.2.31) and implicitly (eq. 2.2.30) via the dressing of the interaction potential. These gradients spike when the dynamics is dominated by a coherent flow in regions within the cluster where the effective moment of inertia of the orbits is small and positive (e.g., at the inner Lindblad resonance), allowing self-torquing to operate for a long time (Rozier et al., 2019). In effect rotation provides a source of free energy, allowing the cluster to do work to reshuffle its orbital structure more efficiently towards more likely configurations while amplifying shot noise. Yet, historically, the study of globular clusters has been limited to initially isotropic, non-rotating, old globular clusters with a single stellar population (Aarseth et al., 1974; Spitzer & Shull, 1975; Cohn, 1979; Trager et al., 1995; Miocchi et al., 2013). The reasons behind this are two-fold: just as in the anisotropic case, it is easier numerically and analytically to neglect the effect of rotation. Indeed, spherical isotropic models – e.g., the King models (King, 1966) or the Wilson models (Wilson, 1975) – provided a satisfactory zeroth-order description of their main observed dynamical properties (see, e.g., McLaughlin & van der Marel, 2005).

However, the large scale structures in which stellar systems evolve exhibit some degree of anisotropy related to the primordial density field (West, 1994). These spin up stellar systems either through their relative alignments (Plionis & Basilakos, 2002) or through the infall of satellites onto the main cluster (Tormen, 1997; Aubert et al., 2004; Pichon et al., 2011). Angular momentum may also be generated through the violent relaxation of initially non-rotating cold self-gravitating systems in some cases (Benhaiem et al., 2016). Additionally, the last decade has seen the emergence of new data (Fig. 5.1.1) – e.g., HST (see Fig. 5.1.2 and Bellini et al., 2017) and Gaia DR2 (Bianchini et al., 2018; Sollima et al., 2019). These surveys gave the astrophysical community access to numerous and detailed observations of the internal kinematics of several globular clusters of the MW (Bianchini et al., 2013; Fabricius et al., 2014; Watkins et al., 2015; Ferraro et al., 2018; Kamann et al., 2018), as well as a quantification of the degree of anisotropy in the three-dimensional velocity space (Jindal et al., 2019). Using these data, the historical static cluster models are not satisfactory anymore. Therefore, a kinetic theory which describes the evolution of globular clusters and accounts for their rotation is needed. Observations show that the angular momentum distribution which is measured in Galactic clusters was shown to contain the signature of their formation process (Lanzoni et al., 2018). While N-body simulations are able to reproduce these results (Tiongco et al., 2016, 2022), the historical context and the complexity of the problem have led to few analytical explorations (Geyer et al., 1983; White & Shawl, 1987; Kontizas et al., 1989). These remain scarce even now (see, e.g., Stetson et al., 2019; Rozier et al., 2019; Livernois et al., 2022).

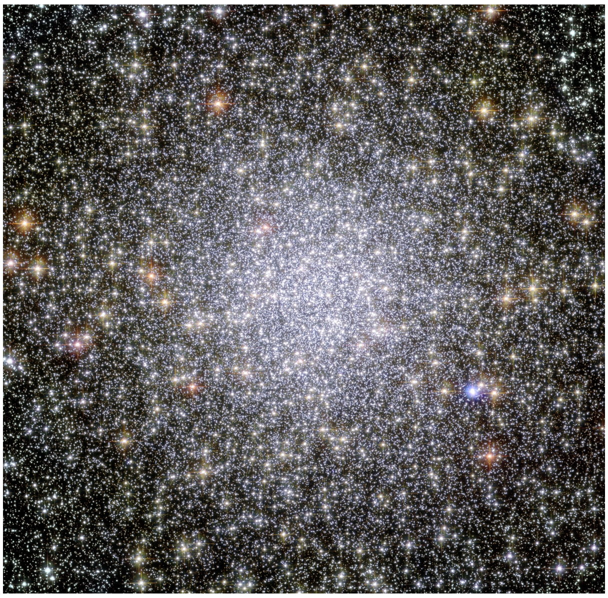

Figure 5.1.2: Image of 47 Tuc, which is one of the most massive globular clusters of the Milky Way. High-precision measurements of Bellini et al. (2017) have shown the existence for rotation in this cluster. Credit: NASA/ESA.

Interestingly, the secular fate of rotating objects still remains an open question. For isolated systems, a non-vanishing total angular momentum can have a significant impact on the cluster's long-term evolution compared to its non-rotating counterpart. It has been shown to induce complex dynamical evolutions such as a *gravo-gyro catastrophe* (Hachisu, 1979; Ernst et al., 2007). This phenomenon has been observed in a range of systems, including rotating gas cylinders (Inagaki & Hachisu, 1978; Hachisu, 1979), rotating gaseous discs (Hachisu, 1982), rotating flattened (quasi-spherical) star clusters (Akiyama & Sugimoto, 1989; Einsel & Spurzem, 1999; Ernst et al., 2007) or embedded BHs (Fiestas & Spurzem, 2010; Kamlah et al., 2022). However, a large part of these studies have used a *rotating King model* to study the impact of rotation (see, e.g., Einsel & Spurzem, 1999; Varri & Bertin, 2012). In particular, changing the rotation parameter impacts the density profile, and may therefore pose a problem when comparing rotation models.

Alternatively, the joint presence of some internal rotation and a stellar mass spectrum seems to produce an oblate core of fast rotating heavy masses (Kim et al., 2004; Tiongco et al., 2021). The orbital inclinations of the heaviest stars decrease over time, inducing mass segregation in the distribution of orbital inclinations in addition to the well-known radial (isotropic) mass segregation (Szölgyén et al., 2019). The generally agreed explanation for this phenomenon is resonant relaxation and resonant friction (Rauch & Tremaine, 1996; Meiron & Kocsis, 2019). While this effect concerns rotating star clusters, nuclear cluster simulations containing a dominant massive black hole (Szölgyén & Kocsis, 2018; Foote et al., 2020; Gruzinov et al., 2020; Magnan et al., 2022) also appear to produce this phenomenon.

In this chapter, I will consider the same isolated, anisotropic Plummer globular cluster from the previous chapter, and will add rotation. I will present the results of a series of N-body simulations of Plummer clusters with a wide range of rotation in section 5.2. I will use these to determine which range of parameters are still compatible with the clusters remaining linearly stable and spherically symmetric. Then, I will measure the time-evolution of both radial and azimuthal diffusion to probe the impact of rotation on both processes. In section 5.3, I will apply the NR formalism (derived in section 2.3.3) to predict these two diffusions. In particular, I will discuss the limitations of the NR theory, which are most visible when studying the azimuthal diffusion.

5.2 N-body simulations

In order to study the impact of rotation on a globular cluster, let me first consider the system from chapter 4 to which I add rotation via orbital flips using the Lynden-Bell demon procedure. In practice, this corresponds to: (i) I draw a sample of stars for the non-rotating cluster using the `PlummerPlus.py` script (see Breen et al., 2017); (ii) then, I switch the sign of L_z for a fraction α of retrograde orbits chosen at random. The larger α, the more rotating the cluster is. This method allows me to preserve the spherical symmetry of the density distribution as well as the positivity of the DF.

As the cluster needs to be recentred in position and velocity, I apply the procedure presented in section 4.4.1.

5.2.1 Sphericality and instabilities

In order to study the evolution of rotating clusters, I compute the actions (J_{r}, L, L_z) of each star in the system. Then, I recover their inclination I using $\cos I = L_z/L$.

Note that Rozier et al. (2019) showed that rotating clusters – with initial spherical symmetry

– could harbour unstable modes (see Fig. 5.2.1), which may induce a flattening of the cluster.

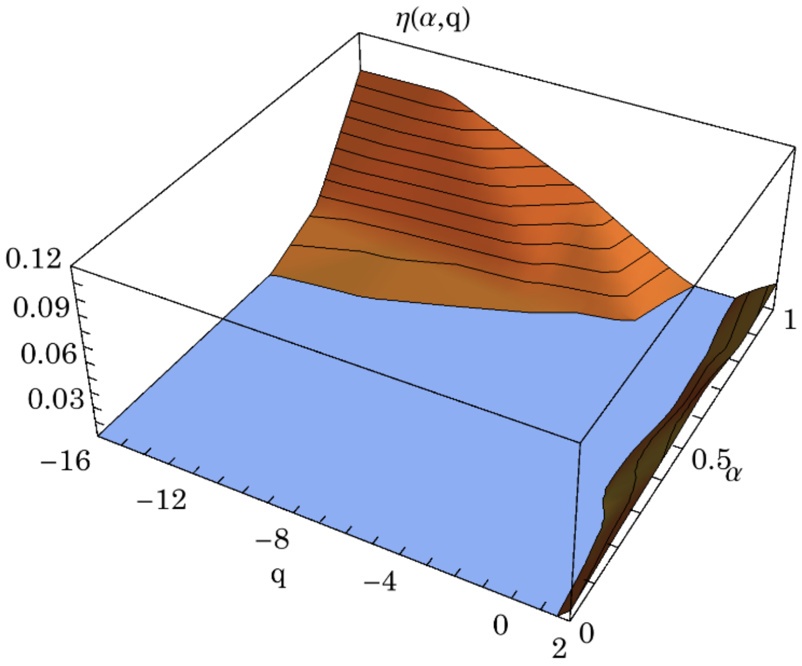

Figure 5.2.1: From fig. 8 of Rozier et al. (2019). Illustration of the dependence of the growth rate, $\eta(\alpha, q)$, of the dominant unstable mode in rotating clusters, as a function of the cluster's parameters (α, q), measured here using N-body methods. Beyond some q-dependent rotation-threshold, rotating clusters are (linearly) unstable, hence breaking away from spherical symmetry.

Computationally, moving beyond spherical symmetry is costly when estimating the potential and makes the orbits more intricate. In addition, in axisymmetric systems, L is not an integral of motion anymore (though L_z remains one).

Hence, I will restrict myself to (linearly) stable rotating systems which conserve their spherical symmetry, at least initially. To probe the conservation of symmetry, I rely on *sphericality*, as introduced in appendix 4.D. I follow its evolution for a range of rotating clusters in Fig. 5.2.2, using N-body simulations. In that figure, all the clusters appear to approximately conserve their spherical symmetry, with the clear exception of the radially-anisotropic cluster $(q, \alpha) = (1, 0.5)$. In that particular case, the cluster flattens quickly. This is in agreement with the measurements from Fig. 5.2.1, as this cluster falls into the region of instability.

5.2.2 Radial diffusion

Having identified stable rotating globular clusters, I rely on N-body simulations to study the impact of rotation on their long-term evolutions. Following chapter 4, a natural starting point is to look at the evolution of the core radius. The result is presented in Fig. 5.2.3. Rotation does not impact appear to impact the rate of core collapse in rotating clusters. For the unstable cluster $(q, \alpha) = (1, 0.5)$, the corresponding mode likely impacts the efficiency of the cluster's overall relaxation. Indeed, the deviation from the other core collapse plots happens around $t \sim 100\,\mathrm{HU}$. This corresponds to the time where the instabilities begins to grow in Fig. 5.2.2, i.e. when flattening occurs. A slight instability is also occurring for $(q, \alpha) = (1, 0.25)$, as predicted by Fig. 5.2.1, but it is small enough so that I can still assume spherical symmetry during the early evolution of the cluster.

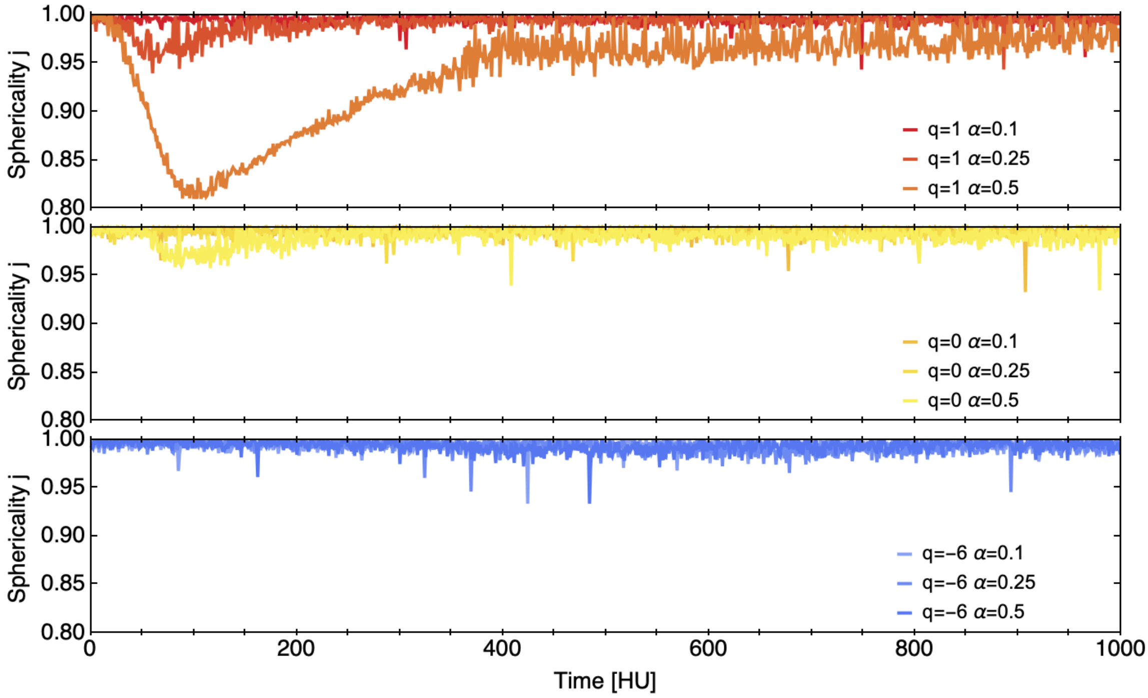

Figure 5.2.2: Sphericality of a sample of rotating clusters, as observed in my N-body simulations. Each of the clusters have been averaged over 50 realisations. I represent radial clusters ($q = 1$) in red, isotropic clusters ($q = 0$) in yellow and tangential ones ($q = -6$) in blue, for three rotating parameters $\alpha = 0.1, 0.25, 0.5$. In agreement with the results from Rozier et al. (2019) shown in Fig. 5.2.1, some of these clusters are unstable – namely $(q, \alpha) = (1, 0.5)$, and in a smaller fashion $(q, \alpha) = (1, 0.25)$, while the others are linearly stable and conserve their spherical symmetry.

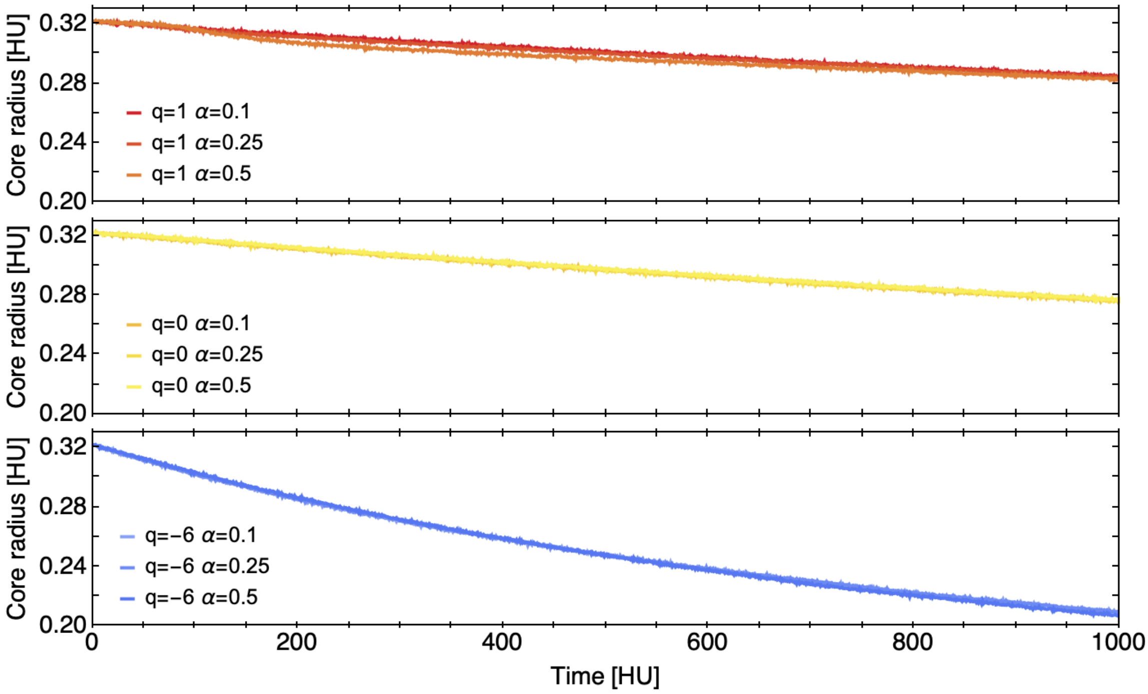

Figure 5.2.3: Evolution of the core radius as measured in N-body simulations. Each of the clusters have been averaged over 50 realisations. Colour-coding is the same as in Fig. 5.2.2. Interestingly, in stable clusters, rotation weakly impacts the rate of core collapse compared to the effect of velocity anisotropy.

In order to probe the impact of rotation on secular evolution, I measure in N-body simulations the diffusion in the (J_{r}, L)-space. This choice is motivated by the fact that the core radius only depends on stellar density, hence is not impacted by orbital inclination. I present this measurement in Fig. 5.2.4. As was already the case in non-rotating clusters, the clusters appear to isotropise. I observe a depletion of radial orbits in clusters with initial radial velocity anisotropy, and I observe a depletion of circular orbits in clusters with initial tangential velocity anisotropy. However, the strength of rotation, α, does not appear to have a significant impact on the geometry of radial diffusion.

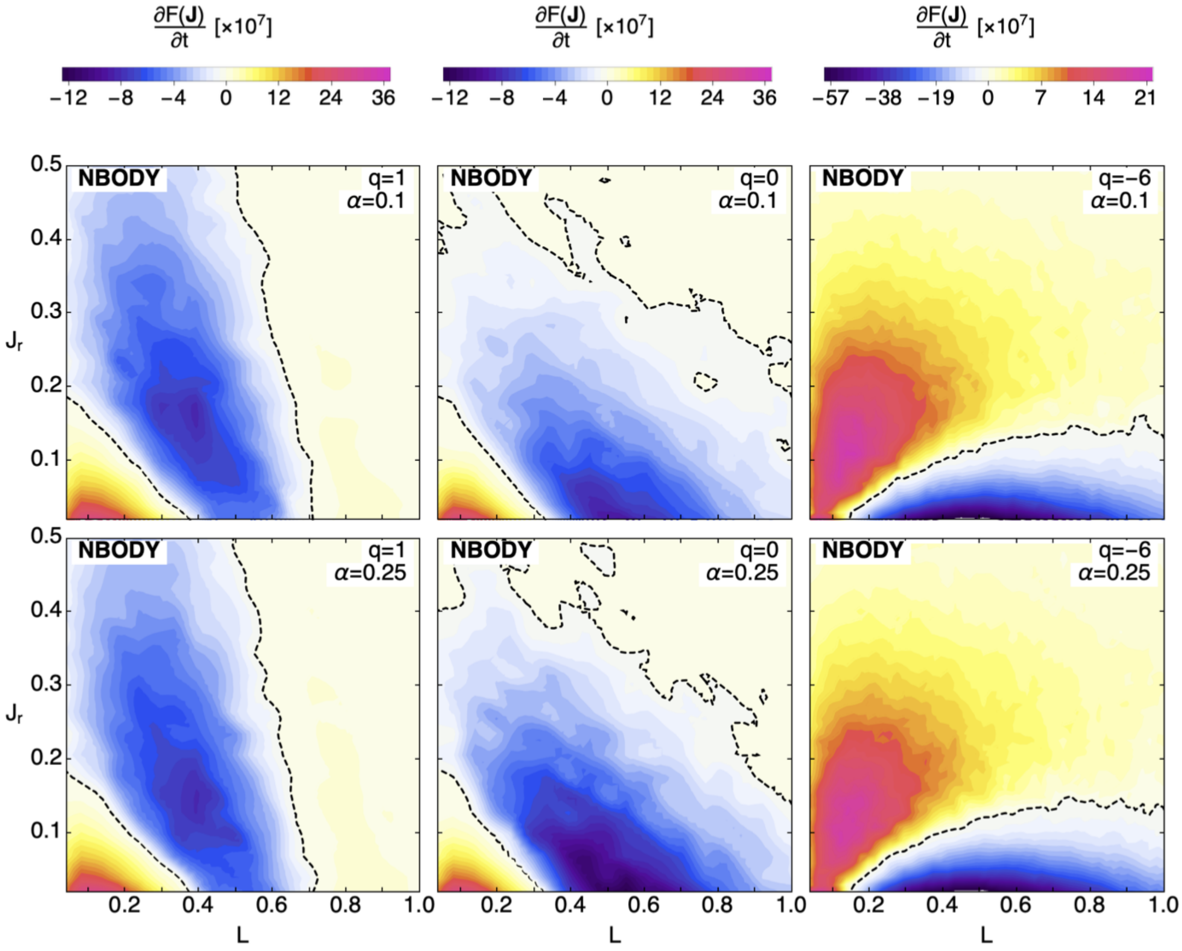

Figure 5.2.4: Illustration of the relaxation rate, $\partial F / \partial t$, for various values of the anisotropy parameter q (left to right) and rotation parameter α (top and bottom), as measured in N-body simulations in the (J_{r}, L)-space. The amplitude of the radial relaxation rate depends on q as seen in chapter 4, but does not appear to depend strongly on the amount of rotation α.

5.2.3 Azimuthal diffusion

I now consider the evolution of the stars' orbital inclinations. This is presented in Fig. 5.2.5. For the rotation-free cluster, as expected, the evolution of the DF is independent of $\cos I$. Therefore, integrating over J_{r} yields a DF in $\cos I$ whose time derivative vanishes: the system does not gain any rotation.

Now, let me consider the case of the rotating clusters. First of all, for the radially anisotropic $(q = 1)$ and isotropic $(q = 0)$ clusters, the systems tend to lose stars in the region $\cos I > 0$

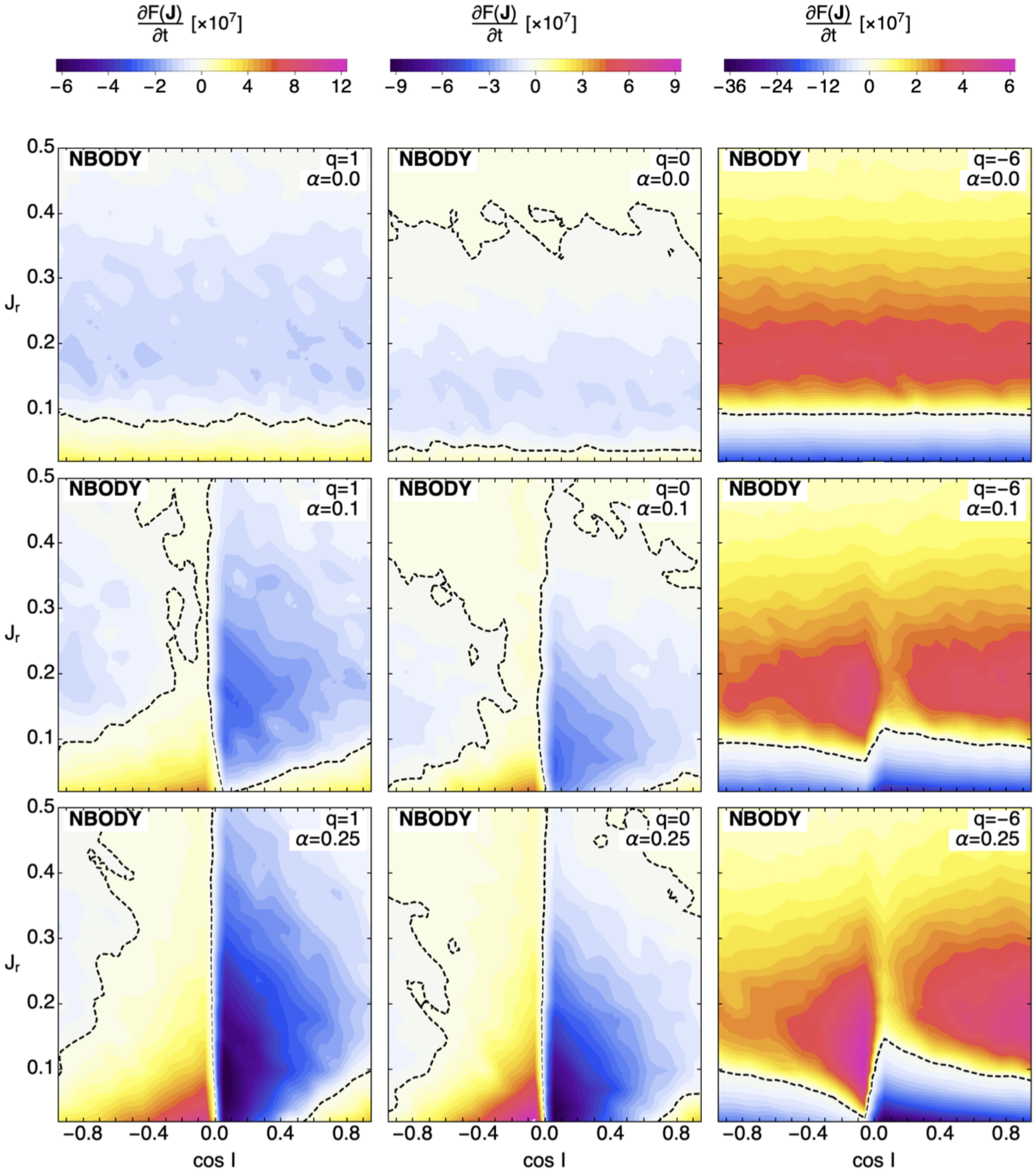

Figure 5.2.5: Illustration of the relaxation rate, $\partial F/\partial t$, for various values of the anisotropy parameter q (left to right) and rotation parameter α (from top to bottom), as measured in N-body simulations in the $(J_{\mathrm{r}}, \cos I)$-space. The amplitude and structure observed depend on anisotropy, and show a reshuffling of orbits towards isotropisation. They also depend on rotation: the orbital inclinations reshuffle toward a more affine distribution in $\cos I$.

(prograde) and gain stars in the region $\cos I < 0$ (retrograde). As I increase the number of prograde orbits in the cluster (i.e. I increase α), I observe that this trend strengthens. This phenomenon is related to the reshuffling of orbits observed in anisotropic clusters, where the systems always seemed to isotropise. The highest diffusion rates in inclination are observed near $\cos I = 0$, where the discontinuity of the LBD occurs (eq. 2.3.36). Overall, the systems appear to evolve towards a state in which the inclination distribution is smoother.

At first glance, the case $q = -6$ may appear to be slightly different. Indeed, a depletion in orbits is observed for low J_{r} of any $\cos I$ (as a result of isotropisation). On the other hand, an increase in orbits is observed for higher J_{r}, yet again for any $\cos I$. This reshuffling is to be linked to the isotropisation of the cluster, which was initially tangentially biased. Now, if I focus on the amplitude of depletion, I observe that more orbits are depleted in the $\cos I > 0$ region than in the $\cos I < 0$ region. This is the orientation reshuffling which I observed for the $q = 1$ and $q=0$ cluster, and is the signature of rotation.

As a complement, diffusion maps in the $(L, \cos I)$-space are shown in appendix 5.B. There, I observe a similar reshuffling of inclinations from the over-populated regions toward the under-populated regions. Orbital reshuffling due to anisotropy also occurs: I observe either a depletion $(q=1)$ or an increment $(q=-6)$ of radial orbits $(L=0)$.

5.2.4 Inclination relaxation

Finally, I measure the time evolution of the DF in $\cos I$ in Fig. 5.2.6 (averaged over 50 realisations of rotating clusters). It appears that the systems tend towards a more affine distribution of inclinations, as if relaxation was erasing the discontinuity. Indeed, the sharp discontinuity at $\cos I = 0$ has already been washed away after $50\,\mathrm{HU}$, which corresponds to a small fraction of the cluster's relaxation time (namely to $0.05\,t_{\mathrm{rh}}$, with the half-mass relaxation time t_{rh} defined in eq. 5.2.1). Additionally, the more rotation the cluster initially has, the faster the discontinuity disappears. To draw a definitive conclusion on the universality of this observation, it would be

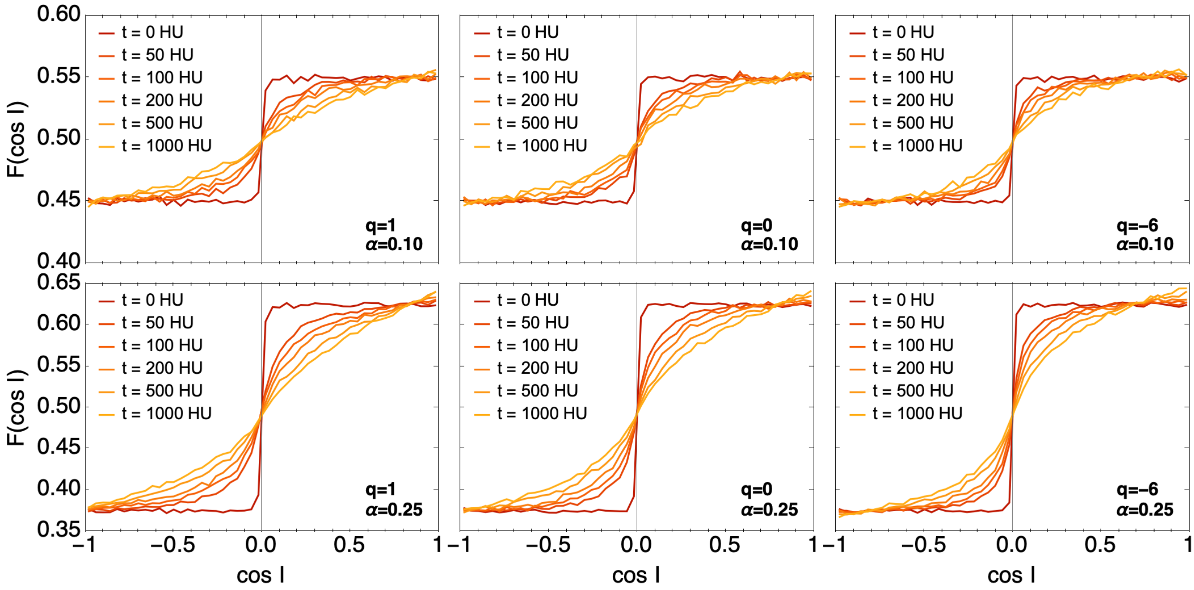

Figure 5.2.6: Evolution of the DF, $F(\cos I)$, describing orbital inclinations, as measured in N-body simulations. The relaxation of orbital inclinations does not depend much on the initial anisotropy. The time evolution appears to converge towards a more affine distribution of orbital inclinations.

of interest to repeat this experiment with other parameterisations for the rotation. This is left for future investigations.

Note that the loss and gain of prograde or retrograde orbit does not contradict the conservation of angular momentum. Indeed, I consider the evolution of $\cos I = L_z/L$, whose average is not constrained by a conservation law, contrary to L_z. To resolve this apparent paradox, one can point that even if the number of particles with positive and negative $\cos I$ (hence L_z) changes, the conservation of angular momentum can be still ensured by a modulation of the norm of each star's angular momentum.

5.2.5 Long-term relaxation

In the previous sections, I considered a cluster with $N = 10^5$ stars (i.e. the typical number of stars in a globular cluster). This large number of particles allowed me to reduce fluctuations when measuring $\partial F/\partial t$ in N-body simulations. However, such a large number of particles induces a very slow relaxation. This timescale can be estimated using the *half-mass relaxation time* (see, e.g., section 14 of Heggie & Hut, 2003, for more details), defined by

$$t_{\mathrm{rh}} = \frac{0.138\, N^{1/2} r_{\mathrm{h}}^{3/2}}{(Gm)^{1/2} \ln(0.11\, N)}, \tag{5.2.1}$$

where r_{h} is the *half-mass radius*. In Breen et al. (2017), core collapse occurs at $\sim 17 t_{\mathrm{rh}}$ for an isotropic cluster (see tab. 1 of their work for a proper measurement w.r.t. anisotropies). For a cluster with $N = 10^5$ stars, a quick computation yields $t_{\mathrm{rh}} = 994\,\mathrm{HU}$, meaning that my studies have been limited to the very early evolution of the clusters. Because I was interested in the initial evolution of the cluster (as a probe of its secular evolution), this was not a limitation. However, if I had wished to reach core collapse, I would have had to push the numerical integration of orbits up to $\sim 17000\,\mathrm{HU}$. As a single run of `NBODY6++GPU` takes about a day (parallelised over 40 threads) to integrate until $\sim t_{\mathrm{rh}}$, integrating up to core collapse would not be feasible.

Therefore, in this section I now temporarily consider clusters with $N = 10^4$ stars. In this case, $t_{\mathrm{rh}} = 132\,\mathrm{HU}$, meaning that core collapse is reached after $\sim 2200\,\mathrm{HU}$ for an isotropic cluster. With the lower number of stars, as well as the shorter core collapse time, the time integration is much swifter and the core collapse is reached in approximatively $10\mathrm{h}$. Furthermore, as I am interested in computing the core radius evolution – a very integrated quantity – fluctuations do not impact its measurement as much as they impact $\partial F/\partial t$. In practice, I average these measurements over 10 runs.[a]

Figure 5.2.7 shows the averaged evolution of the core radius for the usual sets of anisotropies and rotations ($q = 1, 0, -6$ and $\alpha = 0, 0.1, 0.25, 0.5$). It is the analogue of Fig. 4.1.2, where time integration has been pushed forwards. For these sets of rotating clusters, the impact of rotation is not as important as the one observed in Einsel & Spurzem (1999) for *rotating King models*. Furthermore, the spread of core collapse times between individual realisations of clusters with the same anisotropy does not allow me to distinguish clearly between, say, a non-rotating cluster ($\alpha = 0$) and a very rotating cluster ($\alpha = 0.5$) for the same value of q.

---

[a] One run in the cluster $(q, \alpha) = (0, 0.1)$ was arbitrarily discarded, as it deviated too much from the typical averaged evolution of the core radius. Two runs, which did not reach $R_{\mathrm{c}} = 0.001\,\mathrm{HU}$, were also discarded and replaced by runs which did so. Because the spread between realisations is quite large in practice, this does not affect the trend observed in Fig. 5.2.7.

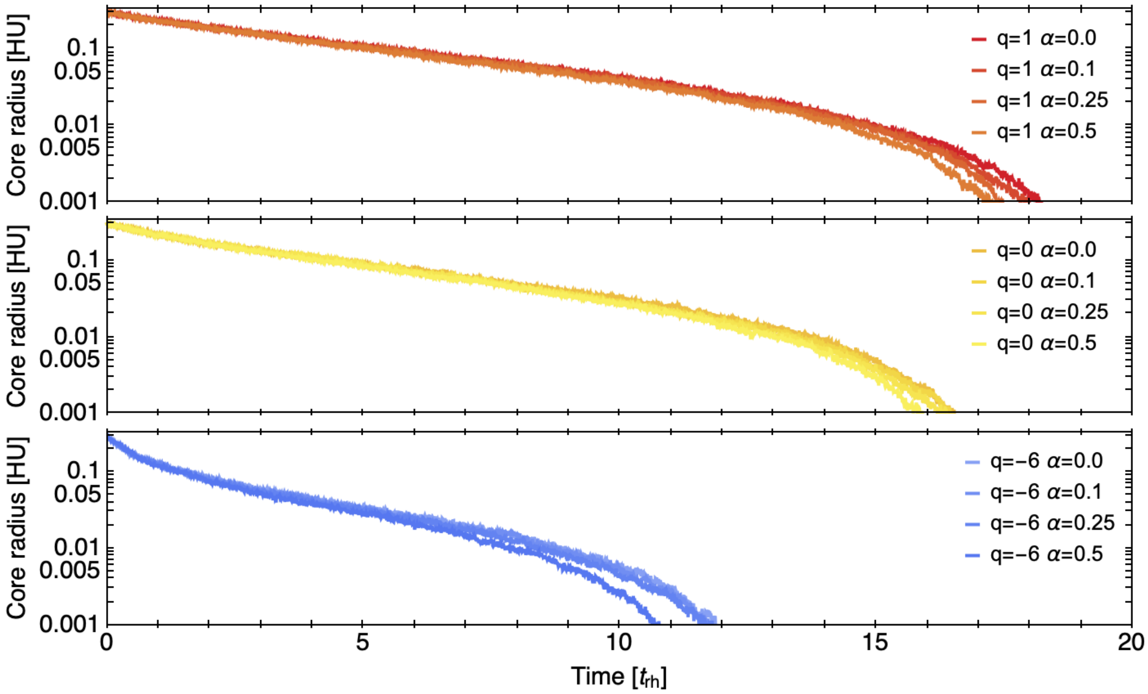

Figure 5.2.7: Evolution of the core radius as measured in N-body simulations. Each of the clusters have been averaged over 10 realisations with $N = 10^4$. Increasing the rotation strength α slightly reduces the time of core collapse. Nevertheless, the impact of rotation (i.e. the gravo-gyro catastrophe) is not as pronounced as what was observed in, e.g., Einsel & Spurzem (1999).

This does not necessarily contradict the measurements made by Einsel & Spurzem (1999). In their study, they considered the secular evolution of a rotating King model with the DF (at initial time)

$$F_{\mathrm{tot}}(E, L_z) = \mathrm{cst.}\,(\mathrm{e}^{-\beta E} - 1)\,\mathrm{e}^{-\beta\Omega_0 L_z}. \tag{5.2.2}$$

In this DF, $\beta = 1/\sigma_{\mathrm{c}}^2$ is an inverse temperature, with σ_{c} the central velocity dispersion, and $\omega_0 = \sqrt{9/(4\pi G n_{\mathrm{c}})}\Omega_0$ is a rotation parameter, with n_{c} the central density. In particular, β is related to the so-called King parameter, defined by $W_0 = -\beta(\psi - \psi_{\mathrm{t}})$ where ψ_{t} is the potential at the edge of the cluster. The rotating King models can therefore be parametrised by (W_0, ω_0). Using this convention, the rotating King cluster is integrated forward in time using a Fokker-Planck scheme until core collapse for a set of different rotation parameters, ω_0, as represented in Fig. 5.2.8. Einsel & Spurzem (1999) clearly showed the strong dependence of the core collapse time with the rotation parameter of the King model. For the model $W_0 = 6.0$, a non-rotating cluster reaches core collapse at $t \sim 12 t_{\mathrm{rh}}$, and the cluster with rotation parameter $\omega_0 = 0.4$ does so at $t \sim 9 t_{\mathrm{rh}}$. This difference is much more significant than for the Plummer cluster studied in this chapter.

Let me finally stress that the parameters α (Plummer) and ω_0 (King) do not describe rotation in the same way. Beyond the obvious question of defining precisely how they parametrise some sort of *rotation strength*, I can remark that ω_0 impacts the mean density profile while α does not. This is because the DF of the rotating King model does not decompose into an even part and an odd part in L_z (see, e.g., Dejonghe, 1986). Therefore, definitive conclusions should only be drawn with care. The LBD DF (eq. 2.3.36) does not suffer from this issue, as it keeps the mean density the same. This makes the comparison between two rotating models, as in Fig. 5.2.7, in some sense fairer.

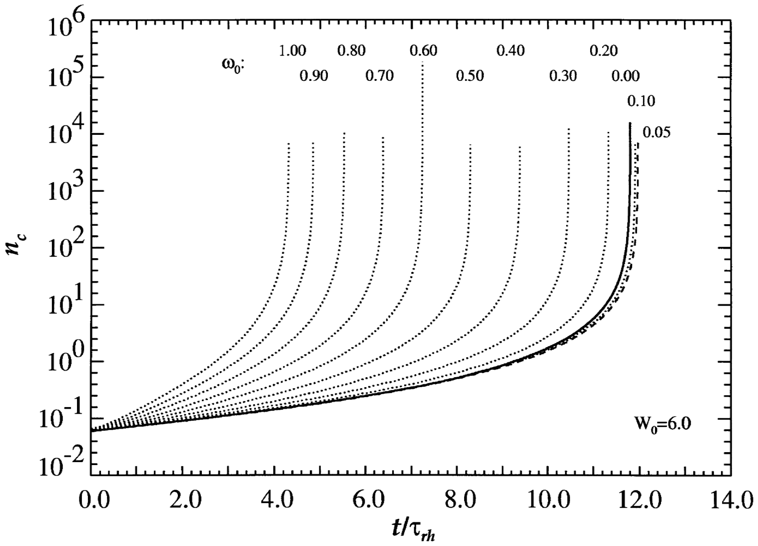

Figure 5.2.8: From fig. 2 of Einsel & Spurzem (1999). Evolution of the central density for the model $W_0 = 6.0$, with varying initial angular velocity parameters ω_0. Core collapse is deeply impacted by the amount of rotation introduced in the King model, and we observe a great acceleration of core collapse when more rotation is injected initially. This is much different from what I observe in Fig. 5.2.7 for the rotating Plummer cluster, where rotation only weakly impacts the core collapse time.

5.3 Theoretical predictions

In the previous section, I used N-body simulations to investigate the relaxation of the (J_r, L)-DF the $(J_\mathrm{r}, \cos I)$-DF and the $\cos I$-DF. Both of these distributions can be obtained by integrating over the full DF in $(J_\mathrm{r}, L, \cos I)$ via

$$\boxed{\begin{aligned} F(J_\mathrm{r}, L) &= \int_{-1}^{1} \mathrm{d}\cos I \, F(J_\mathrm{r}, L, \cos I), && (5.3.1a) \\ F(J_\mathrm{r}, \cos I) &= \int_{0}^{\infty} \mathrm{d}L \, F(J_\mathrm{r}, L, \cos I), && (5.3.1b) \\ F(\cos I) &= \int_{0}^{\infty} \mathrm{d}J_\mathrm{r} \int_{0}^{\infty} \mathrm{d}L \, F(J_\mathrm{r}, L, \cos I). && (5.3.1c) \end{aligned}}$$

The $(J_\mathrm{r}, L, \cos I)$- DF can be expressed in terms of the distribution function in (J_r, L, L_z), which I called $F_\mathrm{rot}(J_\mathrm{r}, L, L_z)$ (see eq. 2.3.36), via the relation $F(J_\mathrm{r}, L, \cos I) = L F_\mathrm{rot}(J_\mathrm{r}, L, L \cos I)$. The time-evolution of each of these reduced DFs can be computed using the Fokker–Planck equations I derived in section 2.3.3. Therefore, I need a practical way of numerically evaluating the diffusion coefficients involved therein.

5.3.1 Orbit averaging for rotating clusters

The computation of the local velocity deflection coefficients is now much more complex than in the non-rotating case. Indeed, I need to evaluate the background DF at an additional parameter L_z', whose evaluation is presented in appendix 2.C. Having obtained these local coefficients, I then need to perform the orbit-average.

I start from the general formula of eq. (2.3.21). Here, the (new) θ-average cannot be done trivially due to the θ-dependency in the L_z' parameter (see eq. 2.C.6) of the velocity integral for the local velocity deflection coefficients. Taking advantage of the structure of the coefficients in E, L and L_z (see eqs. 2.3.22 and 2.3.37), I can push the θ-integral all the way down to the velocity integrals involved in the local deflection coefficients. In the end, I need to compute the following quantities

$$\int \frac{\mathrm{d}\theta}{2\pi} \langle \Delta v_\parallel \rangle, \quad \int \frac{\mathrm{d}\theta}{2\pi} \langle (\Delta v_\parallel)^2 \rangle, \quad \int \frac{\mathrm{d}\theta}{2\pi} \langle (\Delta v_\perp)^2 \rangle, \quad \int \frac{\mathrm{d}\theta}{2\pi} \cos 2\theta \, \langle (\Delta v_\perp)^2 \rangle, \tag{5.3.2}$$

where I used the formula $\sin^2\theta = \frac{1}{2}(1 - \cos 2\theta)$. This leaves me with the following non-trivial

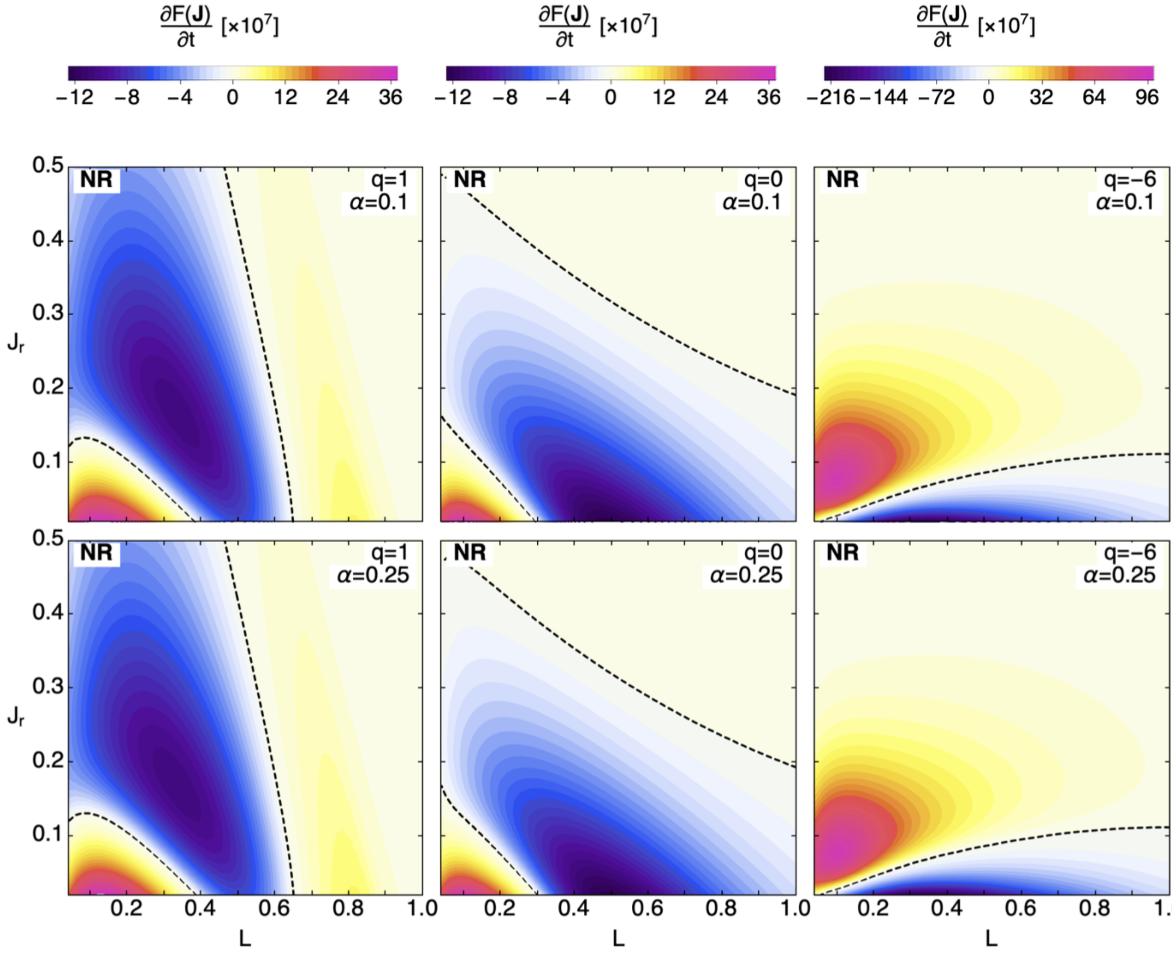

Figure 5.3.1: Illustration of the relaxation rate, $\partial F/\partial t$, for various values of the anisotropy parameter q (left to right) and rotation parameter α (from top to bottom), as predicted from the NR theory in the (J_r, L)-space. The prediction matches the measurements from N-body simulations shown in Fig. 5.2.4, up to an overall prefactor which depends on q, and very weakly on α. This computation requires the evaluation of five embedded integrations, which makes this prediction numerically very intensive.

θ-integrals to compute

$$\boxed{A_1 = \int \frac{\mathrm{d}\theta}{2\pi} g(L_z'/L'), \quad A_2 = \int \frac{\mathrm{d}\theta}{2\pi} \cos 2\theta \, g(L_z'/L'),} \tag{5.3.3}$$

which come from the L_z'-dependent part of the background DF involved in eqs. (2.3.31). For the particular choice of the LBD (eq. 2.3.36), these integrals can be computed analytically (see appendix 5.A). This makes the numerical evaluation of the theory both easier and faster.

5.3.2 Radial diffusion

Using eq. (2.3.45), I can now compute the time derivative of the DF in (J_{r}, L)-space. In addition to the extra dimension in orbit-averaging induced by the background, I have to integrate the test star's DF over $\cos I = L_z/L$ in order to recover the reduced two-dimensional DF, which gives much less leeway to a precise prediction of the diffusion rate given by eq. (2.3.45).

Figure 5.3.1 represents the impact of anisotropy and rotation on radial diffusion – the (J_{r}, L)-orbital space – as predicted using kinetic theory. As with the non-rotating case (chapter 4), the NR theory appears to be successful in recovering the evolution of the radial DF in stable rotating clusters. Comparing with the measurements of Fig. 5.2.4, the NR theory recovers the observed action space structures with a remarkable accuracy. As expected, even though the amplitudes from both methods are comparable, there is still an overall mismatch prefactor. Interestingly, I find that rotation does not appear to have a significant impact on this prefactor whatsoever for the clusters I considered. At most, I can measure a slight increase in the relaxation rate as I increase the rotation parameter α. This is compatible with the behaviour of the core radius evolution observed in Figs. 5.2.3 and 5.2.7, where rotation had a (very) weak impact on the rate of core collapse. A more quantitative comparison would require performing more N-body runs in order to refine the measurement of the core radius down to acceptable error bars.

5.3.3 Azimuthal diffusion

N-body simulations suggested in Fig. 5.2.5 that the impact of rotation is visible in the $(J_{\mathrm{r}}, \cos I)$-space, which involves orbital inclinations. They showed evidence of a *smoothing* process: the region with an extra amount of orbits loses a portion of its orbits to the benefit of the depleted region.

The NR prediction is shown in Fig. 5.3.2 for the same process. This figure shows a very different trend compared to the N-body measurements. First, the non-rotating response is accurately recovered by the NR theory. The time derivative of the DF does not depend on $\cos I$, hence $\partial F/\partial t(\cos I) = 0$. This is a reassuring sanity check. However, I note some discrepancies in the locations of the structures present in both approaches (see top panels of Fig. 5.2.5 for the N-body measurements). The location in J_{r} of the null line (in dark dashed lines) predicted by the NR theory might slightly underestimate the measurement made with N-body simulations (see Fig. 5.3.3 for a direct comparison between N-body simulations and the NR theory for $q = 0$).

For rotating clusters, the difference is much more striking. While the basic observations of orbital reshuffling still holds – in particular, the system loses more prograde orbits than retrograde ones – the structures predicted by the NR theory do not match accurately those observed in N-body simulations. Indeed, the N-body measurements yield round structures as one goes from $\cos I = 0$ to $\cos I = 1$. On the contrary, I observe straighter structures in the NR predictions. This seems to be a robust conclusion, as the mismatch remains as I increase the sampling of the various integrations performed in the NR prediction. I reach the same conclusion in appendix 5.B when considering the relaxation in the $(L, \cos I)$-space.

Now, $\cos I = 0$ corresponds to orbits perpendicular to the rotation plane, whereas $\cos I = \pm 1$ corresponds to orbits within the rotation plane. As I increase the rotation parameter α, I increase the overall rotation of the cluster. In particular, I expect that stars orbiting near the rotation plane will be subject to coherent interactions with other stars contributing to the overall rotation. On the contrary, stars orbiting on a plane perpendicular to the rotation plane will not be impacted as much by them. Because the NR theory only takes into account local deflections

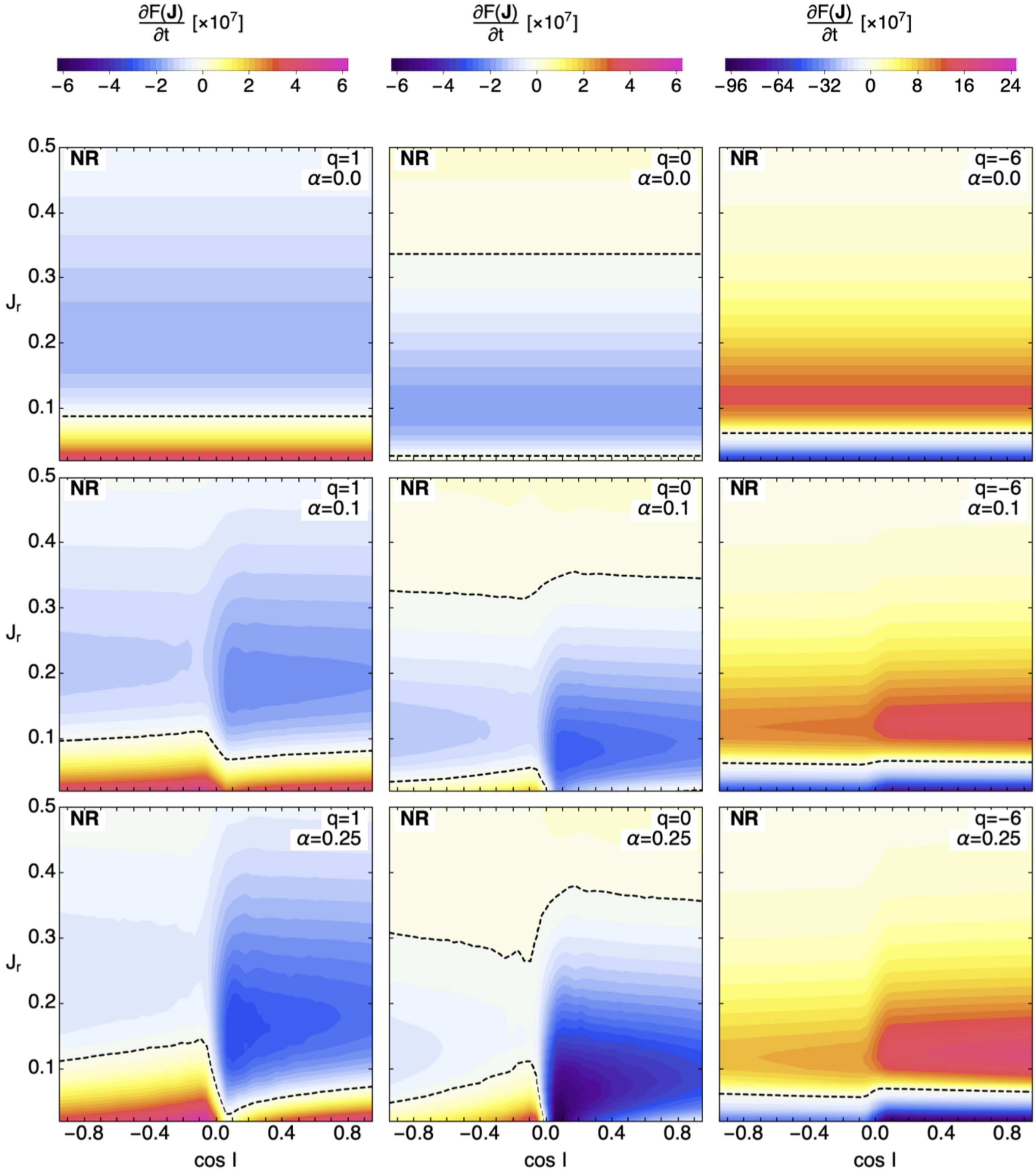

Figure 5.3.2: Illustration of the relaxation rate, $\partial F/\partial t$, for various values of the anisotropy parameter q (left to right) and rotation parameter α (top and bottom), as predicted from the NR theory in $(J_{\rm r}, \cos I)$-space. Contrary to radial diffusion, the prediction fails to recover the structures observed numerically in Fig. 5.2.5. While the isotropisation and inclination smoothing is qualitatively recovered, the NR theory fails to predict the finer details. In order to obtain a satisfying prediction near $\cos I = 0$, I had to finely sample some of the required orbital integrals.

to source orbital relaxation, it cannot account for the corresponding amplification. As a result, I expect that low-$\cos I$ stars can be described accurately by the NR theory, while high-$\cos I$ stars cannot.

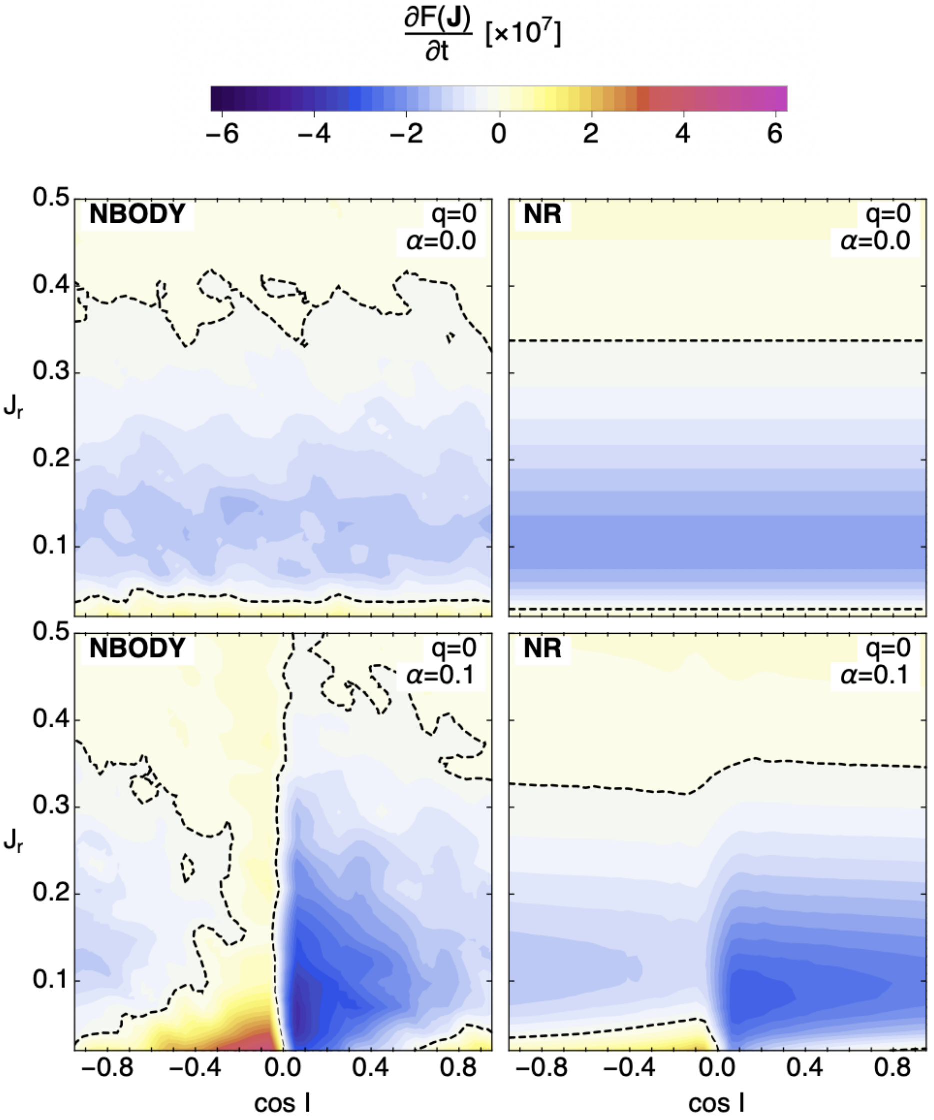

Figure 5.3.3: Comparison of the relaxation rate, $\partial F/\partial t(J_{\mathrm{r}}, \cos I)$, at $q = 0$, for various values of the rotation parameter α (from top to bottom), between the NR theory (right panels) and N-body simulations (left panels). The NR theory matches the N-body predictions for non-rotating clusters, though it might underestimate the null lines. However, it only very roughly predicts the shape of action space structure for rotating clusters. Because rotating clusters' orbits are populated more coherently (as they are dynamically colder), the NR theory, which cannot take into account coherent interactions in the secular response, fails.

The shortcomings of the NR theory in predicting azimuthal diffusion is undoubtedly a motivation to extend the current RR theory (section 2.3.1) to the study of rotating clusters. Because of the spherical symmetry of the cluster, such a system is degenerate in the z-direction. As a consequence, the RR theory predicts no diffusion along the azimuthal direction. However, due to the finite-N nature of the potential, stochastic deviations from the spherical potential are nonetheless expected to occur. This drives a reshuffling of the orbital orientation of the stars while conserving the norm of their angular momentum, i.e. drives a diffusion of $\hat{\boldsymbol{L}}$. This process is called *vector resonant relaxation* (VRR) (see, e.g., Rauch & Tremaine, 1996; Kocsis &

Tremaine, 2015; Meiron & Kocsis, 2019). By applying this formalism to predict the azimuthal relaxation within the rotation plane, I should be able to take in account the coherent motion of the stars. This would hopefully provide a better match to N-body simulation (Fig. 5.3.3).

5.4 Concluding remarks

In this chapter, I extended the NR theory to study the impact of rotation in the secular evolution of sequences of Plummer globular clusters. By relying on a large sample of N-body simulations (section 5.2), I first identified a range of rotating clusters displaying no linear instabilities. This allowed me to limit myself to spherically symmetric rotating clusters. Then, I was able to determine which quantities are useful to study the impact of rotation on secular evolution. I observed that while rotation does not appear to impact radial diffusion, it does impact the distribution of orbital inclinations, which tends to become more affine.

In section 5.3, I used the NR formalism to predict the long-term time-evolution of the DF measured in N-body simulations. The special form of the LBD allowed me to explicitly integrate over the θ-angle average (section 5.3.1), which improved numerical efficiency and stability. Regarding radial diffusion, I was able to recover the N-body measurements with an accuracy similar to the one observed in the non-rotating case (section 5.3.2). Namely, the structures in both predictions match, up to an overall prefactor weakly dependent on rotation. Using a set of clusters with fewer stars, I explored the evolution of the cluster up to its core collapse. I also confirmed that rotation had a weak impact on radial relaxation by measuring the core collapse time of a set of rotating, anisotropic clusters. Contrary to previous works on the subject (see, e.g., Hachisu, 1979), I was not able to observe a strong *gravo-gyro catastrophe* accelerating core collapse (see, e.g., Einsel & Spurzem, 1999). Since I did not use the same rotation parametrisation for the cluster, their studies do not contradict my result.

However, the NR theory does not predict exactly the same out-of-plane relaxation as what I measured in N-body simulations. On the positive side, I observe in both cases a reshuffling of orbital inclination from the overpopulated regions to the underpopulated ones, as well as an acceleration of the relaxation as I increase the rotation parameter α (section 5.3.3). However, as I consider orbits which are closer and closer to the rotating plane, the prediction of the local NR theory fail to match numerical observations. Indeed, these orbits follow coherent motions contributing to the overall rotation of the cluster. The boosted interactions between the more numerous stars participating in this coherent motion is not taken into account by the NR formalism, which only deals with local deflections. In contrast, stars with orbits perpendicular to the mid-plane are impacted by rotation. Therefore, most of the relaxation they undergo is sourced by local interactions captured by the NR formalism.

5.4.1 Future works

As rotating systems can be dynamically cold, it would be of interest to implement the RR formalism for them. While the inhomogeneous Landau equation was investigated in non-rotating systems (see, e.g., Hamilton et al., 2018), its implementation for rotating systems with an explicit dependence on L_z is still to be done. Furthermore, because collective effects can significantly amplify fluctuations in cold dynamical systems, an implementation of the Balescu–Lenard equation might prove necessary to recover the N-body measurements I obtained in this chapter.

In section 5.2.4, I followed the evolution of the DF describing orbital inclinations. Though all of them seem to display the same behaviour – a convergence toward the same type of distribution – the small time range and the limited sample of initial conditions prevented me from reaching definite conclusions on certain aspects. In order to determine the asymptotic distribution of orbits, it might be interesting to push N-body simulations further in time. While some studies did such long-term N-body simulations (Tiongco et al., 2020; Livernois et al., 2022), inclinations were not their focus. In addition, the DF I investigated corresponds to a very early period of the cluster's core collapse. One may be able to observe a different behaviour when analysing the final stages of core collapse. As a complement to N-body simulations, it would be of interest to integrate the 3D Fokker–Planck equation itself. While this has recently been implemented in the context of isotropic clusters (Vasiliev, 2015), its application to anisotropic, rotating systems is another possible extension of this work. Taking into account that rotation can induce a flattening of the cluster during its evolution and studying the implementation of kinetic theory in the case of flattened axisymmetric systems (and eventually, their evolution) will be the subject of future works.

Nonetheless, before treating as challenging a project, one might first try to follow the evolution of the angular momentum orientation $\widehat{\boldsymbol{L}}$ under the effect of coherent torques between orbits using *vector resonant relaxation*. One would then be able to determine if coherent motions are the missing ingredient separating the NR predictions and the N-body measurements made in this chapter. While its has been intensively applied to the Galactic nucleus (see, e.g., Eilon et al., 2009; Kocsis & Tremaine, 2011, 2015; Szölgyén & Kocsis, 2018; Fouvry et al., 2019b; Szölgyén et al., 2019, 2021; Fouvry et al., 2022; Magnan et al., 2022), its application to globular clusters remains to be developed (see Meiron & Kocsis, 2019, for a preliminary investigation).

Appendices of chapter 5

5.A Computing the θ-integral for $g = \mathrm{sgn}$

Using the particular form of the LBD rotation function in eq. (2.3.36), where $g = \mathrm{sgn}$, allows me to integrate the θ-part of the orbit-average (eq. 2.3.21) explicitly. This speeds up the computation of the NR predictions, as well as its accuracy. I start from the functions defined in eqs. (5.3.3)

$$A_1 = \int \frac{\mathrm{d}\theta}{2\pi}\, \mathrm{sgn}(L'_z), \quad A_2 = \int \frac{\mathrm{d}\theta}{2\pi} \cos 2\theta \, \mathrm{sgn}(L'_z), \tag{5.A.1}$$

where I recall the expression (eq. 2.C.6)

$$L'_z = r\left(v'_1 \frac{v_{\mathrm{t}}}{v} - v'_3 \frac{v_r}{v}\right) \cos I + r v'_2 \sin I \sin\theta. \tag{5.A.2}$$

Let me define $\nu = -(v'_1 v_{\mathrm{t}}/v - v'_3 v_r/v)\cos I$ and $\mu = \nu/(v'_2 \sin I)$. I can then compute A_1 and A_2 explicitly, whose expressions are gathered in Tab. 1.

v'_2	μ	A_1	A_2
0	undefined	$-\mathrm{sgn}(r\nu)$	0
$\neq 0$	> 1	-1	0
$\neq 0$	$[-1, 1]$	$-2\sin^{-1}\mu/\pi$	$-2\mu\sqrt{1-\mu^2}/\pi$
$\neq 0$	< -1	1	0

Table 1: Table of values of A_1 and A_2, as introduced in eq. (5.A.1) for the LBD DF (eq. 2.3.36).

5.B Orbital diffusion in the $(L, \cos I)$-space

I can study the evolution of the system in $(L, \cos I)$-space. I first report in Fig. 5.B.1 the N-body measurements. The conclusions I draw from this figure are analogous to that of Fig. 5.2.5 in $(J_{\mathrm{r}}, \cos I)$-orbital space. Indeed, I observe a reshuffling of the inclinations which depletes the over-populated regions in favour of the under-populated ones. Similarly to the prediction in the $(J_{\mathrm{r}}, \cos I)$-orbital space, the NR theory fails to predict accurately the relaxation rate, as I present in Fig. 5.B.2.

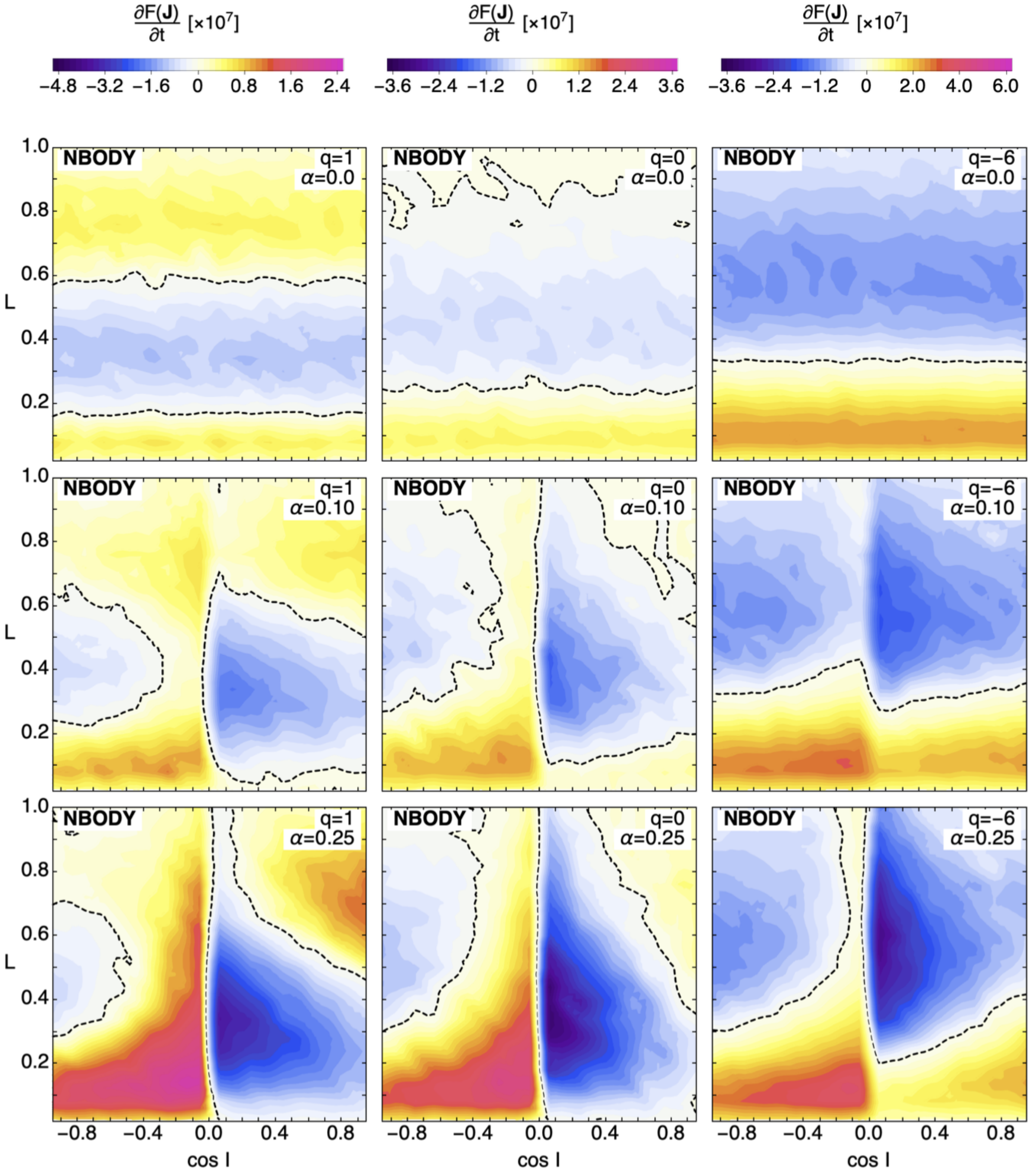

Figure 5.B.1: Illustration of the relaxation rate, $\partial F/\partial t$, for various values of the anisotropy parameter q (left to right) and rotation parameter α (from top to bottom), as measured in N-body simulations in the $(L, \cos I)$-space. I can make the same observations as in Fig. 5.2.5.

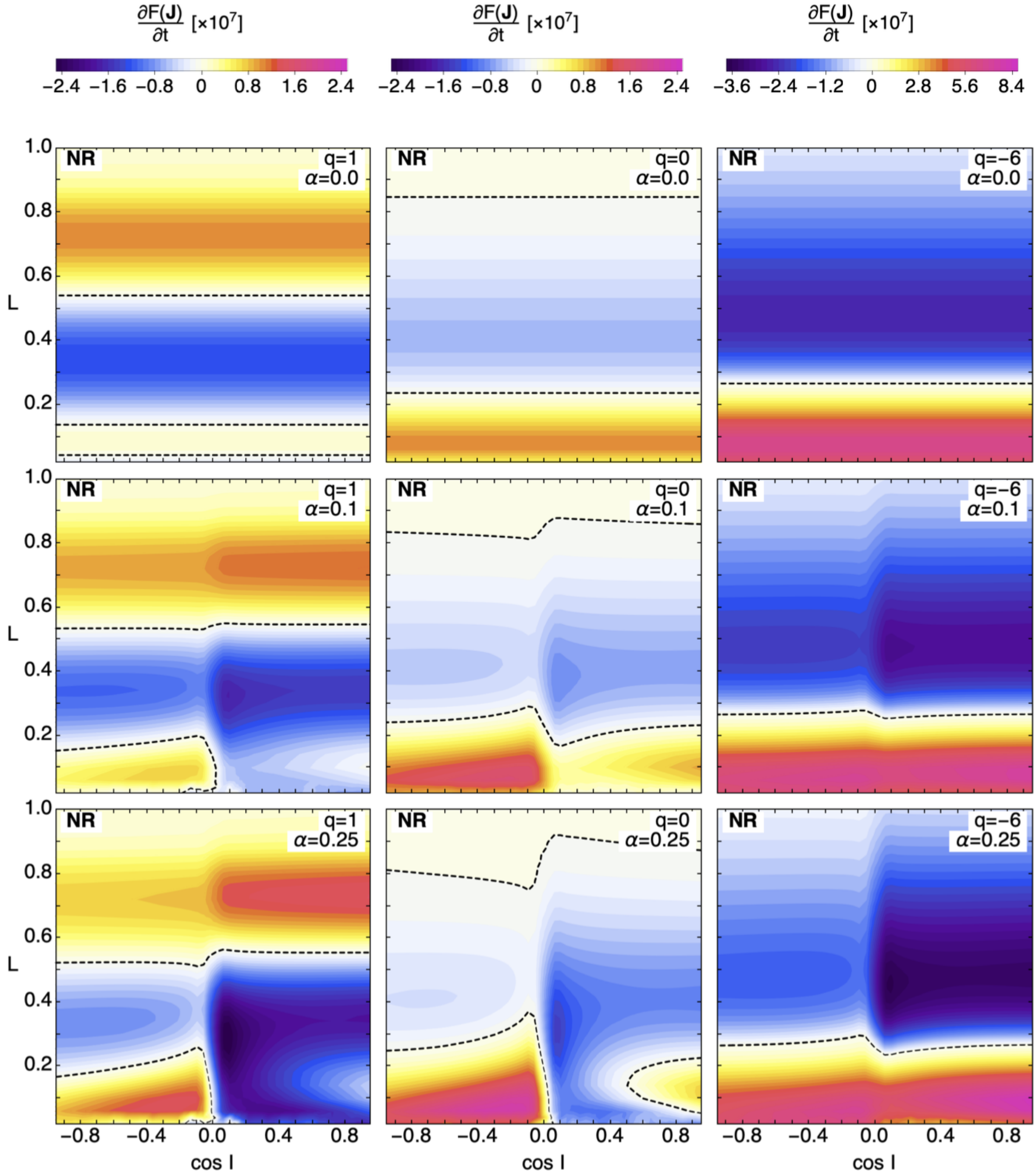

Figure 5.B.2: Illustration of the relaxation rate, $\partial F/\partial t$, for various values of the anisotropy parameter q (left to right) and rotation parameter α (from top to bottom), as predicted by the NR formalism in the $(L, \cos I)$-space. The structures predicted by the NR theory differ from those observed in Fig. 5.B.1, increasingly so as I consider stars orbiting near the rotation plane $(\cos I = \pm 1)$.

5.C Fokker–Planck equation w.r.t. L_z

Let me first reduce the 3D Fokker–Planck equations from the (J_r, L, L_z)-space into the (J_r, L_z)-space. Using the definition

$$F(J_\mathrm{r}, L_z) = \int_{|L_z|}^{\infty} \mathrm{d}L\, F_\mathrm{rot}(J_\mathrm{r}, L, L_z), \tag{5.C.1}$$

I obtain

$$\begin{aligned}\frac{\partial F}{\partial t}(J_\mathrm{r}, L_z) &= -\int_{|L_z|}^{\infty} \mathrm{d}L \left(\frac{\partial F_{J_\mathrm{r}}}{\partial J_\mathrm{r}} + \frac{\partial F_L}{\partial L} + \frac{\partial F_{L_z}}{\partial L_z} \right) \\ &= -\frac{\partial}{\partial J_\mathrm{r}} \int_{|L_z|}^{\infty} \mathrm{d}L\, F_{J_\mathrm{r}} + F_L(J_\mathrm{r}, |L_z|, L_z) - \mathrm{sgn}(L_z) F_{L_z}(J_\mathrm{r}, |L_z|, L_z) - \frac{\partial}{\partial L_z} \int_{|L_z|}^{\infty} \mathrm{d}L\, F_{L_z} \\ &= -\frac{\partial}{\partial J_\mathrm{r}} \int_{|L_z|}^{\infty} \mathrm{d}L\, F_{J_\mathrm{r}} - \frac{\partial}{\partial L_z} \int_{|L_z|}^{\infty} \mathrm{d}L\, F_{L_z},\end{aligned} \tag{5.C.2}$$

since $F_{L_z}(J_\mathrm{r}, L, \pm L) = \pm F_L(J_\mathrm{r}, L, \pm L)$. This reflects the fact that the flux cannot leave the (L, L_z)-space (Hamilton et al., 2018). Equation (5.C.2) can be written as a 2D-continuity equation of the form

$$\frac{\partial F}{\partial t}(J_\mathrm{r}, L_z) = -\frac{\partial \overline{\mathcal{F}}_{J_\mathrm{r}}}{\partial J_\mathrm{r}} - \frac{\partial \overline{\mathcal{F}}_{L_z}}{\partial L_z}, \tag{5.C.3}$$

with the flux in the (J_r, L_z)-space given by $\overline{\boldsymbol{\mathcal{F}}} = (\overline{\mathcal{F}}_{J_\mathrm{r}}, \overline{\mathcal{F}}_{L_z})$, where

$$\overline{\mathcal{F}}_{J_\mathrm{r}} = \int_{|L_z|}^{\infty} \mathrm{d}L\, F_{J_\mathrm{r}}(J_\mathrm{r}, L, L_z), \tag{5.C.4a}$$

$$\overline{\mathcal{F}}_{L_z} = \int_{|L_z|}^{\infty} \mathrm{d}L\, F_{L_z}(J_\mathrm{r}, L, L_z). \tag{5.C.4b}$$

Now recall from eqs. (2.3.38) and (2.3.39) that

$$\mathcal{F}_{J_\mathrm{r}} = D_{J_\mathrm{r}} F_\mathrm{rot} - \frac{1}{2}\left(\frac{\partial (D_{J_\mathrm{r}J_\mathrm{r}} F_\mathrm{rot})}{\partial J_\mathrm{r}} + \frac{\partial (D_{J_\mathrm{r}L} F_\mathrm{rot})}{\partial L} + \frac{\partial (D_{J_\mathrm{r}L_z} F_\mathrm{rot})}{\partial L_z} \right), \tag{5.C.5a}$$

$$\mathcal{F}_{L_z} = D_{L_z} F_\mathrm{rot} - \frac{1}{2}\left(\frac{\partial (D_{J_\mathrm{r}L_z} F_\mathrm{rot})}{\partial J_\mathrm{r}} + \frac{\partial (D_{LL_z} F_\mathrm{rot})}{\partial L} + \frac{\partial (D_{L_zL_z} F_\mathrm{rot})}{\partial L_z} \right). \tag{5.C.5b}$$

Using $D_{J_\mathrm{r}L_z} = \mathrm{sgn}(L_z/|L_z|) D_{J_\mathrm{r}L}$ and $D_{LL_z} = \mathrm{sgn}(L_z/|L_z|) D_{LL}$ at $L = |L_z|$, it follows that

$$\overline{\mathcal{F}}_{J_\mathrm{r}} = \int_{|L_z|}^{\infty} \mathrm{d}L\, D_{J_\mathrm{r}} F_\mathrm{rot} - \frac{1}{2}\left(\frac{\partial}{\partial J_\mathrm{r}} \int_{|L_z|}^{\infty} \mathrm{d}L\, D_{J_\mathrm{r}J_\mathrm{r}} F_\mathrm{rot} + \frac{\partial}{\partial L_z} \int_{|L_z|}^{\infty} \mathrm{d}L\, D_{J_\mathrm{r}L_z} F_\mathrm{rot} \right), \tag{5.C.6a}$$

$$\overline{\mathcal{F}}_{L_z} = \int_{|L_z|}^{\infty} \mathrm{d}L\, D_{L_z} F_\mathrm{rot} - \frac{1}{2}\left(\frac{\partial}{\partial J_\mathrm{r}} \int_{|L_z|}^{\infty} \mathrm{d}L\, D_{J_\mathrm{r}L_z} F_\mathrm{rot} + \frac{\partial}{\partial L_z} \int_{|L_z|}^{\infty} \mathrm{d}L\, D_{L_zL_z} F_\mathrm{rot} \right). \tag{5.C.6b}$$

These equations are satisfactory for two main reasons. First, because the L-integration variable never reaches 0 when $L_z \neq 0$, the singularity in $1/L$ (which comes from D_L, see eq. 2.3.22c) has been avoided. Then, I got rid of the singularities in eq. (5.C.3) by using the exact cancellation of the $1/L$ divergence in the term $F_L(J_\mathrm{r}, |L_z|, L_z) - \mathrm{sgn}(L_z) F_{L_z}(J_\mathrm{r}, |L_z|, L_z) = 0$. This is made possible by the boundary condition $F_{L_z}(J_\mathrm{r}, L, \pm L) = \pm F_L(J_\mathrm{r}, L, \pm L)$.

Now, the integration over J_r in eq. (5.C.3) can be straightforwardly carried, and leads to the

1D Fokker–Planck eq. (5.D.5).

5.D Impact of discontinuities

One of the potential issues of the LBD (eq. 2.3.36) is its discontinuity in $\cos I = 0$. Naturally, one could be worried that it would impact my predictions. To investigate this concern, I can generalise my range of rotating distribution functions to those of the form

$$F_{\mathrm{rot}}(J_{\mathrm{r}}, L, L_z) = F_{\mathrm{tot}}(J_{\mathrm{r}}, L)(1 + \alpha g[L_z/L]), \tag{5.D.1}$$

where $g[\cos I]$ is an odd function such that $g[1] = 1$. The LBD demon is recovered for $g = \mathrm{sgn}$. To approximate this behaviour with a smooth function, I consider the sequence of functions (Rozier et al., 2019)

$$g_a(x) = \mathrm{erf}(ax)/\mathrm{erf}(a), \tag{5.D.2}$$

such that $g_0(x) = x$, while $g_\infty(x) = \mathrm{sgn}(x)$ as illustrated in Fig. 5.D.1. One way to probe the effect of the discontinuity is to compute the $\cos I$ component of the 3D-flux (eq. 2.3.42c) in $(J_{\mathrm{r}}, L, \cos I)$-space for different values of $a > 0$. I represent this behaviour in Fig. 5.D.2. In this figure, I observe a $1/L$ singularity for low L when I consider the smooth approximation of the sgn rotation function. As I increase $a \to \infty$, the flux converges towards the LBD flux pointwise. However, as it stands now, this NR prediction cannot be applied to a smooth DF. Indeed, I can trace back the removal of the $1/L$ singularity to the cancellation of the derivative of sgn, which is a piecewise constant function (see eq. 2.3.48). Such a property is not the norm for arbitrary rotation functions $g(\cos I)$.

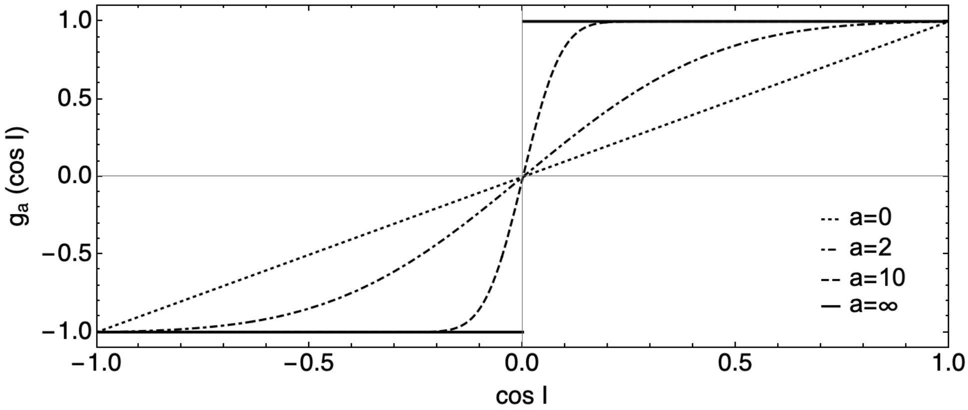

Figure 5.D.1: Representation of the family of functions $g_a(\cos I)$ (eq. 5.D.2) for various values of a. When I let $a \to 0$, the function approaches identity. When I let $a \to \infty$, the function approaches the sgn LBD function. Using this function allows me to study the impact of the discontinuity of the LBD DF against increasingly sharper smooth approximations.

Nevertheless, it is possible to avoid this singularity by considering relaxation in the (J_{r}, L, L_z) space instead of the $(J_{\mathrm{r}}, L, \cos I)$ space. Indeed, I can define the DF in L_z as

$$F(L_z) = \int_0^\infty \mathrm{d}J_{\mathrm{r}} \int_{|L_z|}^\infty \mathrm{d}L\, F_{\mathrm{rot}}(J_{\mathrm{r}}, L, L_z), \tag{5.D.3}$$

so that

$$(2\pi)^3 \int_{-\infty}^\infty \mathrm{d}L_z\, F(J_{\mathrm{r}}, L_z) = M. \tag{5.D.4}$$

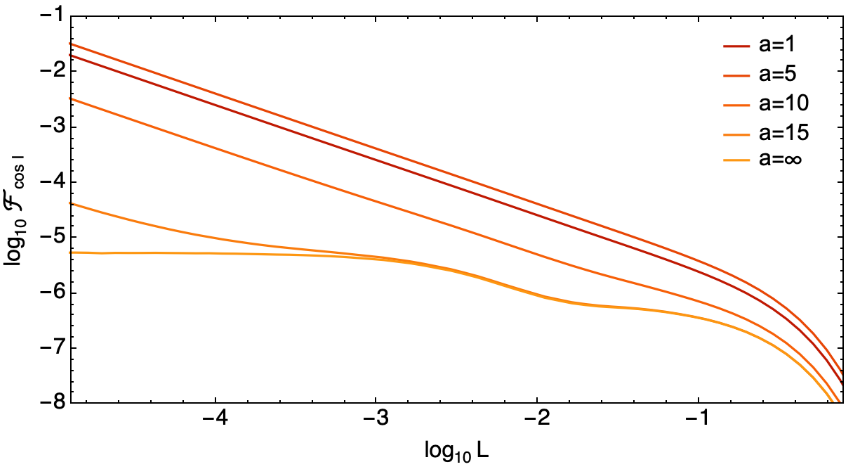

Figure 5.D.2: Representation of $\mathcal{F}_{\cos I}(J_{\mathrm{r}}, L, \cos I)$ at $J_{\mathrm{r}} = 0.1$ and $\cos I = 0.2$ for various smooth rotation functions g_a (eq. 5.D.2). I observe the existence of a $1/L$ divergence as $L \to 0$ when g_a is smooth. As g_a tends to the sgn function, the flux converges to the LBD flux pointwise, though the $1/L$-divergence always remains.

Integrating the $3D$ Fokker–Planck eq. (2.3.38) over J_{r} and L yields (see appendix 5.C)

$$\boxed{\frac{\partial F}{\partial t}(L_z) = -\frac{\partial}{\partial L_z}\big(\overline{D}_{L_z} F[L_z]\big) + \frac{1}{2}\frac{\partial^2}{\partial L_z^2}\big(\overline{D}_{L_z L_z} F[L_z]\big),} \tag{5.D.5}$$

where the L_z-diffusion coefficients are

$$\overline{D}_{L_z} = \int_0^\infty \mathrm{d}J_{\mathrm{r}} \int_{|L_z|}^\infty \mathrm{d}L \, D_{L_z} F_{\mathrm{rot}}(J_{\mathrm{r}}, L \,|\, L_z), \tag{5.D.6a}$$

$$\overline{D}_{L_z L_z} = \int_0^\infty \mathrm{d}J_{\mathrm{r}} \int_{|L_z|}^\infty \mathrm{d}L \, D_{L_z L_z} F_{\mathrm{rot}}(J_{\mathrm{r}}, L \,|\, L_z), \tag{5.D.6b}$$

with $F_{\mathrm{rot}}(J_{\mathrm{r}}, L \,|\, L_z) = F_{\mathrm{rot}}(J_{\mathrm{r}}, L, L_z)/F(L_z)$ the DF in (J_{r}, L) given the angular momentum L_z, normalised to unity. The barred notation means that the diffusion coefficients are averaged over the other actions (J_{r}, L). When I consider $L_z \neq 0$, the coefficients D_{L_z} and $D_{L_z L_z}$ are well-defined everywhere for any distribution function with some rotation.

Chapter 6

Bar growth within thin galactic discs

The work presented in this chapter is based on section 5.4 of Reddish et al. (2022), which I cosigned.

6.1 Introduction

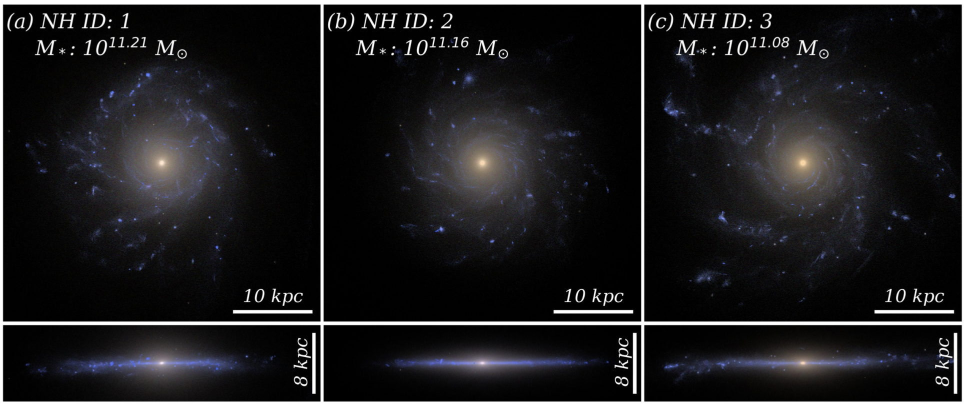

Figure 6.1.1: From fig. A1 of Yi et al. (2023). The face-on (top panels) and edge-on (bottom panels) images of the three most massive sample galaxies from NewHorizon at $z = 0.17$. No bars are observed at this redshift.

In the previous chapters, I applied the formalism of orbital diffusion to stellar systems in order to predict their secular evolution. Depending on the form of the potential, my studies used either the NR formalism on its own – for a galactic potential – or a combination of the RR and NR formalisms – for the degenerate Keplerian potential. In both cases, I used angle-action coordinates in order to capture the mean field trajectories to model precisely the long-term relaxation of isolated stellar systems. In this chapter, I will consider the evolution of an other class of stellar systems – self-gravitating discs – which are essentially centrifugally supported. Such discs are dynamically much colder than the systems I previously studied in this manuscript. Hence, dressing is expected to play a much more important role in their secular evolution (Fouvry et al., 2015c). As a result, I will focus my interest on the description of their linear response. For the sake of simplicity, I will address the issue of their secular evolution from a different standpoint, and chart the range of equilibria which are consistent with their dynamical stability.

As discussed in Reddish et al. (2022), the secular resilience of bars is an open question which is the topic of intense research both in hydrodynamical simulations and in theoretical works. This question is crucial for many reasons. First of all, observations in our local Universe reveal that roughly between 1/3 and 2/3 of nearby spiral galaxies (depending on the detection criterion) host a bar (see, e.g., Nair & Abraham, 2010; Masters et al., 2011; Melvin et al., 2014; Díaz-García et al., 2016).[a] It is believed that bars spontaneously form in stellar discs that are sufficiently massive and dynamically cold to be gravitationally unstable to the *non-linear development of a bi-symmetric instability* (see, e.g., Toomre, 1963; Combes & Sanders, 1981). In addition, they may also be affected by the conditions of their host galaxy (see, e.g., Vogelsberger et al., 2014; Pillepich et al., 2018; Kaviraj et al., 2017)

Cosmological numerical simulations provide an effective tool to study the formation and evolution of bars (Fig. 6.1.1). However, these simulations produce a fraction of barred galaxies from about 20% (Peschken & Łokas, 2019) and 30% (Rosas-Guevara et al., 2022) to about 40%-60% (Rosas-Guevara et al., 2020; Zhao et al., 2020). Most spectacularly, the NewHorizon simulation appears to form only one barred galaxy at $z = 1.3$ out of its 525 galaxies (Fig. 6.1.2).[b] Once formed in simulations, bars can evolve through angular momentum exchange with both the DHs (see, e.g., Debattista & Sellwood, 2000) and with the stellar and gaseous discs (Bournaud & Combes, 2002). Additionally, bars also play an important role in the long-term evolution of disc galaxies, as they are key to the redistribution of their angular momentum (see, e.g., Lynden-Bell, 1979; Tremaine & Weinberg, 1984; Athanassoula & Sellwood, 1986). Determining the requirements for such an instability to occur has been the subject of research for the past six decades.

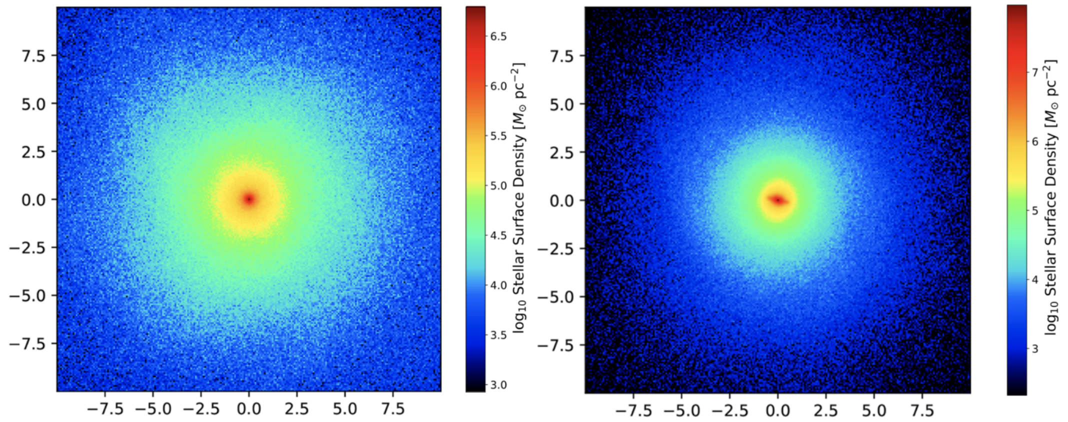

Figure 6.1.2: From figs. 1 and 2 of Reddish et al. (2022). On the left: a non-barred NewHorizon galaxy detected at $z = 0.25$. On the right: the (strongly) barred NewHorizon galaxy detected at $z = 1.3$. Axes are in kpc.

Lin & Shu (1964) have attempted to solve this question through the so-called density wave theory. They showed how density waves can survive the differential rotation in the WKB approximation. They are subject to the self-gravity, pressure and inertia, and obey the dispersion relation (for a gaseous disc) (Safronov, 1960)

$$(\omega - m\Omega)^2 = \kappa^2 - 2\pi\Sigma k + k^2 c^2, \tag{6.1.1}$$

where ω is the frequency, k the spatial frequency, m the pattern number and Ω the angular

---

[a] As observations show, about two-third of the observed galaxies display a clear bi-symmetric spiral structure (de Vaucouleurs, 1963; Dressler, 1980; Loveday, 1996; Nakamura et al., 2004; Hammer et al., 2005; Delgado-Serrano et al., 2010; Haslbauer et al., 2022), in which bars can then form.

[b] This corresponds to a minimum of 2000 particles in a given galaxy, i.e. with a mass above $10^{7.25} M_\odot$.

velocity. In that expression, the destabilising term is the self-gravity contribution $2\pi\Sigma k$, which depends on the surface density Σ. The inertial term depends on the epicyclic frequency κ while the pressure term k^2c^2 stabilises the disc, with c the sound speed. Although this local analysis is useful to probe the competition between the forces in play, this approach is doomed to fail in realistic setups. Indeed, the WKB approximation cannot hold on the long-term, because a tightly wound leading wave satisfying this dispersion relation (a requirement for the WKB approximation) will eventually unwind itself (Toomre, 1969). Such a problem must therefore be treated *globally* using linear response theory.

The study of the non-linear development of a bi-symmetric instability would require a complex theory beyond the scope of this thesis. Nevertheless, I can probe whether or not this instability process can occur by first determining the *linear growth rate for the bi-symmetric modes of the galactic disc*. To achieve this purpose, linear response theory can be used to chart the range of equilibria which are stable against bar formation. A first step was made by Aoki et al. (1979) where he established a link between temperature, disc wounding and linear stability for a self-gravitating razor-thin galaxy made of polytropic gas. Eventually, a satisfying model would have to be able to reproduce the observations made in hydrodynamical simulations. Bars can be weakened and even destroyed if they gain too much angular momentum from the infalling gas (Bournaud et al., 2005). Furthermore, simulations have suggested that an excessive growth of a central galactic bulge may destroy bars (see, e.g, Hasan & Norman, 1990; Shen & Sellwood, 2004) which in turn can disrupt the growth of the bar without any merger event (see, e.g., Du et al., 2017; Guo et al., 2020). Additionally, they may be reinforced or reformed given sufficient accretion of external gas onto the disc (Bournaud & Combes, 2002) as well as also being destroyed or (re-)formed as a result of environmental factors such as tidal interactions or galaxy mergers (see, e.g., Hohl, 1971; Noguchi, 1987; Berentzen et al., 2004; Moetazedian et al., 2017; Zhou et al., 2020). In practice, for the sake of simplicity, I nonetheless restrict my analysis here to gaseous linear response.

In this chapter, I will therefore extend the formalism from Aoki et al. (1979) to study the linear response of a gaseous self-gravitating razor-thin galactic disc with a spherical bulge and a spherical DH. Assuming a small enough response of the disc, I will convert in section 6.2 the Euler–Poisson equations into an eigenvalue problem using the matrix method (Kalnajs, 1977) along with the bi-orthogonal basis developed by Aoki & Iye (1978). For the sake of simplicity, I will be interested in probing the regime for instabilities w.r.t. a few parameters describing the geometry of the thin disc, which I will take as isolated. To do so, I will compute (complex) frequency diagrams depending on the bulge mass fraction, the disc mass fraction, and predict a proxy for the (secular) growth rate of the bar in the galaxy. In section 6.3, I will apply this formalism to the parameters of the NewHorizon simulation (Dubois et al., 2021; Reddish et al., 2022). I will show that most of the galaxies it forms have a low growth rate according to my model, and hence are unlikely to form the bi-symmetric instability required to induce bar formation in the non-linear regime. As for the single bar that is formed in NewHorizon, I will show that the geometric structure of its host galaxy corresponds to the fastest linear growth rate of the whole simulation.

6.2 Self-gravitating fluid dynamics

6.2.1 Evolution equation

I consider a self-gravitating razor-thin disc with a central spherical bulge and a spherical DH, with surface density Σ and gravitational potential Φ. Importantly, for simplicity I will model this disc as though it was made of gas. This will allow me to identify all its linear modes at once. Let $\boldsymbol{v}$ be its velocity field and P its pressure. Then the disc obeys the hydro-dynamical and mean field equations (see, e.g., Clarke & Carswell, 2007)

$$\boxed{\begin{aligned}&\frac{\partial \Sigma}{\partial t}+\boldsymbol{\nabla}\cdot(\Sigma\boldsymbol{v})=0\,, && (6.2.1a)\\ &\frac{\partial \boldsymbol{v}}{\partial t}+(\boldsymbol{v}\cdot\boldsymbol{\nabla})\boldsymbol{v}=-\frac{1}{\Sigma}\boldsymbol{\nabla}P-\boldsymbol{\nabla}\Phi\,, && (6.2.1b)\\ &\Delta\Phi_{\mathrm{disc}}=4\pi G\Sigma\delta_{\mathrm{D}}(z), && (6.2.1c)\end{aligned}}$$

where the total potential reads $\Phi=\Phi_{\mathrm{bulge}}+\Phi_{\mathrm{halo}}+\Phi_{\mathrm{disc}}$. Let me assume that the gas is a polytrope with index $\Gamma=4/3$ (Aoki et al., 1979), and fix the baryonic mass of the disc and bulge to be $M\!=\!M_{\mathrm{disc}}+M_{\mathrm{bulge}}$. Then the present system is described by the two parameters

$$p=\frac{M_{\mathrm{bulge}}}{M_{\mathrm{disc}}+M_{\mathrm{bulge}}}\quad;\quad q=\frac{M_{\mathrm{disc}}}{M_{\mathrm{disc}}+M_{\mathrm{halo}}}, \tag{6.2.2}$$

where p is the bulge fraction and q the disc fraction.

The equilibrium state is modelled for simplicity by a Kuzmin-Toomre disc as

$$\Phi_{\mathrm{disc}}=-\frac{GM}{a_{\mathrm{d}}}\frac{1-p}{\sqrt{1+(r/a_{\mathrm{d}})^2}}\,, \tag{6.2.3}$$

and Plummer spheres for the bulge and DH as

$$\Phi_{\mathrm{bulge}}+\Phi_{\mathrm{halo}}=-\frac{GM}{a_{\mathrm{d}}}\left[\frac{a_{\mathrm{d}}}{a_{\mathrm{b}}}\frac{p}{\sqrt{1+(r/a_{\mathrm{b}})^2}}+\frac{a_{\mathrm{d}}}{a_{\mathrm{h}}}\left(\frac{1}{q}-1\right)\frac{1-p}{\sqrt{1+(r/a_{\mathrm{h}})^2}}\right], \tag{6.2.4}$$

where a_{d} is the scale length of the disc, a_{h} the scale length of the DHand a_{b} that of the bulge. I can then express the angular velocity, Ω, and the epicyclic frequency, κ, of the whole system w.r.t. these variables and parameters (see appendix 6.A.8).

The system of eqs. (6.2.1a)-(6.2.1b), expressed in polar coordinates (r,θ), can be linearised assuming an angular- and time-dependent scaling in $\exp(\mathrm{i}m\theta-\mathrm{i}\omega_m t)$. Here, I expand the first order perturbation of the two components of Euler and Poisson equation using the decomposition

$$\boxed{X(r,\theta,t)=X_0(r)+\delta X(r,\theta,t)\quad;\quad \delta X(r,\theta,t)=\sum_{m\in\mathbb{Z}}X_m(r)\,\mathrm{e}^{\mathrm{i}(m\theta-\omega_m t)},} \tag{6.2.5}$$

where X is a quantity which can be density, potential, etc., with X_0 the mean quantity and δX the fluctuations around the mean value. In the case of the density decomposition, $\delta\Sigma_m(r)$ can be expanded over normalised Legendre polynomials $P_n^{|m|}(\xi)$ in ξ as, e.g.,

$$\delta\Sigma_m(r) = \frac{M(1-p)}{2\pi a_{\mathrm{d}}^2}\left(\frac{1-\xi}{2}\right)^{3/2}\sum_{n=|m|}^{\infty} a_n^m P_n^{|m|}(\xi)\,, \tag{6.2.6}$$

where I introduced the reduced radius, $\xi = (r^2 - a_{\mathrm{d}}^2)/(r^2 + a_{\mathrm{d}}^2)$, and where the normalised Legendre polynomials obey the orthogonality relations

$$\int_{-1}^{1} \mathrm{d}\xi\, P_n^{|m|}(\xi) P_l^{|m|}(\xi) = \delta_{nl}. \tag{6.2.7}$$

I introduce similar expressions for the radial and the azimuthal components of the perturbed velocity field involving some b_n^m and c_n^m coefficients (see eq. 6.A.5).

6.2.2 Matrix method

By design, this expansion satisfies Poisson eq. (6.2.1c). Following closely Aoki et al. (1979), I inject these expansions in the linearised system (see eqs. 6.A.6). Making use of the orthogonality relation given by eq. (6.2.7), I obtain an infinite linear eigenproblem for the complex dimensionless frequency $\widehat{\omega} = \mathrm{sgn}(m)\,\omega_m/\Omega_{\mathrm{ref}}$, which can be expressed as an linear, infinite matrix eigenproblem of the form

$$\boxed{\mathbf{M}\,\mathbf{a} = \widehat{\omega}\,\mathbf{a}.} \tag{6.2.8}$$

The matrix elements, as well as the method of their computation, are detailed in appendix 6.A and 6.B. In particular, the matrix elements depend on p and q the bulge and DH parameters (eqs. 6.2.2), as well as the disc's temperature ε_0 (see, e.g., Aoki et al., 1979), which is defined as the ratio between the internal energy and the total energy. Small values of ε_0 correspond to gravitationally-dominated disc, whereas large values of ε_0 correspond to pressure-dominated discs.

The determination of the physical eigenvalues of this problem is slightly tricky, and needs a rigorous analysis. The details are given in appendix 6.C.

6.3 Accounting for the bar fraction in NewHorizon

I will now apply this toy model to provide insight into the lack of bars in NewHorizon. While galaxies in the previous model live in a four-dimensional space, we can reduce that space to a two-dimensional space parameterised by (p, q) by using typical values for $a_{\mathrm{b}}/a_{\mathrm{d}}$ and $a_{\mathrm{h}}/a_{\mathrm{d}}$ motivated by a mapping from the NewHorizon galaxies to the model (see appendix D2 of Reddish et al., 2022). For each (p, q), I select the (physical) eigenvalue with the highest imaginary part, $\mathrm{Im}(\widehat{\omega})$, and build the corresponding map of the growth rate in parameter space. In addition, I can assign some threshold below for which I consider that the $2-$fold symmetric mode grows too slowly to drive any significant bar formation. In practice, the fastest growing mode's shape and pattern speed display discontinuities as one increases p (or decreases q), as eigenvalues corresponding to distinct physical branches become dominant. This can be seen as wiggles in the bottom left part of the light contours in Fig. 6.3.1.

I focus on linear instabilities possibly leading to bar formation: the bi-symmetric $m = 2$ mode. Figure 6.3.1 shows the fastest growth rate, $\mathrm{Im}(\widehat{\omega})$, of a sequence of models parametrised by p and q, with $a_{\mathrm{b}}/a_{\mathrm{d}} = 20$ and $a_{\mathrm{h}}/a_{\mathrm{d}} = 2.8$. Light (resp. dark) contours correspond to slow (resp. fast) growth. The inverse of this growth rate quantifies the time it would take for a linear instability to grow (in units of the dynamical time). As seen in this figure, DM-dominated and bulge-hosting galaxies both have slow growth rates[c] (lower right light region), unlikely to develop linear instabilities, hence unlikely to grow strong non-linear bars.

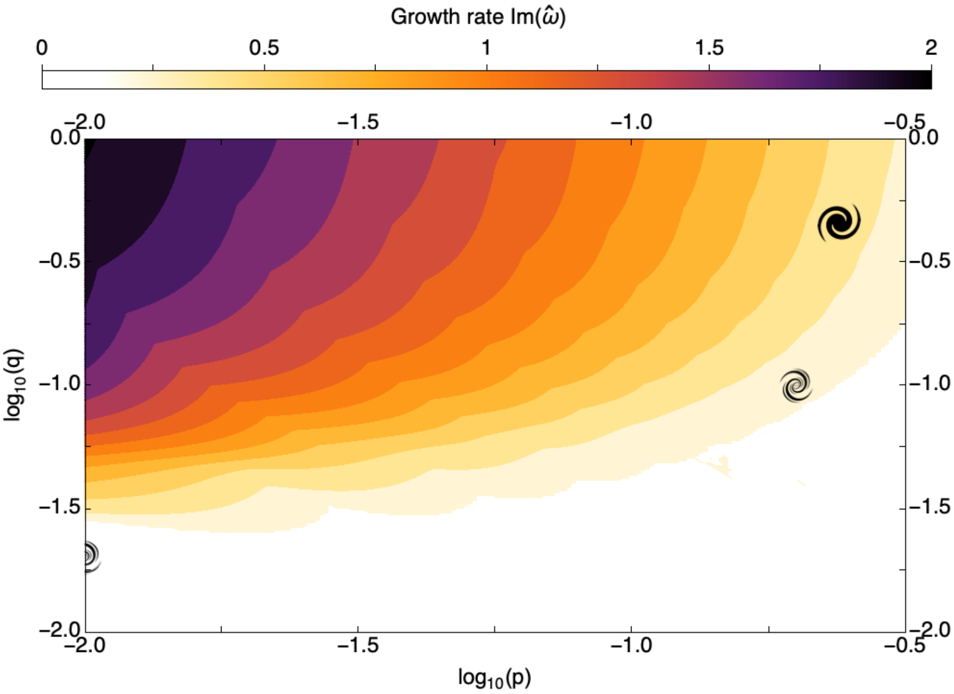

Figure 6.3.1: Representation of the fastest growth rate of $m = 2$ modes predicted by my toy model. It is a function of the bulge fraction p and disc fraction q, as defined in eqs. (6.2.2). The other parameters (typical scales of disc, bulge and DH) are chosen to match those of NewHorizon. The completely white region corresponds to a region of low growth rate (less than $0.1\sqrt{GM/a_{\mathrm{d}}^3}$), which would lead to too slow a bar growth. As a function of cosmic time, via accretion, star formation and mergers, the galaxies move within this diagram and may cross this threshold, triggering the spontaneous formation of a bar. I place three representative points within this space: (i) the bottom left represents a typical barless bulgeless galaxy; (ii) the central one a typical barless bulge-hosting galaxy; (iii) and the top one showing the approximate location of the most prominent barred galaxy in the simulated sample at $z = 1.3$. The NewHorizon simulation does not produce bi-symmetric unstable discs, with the exception of that one galaxy (out of 525), which only hosts a bar for a fraction of a Hubble time.

With the mapping derived in appendix D2 of Reddish et al. (2022), I find that the bulge-less and bulge-hosting galaxies may be roughly split into distinct populations in (p, q) space. I therefore select *typical values* to represent these two populations. I place an open galaxy symbol in Fig. 6.3.1 at $(\log p, \log q) = (-2, -1.7)$ representing the typical bulge-less galaxy in the sample at $z = 1.3$. I also place an open galaxy symbol at the location of the typical bulge-hosting galaxy at $(\log p, \log q) = (-0.7, -1.0)$. Comparing the bulge-less and bulge-hosting galaxies, I find that while galaxies would be considered unstable with a modestly larger $\log q$ values than the bulge-less counterparts, the bulge acts as a stabiliser when interpreted in the framework of my toy model. Interestingly, the most prominent barred galaxy at $z = 1.3$ is by far the most massive disc in the $z = 1.3$ sample, and lies at $(\log p, \log q) = (-0.62, -0.34)$. This corresponds to a region where the bulge mass is too small for the bulge to stabilise the disc against bar formation. This galaxy is shown as a filled galaxy symbol in Fig. 6.3.1.[d]

---

[c] I set up a growth time threshold at a fraction η of the dynamical time $\sqrt{a_{\mathrm{d}}^3/GM_\star}$ which I somewhat arbitrarily set to $\eta = 10$. For a typical stellar mass of $10^{10}\ M_\odot$ and $a_{\mathrm{d}} = 3$ kpc, this corresponds to 0.25 Gyr.

[d] However, tracking the same galaxy forward to lower redshift reveals that $\log q$ decreases while $\log p$ (defined in eq. 6.2.2) modestly increases. Both trends act to stabilise the galaxy against bar formation. Indeed, the observed

At the level of this admittedly crude model, I show that nearly all NewHorizon discs fall in the linearly stable part of parameter space. This suggests that secular processes alone cannot here trigger bi-symmetric instabilities leading to bar formation.

6.4 Concluding remarks

In this chapter, I extended the toy model of self-gravitating razor-thin galactic discs first proposed by Aoki et al. (1979) to study the linear response of galactic discs with a central bulge and a spherical DH. My motivation was the formation of bars. The description of this process required the computation of its response matrix. To that end, I based my approach on the Euler–Poisson equations – which describe the dynamics of a self-gravitating fluid. In section 6.2, I linearised these equations around a Toomre equilibrium (Toomre, 1963). This led to a system of linear equations describing the perturbations of the disc. By using a bi-orthogonal basis, I converted this infinite system of linear equations into an eigenproblem involving a truncated response matrix, whose convergence I studied. In particular, the components of this response matrix depend on the disc's temperature – the ratio between the internal energy and the total energy of the disc – the bulge fraction p and the DH fraction q.

I recovered the results from Aoki et al. (1979) in the disc-only case: beyond a temperature threshold, no physical growing eigenvalues exist, hence the disc is stabilised by its pressure. Second, I studied the impact of the presence of a central bulge and a DH. I determined that beyond a certain fraction threshold, both the bulge and the DH have the effect of stabilising the disc. In these cases, no growing modes exist, and therefore no bar can form. I applied this formalism to the interpretation of the NewHorizon simulation in section 6.3. It is observed that only one galaxy out of 525 has formed a bar at $z = 1.3$. I computed their characteristic growth rate using the method developed in this chapter. Then, I observed that the galaxies ended up in a region of low growth rate – hence explaining their lack of bars – apart from a single barred galaxy. I conclude that the cosmic assembly of galaxies in NewHorizon is such that the macroscopic properties of present day galaxies within the simulation are not prone to bi-symmetric instabilities.

6.4.1 Future works

Because the present toy model explores a summary statistics space, (p, q), it leads to an easily computed, physically motivated threshold for secular bar formation. Nevertheless, it clearly does not allow me to capture in full the realm of non-linear processes relevant to bar formation. For instance, beyond the aforementioned caveats, Aoki et al. (1979)'s formalism cannot rule out some induced bar growth, e.g., via strong tidal perturbations (Noguchi, 1996; Zana et al., 2018; Peschken & Łokas, 2019) nor does it account for the impact of a live halo (Athanassoula, 2002; Curir et al., 2007; DeBuhr et al., 2012). Yet, within that framework, I can conclude that the measured bulge size and disc mass fractions are consistent with the lack of bars in NewHorizon. I expect that this will apply to all cosmological simulations which have enough resolution to capture secular processes such as those discussed in this thesis.

Eventually, it could be of interest and more realistic to implement the fitting strategy presented in Ueda et al. (1985) to my sets of galaxies, while accounting for the detailed shape of the rotation curves (bulge included) and surface densities. One could then quantify statistically the dynamical stability of the discs in NewHorizon. Another possible improvement would

---

bar is gone by $z = 0.7$.

involve implementing a proper stellar stability analysis, (see, e.g., Kalnajs, 1977; Pichon & Cannon, 1997; Jalali & Hunter, 2005; Polyachenko & Just, 2015; De Rijcke & Voulis, 2016; De Rijcke et al., 2019b). This would provide a welcome flexibility in matching the DF and potential to that of the simulated galaxies. One could eventually account for the disc's thickness, the live halo, or use the shape of the eigenvectors to match the pitch angle of the spiral response.

While the NewHorizon simulation has been shown to reproduce several key properties that define galaxies in reasonable agreement with observations (Dubois et al., 2021; Reddish et al., 2022), the sub-grid physics encoded in NewHorizon (and more generally in recent cosmological simulations resolving discs scale heights down to low redshifts, e.g., Hopkins et al., 2018; Agertz et al., 2021) seems to either lack resolution or induce a galactic assembly history statistically incompatible with secular bar formation. This *bar problem* will need to be addressed in future work. In closing, kinetic theory in the spirit of the previous chapters (i.e. driven by fluctuations) should of course be applied to the bar resilience problem (see, e.g., Hamilton, 2023).

Finally, going beyond linear stability analysis may provide interesting insights regarding the secular evolution of these discs. Computing their secular relaxation using the Balescu–Lenard equation would allow one to study some of the non-linear processes which are out of reach of a linear response theory. Whereas this chapter explores how the disc's geometry could lead later on to a bi-symmetric instability, the solutions to the Balescu–Lenard equation would predict whether or not the disc's inherent noise could lead to other types of secular evolution (see, e.g., De Rijcke et al., 2019a). The relaxation of open systems is typically subject to both the non-stochastic, adiabatic evolution of its core properties (e.g., the mass, the disc-to-bulge ratio, etc. , as investigated in this chapter) and to stochastic perturbations (finite-N noise, supernova explosions, turbulence, fly-bys, etc.). Both will impact the secular fate of the system. In this thesis, I mostly studied how finite-N noise can drive the secular relaxation of a system. Nonetheless, the slow, adiabatic evolution of the system's geometry can also drive it closer to marginal stability, hence amplify its gravitational susceptibility and therefore accelerate its noise-driven secular evolution. The implementation of an extended kinetic theory with stochastic (via Fokker–Planck terms) and non-stochastic sources (e.g., injection of matter, dissipation, etc.) should therefore be the topic of upcoming investigations (following, e.g., Pichon & Aubert, 2006).

Appendices of chapter 6

6.A Matrix elements

Let me compute the matrix elements of $\mathbf{M}$, involved in eq. (6.2.8). First, let me define the potential ψ such that $\boldsymbol{\nabla} P = \Sigma \boldsymbol{\nabla} \psi$. Because I consider a polytropic gaseous disc, I can relate the density to the pressure through the relation $P = \alpha \Sigma^{\Gamma}$, where α, Γ are constants. Following Aoki et al. (1979), I set $\Gamma = 4/3$, which yields $\psi = 4\alpha\Sigma^{1/3}$. Letting $\Psi = \Phi + \psi$, eqs. (6.2.1) can be developed into

$$\frac{\partial \Sigma}{\partial t} + \frac{1}{r}\frac{\partial (r\Sigma v_r)}{\partial r} + \frac{1}{r}\frac{\partial (\Sigma v_{\mathrm{t}})}{\partial \theta} = 0, \tag{6.A.1a}$$

$$\frac{\partial v_r}{\partial t} + v_r \frac{\partial v_r}{\partial r} + \frac{v_{\mathrm{t}}}{r}\frac{\partial v_r}{\partial \theta} - \frac{(v_{\mathrm{t}})^2}{r} = -\frac{\partial \Psi}{\partial r}, \tag{6.A.1b}$$

$$\frac{\partial v_{\mathrm{t}}}{\partial t} + v_r \frac{\partial v_{\mathrm{t}}}{\partial r} + \frac{v_{\mathrm{t}}}{r}\frac{\partial v_{\mathrm{t}}}{\partial \theta} + \frac{v_r v_{\mathrm{t}}}{r} = -\frac{1}{r}\frac{\partial \Psi}{\partial \theta}, \tag{6.A.1c}$$

$$\Delta \Phi_{\mathrm{disc}} = 4\pi G \Sigma \delta_{\mathrm{D}}(z). \tag{6.A.1d}$$

I fix $\Phi^0_{\mathrm{bulge}} = -GM_{\mathrm{bulge}}/\sqrt{a_{\mathrm{b}}^2 + r^2} = -GMp/\sqrt{a_{\mathrm{b}}^2 + r^2}$ where $p \in [0,1]$ is defined by eq. (6.2.2). Letting $\xi = (r^2 - a_{\mathrm{d}}^2)/(r^2 + a_{\mathrm{d}}^2)$, an equilibrium state is given by the Plummer equilibrium (Toomre, 1963)

$$v_r^0 = 0, \qquad (v_{\mathrm{t}}^0)^2 = r\frac{\partial \Psi^0}{\partial r}, \tag{6.A.2a}$$

$$\psi^0 = 4\alpha(\Sigma^0)^{1/3}, \tag{6.A.2b}$$

$$\Sigma^0 = \frac{M_{\mathrm{disc}}}{2\pi a_{\mathrm{d}}^2}\frac{1}{(1+(r/a_{\mathrm{d}})^2)^{3/2}} = \frac{(1-p)M}{2\pi a_{\mathrm{d}}^2}\left(\frac{1-\xi}{2}\right)^{3/2}, \tag{6.A.2c}$$

$$\Phi^0_{\mathrm{DH}} = -\frac{GM_{\mathrm{DH}}}{a_{\mathrm{h}}}\frac{1}{\sqrt{1+(r/a_{\mathrm{h}})^2}} = -\frac{GM(1-p)}{a_{\mathrm{d}}}\left(\frac{1}{q}-1\right)\frac{a_{\mathrm{d}}}{a_{\mathrm{h}}\sqrt{1+(r/a_{\mathrm{h}})^2}}, \tag{6.A.2d}$$

$$\Phi^0_{\mathrm{disc}} = -\frac{GM_{\mathrm{disc}}}{a_{\mathrm{d}}}\frac{1}{\sqrt{1+(r/a_{\mathrm{d}})^2}} = -\frac{GM(1-p)}{a_{\mathrm{d}}}\left(\frac{1-\xi}{2}\right)^{1/2}, \tag{6.A.2e}$$

$$\Phi^0_{\mathrm{bulge}} + \Phi^0_{\mathrm{DH}} = -\frac{GM}{a_{\mathrm{d}}}\left[\frac{a_{\mathrm{d}}}{a_{\mathrm{b}}}\frac{p}{\sqrt{1+(r/a_{\mathrm{b}})^2}} + \frac{a_{\mathrm{d}}}{a_{\mathrm{h}}}\left(\frac{1}{q}-1\right)\frac{1-p}{\sqrt{1+(r/a_{\mathrm{h}})^2}}\right], \tag{6.A.2f}$$

where

$$M_{\mathrm{bulge}} = pM \quad ; \quad M_{\mathrm{disc}} = (1-p)M \quad ; \quad M_{\mathrm{DH}} = \left(\frac{1}{q}-1\right)(1-p)M. \tag{6.A.3}$$

Let me define $\delta X(r,\theta,t)=\sum_{m\in\mathbb{Z}} X_m(r)\,\mathrm{e}^{\mathrm{i}(m\theta-\omega_m t)}$, where I look for a temporal dependency in $\mathrm{e}^{-\mathrm{i}\omega_m t}$. Following Aoki & Iye (1978), there is a correspondence between the surface density and the gravitational potential through Poisson equation

$$\delta\Sigma_m^{\mathrm{disc}}(r) = \frac{M(1-p)}{2\pi a_{\mathrm{d}}^2}\left(\frac{1-\xi}{2}\right)^{3/2} \sum_{n=|m|}^{\infty} a_n^m P_n^{|m|}(\xi), \tag{6.A.4a}$$

$$\delta\Phi_m^{\mathrm{disc}}(r) = -\frac{GM(1-p)}{a_{\mathrm{d}}}\left(\frac{1-\xi}{2}\right)^{1/2} \sum_{n=|m|}^{\infty} \frac{a_n^m}{2n+1} P_n^{|m|}(\xi), \tag{6.A.4b}$$

$$\delta\psi_m(r) = \frac{4\alpha}{3}\left(\frac{M}{2\pi a_{\mathrm{d}}^2}\right)^{1/3}(1-p)^{1/3}\left(\frac{1-\xi}{2}\right)^{1/2} \sum_{n=|m|}^{\infty} a_n^m P_n^{|m|}(\xi), \tag{6.A.4c}$$

$$\delta\Psi_m(r) = \frac{GM(1-p)}{a_{\mathrm{d}}}\left(\frac{1-\xi}{2}\right)^{1/2} \sum_{n=|m|}^{\infty} \left[\frac{\varepsilon_0}{3(1-p)^{2/3}} - \frac{1}{2n+1}\right] a_n^m P_n^{|m|}(\xi). \tag{6.A.4d}$$

Let me decompose the velocity components based on their equilibrium expression

$$\delta v_{r,m}(r) = \mathrm{i}\frac{m}{|m|}\left(\frac{GM(1-p)}{a_{\mathrm{d}}}\right)^{1/2}\left(\frac{1+\xi}{2}\right)^{-1/2}\left(\frac{1-\xi}{2}\right)^{1/4} \sum_{n=|m|}^{\infty} b_n^m P_n^{|m|}(\xi), \tag{6.A.5a}$$

$$\delta v_{\mathrm{t},m}(r) = \left(\frac{GM(1-p)}{a_{\mathrm{d}}}\right)^{1/2}\left(\frac{1+\xi}{2}\right)^{-1/2}\left(\frac{1-\xi}{2}\right)^{1/4} \sum_{n=|m|}^{\infty} c_n^m P_n^{|m|}(\xi). \tag{6.A.5b}$$

For the mode m, this yields the set of equations

$$\mathrm{i}(-\omega_m + m\Omega)\delta\Sigma_m^{\mathrm{disc}} + \frac{1}{r}\frac{\mathrm{d}(r\Sigma^0\delta v_{r,m})}{\mathrm{d}r} + \frac{\mathrm{i}m\Sigma^0\delta v_{\mathrm{t},m}}{r} = 0, \tag{6.A.6a}$$

$$\frac{\mathrm{d}\delta\Psi_m}{\mathrm{d}r} + \mathrm{i}(-\omega_m + m\Omega)\delta v_{r,m} - 2\Omega\delta v_{\mathrm{t},m} = 0, \tag{6.A.6b}$$

$$\mathrm{i}m\frac{\delta\Psi_m}{r} + \frac{\kappa^2}{2\Omega}\delta v_{r,m} + \mathrm{i}(-\omega_m + m\Omega)\delta v_{\mathrm{t},m} = 0, \tag{6.A.6c}$$

where $\Omega = v_{\mathrm{t}}^0/r$ is the angular velocity and $\kappa^2 = 4\Omega^2[1 + r/(2\Omega)(\mathrm{d}\Omega/\mathrm{d}r)]$ is the epicyclic frequency. Using the orthogonality relation given in eq. (6.2.7), and defining $\Omega_{\mathrm{ref}} = \sqrt{GM/a_{\mathrm{d}}^3}$, $\Sigma_{\mathrm{ref}} = M/(2\pi a_{\mathrm{d}}^2)$ such that $\widehat{\omega} = \mathrm{sgn}(m)\,\omega_m/\Omega_{\mathrm{ref}}$, $\widehat{\Omega} = \Omega/\Omega_{\mathrm{ref}}$, $\widehat{\kappa} = \kappa/\Omega_{\mathrm{ref}}$ and $\widehat{\Sigma} = \Sigma/\Sigma_{\mathrm{ref}}$, I obtain the matrix equations

$$\sum_{n=|m|}^{\infty} A_{ln} a_n^m + \sum_{n=|m|}^{\infty} B_{ln} b_n^m + \sum_{n=|m|}^{\infty} C_{ln} c_n^m = \widehat{\omega} a_l^m, \tag{6.A.7a}$$

$$\sum_{n=|m|}^{\infty} D_{ln} a_n^m + \sum_{n=|m|}^{\infty} A_{ln} b_n^m + \sum_{n=|m|}^{\infty} F_{ln} c_n^m = \widehat{\omega} b_l^m, \tag{6.A.7b}$$

$$\sum_{n=|m|}^{\infty} G_{ln} a_n^m + \sum_{n=|m|}^{\infty} H_{ln} b_n^m + \sum_{n=|m|}^{\infty} A_{ln} c_n^m = \widehat{\omega} c_l^m. \tag{6.A.7c}$$

In these expressions, I defined

$$A_{ln} = |m| \int_{-1}^{1} \mathrm{d}\xi P_l^{|m|}(\xi)\widehat{\Omega}(\xi)P_n^{|m|}(\xi), \tag{6.A.8a}$$

$$B_{ln} = 4\sqrt{1-p}\int_{-1}^{1} \mathrm{d}\xi P_l^{|m|}(\xi)\left(\frac{1-\xi}{2}\right)^{1/2}\frac{\mathrm{d}}{\mathrm{d}\xi}\left[\left(\frac{1-\xi}{2}\right)^{5/4}P_n^{|m|}(\xi)\right], \tag{6.A.8b}$$

$$C_{ln} = |m|\sqrt{1-p}\int_{-1}^{1} \mathrm{d}\xi P_l^{|m|}(\xi)\left(\frac{1-\xi}{2}\right)^{3/4}\left(\frac{1+\xi}{2}\right)^{-1}P_n^{|m|}(\xi), \tag{6.A.8c}$$

$$\begin{aligned} D_{ln} &= 4\sqrt{1-p}\left(\frac{1}{2n+1} - \frac{\varepsilon_0}{3}\frac{1}{(1-p)^{2/3}}\right) \\ &\times \int_{-1}^{1} \mathrm{d}\xi P_l^{|m|}(\xi)\left(\frac{1-\xi}{2}\right)^{5/4}\left(\frac{1+\xi}{2}\right)\frac{\mathrm{d}}{\mathrm{d}\xi}\left[\left(\frac{1-\xi}{2}\right)^{1/2}P_n^{|m|}(\xi)\right], \end{aligned} \tag{6.A.8d}$$

$$F_{ln} = 2\int_{-1}^{1} \mathrm{d}\xi P_l^{|m|}(\xi)\widehat{\Omega}(\xi)P_n^{|m|}(\xi), \tag{6.A.8e}$$

$$G_{ln} = -|m|\sqrt{1-p}\left(\frac{1}{2n+1} - \frac{\varepsilon_0}{3}\frac{1}{(1-p)^{2/3}}\right)\int_{-1}^{1} \mathrm{d}\xi P_l^{|m|}(\xi)\left(\frac{1-\xi}{2}\right)^{3/4}P_n^{|m|}(\xi), \tag{6.A.8f}$$

$$H_{ln} = \int_{-1}^{1} \mathrm{d}\xi P_l^{|m|}(\xi)\frac{\widehat{\kappa}^2(\xi)}{2\widehat{\Omega}(\xi)}P_n^{|m|}(\xi). \tag{6.A.8g}$$

with

$$\begin{aligned} \widehat{\Omega}(\xi) = \sqrt{1-p}\left(\frac{1-\xi}{2}\right)^{3/4}\Bigg[&\left(\frac{a_\mathrm{d}}{a_\mathrm{b}}\right)^3\frac{p}{1-p}\left(\frac{1-\xi}{2}\right)^{-3/2}\left(\frac{1}{1+(r/a_\mathrm{b})^2}\right)^{3/2} \\ &+\left(\frac{a_\mathrm{d}}{a_\mathrm{h}}\right)^3\left(\frac{1}{q}-1\right)\left(\frac{1-\xi}{2}\right)^{-3/2}\left(\frac{1}{1+(r/a_\mathrm{h})^2}\right)^{3/2} + \left(1-\frac{\varepsilon_0}{(1-p)^{2/3}}\right)\Bigg]^{1/2}, \end{aligned} \tag{6.A.9a}$$

$$\frac{\widehat{\kappa}^2(\xi)}{2\widehat{\Omega}(\xi)} = 2\widehat{\Omega}(\xi)\left[1+\frac{(1+\xi)(1-\xi)}{2\widehat{\Omega}}\frac{\mathrm{d}\widehat{\Omega}}{\mathrm{d}\xi}\right]. \tag{6.A.9b}$$

Here, I introduced ε_0, the ratio of the internal and total energy, which accounts for the strength of the pressure forces in the disc (given my choice of Γ, the polytropic index, see Aoki et al., 1979).

6.B Evaluation of the matrix elements

The integrals A_{ln} (eq. 6.A.8a) and F_{ln} (eq. 6.A.8e) are proportional. With H_{ln} (eq. 6.A.8g), these three integrals must be computed numerically because of the non-trivial shift in their expression induced by the bulge potential. As for B_{ln}, C_{ln}, D_{ln} and G_{ln}, they can be can expressed in terms of the two following integrals

$$\widehat{I}(l,n) = \int_{-1}^{1} \mathrm{d}\xi\left(\frac{1-\xi}{2}\right)^{3/4}P_l^{|m|}(\xi)P_n^{|m|}(\xi), \tag{6.B.1a}$$

$$\widehat{J}(l,n) = \int_{-1}^{1} \mathrm{d}\xi\left(\frac{1-\xi}{2}\right)^{3/4}\left(\frac{1+\xi}{2}\right)^{-1}P_l^{|m|}(\xi)P_n^{|m|}(\xi), \tag{6.B.1b}$$

since

$$B_{ln} = \frac{\sqrt{1-p}}{2}\left[\sqrt{\frac{(2l+1)(l+m+1)(l-m+1)}{2l+3}}\widehat{J}(l+1,n)+\widehat{J}(l,n)\right. \qquad \text{(6.B.2a)}$$

$$\left. -\sqrt{\frac{(2l+1)(l+m)(l-m)}{2l-1}}\widehat{J}(l-1,n)\right],$$

$$C_{ln} = m\sqrt{1-p}\widehat{J}(l,n), \qquad \text{(6.B.2b)}$$

$$D_{ln} = \frac{\sqrt{1-p}}{2}\left(\frac{1}{2n+1}-\frac{\varepsilon_0}{3}\frac{1}{(1-p)^{2/3}}\right)\left[-\sqrt{\frac{(2n+1)(n+m+1)(n-m+1)}{2n+3}}\widehat{I}(l,n+1)\right. \qquad \text{(6.B.2c)}$$

$$\left. -\widehat{I}(l,n)+\sqrt{\frac{(2n+1)(n+m)(n-m)}{2n-1}}\widehat{I}(l,n-1)\right],$$

$$G_{ln} = -|m|\sqrt{1-p}\left(\frac{1}{2n+1}-\frac{\varepsilon_0}{3}\frac{1}{(1-p)^{2/3}}\right)\widehat{I}(l,n). \qquad \text{(6.B.2d)}$$

Here, $\widehat{I}(l,n)$ and $\widehat{J}(l,n)$ can be computed by recursion and by using the symmetry $l \leftrightarrow n$ (see Aoki et al., 1979, for more details). This makes the computation of the response matrix very efficient, as a large part of it can be obtained through analytical recursion formulae.

6.C Linear growth modes of the disc

6.C.1 Convergence study

Finding the frequency $\widehat{\omega}$ involves the computation of the eigenvalues of the infinite response matrix defined in eq. (6.2.8). In practice, I only have access to sequences of truncated matrices of varying size up to some fixed truncation number $n_{\max}$ – such that $\mathbf{M}$ is a $3n_{\max}\times 3n_{\max}$ matrix – from which I obtain a list of eigenvalues. Among these eigenvalues, I have to determine which ones are physically relevant, and which ones only result from the truncation process. The latter either diverge to infinity or oscillate, which allows me to disregard them in favour of those that converge with $n_{\max}$ (here typically $n_{\max} \leq 170$).

In that view, I proceed as follows. (i) First, I compute a sequence of truncated $3n \times 3n$ matrices $\mathbf{M}_n$ up to some fixed truncation number $n_{\max}$. (ii) For each of these matrices $\mathbf{M}_n$, I compute the set eigenvalues $\mathcal{V}_n$. (iii) I construct $\mathcal{S}(\widehat{\omega}) = \{\widehat{\omega}' \in \mathcal{V}_{\leq n_{\max}} : |\widehat{\omega} - \widehat{\omega}'| < \alpha\}$, the set of eigenvalues of the truncated matrices which are close to $\widehat{\omega}$ an eigenvalue of $\mathbf{M}_{n_{\max}}$ for some fixed threshold $\alpha > 0$. This allows me to probe if an eigenvalue is isolated or not. In particular, diverging eigenvalues do not accumulate at one location, hence they are discarded at this step. (iv) For eigenvalues $\widehat{\omega}$ such that $\mathcal{S}(\widehat{\omega})$ has more than 3 points – if not, $\widehat{\omega}$ is rejected – I compute the variance of the eigenvalues gathered in $\mathcal{S}(\widehat{\omega})$. If these go beyond some threshold value $\delta > 0$, then $\widehat{\omega}$ is rejected. (v) The remaining eigenvalues $\widehat{\omega}$ are considered to be physical eigenvalues, as they do not fluctuate strongly w.r.t. the truncation number and seem to accumulate around some limit point.

Figure 6.C.1 illustrates this procedure. The physical eigenvalues appear to form two symmetric branches about the real axis, due to the fact that the coefficients of the response matrix are real numbers. In particular, the growing modes are the ones above the real axis. However, as can be seen from this figure, a lot of eigenvalues accumulate along the real axis. These do not necessarily correspond to physical values, even though they have passed the previous convergence test. Indeed, a lot of them accumulate on the line as I increase the truncation number, which fools the test.

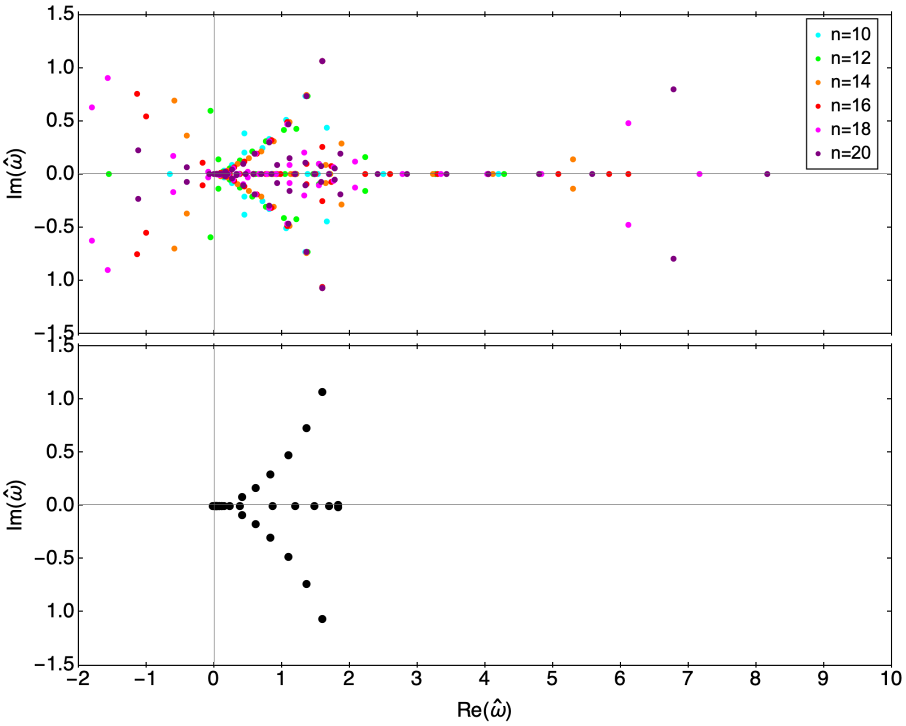

Figure 6.C.1: On the top panel, I illustrate the convergence method (section 6.C.1) by showing the series of truncated eigenvalues obtained for a galactic disc with no bulge and no DH, with $\varepsilon_0 = 0.15$ and $m = 2$. The various colours indicate the truncation numbers, n. On the bottom panel, I represent the physical eigenvalues as determined through the convergence study.

6.C.2 Exploration of the disc's parameters

Let me restrict this study to $m = 2$ modes, as those usually produce the fastest modes. First, following Aoki et al. (1979), I compute the impact of temperature on the eigenvalues of the disc. To that end, I consider a disc with no bulge and no DH, i.e. $p = 0$ and $q = 1$. I represent in Fig. 6.C.2 the evolution of the eigenvalues as I increase the disc's temperature ε_0. The two branches of eigenvalues grow closer to the real axis. In addition, it appears that fewer and fewer eigenvalues are present on the branches. The *critical threshold* is reached around $\varepsilon_0 \sim 0.5$. Beyond this value, no physical eigenvalues – apart from the possibly purely rotating ones on the real axis – exist, hence the disc has been stabilised. Under these conditions, no spiral arms nor any bars will form, as no growing modes can be excited by fluctuations. This $\varepsilon_0 \sim 0.5$ threshold can be understood reasonably well: this is the point where the disc pressure begins to dominate over gravity. Any gravitationally bound structure will be swept away by pressure forces beyond this point.

Second, let me study the impact of the bulge and the DH on the eigenvalues. Because I have observed that warm discs do not produce growing eigenvalues, let me consider a cold disc, with for example $\varepsilon_0 = 0.15$. I represent in Fig. 6.C.3 a series of complex-frequency diagrams for various bulge and DH components.

Increasing the DH component, i.e. reducing the value of q, has the same effect as increasing the temperature of the disc. The DH stabilises the disc, and there exists a threshold beyond which no growing mode exists. Increasing the bulge component, i.e. increasing the value of p, also has the effect of lowering the eigenvalues' branches towards the real axis. However, this convergence is a bit peculiar. Indeed, the mode that was initially the fastest growing mode de-

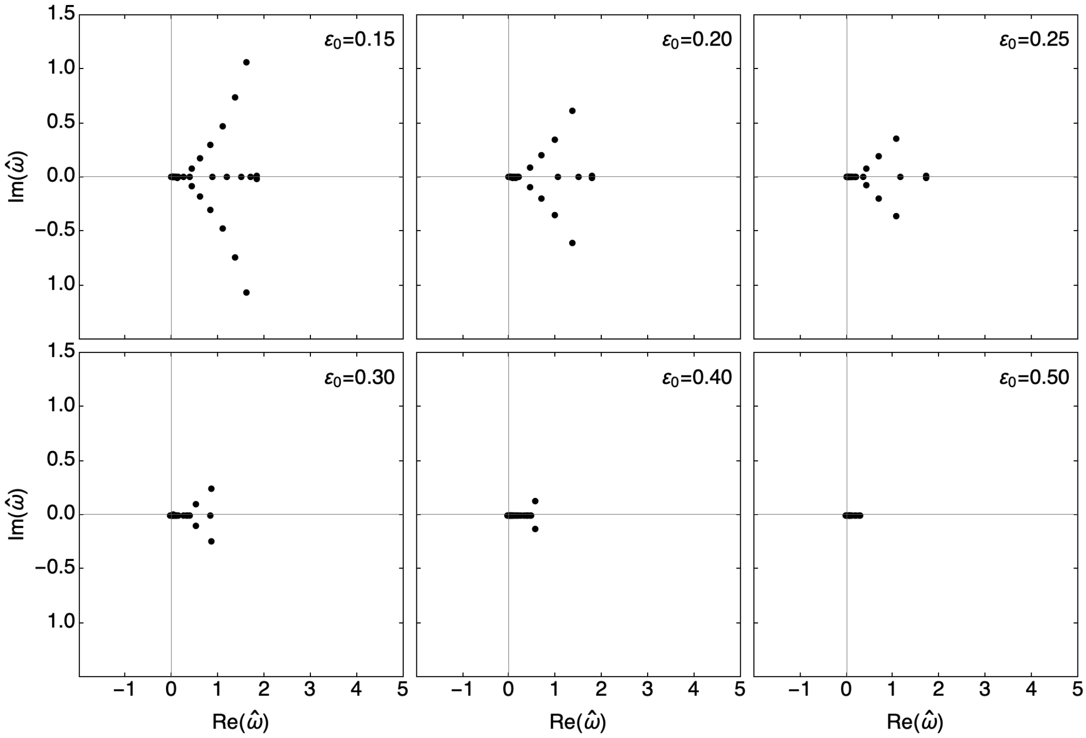

Figure 6.C.2: Evolution of the physical eigenvalues of a galactic disc with no bulge and no DH as I increase the temperature ε_0. From left to right and top to bottom, I show $\varepsilon_0 = 0.15, 0.2, 0.25, 0.3, 0.4, 0.5$. Fewer and fewer eigenvalues are present on the branches. Beyond $\varepsilon_0 \sim 0.5$, the disc is stabilised by pressure forces and no growing eigenvalues remain.

creases quickly enough for the second eigenvalue of the branch to become the fastest growing mode. This process repeats itself with the third eigenvalue, and so on, until the branch eventually merges with the real axis at some finite value of p (depending on q). This process is responsible for the intricate structure observed in Fig. 6.3.1.

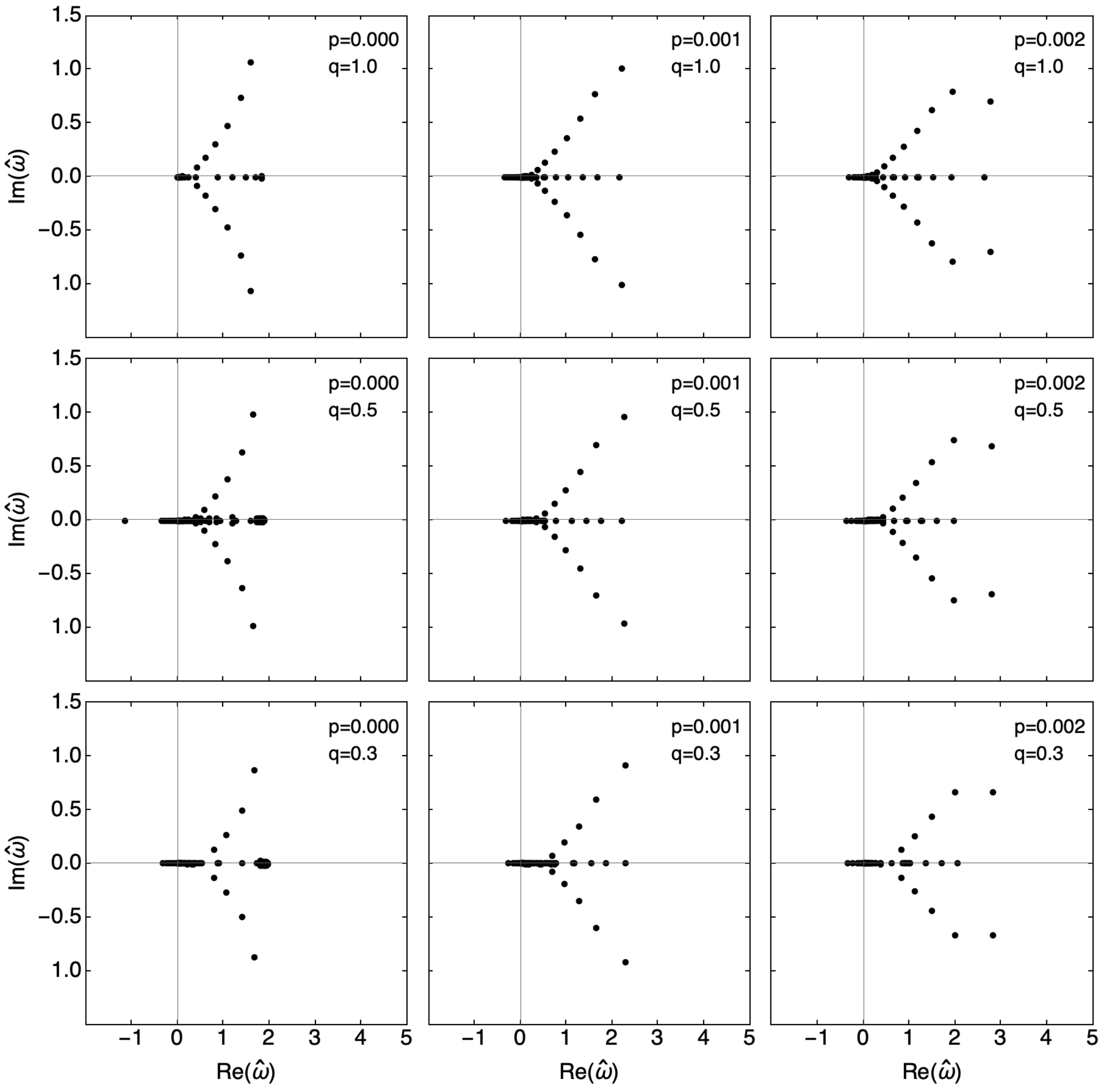

Figure 6.C.3: Evolution of the growing modes of a cold galactic disc with fixed temperature $\varepsilon = 0.1$ and varying bulge fraction $p = 0, 0.01, 0.02$ (columns) and DH fraction $q = 1.0, 0.5, 0.3$ (rows). Increasing the bulge component or the DH component lowers the growth rate of the disc's bar. Furthermore, the branches appear to curl on themselves as the bulge fraction p increases.

Chapter 7

Conclusion

7.1 Overview

The last half century has seen the development of numerical simulations, and in particular the ever-increasing degree of precision and details that they contain (von Hoerner, 1960; Aarseth, 1963; Barnes & Hut, 1986; Hockney & Eastwood, 1988; Makino et al., 1997; Aarseth, 2003; Heggie & Hut, 2003; Springel, 2005; Springel et al., 2005; Trenti & Hut, 2008; Dehnen & Read, 2011; Wang et al., 2015). While these simulations can be used to confront the predictions made from theoretical models, they are also intensively used to model non-linear phenomena such as the core collapse of globular clusters or galaxy evolution (see, e.g., Vogelsberger et al., 2020). These numerical observations motivate analytical models to understand and clarify the underlying mechanisms often hidden therein. For instance, we may then ask what is the impact of anisotropy on the secular evolution of stellar clusters – in particular globular clusters – but also the impact of their inner rotation. Since these systems are in quasi-stationary states, they are subject to small departure from the mean field. Thus, the description of the evolution of their ensemble average falls within the realm of kinetic theory (Binney & Lacey, 1988; Heyvaerts, 2010). Such theories can be tailored to take into account anisotropy and rotation, to break away from the standard paradigm. This was the focus of my Ph.D. work.

Specifically, my thesis aimed at studying the *long-term evolution of stellar systems* in order to address challenging problems posed by recent observations. Recent developments of kinetic theory provided me with the opportunity of numerically addressing these problems:

- I used the existing averaged RR diffusion theory to probe the presence of IMBHs in the *Galactic nucleus*. Making use of existing observations of the S-stars, I implemented a likelihood approach to constrain the space of parameters modelling a background dark cluster.
- I developed the two-body deflection NR theory for *anisotropic*, and then *rotating clusters* to investigate core collapse and *orbital reshuffling*. I found that in-plane diffusion can be predicted rather accurately using NR formalism, suggesting that the role of resonances in the Balescu–Lenard formalism is possibly less important than it seems at face value. Contrarily, I showed that the NR theory is not sufficient to describe out-of-plane relaxation, because this relaxation is impacted by the high degree of coherence of the respective motions of the stars.
- I quantified the specific impact of resonant relaxation in terms of an effective action dependent *Coulomb logarithm*. Using the RR theory and earlier works by Heggie & Ret-

terer (priv), I recovered the observed NR prediction both in numerical and in asymptotic regimes.

- I applied linear response theory to interpret the *lack of bars* in the NewHorizon simulation. I found that most galaxies in the NewHorizon simulation fall within a low linear growth region, hence are less likely to develop the bi-symmetric instability required to later form a bar during their non-linear regime.

In my thesis, I have shown why kinetic theory captures *non-linear phenomena* reflecting the diversity of outcomes induced by different initial phases. This has multiple consequences. First, when a kinetic theory can be applied, it is as potent as large sets of numerical and hydrodynamical simulations, which require many (costly) realisations and subtle stacking strategies to extract the relevant statistical observables.[a] This makes kinetic theory interesting as a prediction tool, beyond a mere checking tool. Additionally, kinetic theory provides a strategy on how to take averages when stacking simulations. Indeed, determining which quantity should be averaged and how to do so is not a trivial question *a priori*. Yet, chapter 2 demonstrates that ensemble average (i.e. stacking) should be carried in action space,[b] so as to correctly recover the secular behaviour of the underlying phase-averaged distribution function. The precise match observed in this thesis between kinetic theory predictions and stacked numerical measurements is a clear illustration of this point. While the stacking of simulations also provides estimates for the spread in the range of outcomes depending on the initial phases, the quantification of the dispersion around the mean kinetic prediction is also the topic of on-going research using, e.g., large deviations theory (see, e.g., Feliachi, 2023).

Let me recap in somewhat more details my findings. First, I sketched in chapter 2 a derivation for the theory of orbital diffusion. This allowed me to describe the *secular fate of isolated, self-gravitating systems* using the Balescu–Lenard equation (eq. 2.2.31). This equation, which drives the secular evolution of the DF of a stellar system, is sourced by potential fluctuations. As such, it can be applied to a wide range of astrophysical systems. For example, for tepid galactic discs, it can be used to explain two phenomena: (i) the *strong amplifications of its fluctuations* are the result of the resonant denominator occurring in its expression; (ii) the resonant ridges occurring in action space are the result of the *resonant interactions* described by the Balescu–Lenard equation. However, there are also systems for which the Balescu–Lenard equation does not predict a strong amplification nor does it display the resonant features one might have expected from its structure. In the first case, the Balescu–Lenard equation becomes to the inhomogeneous Landau equation (eq. 2.3.1, Fig. 7.1.1). When also assuming the local homogeneity approximation, it reduces to the classical Chandrasekhar equation (eq. 2.3.9, Fig. 7.1.1).

In chapter 3, I focused on the relaxation of stars in the Galactic nucleus. In particular, I attempted to *probe the existence of a family of unresolved heavy objects hidden in the S-cluster*, and whether these could be IMBHs. While the secular evolution of this system can be described exactly by the Landau formalism (i.e. the RR theory), the presence of an SMBH at its centre induces a clear separation of timescales. This motivated an orbit-average over the fast Keplerian motion of every star (eq. 3.3.1, Fig. 7.1.1). With this formalism, I identified regions in orbital spaces where the RR dynamics is very efficiently damped: the Schwarzschild barrier (Fig. 3.3.4) observed by Merritt et al. (2011). However, as this description is an orbit-averaged version of the real dynamics, higher-order resonances have been neglected. Because these res-

---

[a] A possible illustration of the *no free lunch* principle!

[b] This is because actions label orbits which are preserved in the mean field, and only change when exposed to a given realisation of the noise-driven fluctuation.

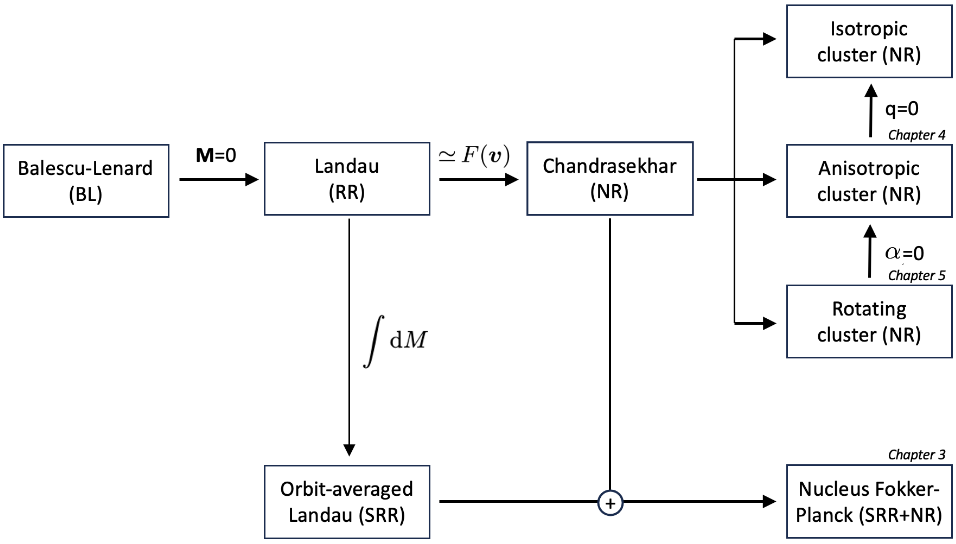

Figure 7.1.1: The Balescu–Lenard equation can be used to predict the secular fate of a wide range of self-gravitating systems. Using a series of approximations, I could derive a resonant relaxation theory (RR) to describe eccentricity relaxation in the Galactic nucleus, but also a non-resonant theory (NR) to describe orbital diffusion in globular clusters.

onances correspond to small-scale interactions, this justifies that I include the NR contribution on top of the orbit-averaged RR one (eq. 3.3.2 and Fig. 3.3.5). Using this unified theory, I was able to predict, for parametrised models, the secular fate of the Galactic nucleus (Fig. 7.1.1). Using observational data, this allowed me to perform a *dark matter experiment*, in which I constrained the presence of IMBHs within the Galactic cluster using a *likelihood analysis* (eq. 3.4.5 and Fig. 3.4.4) on the eccentricity distribution of the S-stars. Interestingly, recent works from Fouvry et al. (2023) produced results in general agreement with my predictions, by relying on the observed disc of stars which did not have time to reshuffle in orientation via resonant relaxation.

Globular clusters display a completely different behaviour. In chapter 4, I focused on non-rotating globular clusters. Under the effect of self-gravity, the core of these dense stellar clusters contract. Numerical works from Breen et al. (2017) have suggested that *velocity anisotropies can impact the rate of core collapse*, with tangential anisotropy accelerating the process (Fig. 4.1.2). Using the NR relaxation formalism, which I extended to anisotropic clusters in chapter 2, I derived the orbit-averaged Fokker–Planck equation (eq. 2.3.34) describing the evolution of the orbital distribution of this system. I was able to show that the NR theory can recover remarkably well the shape of the orbital diffusion observed in my N-body simulations, in the sense that I was able to predict both the distortion and the isotropisation observed in statistical averages of direct numerical simulations (Fig. 4.5.2). Nonetheless, differences do occur between theory and simulations, in the form of an anisotropy-dependent prefactor (Fig. 4.5.3). I argued that this discrepancy stems from far-away encounters, which are not correctly taken into account in the NR theory. I also showed how an effective pseudo-isotropic approach (eq. 4.6.1) to the theory could yield a good fit to the numerical observations, due to the weak anisotropy of the cluster. I recalled that the NR formalism can be obtained from the exact Balescu–Lenard description of the self-gravitating system while relying on two assumptions: *no collective effects* and *local homogeneity* (as discussed in chapter 2), which removes any resonant interaction which appears in the Balescu–Lenard equation. Hence, the secular theory of relaxation for hot systems appears not to be as resonant as naively expected, as can be seen from the successive harmonics contributions in the RR formalism (eq. 4.7.1). Higher harmonic orders, which describe small-scale interactions, tend towards the NR prediction up to some weakly action-dependent prefactor which can formally be connected back to the *Coulomb logarithm* (eq. 4.7.8 and Fig. 4.7.5). Heggie & Retterer (priv) obtained insightful analytical results along those lines. They recovered exactly the orbit-averaged NR expression of a given diffusion coefficient from RR theory, down to its numerical prefactor, despite the numerous hypotheses they made to perform their computation.

Rotating clusters are yet another example of how kinetic diversity can impact secular relaxation. Observations show that almost all systems display some degree of rotation. In chapter 5, I extended my kinetic theory to these systems. Rotating clusters are indeed dynamically colder than the anisotropic clusters studied in chapter 4, i.e. the velocity dispersion of their stars is lower. As a consequence, it is expected that their gravitational susceptibility is amplified by the amount of rotation, through resonant interactions between co-rotating orbits. I studied the impact of rotation in orbital space against N-body simulations by computing the two-dimensional Fokker–Planck equation in (J_r, L)-space. I showed that rotation does not appear to have a significant impact on the shape of radial orbital distortions (for stable clusters, see Fig. 5.2.7). I also computed the two-dimensional Fokker–Planck equation in the $(J_\mathrm{r}, \cos I)$-space, and found that relaxation tended to *reshuffle orbital inclinations* so as to *erase sharp gradients* in the DF (e.g., around $\cos I = 0$ for the LBD, see Fig. 5.2.6). Interestingly, whereas the NR theory provides a prediction of the *in-plane relaxation which closely matches* that of N-body simulations (up to the aforementioned prefactor, see Figs. 5.2.4 and 5.3.1), it is *not so accurate in predicting out-of-plane relaxation* (Figs. 5.2.5, 5.3.2 and 5.3.3). This highlights the limits of the NR formalism in describing colder systems. While *no strong amplification is numerically observed*, it is likely that *coherent interactions* between co-rotating orbits can drive the relaxation of the orbital inclinations (probed by $\cos I$ in this manuscript). Because the NR theory drives the $\cos I$-diffusion only through local encounters, it will fail to recover this phenomenon. However, because it is fundamentally degenerate for 3D spherically symmetric systems ($\Omega_3 = 0$, see, e.g., Hamilton et al., 2018), the Balescu–Lenard equation cannot be used to study the impact of resonant and collective effects on azimuthal relaxation. The alternative *VRR formalism* circumvents this caveat, and may be key to understanding the shortcoming of NR theory.

In chapter 6, I considered the secular evolution of a self-gravitating thin disc, focusing on the problem of secular bar growth. To that end, I revisited the method put forward in Aoki et al. (1979) in order to study a self-gravitating thin gaseous disc with a central spherical bulge and a spherical dark halo. This allowed me to convert the problem into an *eigenproblem* involving infinite matrices (eq. 6.2.8). Using this formalism, I extracted the physical eigenvalues of the system to study their dependence on the geometry of the galaxy, i.e. the bulge to disc ratio, the dark halo to disc ratio and the disc's temperature. Comparing these findings to the hydrodynamical simulation NewHorizon (Reddish et al., 2022), I explained the *very small number of bars* observed in the simulation. Indeed, most galaxies in the simulation fall within the region of low growth rate (Fig. 6.3.1). Therefore, I expect that *no bi-symmetric instability* should occur within these discs, hence no bar formation during the non-linear regime. Conversely, the only barred galaxy observed in the simulation is the one expected to have the highest growth rate of the simulation, hence in agreement with the linear prediction.

Overall, through a variety of approximations, I have argued in this thesis that secular relaxation has reached the point where it can be used to explain observations, stacked N-body simulations (e.g., globular clusters) or large hydrodynamical simulations (e.g., bar formation in discs). I have also shown that it can now be used against real data to conduct likelihood analysis of astrophysical models (e.g., for the research of IMBHs in the Galactic nucleus). The ever-increasing size of data samples produced by modern instruments, together with the explosion of very precise simulations, require a flexible, parametric formalism able to deal with the whole complexity of self-gravitating systems, on long timescales and on a large panel of physical scales. As such, modern secular kinetic theory has proven to be effective in dealing with the richness and complexity of evolved astrophysical systems.

7.2 Prospects

As a complement to the perspectives within each chapter, let me conclude this manuscript by discussing possible future works at the intersection of the various themes investigated in this thesis.

Time integration. In this manuscript, all the predictions concerning orbital diffusion were made at $t = 0^+$. Yet, orbital space evolution to later times is also of immediate interest. To that end, the relevant evolution equation – the Fokker–Planck equation for the RR (eq. 2.3.1) or NR (eq. 2.3.18) diffusions – would have to be integrated forward in time. However, as highlighted by Weinberg (2001a,b), time integration presents a few difficulties. The first one comes from the computation of the diffusion coefficients. Their evaluation is made difficult by the *self-consistency* inherent to this problem, as the DF appears twice in the Landau equation (eqs. 2.2.30 and 2.2.31). Furthermore, one would have to evolve not only the DF, but also the system's potential, which are related through Poisson equation. The self-consistent potential also defines the new angle-action coordinates, which must be determined from the self-consistent potential. The second issue comes from the *numerical challenge* imposed by the various computational resources required to compute the diffusion rate. This difficulty is strengthened as one adds anisotropy and rotation to the system. One may integrate the corresponding stochastic Langevin equation using a *Monte Carlo* approach (Hénon, 1971) following the method I use to validate my results in chapter 3 (see, e.g., Vasiliev, 2015, 2017). This method could be generalised to validate N-body codes on secular timescales.

A prescription for the Coulomb logarithm. When studying anisotropic and rotating globular clusters, I assumed in particular *local homogeneity*. After phase averaging, this leads to the incoherent NR formalism. The properties of isotropic clusters (Hamilton et al., 2018) and comparisons to N-body simulations motivated this approximation. While this approach yields satisfying results when predicting diffusion rates for a non-rotating cluster, there are still caveats to it, such as the overall anisotropic-dependent prefactor quantified in chapter 4 (Fig. 4.5.3). On a practical level, the RR theory now provides us with an estimate for this prefactor. On a more theoretical level, RR should be a way to express the Coulomb logarithm $\ln\Lambda$ without resorting to any heuristic arguments (Heggie & Retterer, priv). In addition, rotating systems, where the action space structures predicted by NR do not match the N-body predictions as well, requires the development of a more complex theory beyond NR. While some theoretical work has started (Rozier et al., 2019), the implementation of kinematically more complex theories – such as the inhomogeneous Landau equation, the Balescu–Lenard equation or VRR (Meiron & Kocsis, 2019) – will be the topic of my upcoming research.

Flattened systems. Observed globular clusters are typically flattened at some level. Generalising the orbital diffusion formalism to flattened objects would broaden the scope of applicability of kinetic theory to a wider range of astrophysical objects (such as, e.g., elliptical galaxies). This may prove challenging. The orbital diffusion formalism is built upon the integrability of the mean potential, i.e. the existence of angle-action coordinates so as to capture

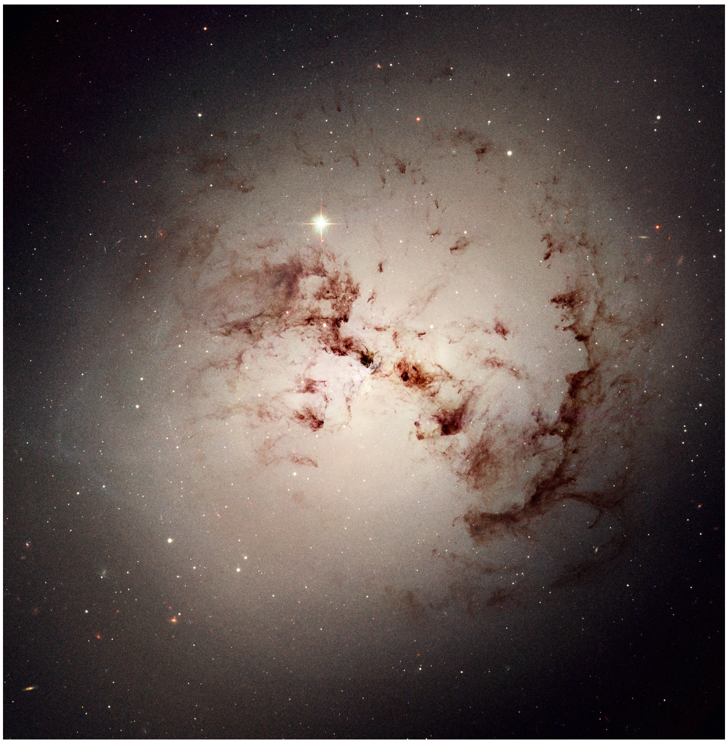

Figure 7.2.1: Image of NGC 1316 by the HST. This galaxy is lenticular, and therefore can be treated neither as a thin disc or as a spherical system. To determine its secular fate using kinetic theory, a more general treatment of axisymmetric and triaxial systems is required. Credit: NASA/ESA.

the trajectories imposed by the mean field. While the spherically symmetric systems I studied here are all integrable, this is not systematically the case in axisymmetric (Fig. 7.2.1) or triaxial systems (see, e.g., Merritt & Vasiliev, 2011, for an example of an integrable triaxial system). Two cases may occur depending on the systems at play. First, the system may *lack integrability*, in which case its dynamics could be partially driven by chaotic diffusion (see, e.g., Weinberg, 2015a,b). Second, the system may be *numerically integrable*. By this, I mean that a third integral of motion could exist (Poincaré sections), but we may lack an analytical expression for it. This case typically occurs in axisymmetric systems, including flattened and rotating stellar systems. Ultimately, *Stäckel systems* (Stäckel, 1889; Dejonghe & de Zeeuw, 1988) may be a way to probe the behaviour and secular evolution of a subclass of such systems, as they have three *analytical actions* and can be used to model real astrophysical observations (Vasiliev, 2019a).[c]

Multi-mass systems. While this thesis focussed mostly on equal mass clusters, chapter 3 has shown that it is astrophysically interesting to leverage multiple masses. First of all, one may be interested in studying the impact of multiple stellar families – instead of the present single-mass component cluster – with the aim of investigating mass segregation effects. The work presented in my thesis can and should straightforwardly be adapted to this matter. This is particularly motivated by recent observations of nuclear and galactic stellar clusters. One could revisit the entropic analysis of Szölgyén & Kocsis (2018) and Magnan et al. (2022) while relying on kinetic theory to predict the time evolution of the mass segregation of massive discs in galactic centres. Conversely, Dekel et al. (2023) argues for instance that the excess of massive galaxies found at very high redshift by the JWST could originate from early feedback-free star

---

[c] More generally, developing a secular theory for non-integrable systems would clearly extend its realm of applicability. Since diffusion remains a local process, local Stäckel fits might be a venue (see, e.g., Sanders & Binney, 2016, for a review).

formation within dense stellar clusters made of massive stars. The fate of such clusters should be captured by the kinetic theory presented in chapters 4 and 5, and could lead to the formation of IMBHs and possibly the seed for SMBHs.

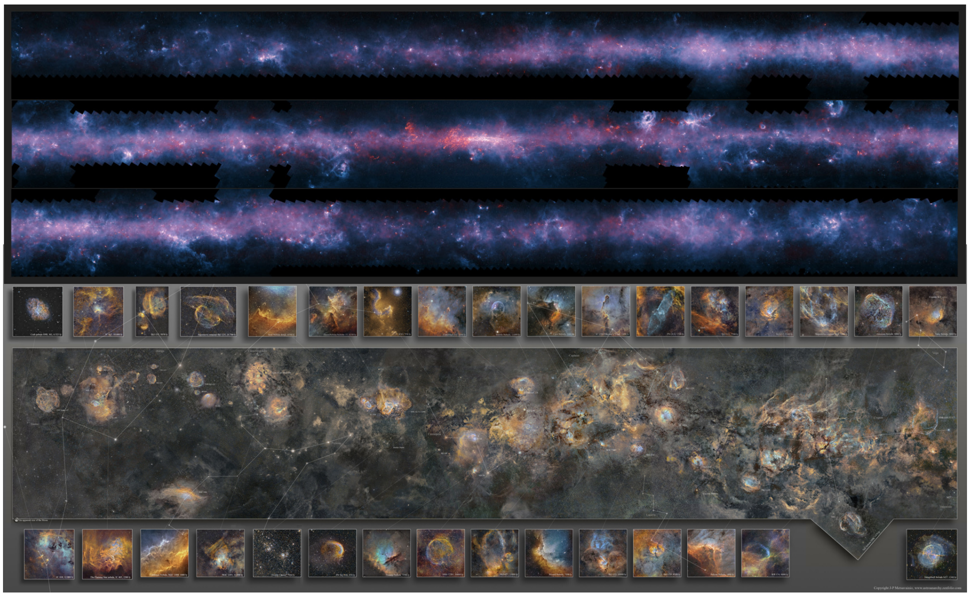

Figure 7.2.2: Illustration of the turbulent processes which occur in the Galactic medium. On the top panel, the three slices show the full area of the Galactic Plane visible from the southern hemisphere at submillimetre wavelengths, by the APEX telescope. These images are complemented with observations from the NASA Spitzer Space Telescope and ESA's Planck satellite. On the bottom panel, observations show how turbulent flows and supernovae remnant impact the Milky Way's internal structure. Credits: ESO/APEX/ATLASGAL, NASA/ESA and J.-P. Metsavainio.

Open systems. The orbital diffusion formalism is interesting in the way it can describe self-gravitating systems subject to very non-linear phenomena. In the context of this thesis, I focused on isolated stellar systems. While one could maybe argue that this assumption is a good proxy for systems such as galactic nuclei, it is less applicable to globular clusters or galaxies. Indeed, galaxies, for instance, are impacted by *inflows* and *external potential perturbations* such as fly-bys, minor mergers, turbulence and supernovae explosions (Fig. 7.2.2). Accounting for the effects of the corresponding dissipative processes is all the more important that the baryonic component seems to induce the appearance of attractors via self-regulation. Ultimately, external fluctuations could therefore also contribute or indeed dominate secular evolution (Park et al., 2021). The work presented in this thesis should therefore eventually be generalised to account for inflow and dissipation. This should lead to a wealth of new phenomena, such as the *emergence of orderly low entropy structures*. A preliminary investigation was recently attempted by Yi et al. (2023) where they averaged (over 30 galaxies, see Fig. 6.1.1 for a sample) the drift coefficient of the circularity parameter, ε (Fig. 7.2.3), within the cosmological simulation NewHorizon (Fig. 1.2). In addition, net inflow should also eventually generically be integrated into the kinetic framework, as it impacts directly the adiabatic response of the clusters (Pichon & Aubert, 2006; Aubert & Pichon, 2007), possibly driving it through stability thresholds (chapter 6 and De Rijcke et al., 2019a), or boosting its rate of diffusion while increasing its gravitational susceptibility. The competing effect of external versus internal fluctuations versus adiabatic drifts could be quantified in this framework.

Timescale separation. Finally, while the accuracy of the *Bogoliubov's ansatz* could in principle challenge the relevance of such endeavour, recent work by Fouvry & Roule (2023) suggest

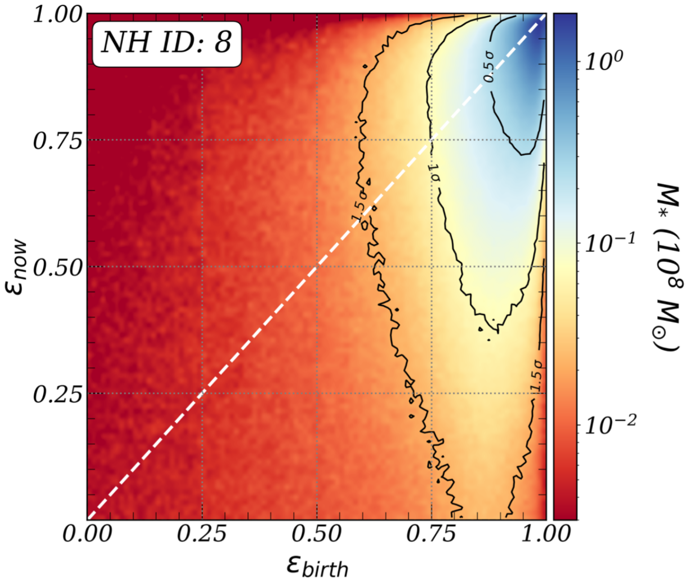

Figure 7.2.3: From fig. 12 of Yi et al. (2023). Comparison between the circularity $\varepsilon = L/L_{\mathrm{c}}$ at birth and at today for one galaxy in NewHorizon. Black lines correspond to 0.5σ, 1.0σ and 1.5σ contours. Most stars are initially very circular (i.e. ε is close to 1). However, they tend to become less so as time evolve, as can be seen by the position of the peak under the first diagonal of the figure.

that, e.g., the Balescu–Lenard formalism also holds in the not so large N limit. This kind of measurement should be carried more systematically in the future. Developing the corresponding extended kinetic theory should be the goal of upcoming investigations.

Globally, these various extensions will provide opportunities to go beyond today's closed-box perspective and advance the field towards a detailed understanding of the cosmic fate of inter-connected self-gravitating systems over half a Hubble time.

Bibliography

Aarseth S. J., 1963, MNRAS, 126, 223

Aarseth S. J., 2003, Gravitational N-Body Simulations. Cambridge University Press

Aarseth S. J., Hénon M., Wielen R., 1974, A&A, 37, 183

Abbott B. P., Abbott R., Abbott T. D., Abernathy M. R., 2016, Phys. Rev. Lett., 116, 061102

Abbott B. P., Abbott R., Abbott T. D., 2017, Phys. Rev. Lett., 119, 141101

Abel T., Bryan G. L., Norman M. L., 2000, ApJ, 540, 39

Agertz O., et al., 2021, MNRAS, 503, 5826

Akiyama K., Sugimoto D., 1989, PASJ, 41, 991

Alexander T., 2005, Phys. Rep., 419, 65

Alexander T., 2017, Ann. Rev. Astron. Astrophys., 55, 17

Aoki S., Iye M., 1978, PASJ, 30, 519

Aoki S., Noguchi M., Iye M., 1979, PASJ, 31, 737

Arad I., Lynden-Bell D., 2005, MNRAS, 361, 385

Arnold V. I., 1978, Mathematical methods of classical mechanics. Springer-Verlag New York

Athanassoula E., 2002, ApJL, 569, L83

Athanassoula E., Sellwood J. A., 1986, MNRAS, 221, 213

Aubert D., Pichon C., 2007, MNRAS, 374, 877

Aubert D., Pichon C., Colombi S., 2004, MNRAS, 352, 376

Balescu R., 1960, Physics of Fluids, 3, 52

Bar-Or B., Alexander T., 2016, ApJ, 820, 129

Bar-Or B., Fouvry J.-B., 2018, ApJL, 860, L23

Bardeen J. M., Bond J. R., Kaiser N., Szalay A. S., 1986, ApJ, 304, 15

Barnes J., Hut P., 1986, Nature, 324, 446

Barré J., Olivetti A., Yamaguchi Y. Y., 2010, J. Stat. Mech., 2010, 08002

Barré J., Olivetti A., Yamaguchi Y. Y., 2011, J. Phys. A Math. Theor., 44, 405502

Bartko H., et al., 2009, ApJ, 697, 1741

Baumgardt H., Makino J., Ebisuzaki T., 2004, ApJ, 613, 1143

Begelman M. C., Volonteri M., Rees M. J., 2006, MNRAS, 370, 289

Begelman M. C., Rossi E. M., Armitage P. J., 2008, MNRAS, 387, 1649

Bellini A., Anderson J., Bedin L. R., King I. R., van der Marel R. P., Piotto G., Cool A., 2017, ApJ, 842, 6

Benetti F. P. C., Marcos B., 2017, Phys. Rev. E., 95, 022111

Benhaiem D., Joyce M., Sylos Labini F., Worrakitpoonpon T., 2016, A&A, 585, A139

Berentzen I., Athanassoula E., Heller C. H., Fricke K. J., 2004, MNRAS, 347, 220

Bertin G., Varri A. L., 2008, ApJ, 689, 1005

Bertrand J., 1873, C. R. Acad. Sci., Paris, 77, 849

Bianchini P., Varri A. L., Bertin G., Zocchi A., 2013, ApJ, 772, 67

Bianchini P., van der Marel R. P., del Pino A., Watkins L. L., Bellini A., Fardal M. A., Libralato M., Sills A., 2018, MNRAS, 481, 2125

Binney J., Lacey C., 1988, MNRAS, 230, 597

Binney J., Tremaine S., 2008, Galactic Dynamics: Second Edition. Princeton Univ. Press

Boehle A., et al., 2016, ApJ, 830, 17

Bond J. R., Kofman L., Pogosyan D., 1996, Nat, 380, 603

Bournaud F., Combes F., 2002, A&A, 392, 83

Bournaud F., Combes F., Semelin B., 2005, MNRAS, 364, L18

Breen P. G., Varri A. L., Heggie D. C., 2017, MNRAS, 471, 2778

Breen P. G., Rozier S., Heggie D. C., Varri A. L., 2021, MNRAS, 502, 4762

Brodie J. P., Strader J., 2006, Ann. Rev. Astron. Astrophys., 44, 193

Bromm V., Coppi P. S., Larson R. B., 1999, ApJL, 527, L5

Bromm V., Coppi P. S., Larson R. B., 2002, ApJ, 564, 23

Carr B. J., Bond J. R., Arnett W. D., 1984, ApJ, 277, 445

Casertano S., Hut P., 1985, ApJ, 298, 80

Chandrasekhar S., 1942, Principles of stellar dynamics. The University of Chicago press

Chandrasekhar S., 1943, ApJ, 97, 255

Chandrasekhar S., von Neumann J., 1942, ApJ, 95, 489

Chavanis P.-H., 2012, Physica A, 391, 3680

Chavanis P.-H., 2013a, Eur. Phys. J. Plus, 128, 126

Chavanis P.-H., 2013b, A&A, 556, A93

Chavanis P.-H., 2023, Eur. Phys. J. Plus, 138, 136

Chernoff D. F., Weinberg M. D., 1990, ApJ, 351, 121

Churchill R. V., Brown J. W., 2009, Complex variables and applications: Eighth Edition. McGraw-Hill Higher Education

Clarke C., Carswell B., 2007, Principles of Astrophysical Fluid Dynamics. Cambridge University Press

Cohn H., 1979, ApJ, 234, 1036

Cohn H., 1980, ApJ, 242, 765

Cohn H., Kulsrud R. M., 1978, ApJ, 226, 1087

Combes F., Elmegreen B. G., 1993, A&A, 271, 391

Combes F., Sanders R. H., 1981, A&A, 96, 164

Curir A., Mazzei P., Murante G., 2007, A&A, 467, 509

Dalton G., et al., 2012, in Ground-based and Airborne Instrumentation for Astronomy IV. p. 84460P

Dalton G., et al., 2016, in Ground-based and Airborne Instrumentation for Astronomy VI. p. 99081G

Davies R., et al., 2018, in Ground-based and Airborne Instrumentation for Astronomy VII. p. 107021S

Davis M., Efstathiou G., Frenk C. S., White S. D. M., 1985, ApJ, 292, 371

De Rijcke S., Voulis I., 2016, MNRAS, 456, 2024

De Rijcke S., Fouvry J.-B., Pichon C., 2019a, MNRAS, 484, 3198

De Rijcke S., Fouvry J.-B., Dehnen W., 2019b, MNRAS, 485, 150

DeBuhr J., Ma C.-P., White S. D. M., 2012, MNRAS, 426, 983

Debattista V. P., Sellwood J. A., 2000, ApJ, 543, 704

Dehnen W., Read J. I., 2011, European Physical Journal Plus, 126, 55

Dejonghe H., 1986, Phys. Rep., 133, 217

Dejonghe H., 1987, MNRAS, 224, 13

Dejonghe H., de Zeeuw T., 1988, ApJ, 333, 90

Dekel A., Sarkar K. C., Birnboim Y., Mandelker N., Li Z., 2023, MNRAS, 523, 3201

Delaunay C.-E., 1860, Théorie du mouvement de la lune. Mallet-Bachelier

Delgado-Serrano R., Hammer F., Yang Y. B., Puech M., Flores H., Rodrigues M., 2010, A&A, 509, A78

Diamond P. H., Itoh S.-I., Itoh K., 2010, Modern Plasma Physics. Cambridge University Press

Díaz-García S., Salo H., Laurikainen E., Herrera-Endoqui M., 2016, A&A, 587, A160

Do T., et al., 2019, BAAS, 51, 530

Do T., et al., 2020, ApJ, 901, L28

Dressler A., 1980, ApJs, 42, 565

Drukier G. A., Cohn H. N., Lugger P. M., Yong H., 1999, ApJ, 518, 233

Du M., Debattista V. P., Shen J., Ho L. C., Erwin P., 2017, ApJL, 844, L15

Dubois Y., et al., 2021, A&A, 651, A109

Duncan M. J., Levison H. F., Lee M. H., 1998, AJ, 116, 2067

Eddington A. S., 1916, MNRAS, 76, 572

Eilon E., Kupi G., Alexander T., 2009, ApJ, 698, 641

Einsel C., Spurzem R., 1999, MNRAS, 302, 81

Einstein A., 1905, Annalen der Physik, 322, 549

Eisenhauer F., 2019, in The Very Large Telescope in 2030. p. 30

Eisenstein D. J., Loeb A., 1995, ApJ, 443, 11

Ernst A., Glaschke P., Fiestas J., Just A., Spurzem R., 2007, MNRAS, 377, 465

Event Horizon Telescope Collaboration et al., 2019, ApJL, 875, L1

Event Horizon Telescope Collaboration et al., 2022, ApJL, 930, L14

Fabricius M. H., et al., 2014, ApJL, 787, L26

Feldmeier A., et al., 2014, A&A, 570, A2

Feliachi O., 2023, PhD thesis, Université d'Orléans

Ferraro F. R., et al., 2018, ApJ, 860, 50
Fiestas J., Spurzem R., 2010, MNRAS, 405, 194
Fiorentino G., et al., 2019, arXiv: 1712.04222
Foote H. R., Generozov A., Madigan A.-M., 2020, ApJ, 890, 175
Fouvry J.-B., 2020, Kinetic theory of self-gravitating systems
Fouvry J.-B., 2022, Phys. Rev. E., 106, 054123
Fouvry J.-B., Bar-Or B., 2018, MNRAS, 481, 4566
Fouvry J.-B., Prunet S., 2022, MNRAS, 509, 2443
Fouvry J.-B., Roule M., 2023, arXiv:2306.04613,
Fouvry J.-B., Pichon C., Prunet S., 2015a, MNRAS, 449, 1967
Fouvry J.-B., Pichon C., Chavanis P.-H., 2015b, A&A, 581, A139
Fouvry J.-B., Pichon C., Magorrian J., Chavanis P.-H., 2015c, A&A, 584, A129
Fouvry J.-B., Binney J., Pichon C., 2015d, ApJ, 806, 117
Fouvry J.-B., Chavanis P.-H., Pichon C., 2016, Physics Letters A, 380, 2589
Fouvry J.-B., Pichon C., Magorrian J., 2017, A&A, 598, A71
Fouvry J.-B., Bar-Or B., Chavanis P.-H., 2019a, Phys. Rev. E., 99, 032101
Fouvry J.-B., Bar-Or B., Chavanis P.-H., 2019b, ApJ, 883, 161
Fouvry J.-B., Hamilton C., Rozier S., Pichon C., 2021, MNRAS, 508, 2210
Fouvry J.-B., Dehnen W., Tremaine S., Bar-Or B., 2022, ApJ, 931, 8
Fouvry J.-B., José Bustamante-Rosell M., Zimmerman A., 2023, arXiv: 2305.15998,
Frenk C. S., White S. D. M., 2012, Annalen der Physik, 524, 507
Frisch U., 1995, Turbulence. The legacy of A.N. Kolmogorov. Cambridge University Press
Gaia Collaboration et al., 2016, A&A, 595, A2
Gaia Collaboration et al., 2018, A&A, 616, A1
Gaia Collaboration et al., 2021, A&A, 649, A1
Gardner J. P., et al., 2006, SSR, 123, 485
Generozov A., Madigan A.-M., 2020, ApJ, 896, 137
Genzel R., Eckart A., 1999, in The Central Parsecs of the Galaxy. p. 3
Geyer E. H., Hopp U., Nelles B., 1983, A&A, 125, 359
Ghez A. M., et al., 2008, ApJ, 689, 1044
Giersz M., Heggie D. C., 1994, MNRAS, 268, 257
Gillessen S., et al., 2017, ApJ, 837, 30
Giral Martínez J., Fouvry J.-B., Pichon C., 2020, MNRAS, 499, 2714
Goldstein H., 1980, Classical Mechanics. Addison-Wesley
Gould A., Quillen A. C., 2003, ApJ, 592, 935
Gravity Collab. et al., 2020, A&A, 636, L5
Gravity Collab. et al., 2021, A&A, 645, A127
Gravity+ Collab. et al., 2022, The Messenger, 189, 17
Gravity Collab. et al., 2023, A&A, 672, A63
Gruzinov A., Levin Y., Zhu J., 2020, ApJ, 905, 11
Guo M., Du M., Ho L. C., Debattista V. P., Zhao D., 2020, ApJ, 888, 65
Guth A. H., 1981, Phys. Rev. D., 23, 347
Habibi M., et al., 2017, ApJ, 847, 120
Hachisu I., 1979, PASJ, 31, 523
Hachisu I., 1982, PASJ, 34, 313
Haehnelt M. G., Rees M. J., 1993, MNRAS, 263, 168
Hamilton C., 2021, MNRAS, 501, 3371
Hamilton C., 2023, arXiv: 2302.06602,
Hamilton C., Heinemann T., 2020, arXiv: 2011.14812,
Hamilton C., Heinemann T., 2023, arXiv: 2304.07275,
Hamilton C., Fouvry J.-B., Binney J., Pichon C., 2018, MNRAS, 481, 2041
Hammer F., Flores H., Elbaz D., Zheng X. Z., Liang Y. C., Cesarsky C., 2005, A&A, 430, 115
Harris W. E., 1991, Ann. Rev. Astron. Astrophys., 29, 543
Harris W. E., Racine R., 1979, Ann. Rev. Astron. Astrophys., 17, 241
Hartle J. B., 2003, Gravity: An Introduction to Einstein's General Relativity, illustrate edn. Benjamin Cummings
Hasan H., Norman C., 1990, ApJ, 361, 69
Haslbauer M., Banik I., Kroupa P., Wittenburg N., Javanmardi B., 2022, ApJ, 925, 183
Hees A., et al., 2017, Phys. Rev. Lett., 118, 211101
Heggie D., Hut P., 2003, The Gravitational Million-Body Problem. Cambridge University Press
Heggie D. C., Retterer J. M., priv., Resonant Relaxation in Nonuniform Stellar Systems
Hénon M., 1958, Annales d'Astrophysique, 21, 186
Hénon M., 1961, Annales d'Astrophysique, 24, 369
Hénon M., 1964, Annales d'Astrophysique, 27, 83
Hénon M., 1971, APSS, 14, 151
Hénon M., 1973, in Contopoulos G., Henon M., Lynden-Bell D., eds, Saas-Fee Advanced Course 3: Dynamical Structure and Evolution of Stellar Systems. p. 183
Hernquist L., Ostriker J. P., 1992, ApJ, 386, 375
Heyvaerts J., 2010, MNRAS, 407, 355
Hills J. G., 1988, Nature, 331, 687
Hinshaw G., et al., 2013, ApJS, 208, 19
Hockney R. W., Eastwood J. W., 1988, Computer simulation using particles. CRC Press
Hohl F., 1971, ApJ, 168, 343
Hong J., Kim E., Lee H. M., Spurzem R., 2013, MNRAS, 430, 2960
Hopkins P. F., et al., 2018, MNRAS, 480, 800
Ichimaru S., 1973, Basic Principles of Plasma Physics: A Statistical Approach. W. A. Benjamin
Inagaki S., Hachisu I., 1978, PASJ, 30, 39
Inagaki S., Wiyanto P., 1984, PASJ, 36, 391
Jalali M. A., Hunter C., 2005, ApJ, 630, 804
Jeans J. H., 1915, MNRAS, 76, 70
Jin S., et al., 2023, MNRAS,
Jindal A., Webb J. J., Bovy J., 2019, MNRAS, 487, 3693
Joyce M., Morand J., Viot P., 2016, Phys. Rev. E., 93, 052129
Kalnajs A. J., 1976, ApJ, 205, 745
Kalnajs A. J., 1977, ApJ, 212, 637
Kamann S., et al., 2018, MNRAS, 473, 5591
Kamlah A. W. H., et al., 2022, MNRAS, 516, 3266
Katz N., Kereš D., Dave R., Weinberg D. H., 2003, in The IGM/Galaxy Connection. The Distribution of Baryons at z=0. p. 185
Kaviraj S., et al., 2017, MNRAS, 467, 4739
Kereš D., Katz N., Weinberg D. H., Davé R., 2005, MNRAS, 363, 2
Kim E., Lee H. M., Spurzem R., 2004, MNRAS, 351, 220
Kim E., Yoon I., Lee H. M., Spurzem R., 2008, MNRAS, 383, 2
King I. R., 1966, AJ, 71, 64
Klimontovich Y. L., 1967, The statistical theory of non-equilibrium processes in a plasma. Pergamon Press
Kocsis B., Tremaine S., 2011, MNRAS, 412, 187
Kocsis B., Tremaine S., 2015, MNRAS, 448, 3265
Kontizas E., Kontizas M., Sedmak G., Smareglia R., 1989, AJ, 98, 590
Koposov S. E., et al., 2019, MNRAS, 491, 2465
Kormendy J., Richstone D., 1995, Ann. Rev. Astron. Astrophys., 33, 581
Koushiappas S. M., Bullock J. S., Dekel A., 2004, MNRAS, 354, 292
Kuijken K., Dubinski J., 1994, MNRAS, 269, 13
Landau L., 1936, Phys. Z. Sowjetunion, 10, 154–164
Langevin P., 1908, Compt. Rendus, 146, 530
Lanzoni B., et al., 2018, ApJ, 865, 11
Larson R. B., 1998, MNRAS, 301, 569
Lau J. Y., Binney J., 2019, MNRAS, 490, 478
Lee H. M., 1987, ApJ, 319, 801
Lenard A., 1960, Annals of Physics, 10, 390
Levin Y., 2006, MNRAS, 374, 515
Lightman A. P., Shapiro S. L., 1978, Rev. Mod. Phys., 50, 437
Lin C. C., Shu F. H., 1964, ApJ, 140, 646
Linde A. D., 1982, Physics Letters B, 108, 389
Livernois A. R., Vesperini E., Varri A. L., Hong J., Tiongco M., 2022, MNRAS, 512, 2584
Loeb A., Rasio F. A., 1994, ApJ, 432, 52
Longaretti P.-Y., Lagoute C., 1997, A&A, 319, 839
Loveday J., 1996, MNRAS, 278, 1025
Lynden-Bell D., 1960, MNRAS, 120, 204
Lynden-Bell D., 1967, MNRAS, 136, 101
Lynden-Bell D., 1979, MNRAS, 187, 101
Lynden-Bell D., 2015, MNRAS, 447, 1962
Madau P., Dickinson M., 2014, ARAA, 52, 415
Madigan A.-M., Levin Y., 2012, ApJ, 754, 42
Madigan A.-M., Levin Y., Hopman C., 2009, ApJ, 697, L44
Magnan N., Fouvry J.-B., Pichon C., Chavanis P.-H., 2022, MNRAS, 514, 3452
Magorrian J., 2021, MNRAS, 507, 4840
Magorrian J., et al., 1998, AJ, 115, 2285
Makino J., Taiji M., Ebisuzaki T., Sugimoto D., 1997, ApJ, 480, 432
Marcos B., Gabrielli A., Joyce M., 2017, Phys. Rev. E., 96, 032102
Maréchal L., Perez J., 2011, Transport. Theory. Stat., 40, 425
Masters K. L., et al., 2011, MNRAS, 411, 2026
McLaughlin D. E., van der Marel R. P., 2005, ApJs, 161, 304
Meiron Y., Kocsis B., 2019, ApJ, 878, 138

Melia F., Falcke H., 2001, Ann. Rev. Astron. Astrophys., 39, 309

Melvin T., et al., 2014, MNRAS, 438, 2882

Merritt D., 2009, ApJ, 694, 959

Merritt D., 2013, Dynamics and Evolution of Galactic Nuclei. Princeton University Press

Merritt D., Vasiliev E., 2011, ApJ, 726, 61

Merritt D., Alexander T., Mikkola S., Will C. M., 2011, PrD, 84, 044024

Meylan G., Heggie D. C., 1997, Astron. Astrophys. Rev., 8, 1

Mikkola S., Aarseth S. J., 1990, Celest. Mech. Dyn. Astro., 47, 375

Miocchi P., et al., 2013, ApJ, 774, 151

Moetazedian R., Polyachenko E. V., Berczik P., Just A., 2017, A&A, 604, A75

Morbidelli A., 2002, Modern celestial mechanics : aspects of solar system dynamics. CRC Press

Murali C., Katz N., Hernquist L., Weinberg D. H., Davé R., 2002, ApJ, 571, 1

Murphy B. W., Cohn H. N., Durisen R. H., 1991, ApJ, 370, 60

Murray C. D., Dermott S. F., 2000, Solar System Dynamics. Cambridge University Press

Nair P. B., Abraham R. G., 2010, ApJs, 186, 427

Nakamura O., Fukugita M., Brinkmann J., Schneider D. P., 2004, AJ, 127, 2511

Noguchi M., 1987, MNRAS, 228, 635

Noguchi M., 1996, ApJ, 469, 605

Palmer P. L., Papaloizou J., Allen A. J., 1990, MNRAS, 243, 282

Park M. J., et al., 2021, ApJS, 254, 2

Peißker F., Eckart A., Parsa M., 2020, ApJ, 889, 61

Perets H. B., Hopman C., Alexander T., 2007, ApJ, 656, 709

Peschken N., Łokas E. L., 2019, MNRAS, 483, 2721

Pichon C., Aubert D., 2006, MNRAS, 368, 1657

Pichon C., Cannon R. C., 1997, MNRAS, 291, 616

Pichon C., Pogosyan D., Kimm T., Slyz A., Devriendt J., Dubois Y., 2011, MNRAS, 418, 2493

Pillepich A., et al., 2018, MNRAS, 473, 4077

Planck Collaboration et al., 2016, A&A, 594, A1

Planck Collaboration et al., 2020, A&A, 641, A6

Plionis M., Basilakos S., 2002, MNRAS, 329, L47

Plummer H. C., 1911, MNRAS, 71, 460

Polyachenko E. V., Just A., 2015, MNRAS, 446, 1203

Polyachenko V. L., Shukhman I. G., 1982, SovAst, 26, 140

Portegies Zwart S. F., McMillan S. L. W., 2002, ApJ, 576, 899

Pott J.-U., et al., 2018, in Ground-based and Airborne Instrumentation for Astronomy VII. p. 1070290

Quinlan G. D., 1996, New. Astron., 1, 255

Quinlan G. D., Shapiro S. L., 1989, ApJ, 343, 725

Rauch K. P., Tremaine S., 1996, New. Astron., 1, 149

Reddish J., et al., 2022, MNRAS, 512, 160

Richstone D., et al., 1998, Nature, 385, A14

Risken H., 1996, The Fokker-Planck Equation, 2nd edn. Springer, Berlin

Rosas-Guevara Y., et al., 2020, MNRAS, 491, 2547

Rosas-Guevara Y., et al., 2022, MNRAS, 512, 5339

Rosenbluth M. N., MacDonald W. M., Judd D. L., 1957, Phys. Rev., 107, 1

Roule M., Fouvry J.-B., Pichon C., Chavanis P.-H., 2022, Phys. Rev. E., 106, 044118

Rozier S., Fouvry J.-B., Breen P. G., Varri A. L., Pichon C., Heggie D. C., 2019, MNRAS, 487, 711

Safronov V. S., 1960, Annales d'Astrophysique, 23, 979

Sanders J. L., Binney J., 2016, MNRAS, 457, 2107

Schlegel D. J., Finkbeiner D. P., Davis M., 1998, ApJ, 500, 525

Schödel R., et al., 2017, A&A, 609, A27

Sellwood J. A., 2012, ApJ, 751, 44

Sellwood J. A., 2015, MNRAS, 453, 2919

Sellwood J. A., Valluri M., 1997, MNRAS, 287, 124

Seth A., Agüeros M., Lee D., Basu-Zych A., 2008a, ApJ, 678, 116

Seth A. C., Blum R. D., Bastian N., Caldwell N., Debattista V. P., 2008b, ApJ, 687, 997

Shen J., Sellwood J. A., 2004, ApJ, 604, 614

Sollima A., Baumgardt H., Hilker M., 2019, MNRAS, 485, 1460

Spitzer L., 1975, in Dynamics of the Solar Systems. p. 3

Spitzer L., 1978, Physical processes in the interstellar medium. Wiley-Interscience Publication

Spitzer L., 1987, Dynamical evolution of globular clusters. Princeton Univ. Press

Spitzer L., Shapiro S., 1972, ApJ, 173, 529

Spitzer L., Shull J., 1975, ApJ, 200, 339

Springel V., 2005, MNRAS, 364, 1105

Springel V., et al., 2005, Nature, 435, 629

Springel V., Frenk C. S., White S. D. M., 2006, Nature, 440, 1137

Stetson P. B., Pancino E., Zocchi A., Sanna N., Monelli M., 2019, MNRAS, 485, 3042

Stäckel P., 1889, Mathematische Annalen, 35, 91

Szölgyén Á., Kocsis B., 2018, PRL, 121, 101101

Szölgyén Á., Meiron Y., Kocsis B., 2019, ApJ, 887, 123

Szölgyén Á., Máthé G., Kocsis B., 2021, ApJ, 919, 140

Takahashi K., 1993, PASJ, 45, 233

Tep K., Fouvry J.-B., Pichon C., Heißel G., Paumard T., Perrin G., Vincent F., 2021, MNRAS, 506, 4289

Tep K., Fouvry J.-B., Pichon C., 2022, MNRAS, 514, 875

The LIGO Scientific Collaboration et al., 2019, Phys. Rev. D, 100, 064064

Theuns T., 1996, MNRAS, 279, 827

Tiongco M., Vesperini E., Varri A. L., 2016, MNRAS, 461, 402

Tiongco M., Vesperini E., Varri A. L., 2020, in Star Clusters: From the Milky Way to the Early Universe. pp 524–527

Tiongco M., Collier A., Varri A. L., 2021, MNRAS, 506, 4488

Tiongco M., Vesperini E., Varri A. L., 2022, MNRAS, 512, 1584

Toomre A., 1963, ApJ, 138, 385

Toomre A., 1969, ApJ, 158, 899

Toomre A., 1981, in Structure and Evolution of Normal Galaxies. pp 111–136

Tormen G., 1997, MNRAS, 290, 411

Torrielli A., 2016, J. Phys. A Math. Theor., 49, 323001

Touma J. R., Tremaine S., Kazandjian M. V., 2009, MNRAS, 394, 1085

Trager S. C., King I. R., Djorgovski S., 1995, AJ, 109, 218

Trefethen L. N., Weideman J. A. C., 2014, SIAM Review, 56, 385

Tremaine S., 2005, ApJ, 625, 143

Tremaine S., Weinberg M. D., 1984, MNRAS, 209, 729

Trenti M., Hut P., 2008, arXiv:0806.3950,

Ueda T., Noguchi M., Iye M., Aoki S., 1985, ApJ, 288, 196

Umemura M., Loeb A., Turner E. L., 1993, ApJ, 419, 459

Varri A. L., Bertin G., 2012, A&A, 540, A94

Vasiliev E., 2015, MNRAS, 446, 3150

Vasiliev E., 2017, ApJ, 848, 10

Vasiliev E., 2019a, MNRAS, 482, 1525

Vasiliev E., 2019b, MNRAS, 489, 623

Vesperini E., Varri A. L., McMillan S. L. W., Zepf S. E., 2014, MNRAS, 443, L79

Vogelsberger M., et al., 2014, MNRAS, 444, 1518

Vogelsberger M., Marinacci F., Torrey P., Puchwein E., 2020, Nature Reviews Physics, 2, 42

Wang L., Spurzem R., Aarseth S., Nitadori K., Berczik P., Kouwenhoven M. B. N., Naab T., 2015, MNRAS, 450, 4070

Wasserman L., 2004, All of Statistics: A Concise Course in Statistical Inference. Springer, New York

Watkins L. L., van der Marel R. P., Bellini A., Anderson J., 2015, ApJ, 803, 29

Webb J. J., Hunt J. A. S., Bovy J., 2023, MNRAS,

Weinberg M. D., 1993, ApJ, 410, 543

Weinberg M. D., 1998, MNRAS, 297, 101

Weinberg M. D., 2001a, MNRAS, 328, 311

Weinberg M. D., 2001b, MNRAS, 328, 321

Weinberg M. D., 2015a, arXiv: 1508.06855,

Weinberg M. D., 2015b, arXiv: 1508.05959,

Weinberg D. H., Mortonson M. J., Eisenstein D. J., Hirata C., Riess A. G., Rozo E., 2013, Phys. Rep., 530, 87

West M. J., 1994, MNRAS, 268, 79

White R. E., Shawl S. J., 1987, ApJ, 317, 246

Wilson C. P., 1975, AJ, 80, 175

Wisnioski E., et al., 2019, ApJ, 886, 124

Yelda S., et al., 2014, ApJ, 783, 131

Yi S.-K., et al., 2023, in prep.

Zana T., Dotti M., Capelo P. R., Bonoli S., Haardt F., Mayer L., Spinoso D., 2018, MNRAS, 473, 2608

Zhao D., Du M., Ho L. C., Debattista V. P., Shi J., 2020, ApJ, 904, 170

Zhou Z.-B., Zhu W., Wang Y., Feng L.-L., 2020, ApJ, 895, 92

de Jong R. S., et al., 2019, The Messenger, 175, 3

de Vaucouleurs G., 1963, ApJs, 8, 31

von Hoerner S., 1960, Z. Astrophys., 50, 184

Long résumé

L'étude de l'évolution à long terme des objets astrophysiques est une tâche difficile en raison de la nature complexe et non-linéaire des processus impliqués. La gravité, une interaction à longue portée, joue un rôle fondamental dans l'évolution des objets les plus massifs de l'Univers, donnant lieu à la formation de structures complexes telles que les galaxies et les amas stellaires comme les amas globulaires. Au fil des ans, les physiciens ont utilisé trois techniques principales pour relever ce défi, à savoir l'observation, la simulation et la théorie cinétique.

Les dernières décennies ont été marquées par des avancées significatives dans les techniques d'observation, notamment l'utilisation d'instruments – tels que le télescope spatial Hubble (HST), le Very Large Telescope (VLT) et la mission GAIA – qui ont permis d'améliorer considérablement la précision des observations. Ces observations ont révélé que les amas globulaires, que l'on pensait isotropes et sans rotation, présentent une anisotropie et une rotation à des degrés divers. De même, la spectroscopie intégrale de champ a permis de mieux comprendre les propriétés cinématiques des galaxies sphéroïdales et des amas stellaires (e.g., des amas globulaires ou le noyau Galactique), mettant en lumière leur histoire dynamique passée et le rôle du moment angulaire.

Le modèle Λ-CDM s'est imposé comme étant la description la plus précise de l'Univers. Ce modèle retrace l'évolution de l'Univers depuis les premiers stades après le Big Bang jusqu'à la formation des structures à grande échelle. Les fluctuations du champ quantique dans la densité de la matière noire non baryonique, suivies d'une période d'inflation, ont donné lieu aux fluctuations de température observées dans le fond diffus cosmologique. La gravité a amplifié ces fluctuations de densité au fil du temps, conduisant à la formation hiérarchique de régions surdenses où les galaxies se sont développées.

Les galaxies et les autres objets astrophysiques sont influencés par une combinaison de perturbations violentes et plus douces provenant de sources internes et externes. Les événements violents tels que les fusions avec d'autres galaxies ou les explosions de supernova, ainsi que les perturbations plus douces telles que les injections de gaz froid, peuvent avoir un impact sur leur évolution. En outre, la nature finie de ces systèmes et les fluctuations de Poisson qu'ils subissent peuvent également conduire à une évolution lente et à long terme. L'évolution séculaire, induite par l'interaction entre ces perturbations internes et externes, peut donner lieu à des phénomènes tels que la formation de barres dans les centres de galaxies.

Plusieurs facteurs motivent l'étude de l'évolution à long terme de ces objets astrophysiques. La disponibilité de nouvelles données provenant d'études telles que GAIA et les progrès de la théorie cinétique gravitationnelle permettent l'étude des mécanismes opérant sur des échelles de temps séculaires. Ces modèles analytiques peuvent aider à clarifier les mécanismes sous-jacents cachés dans les simulations numériques et donner un aperçu de l'impact de l'anisotropie et de la rotation sur l'évolution des amas stellaires.

Dans cette thèse, j'étudie le domaine complexe de la relaxation séculaire et de ses implications pour divers systèmes astrophysiques. Je présente des résultats qui éclairent le comportement des systèmes autogravitants sur le long terme. Ces résultats, obtenus grâce à divers formalismes et techniques, donnent un aperçu de phénomènes tels que la diffusion orbitale dans les noyaux galactiques, les amas globulaires, les amas en rotation, et les disques galactiques minces autogravitants. Mes travaux cherchent à : (i) comprendre les mécanismes particuliers qui opèrent sur ces échelles de temps longs ; (ii) identifier l'origine des différences observées en fonction de la nature de ces objets (géométrie, cinématique, composition...) ; (iii) déduire des diagnostics pour des expériences de matière noire (par exemple, l'identification des populations de trous noirs de masse intermédiaire).

Le chapitre 2 pose les bases en revisitant la théorie de la diffusion orbitale. J'explore le destin séculaire des systèmes isolés et autogravitants, en m'appuyant sur l'équation de Balescu–Lenard, qui décrit la théorie cinétique de leur évolution. Cette équation s'avère polyvalente, permettant d'expliquer l'amplification des fluctuations et l'apparition de crêtes de résonance dans l'espace d'action. Pour les amas sphériques anisotropes, il semble cependant que l'emphase mise par cette équation sur l'amplification résonante soit peu pertinente. Dans ces cas, d'autres approximations, telles que l'équation de Landau inhomogène et l'équation classique de Chandrasekhar, offrent des descriptions plus utiles.

Le chapitre 3 se concentre sur la structure du noyau galactique. En utilisant le formalisme de Landau, j'infère la présence d'objets lourds non résolus, potentiellement des trous noirs de masse intermédiaire, à l'intérieur de l'amas S. J'identifie les régions de l'espace orbital où la diffusion est efficace. Ainsi, en m'appuyant sur les données d'observation, je mène une analyse de vraisemblance pour contraindre la présence de trous noirs de masse intermédiaire dans l'amas galactique. Remarquablement, mes prédictions s'alignent sur des études récentes indépendantes.

Le chapitre 4 explore le comportement des amas globulaires sans rotation. En étendant le formalisme de relaxation non-résonante aux amas anisotropes, je dérive l'équation de Fokker–Planck moyennée sur les orbites afin de décrire l'évolution séculaire de la distribution orbitale. La théorie non-résonante capture avec succès la diffusion orbitale observée dans les moyennes statistiques des simulations numériques directes, au prix d'un préfacteur numérique dépendant peu des paramètres orbitaux. Une approche pseudo-isotrope offre une méthode de calcul efficace pour obtenir une bonne adéquation avec les observations numériques. Je souligne les limites du formalisme non-résonant dans la description des systèmes plus froids et discute du lien entre celui-ci et les ordres harmoniques supérieurs de la théorie de Landau inhomogène.

Dans le chapitre 5, j'élargis la théorie cinétique pour inclure les amas en rotation, qui sont dynamiquement plus froids et présentent une dispersion de vitesse plus faible. En analysant l'impact de la rotation sur l'espace orbital à travers l'équation de Fokker–Planck bi-dimensionnelle, je montre que la rotation n'affecte pas de manière significative la relaxation radiale. Contrairement aux travaux précédents, je n'observe pas de catastrophe gravo-gyro. De plus, alors que la théorie NR prédit avec précision la relaxation radiale, elle ne parvient pas à prédire la relaxation azimutale sourcée par des interactions cohérentes entre les orbites. Les limites de la théorie NR dans les systèmes froids motivent une implémentation future de la relaxation résonante vectorielle.

Le chapitre 6 se concentre sur l'évolution séculaire des disques minces autogravitants, en particulier la croissance des barres. Après avoir réécrit ce problème en une recherche de valeurs propres, j'étudie la dépendance des taux de croissance de la barre par rapport à la géométrie de la galaxie. En comparant ces résultats aux simulations hydrodynamiques, j'explique la rareté des barres observées dans les simulations, en montrant que la plupart des galaxies se situent dans une région des paramètres associée à un faible taux de croissance qui empêche la formule d'instabilités bi-symétriques. Une unique galaxie barrée avec un taux de croissance relativement plus élevé fait figure d'exception.

Pour conclure, cette thèse illustre la pertinence et l'efficacité croissantes de la relaxation séculaire pour expliquer divers phénomènes astrophysiques. La théorie cinétique est un outil pertinent pour interpréter les données d'observation, effectuer des analyses de vraisemblance et faire des prédictions robustes. Elle complète les simulations numériques et hydrodynamiques en capturant les différents phénomènes non-linéaires en jeu afin de construire des estimateurs explicites. Avec l'augmentation constante de la taille des échantillons de données et les progrès des simulations, la nature flexible et paramétrique de la théorie cinétique séculaire moderne s'avère donc inestimable pour démêler la complexité des systèmes autogravitants à différentes échelles de temps et d'espace.